UNIVERSIDAD COMPLUTENSE DE MADRID

FACULTAD DE CIENCIAS FÍSICAS

Departamento de Física Atómica, Molecular y Nuclear

TESIS DOCTORAL

Time domain image reconstruction methods for transmission ultrasound computed tomography

Métodos de reconstrucción en dominio temporal para tomografía por transmisión de ultrasonidos

MEMORIA PARA OPTAR AL GRADO DE DOCTOR

PRESENTADA POR

Mailyn Pérez Liva

Directores

José Manuel Udías Moinelo
Joaquín López Herraiz

Madrid, 2017

UNIVERSIDAD COMPLUTENSE DE MADRID
FACULTAD DE CIENCIAS FÍSICAS
Departamento de Física Atómica, Molecular y Nuclear

TESIS DOCTORAL:

TIME DOMAIN IMAGE RECONSTRUCTION METHODS FOR TRANSMISSION ULTRASOUND COMPUTED TOMOGRAPHY

Métodos de Reconstrucción en Dominio Temporal para Tomografía por Transmisión de Ultrasonidos

---

Realizada por:
Mailyn Pérez Liva

Directores:
Dr. José Manuel Udías Moinelo
Dr. Joaquín López Herraiz

A mis padres: Marilyn y Eduardo,
a mis abuelitos: Pilar y José,
y a Edu.

No hay dicha mayor en este
mundo que el amor que recibo
de cada uno de ustedes.

“Science is not only a disciple of reason but, also, one of romance and passion.”

— *Stephen Hawking*

Agradecimientos

"No hacen falta alas para hacer un sueño,
basta con las manos, basta con el pecho,
basta con las piernas y con el empeño.
No hacen falta alas para alzar el vuelo"

Silvio Rodríguez

¡Finalmente! Llevo mucho tiempo queriendo escribir estos agradecimientos, porque significan el fin de un largo camino y de una de las etapas más trascendentales de mi vida. Han sido varios años de mucho esfuerzo y muchos sacrificios, pero también de muchas alegrías y momentos especiales que recordaré por siempre. Estoy segura de ello. Por eso, quiero agradecer a todos los que han hecho posible que esta etapa haya sido tan especial en mi vida.

En primer lugar, quiero dar las gracias a mis directores. A José Manuel, que me dio la tremenda oportunidad de venir desde mi islita y me abrió las puertas del GFN. Muchas gracias por todo lo que me has enseñado, he aprendido mucho de ti. Gracias por todos los consejos, oportunidades y revisiones, en esto último debo agradecer también a tus niñas que hicieron un gran trabajo pictórico en el manuscrito de correcciones :-). A Joaquín, muchísimas gracias por el entusiasmo que le pones a todo, y por toda tu ayuda siempre. He disfrutado mucho de todas las reflexiones, no sólo acústicas :-) (chiste a tu estilo jeje) de cualquier tema de ciencia, pero sobre todo, muchas gracias por la confianza y el apoyo.

En mi criterio, lo que hace al GFN tan especial, es su gente, que te hace sentir como en familia a los pocos días de llegar. En este sentido las primeras y más gigantes gracias son para mis gallinitas: Pau, Vicky, Esther, Elena y Marie, tengo los mejores recuerdos de nuestra etapa juntas, me divertí muchísimo, las quiero muchísimo, son las mejores amigas que se puede tener, y sobre todo, gracias porque a pesar de la distancia, cuando nos vemos parece que no ha pasado el tiempo. No obtante, siento que tengo que dar un agradecimiento muy especial a Pau y a Vicky, que me han soportado como titanes en estos últimos momentos de agonía con la tesis. Gracias por todas las risas, por estar siempre, las cañitas, las salidas, el hombro donde echar alguna lagrimita, por nuestras locuras, nuestros disfraces, nuestros viajes, muchas gracias por ser tan especiales mis preciosas!, por cierto, es viernes? Eeeeooooo, eeeeo, no podía faltar mencionar la canción de la banana.

También quiero agradecer a los integrantes del clan inicial del 'gallinitas y cerditos', con los

que he compartido tantos buenos momentos! A Jacobiño (lo sabes Jaco, ninguno olvidaremos jamás tu bar de las aceitunas y tu Ay! la Leti, ah! y el tántántántántán tán!). Al Vadymaco, por su gran corazón, a Richy-chop (que ha cambiado el nombre de los palillos a 'Richys' para siempre), a Armando (fiel compi del desayuno). A Bruno y Esteban, que siempre fueron tan geniales conmigo. A Borja, Alex, Pablo, Cris, Raquel, Laura, Cesar, Rocío, Paloma, Natalia, Luis Mario: muchas gracias a todos por los excelentes momentos compartidos.

Cuando todos los gfn_itos iniciales se fueron pensábamos que no superaríamos la tristeza, pero es lo que tiene el grupo, un día, sin darte cuenta, pasas de ser el pequeño y te conviertes en el veterano, pero eso sí, la gente buena nunca falta a tu alrededor. Y aparecieron los pequeños: Amaia, Jaime, Victor, Pablo, Alex, Oli, que nos han vuelto a llenar de alegrías, tenemos garantizado un buen relevo, ah! y llegaron también algunos no tan pequeños, y hasta con teléfono fijo! y sabes que va por ti Dani.

Muchas gracias también a los amigos de los despachos vecinos, Tarek, Simón, David, Rafita, Marco, gracias chicos! nunca olvidaré los paseos en el pasillo en el patinete Simón cuando faltaba internet!

De la etapa del máster me gustaría agradecer a todos los compañeros: Maribel, eah!, Gabi, Sergio, Jesus, los Guilles, Fran, Robert, Antonio, Juanma, Pablo, Albert, Karina diversión a chorros! y las clases ni se siga ;-)

De mi etapa por Boston, quiero agradecer a Eric Miller, it was great to meet you and also to work with you! thanks for the opportunity! También por ahí quiero agradecer a Joaquín, a Ele, Borja, Adrian, Shivi, Oscar. Fue muy divertido!

De mi estancia en Londres quiero dar las gracias a Bradley Treeby y Ben Cox: thanks a lot for everything, to work with you was one of the best experiences of my PhD. Also, I would like to thank my office mates in BUG: Panayotis, Elly, Michael, Elliot and Lois for being so nice with me.

Muchas gracias a Carlos Fritsch, a Jorge Camacho, a Luis y a Nuria, en el CSIC, por toda la ayuda que me han dado, por estar siempre disponibles cuando lo he necesitado, mil gracias por todo.

También quiero agradecer a Ana Guitierrez, que ha sido como una madre para mi aquí en Madrid y a Carmen, Rían, Conchita.

Muchas gracias a Rosa, Guillermo y Ali por acogerme en su familia y por todo el cariño. A Fede, Zarita, Emi, muchas gracias muchachos por la amistad, por todos esos momentos felices que hemos pasado juntos. A los cubanitos en los madriles: Gilber, Janet, Haydee y Ale. A mis queridos Lipri y Gilber que aunque lejos siempre se preocupan por mi y siento su cariño a pesar de la distancia. A Ali y a Jonhny por la buena amistad. A Leo, Juano, los Camis, Suse, Lili, Carlos, Fati, Neivy, Ali, Yuca, Fela, a todos mis profes y amigos del Instec que han mantenido el contacto a pesar de los años y la distancia.

Y finalmente, mis gracias más especiales son para mi familia. A mis padres, el más grande y mejor ejemplo de mi vida, gracias por inculcarme el amor a la ciencia, la curiosidad y la entrega

profesional, gracias por todo el amor, el apoyo, las fuezas. Ustedes son los mejores padres del mundo y los quiero mucho. A mis abuelitos, que son lo más dulce y lo más precioso que hay. Ustedes saben todo lo que los quiero, y la alegría que veo en sus ojos cuando logro alguna cosa, por pequeña que sea, es un impulso tremendo. A mi hermano y mi sobri Diego, muchas gracias por todo el cariño, los adoro. Al tío Hecti, que sé que esta tesis le dará mucha alegría. Y a mi querido Edu, como le digo siempre, que se ha ganado el cielo con la carga que le ha tocado (o sea, yo), muchas gracias por tu cariño y tu apoyo incondicional, por tirar de mi cuando he perdido las fuerzas, es una dicha muy grande tenerte, te quiero muchísimo.

¡Y ya está! ¡ahora a leer la tesis! ¡Muchas gracias a todos!

Contents

List of Figures

List of Tables

Summary

Summary

Introduction and objectives

Breast cancer (BC) is the leading cause of cancer-related death for women in Europe, and the second one after lung cancer in the US [World Cancer Report, 2008]. Early detection is very important for the survival rate of BC, because the smaller the local extension of the neoplasia, the better the output of the surgical treatments employed. Besides, early detection increases the possibility of preserving the breast and decreases the probability of needing more invasive treatments [Secretaría de Salud, 2007, Alteri et al., 2011].

Mammography is currently the standard procedure employed for breast screening programs around the world. Nevertheless, its efficiency has been questioned lately because: (i) it generates many abnormal findings not related to cancer, (ii) it requires irradiating the patient and (iii) it has low specificity with dense breasts [Santen and Mansel, 2005]. Consequently, complementary techniques to mammography are being proposed to improve the detection and characterization of BC. Among these techniques, is the Ultrasound Computed Tomography (USCT), in reflection mode (which provides qualitative maps with the concentration of scatterers in the tissue), and transmission mode (which provides quantitative maps of the sound speed (SS) and the acoustic attenuation (AA) of the tissues). The images provided by the transmission modality have been proposed for BC detection as they can improve the detectability of malignancies in the breast [Mast, 2000, Duric et al., 2009].

In this thesis, the main goal was to set up the transmission modality of USCT in the scanner MUBI, which was created as part of the collaboration of the Ultrasound Systems and Technology Group of the CSIC (USTG-CSIC), and the Nuclear Physics Group of the UCM (GFN-UCM), under the project TOPUS [S2013/MIT-3024, 2013-2017]. Methods for data processing and image reconstruction techniques were developed and implemented to this end. More specifically, we were interested in developing methods for data processing and relevant parameters extraction from the recorded data. We also aimed to implement fast geometrical acoustics methods to obtain both the SS and the AA. W investigated ways to improve the image quality by using of full wave inversion reconstruction. Finally, we aimed to apply the developed methods to the reconstruction of real data obtained from the MUBI scanner.

Materials and methods

Image reconstruction methods in USCT can be separated into two main types: Geometrical Acoustics (GAc) methods and Full Wave Inversion (FWI) method. GAc reconstruction methods are based on a high frequencies approximation that simulates the energy propagation of the waves by means of rays. These methods are computationally efficient but provide lower resolution than FWI methods, as the later employ a computational model to solve the acoustic wave equation.

GAc methods use accurate estimations of the time of flight (TOF) and the amplitude of the signals to perform the reconstructions. We analyzed three methods to estimate the TOF: (i) the maximum method, (ii) the threshold method and (iii) the cross-correlation method. For the amplitude estimation we analyzed two methods: (i) the maximum method and (ii) the maximum of the envelope method. We used synthetic data to test the before mentioned methods.

We studied two types of GAc methods: using straight and bent rays. The former can be done through an analytic reconstruction based on the Radon transform. The later includes the effect of refraction due to changes of impedance in the tissues and are performed by means of iterative algorithms. We implemented a classical bent-rays method based on the Fast Marching Method (FMM) and compared its performance against a simple, fast and straightforward method for bent-rays based on the Bézier polynomials, firstly proposed in this thesis.

Regarding the FWI reconstructions, in this thesis a common framework in time domain to perform the reconstructions of both SS and AA was proposed. We used the Adjoint method [Pérez-Liva et al., 2017] to derive the functional gradients of the gradient-descent method used for reconstruction. To test the performance of the method, we used simulated data obtained with k-Wave [Treeby and Cox, 2010b], which is also the model used for forward and backward propagation in our FWI reconstructions. To improve the performance of our FWI reconstructions, we also proposed a generalized cost function that provides higher quality for the AA reconstruction and facilitates the obtainment of an initial model to update the SS distribution.

Finally, our methods were applied to the reconstruction of real data from the scanner MUBI. Several method for data processing and calibration of the scanner were analyzed. Tissue mimicking phantoms were studied.

Results and conclusions

In this thesis, we successfully included the transmission modality in the MUBI scanner. We provided several approaches for SS and AA reconstruction capable of producing fast and high quality images. To perform real-time reconstructions, we proposed to use analytical methods which are able to give general information of the inspected regions without the finest details. We obtained the TOF and amplitude values to feed our ray-based algorithms using the cross-

correlation and the envelope methods respectively, as these methods provided the best results among all the methods tested.

To improve the information provided by our analytic algorithm, our Bézier-based bent-rays method can be used during post-processing of the data for SS reconstructions. It provides fasted and higher-quality results in comparison with our implementation of the classical FMM. However, not considerable refinements were observed for the reconstruction of the AA with this method. GAc algorithms are not suitable to reconstruct high image quality AA maps.

In case that any suspicious region is observed (very high SS), complimentary information can be obtained from the FWI reconstruction of the AA, as this method provides high-quality reconstructions of both SS and AA properties. Further experimental tests are still required to fully validate our reconstruction algorithms. Nevertheless, either with the ray-based methods and the FWI, our algorithms have been tested with both synthetic and experimental data, showing very encouraging results in terms of quality and reconstruction times. We expect these results could be useful to expand and improve this promising technique.

Resumen en castellano

Introducción y objetivos

El cáncer de mama (CM) es el cáncer más mortal entre las mujeres europeas, y el segundo más común en Estados Unidos [World Cancer Report, 2008]. La detección temprana es un factor que condiciona en gran medida la tasa de supervivencia a esta enfermedad, ya que a menor tamaño de la neoplasia detectada, mejores resultados pueden esperarse para los tratamientos quirúrgicos que se realicen. Además, la detección temprana aumenta la posibilidad de conservar la mama después de la cirugía y disminuye la necesidad de emplear otros tratamientos más invasivos[Secretaría de Salud, 2007, Alteri et al., 2011].

La mamografía es actualmente el procedimiento estándar que se emplea para el cribado del CM. Sin embargo, en los últimas años su eficiencia está siendo muy cuestionada por varios factores: (i) alta tasa de falsos positivos, (ii) requiere la irradiación del paciente y (iii) baja especificidad en mamas densas 2. Debido a lo anterior, para mejorar la detección y caracterización del CM se han propuesto varias técnicas complementarias. Entre ellas está la tomografía ultrasónica (TU), que es una técnica en desarrollo que presenta dos modalidades principales: la reflexión (proporciona mapas cualitativos de la concentración de dispersores en el tejido) y la transmisión (proporciona mapas cuantitativos de la velocidad y atenuación del sonido en el tejido). Los mapas del modo transmisión han sido propuestos como una eficiente alternativa, libre de radiación, para la detección del CM, ya que proporcionan alto contraste y especificidad [Mast, 2000, Duric et al., 2009].

En esta tesis, el principal objetivo fue la habilitación de la modalidad de transmisión en el tomógrafo MUBI, desarrollado mediante la colaboración del grupo de Tecnologías y Sistemas Ultrasónicos del CSIC (USTG-CSIC) y el Grupo de Física Nuclear de la UCM (GFN-UCM). Para ello, primeramente nos centramos el desarrollo de métodos para el procesamiento y extracción de parámetros relevantes de las señales ultrasónicas obtenidas mediante medidas de transmisión. En segundo lugar, nos propusimos implementar un conjunto de algoritmos de alta eficiencia computacional usando acústica geométrica para reconstruir tanto mapas de velocidad como de atenuación. Adicionalmente, para mejorar la calidad de las imágenes reconstruidas, nos enfocamos en el estudio de métodos de reconstrucción de onda completa en dominio temporal. Finalmente, los métodos desarrollados fueron adaptados para ser aplicados a la reconstrucción de datos reales de nuestro tomógrafo MUBI.

Materiales y métodos

Los métodos de reconstrucción en TU se pueden dividir en dos grupos: métodos que emplean acústica geométrica (AG) y métodos de inversión de onda completa (OC). Los métodos de AG aproximan la propagación de las ondas ultrasónicas mediante rayos. Estos métodos son computacionalmente eficientes, pero proporcionan una resolución más baja que los métodos de OC, ya que estos últimos resuelven de modo preciso la ecuación de ondas acústica.

Los métodos de AG requieren estimaciones precisas del tiempo de vuelo (TdeV) y la amplitud de las señales. Para ello se analizaron tres métodos para la estimación del TdeV: (i) método del máximo valor, (ii) método de umbral y (iii) método de la correlación cruzada. Para la estimación de la amplitud se analizaron dos métodos: (i) método del máximo valor y (ii) método de la envolvente. Para comprobar los métodos mencionados se utilizaron datos sintéticos obtenidos con k-Wave [Treeby and Cox, 2010b].

Se estudiaron dos tipos de métodos basados en AG: empleando rayos rectos y curvos. El primero puede desarrollarse mediante una reconstrucción analítica basada en la transformada de Radon. El segundo incluye el efecto de la refracción debido a cambios de impedancia y tiene naturaleza iterativa. En este trabajo comparamos el desempeño de un método simple y rápido para la obtención de rayos curvos basado en polinomios de Bézier (propuesto en por primera vez en esta tesis) contra un método clásico de rayos curvos basado en el algoritmo de Fast Marching (FM).

Para las reconstrucciones de OC, en esta tesis se propuso por primera vez, un marco común en dominio temporal para realizar las reconstrucciones tanto de velocidad como de atenuación. Se utilizó el método adjunto [Pérez-Liva et al., 2017] para derivar los gradientes funcionales empleados para la reconstrucción. Para comprobar el método, se utilizaron datos simulados. Se propuso una función de coste generalizada que proporciona mayor calidad para la reconstrucción de atenuación y facilita la obtención de un modelo inicial para actualizar la velocidad.

Finalmente, nuestros métodos se aplicaron a la reconstrucción de datos reales de nuestro tomógrafo MUBI. Se analizaron varios métodos para el procesamiento de datos y la calibración del tomógrafo.

Resultados y conclusiones

En esta tesis, incluimos exitosamente la modalidad de transmisión en el tomógrafo MUBI. Para realizar reconstrucciones en tiempo real, proponemos utilizar nuestro método analítico que provee de información general de la región inspeccionada aunque sin proporcionar detalles finos. Los valores de TdeV y amplitud para nuestros algoritmos de rayos son obtenidos utilizando los métodos de correlación cruzada y de la envolvente respectivamente, ya que estos proporcionaron los mejores resultados entre todos los implementados.

La información obtenida con nuestro algoritmo analítico es mejorada usando el método

de rayos curvos propuesto basado polinomios de Bézier, pues ofrece resultados más rápidos y mejores en cuanto a calidad de imagen para reconstrucciones de velocidad comparado con nuestra implementación del clásico método FM. Sin embargo, no se observaron mejoras considerables para la reconstrucción de la atenuación con este método. Los algoritmos basados en AG no resultan adecuados para reconstruir mapas atenuación con alta calidad.

Del trabajo realizado en esta tesis también concluimos que en caso de que se observe alguna región sospechosa (muy alta velocidad), se puede obtener información complementaria a partir de la reconstrucción de OC de atenuación, ya que este método proporciona reconstrucciones de alta calidad tanto para la velocidad como para la atenuación pero en tiempos superiores.

Aún se requieren pruebas experimentales adicionales para validar completamente nuestros algoritmos de reconstrucción. Sin embargo, ya sea con los métodos de rayos o de OC, nuestros algoritmos han sido comprobados con datos tanto sintéticos como experimentales, demostrando resultados muy alentadores en términos de calidad y tiempos de reconstrucción. Esperamos que estos resultados puedan ser útiles para expandir y mejorar esta prometedora técnica.

General overview and motivation of this thesis

Breast cancer

Breast cancer (BC) is the leading cause of cancer-related death for women in Europe, and second one after lung cancer in the US. It comprises around the 23% of invasive cancers in women [World Cancer Report, 2008] and the 16% of all female cancers [World Health Organization, 2012]. This numbers can be even more alarming if one thinks that every 2.5 minutes a woman is diagnosed of BC in the European Union and every 7.5 minutes a woman will die for the disease [Barnett et al., 2005].

BC originates in the glandular tissues, also called lobes, and in the ducts that connect them with the nipple (see Fig. 1). This process produces regions in the breast of abnormal cells growing, and therefore, these regions present higher densities than normal tissue. The rest of the breast is mainly comprised by connectivity tissue and fat, which present a composition that can change with the age and other factors. The size at which the tumor is detected is determinant because, the larger the size, the higher the possibility of presenting dissemination (metastasis), by mean of the lymphatic and/or the hematic systems. The metastasis of BC mainly occurs through the lymphatic system. The lymph node that primary captures this process is known as the "Sentinel" ganglion, which is generally subjected to study to characterize the staging of the disease [Secretaría de Salud, 2007].

Early detection is a very important fact for the survival rate of BC: the 5 years survival rate for woman with BC larger than 20 mm is 80% and for 10 mm the survival rate is 98% [Alteri et al., 2011]. The smaller the local extension of the neoplasia, the better the output of the surgical treatments employed, increasing as well the possibility of preserving the breast. Moreover, early detection could also be useful to avoid the need for invasive treatments such as radiotherapy or chemotherapy, which could carry out side effects to the patient [Secretaría de Salud, 2007].

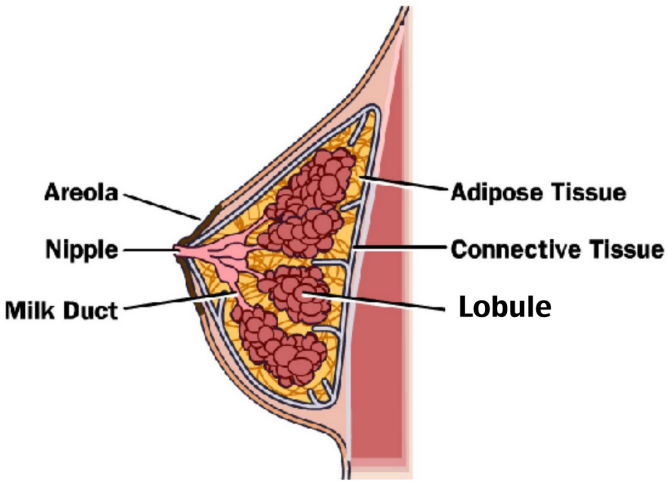

Figure 1: Schematic representation of the breast composition [Goldie, 2011]

For the aforementioned reasons, screening programs have been created. The BC screening consists on the regular examination by mean of imaging systems of women's breasts to help finding BC at an early stage.

Imaging systems for breast cancer studies

Mammography is currently the standard procedure employed for breast screening programs around the world. Even when at present the outcomes of mammography constitutes a very polemic topic, the most generalize criterion between clinicians is that periodic mammograms of age-appropriate asymptomatic women, helps decreasing BC mortality [Feig, 2014, McTiernan, 2001, Smart et al., 1995, Tabar et al., 1992].

Nevertheless, mammography presents an elevated number of detractors based on several factors [Rakowski et al., 1997, Heywang-Köbrunner et al., 2011]. First, it generates many abnormal findings not related to cancer, leading to a high false positive rate. Second, it requires irradiating the patient with levels around 2-4 times the natural radiation levels. Besides, mammography has low specificity with dense breast (typical of young woman) which are particularly prone to develop cancer (see Fig. 2) [Santen and Mansel, 2005]. In those cases, mammography has up to a 50% rate of obtaining false negatives [Jovanović, 2008]. Moreover, mammography results a very painful procedure for woman, as the breast needs to be strongly compressed during the procedure. After decompression, the localization of the lesions can drastically change, which complicates the posterior clinical proceedings required.

Due to the mentioned reasons, several other complementary techniques are frequently joined to mammography, for example, Magnetic Resonance Imaging (MRI) and echography (or conventional ultrasound imaging). MRI is generally recommended for people with a family history of BC or with genetic predisposition to suffer the disease. This imaging modality

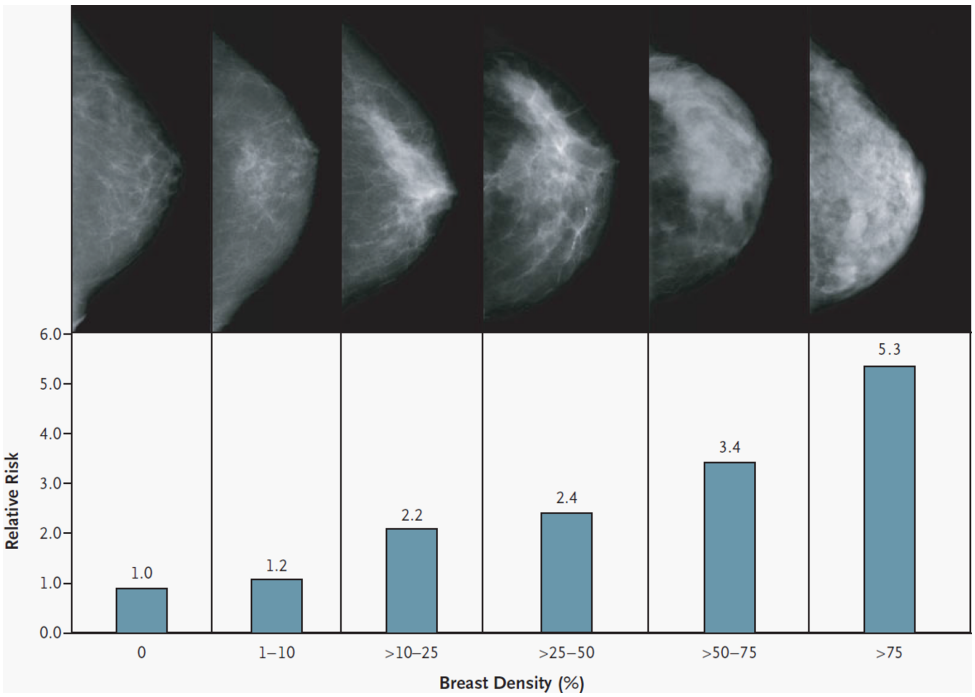

Figure 2: Quantifying breast cancer risk [Santen and Mansel, 2005].

posses an excellent sensitivity, even for dense breast, and excellent image quality. Nevertheless, not everybody results being a suitable candidate for MRI due to claustrophobia, metallic implant, among other reasons. On the other hand, MRI, for the study of soft tissues, generally requires employing contrast agents like Gadolinium, which is known to present high toxicity [Perazella, 2009]. Besides, MRI is a very expensive technique (10 times more expensive than mammography, which has a relative low cost [André et al., 2013]) which complicates the availability of MRI equipment in all the clinics, especially the rural ones.

Echography is another very valuable tool for breast imaging. Its cost is only about 2-3 time the cost of mammography, and it is much more sensitive in dense breast. A major strength of breast ultrasound, and its most common clinical use, is fot the differentiation of cystic and solid lesions with nearly 100% accuracy [Brogoch et al., 2010]. Echography is also a non-ionizing and non-invasive technique. However, the clinical analysis currently performed for breast ultrasound images, is generally done qualitatively. Conventional B-mode images are qualitative. They depend on operator settings and skills, as well as on the system characteristics and tissue-dependent factors. Thus, most solid masses viewed on ultrasound require a biopsy to obtain a definitive diagnosis. Consequently, a large number of additional biopsies are performed, many times corresponding with benign tumors.

Additionally, breast ultrasound is recognized to be a difficult exam to perform and interpret. Besides, another important downside of this technique lies in coordinating manually acquired echograms with other complementary techniques that can be used to obtain supplementary

information. Consequently, multi-modal images concerning the same explored part of the body cannot be merged.

All the previous mentioned factors demonstrate the need for alternative imaging systems that could be able to provide quantitative and high-quality images of the breast. This alternative imaging modalities should be able overcome the mentioned limitations of the actual systems to could be employed for the detection, diagnosis and management of BC.

Ultrasound computed tomography

Due to the many diagnostic advantages provided by echography, efforts to improve the diagnostic accuracy of this technique have been carried out. Based on that, a promising alternative to which our own study belongs, utilizes Ultrasound Computed Tomography (USCT) to characterize breast tissue.

USCT is a non-invasive radiation-free medical imaging technique with promising capabilities to resolve soft tissue structures in the body. Instead of manually acquiring the images of the breast, USCT uses an automatic acquisition system and an arrangement of transducers around the breast that allow covering all the insonification angles in order to obtain isotropic resolution (see Fig. 3). This fact makes USCT systems superior, regarding the resulting image quality, than other automatic breast ultrasonic systems (ABUS) that have been also recently introduced [Gazhonova, 2017]. Whole breast USCT, using transmission and/or reflection techniques, has been proposed as a way to address the shortcomings of conventional echography, and also to provide new ways to assess and characterize masses and other findings in the breast in a quantitative way.

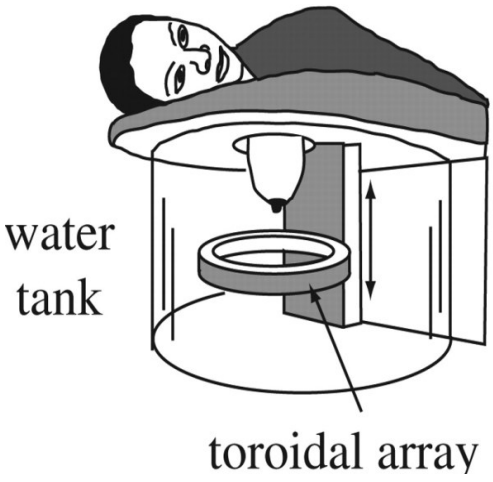

Figure 3: USCT concept with a ring array of tranducers. Taken from Simonetti and Huang [2009]

USCT can be divided into two main modalities: reflection and transmission. In the former, the reflected signals are generally employed to obtain information related to changes in the acoustic impedance and the concentration of scatterers [Duric et al., 2005]. Reflectivity images are usually employed to obtain information about the tissue boundaries, as in conventional ultrasound imaging, but using a tomographic concept [Szabo, 2004, Cobbold, 2006]. As all insonification angles can be covered, biological structures are fully depicted, image noise due to speckle is reduced and spatial resolution is isotropic [Medina et al., 2016]. On the other hand, the transmitted signals provide more direct information about the *speed of sound* (SS) and the *acoustic attenuation* (AA) in the tissues.

The SS is well correlated with the density of the material (see Fig. 4) [Mast, 2000]. Therefore, its use has been proposed for BC detection [Boyd et al., 2010, Li et al., 2008a, Simonetti et al., 2009, Duric et al., 2008, Li et al., 2014, Duric et al., 2015, Li et al., 2008b], as it may yield images with similar contrast, and therefore, analogous structural information to those obtained from X-ray mammograms. As a result, imaging the SS could provide a useful alternative to detect BC with relatively low-cost setups, avoiding the radiation dose, and painful breast compression required in X-ray mammography.

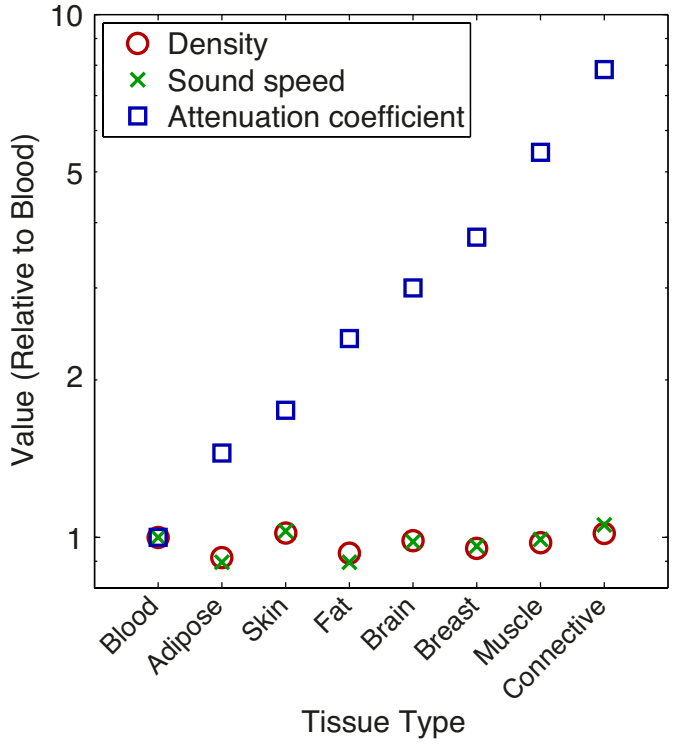

Figure 4: Comparison of density $(g/cm^(3))$, sound speed (m/s), and acoustic attenuation $(dB/(MHz^y cm))$ values relative to blood for different soft tissues, ordered according to the attenuation coefficient. This figure prodives an example of the levels of contrast that can be obtained when using these tissue parameters for imaging. (Data was taken from [Mast, 2000])

The AA can provide enhanced contrast between different tissue types compared to SS (see Fig. 4) [Mast, 2000]. The AA varies more with the tissue type than the density or the SS, consequently it may improve significantly the detectability of masses in the breast. The combination of both the SS and AA parameters may also allow better discrimination between benign and malignant masses[André et al., 2013, Duric et al., 2009]. For example, in reference André et al. [2013], it was performed an study over 75 patients where it was studied the SS and the AA of several tissue type. The idea behind the study was to find any relationship between the measured acoustical properties of the tissues and the characteristic of the cancerous tissues. Fig. 5 shows some of the results of that study. Some of the conclusions were:

- **Fatty normal tissues** (unfilled diamonds) present very low SS and AA. Therefore, fatty tissues appear dark on AA and SS images.
- **Fibroglandular tissues** (clear triangles) have intermediate SS and AA values.
- **Simple cystic masses** (green circles) have consistently low AA and intermediate SS close to the value in water.
- **Complex cystic masses** (blue circles) present higher AA than simple cyst but also similar SS to water.
- **Fibroadenomas** (purple triangles) these are solid benign masses, are wide ranging in SS.
- **Cancers** (red squares) shown both high SS (highest SS values ever measured were confirmed cancers) and high AA.

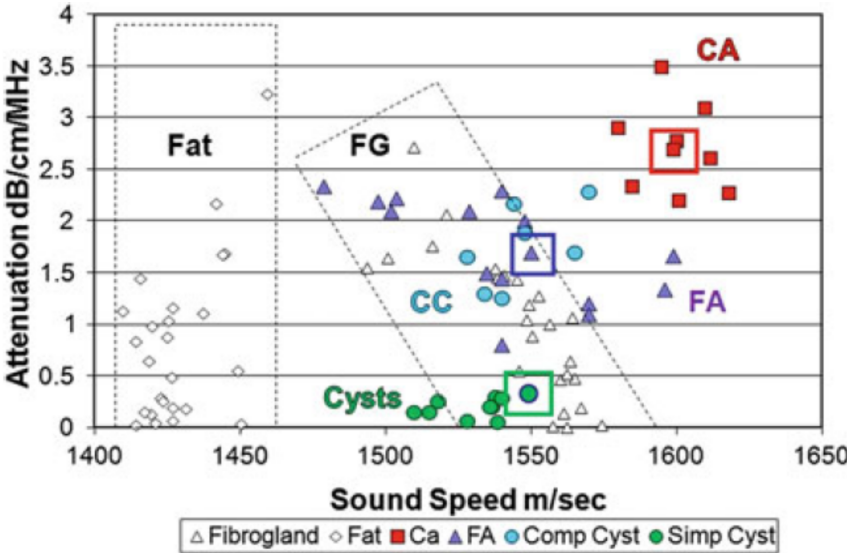

Figure 5: Sound speed vs. acoustic attenuation values for normal tissues in 75 subjects. Figure taken from André et al. [2013]

Even when there is some overlap in the acoustic properties of the studied masses, these data show promising results, demonstrating that quantitative USCT images may be helpful in

differentiating masses, as cancerous tissues appear quite separated from benign ones. These factors reveal the potential of USCT as a primary tool for population screening of BC.

Motivation

The present thesis was developed as part of the collaboration between the Ultrasound Systems and Technology Group (USTG-ITEFI), from the Spanish National Research Council (CSIC) of Madrid, and the Nuclear Physics Group (GFN) from Complutense University of Madrid, under the project TOPUS [S2013/MIT-3024, 2013-2017]. TOPUS (Positron Emission Tomography and Ultrasounds), has been proposed to develop a multi-modal, tomographic imaging system, mainly oriented to BC diagnosis. It will combine a ring of highly segmented positron emission tomography (PET) detectors, and an arrangement of ultrasonic transducers arrays for USCT.

The PET modality of this scanner, is capable of obtaining high resolution images (1 mm or better) and high sensitivity [Vaquero et al., 2016, Cal-González et al., 2015]. The ultrasonic part of the system is called MUBI (Multimodal Ultrasound Breast Imaging System), and it is intended to be a flexible platform for multi-modal ultrasound imaging research.

The objective of the TOPUS project is, that both the multi-modal ultrasonic images and the PET, could be merged to obtain the anatomical and functional information of the region under study. The ultrasonic modality will be used to obtain a complete breast volume acquisitions in a few minutes, avoiding the use of ionizing radiation. For those cases where the US images indicate the presence of some relevant abnormal tissue, the high-resolution PET image can be used to provide a final confirmation of the tissue status. This allows reducing the amount of ionizing radiation supplied to patients in comparison with other multi-modal systems, such as PET-CT and SPET-CT. Reducing exposure to radiation is important either for the patient and clinicians.

The USTG-ITEFI group designed and developed the electronics of the MUBI USCT scanner, and also the reflectivity ultrasound imaging modality. Due to the experience of our group (Nuclear Physics Group of the Complutense of Madrid) in image reconstruction techniques for several tomographic image modalities, we participate in this project in two directions. First, to develop both the electronics and image reconstruction techniques to be used in the PET ring of TOPUS, and second, to include the transmission USCT modality to the branch of possibilities for soft tissue characterization available in the MUBI scanner. The development of the transmission USCT modality, constitutes the framework in which this thesis was developed.

In this thesis, we explored the reconstruction of both SS and AA acoustic distributions from simulated and experimental transmitted USCT data. To obtain those maps, we opted to develop two sets of codes. In one hand, we investigated a group of approximate methods that exhibit high computational efficiency, which allow them to be compatible with the time requirements of the clinical practice. Nevertheless, its resolution and image quality in general, can be low under certain conditions. On the other hand, we developed methods which include accurate

information of the physic of the ultrasound propagation. These codes provide excellent image quality but, due to its iterative nature and high level of detail of the ultrasound propagation, present high computational burden.

All our methods were developed in time domain. There are several reasons to support this decision. First, some of the functionals that intervene in our algorithms are highly non-linear, especially at high frequencies, where these funcionals present a large number of local minima. This fact makes them vulnerable to get stuck on erroneous solutions of the image reconstruction [Lin et al., 2000, Mast, 2000]. To avoid the mentioned non-linearity, several researchers use the strategy of employing frequency domain methods in sequential steps with increasing frequency [Li et al., 2014, Pratt et al., 2007, Sandhu et al., 2016]. This process decreases the effect of non-linearity but, increases the complexity of the reconstruction process, as it requires solving several optimization problems for each frequency used. Therefore, we felt motivated to develop time domain methods, where the entire bandwidth of the signals can be employed in the reconstruction process in a single step. Second, the reconstruction of SS and AA maps is generally performed in time domain and frequency domain respectively, using completely different algorithms. The information required to recover both maps can be obtained from the same measured data. Therefore, the use of a common framework of reconstruction in time domain, would unify the reconstruction of both properties, and consequently, would simplify the reconstruction process. And finally, data in time domain is easier to interpret and handle, basically because we live in time domain and these type of data tends to result more intuitive.

The algorithms developed in this thesis can be implemented in any USCT scanner. They have been designed to be flexible and suitable to be adapt to any scanner configuration under simple modifications.

Objectives

Taking into account the previously exposed considerations about the many advantages that transmission USCT can provide to improve soft tissue characterization, the main goal of this thesis was to include this modality to the MUBI scanner. Methods for data processing and image reconstruction techniques were developed and implemented to this end.

The specif objectives of this thesis were:

- To develop methods for data processing and relevant parameters extraction from the recorded data to be used with geometrical acoustic algorithms of reconstruction.
- To implement a fast algorithm based on geometrical acoustics to obtain both the SS and the AA distribution in the inspected tissues. In this sense, we aimed to provide the MUBI scanner with a method that allow us reconstructing the transmitted information parallel to the data acquisition process.
- To investigate the improvements that refraction correction could provide for geometrical

acoustics algorithms without considerably affecting the reconstruction times. Here we were interested in implementing methods that could improve the image quality of the reconstructed images when a high frequencies approximation is used.

- To design a simplified method to perform bent-ray tracing, that cold improve the performance, both in time and image quality, of the classically employed refraction corrected geometrical acoustic algorithms.
- Being able to account with an efficient numerical model to solve the full wave equation in lossy mediums, and use it to derive the mathematical expressions to perform full wave inversion reconstructions in the time domain. At this point, we were interested in creating a common time domain framework to reconstruct, usign FWI, both the SS and AA distribution.
- To explore modifications to the cost function employed for FWI in order to remark several aspects of the ultrasound field. We aimed to employ these modifications to improve the quality of the reconstructed AA map, and to facilitate the obtainment of the initial model for the SS recovery.
- To apply the developed methods to the reconstruction of real data obtained from the MUBI scanner, and demonstrate their feasibility to provide high quality images for both the SS and the AA distributions in reasonable reconstruction times.

Structure of the thesis

This thesis is organized as follows:

- In Chapter 1 and Chapter 2, we presented a theoretical introduction and the description of the materials and methods employed in this thesis respectively. In Chapter 1, basic concepts about the propagation of acoustic waves, the main characteristics of the acoustic mediums and the fundamental processes that the waves experience during its propagation will be analyzed. The main breast-dedicated imaging systems based on ultrasound will be also presented. Finally, in this chapter the characteristics of the main USCT systems currently available, will be explored together with the most common approaches employed for image reconstruction in those systems. In Chapter 2, we will introduce the MUBI USCT scanner, where the algorithms developed in this thesis have been evaluated. Moreover, we presented the main characteristics of the numerical simulator k-Wave. This code was used in this thesis to generate the numerical data used to test our algorithms and also, this code was included as the model of propagation employed in some of the iterative algorithms of this thesis.
- In Chapter 3, we analyzed the implementation of geometrical acoustic algorithms to reconstruct USCT data. We investigated and implemented several methods to estimate the time of flight and amplitude of the first arrival signals recorded based on synthetic data.

We also explored several approximations to perform the reconstructions using straight and bent rays algorithms.

- In Chapter 4, we developed and implemented a FWI methodology in time domain to reconstruct the SS and AA distributions. All the mathematical derivations of the expressions to update both distributions were also presented. We tasted the algorithm in different situations and used noisy synthetic data to evaluate it.
- In Chapter 5, we proposed a generalized cost function to improve the performance of our FWI reconstructions. Using this cost function, the modified expressions to update both the SS and AA distributions were analyzed. As before, to test the performance of the proposed misfit function we used synthetic data.
- Finally, in Chapter 6, we applied the algorithms developed along the previous chapters to the reconstruction of real data measured in our MUBI USCT scanner. Several configurations of the setup and different in-vitro phantoms were investigated.
- At the end of the manuscript we present the general conclusions of the thesis, and the publications and conference proceedings derived from this work.

Chapter 1

Theoretical background

In this chapter, the main concepts and definitions of acoustics and ultrasonic imaging that will be used in the rest of the thesis will be introduced.

The first section (Sec. 1.1) explains three fundamental aspects of the ultrasound's physics. First, in Sec. 1.1.1 we introduce some general concepts about the acoustic waves and mention some of the features that characterize them. Second, basic definitions to understand several acoustic properties of the materials and tissues are discussed in Sec. 1.1.2. Third, some of the main phenomena that take place during the propagation of the acoustic waves are presented in Sec. 1.1.3. It should be said that the descriptions given in this section are general for acoustic waves, therefore they can be applied to ultrasounds, which are the focus of this work, as ultrasounds are acoustic waves with frequencies over the audible range of the human hearing ($>$20 kHz).

The section 1.2 is dedicated to introduce several types of imaging systems based on ultrasound. First, in Sec. 1.2.1 the conventional ultrasound equipment and its fundamental imaging modalities are presented. After that, the USCT systems, which constitute the foundation of this research, are analyzed in deep in Sec. (1.2.2) and the main imaging modalities and setups employed for this purpose are also shown.

In section 1.3, the main approaches employed for image reconstruction in USCT are discussed. In this topic, two different strategies are followed. First, a set of computationally efficient methods based on geometrical acoustics, which is a high-frequencies approximation, are addressed in Sec. 1.3.1. A second approach, known as full wave inversion, that employs a computational model to accurately simulate the wave propagation is discussed in (1.3.2).

Finally, in section (1.4) some merit figures to quantitatively evaluate the quality of the reconstructed images are analyzed.

1.1 Physics of ultrasound

1.1.1 Acoustic waves properties

The sound is a mechanical disturbance that travels by compression and rarefaction of the medium. This process is not related with mass transfer, and initiates with the change in the stress or pressure field within the medium, which is called *source*. The mechanical energy is transferred to the medium from the source promoting displacements of the molecules from its equilibrium positions by a distance **d**, called *displacement amplitude* and at a rate, or *particle velocity*, **u**. When the particles of a medium are displaced from their equilibrium positions, internal (electrostatic) restoration forces arise. If the medium is not stressed beyond its elastic limit, the combination of the elastic restoring forces and the inertia of the particles, cause the oscillatory motions of the medium. By means of these oscillations and the interaction between these particles, acoustic energy propagates across the medium giving rise to an acoustic wave. The mechanical energy of the acoustic waves, requires (unlike for light waves), an elastic medium for its propagation [Hill et al., 2004, Kyriakou, 2015].

In general, acoustic waves present two vibrational components: longitudinal and transverse. The former mode consist of molecular vibrations in parallel directions to the wave propagation. The later (the transverse ones), also commonly referred to as*shear waves*, originate vibrations in directions perpendicular to the direction of traveling of the wave [Beutel et al., 2000]. In mediums like gases, fluids and soft tissues, the component that is significant is the longitudinal one, because the transverse component dissipates in a small distance [Beutel et al., 2000]. However, in solids (or hard tissues such as bones), the molecules can experience oscillations in many other directions, therefore, a number of different types of sound waves are also possible [Larson, 2010].

Acoustic waves can be classified according with the geometrical shape of their *wave-front*. The wave-front is a surface representing the points of a wave that vibrate in unison. If identical waves originated at the same point propagate through a homogeneous medium, the corresponding maximum and minimum at any instant are *in phase*. This means that both waves have completed identical fractions of their cyclic motion, and the line or surface that connects all the points with the same phase will constitute the wave-front. The two most basic types are the planar and the spherical wave. Planar waves present the wave-front located on a plane that propagates through the medium.

A propagating plane wave can be represented by the following expression:

$$A(x,t) = \mathrm{Re}\ \ A_0 e^{i(kx \pm ft)} \tag{1.1}$$

where sign '$-$' corresponds to propagation in the positive x-direction and sign '$+$' to propagation in the negative x-direction, A_0 is the amplitude of the wave and $k = 2\pi/\lambda$ is the *wavenumber* or *spatial frequency* [rad/m].

Spherical waves propagate away from the source through the medium symmetrically (see

Fig. 1.1). They are useful because many sources can be approximated as a set of emitters of spherical waves. Any distribution of sources can be represented as a collection of point sources, each emitting spherical waves.

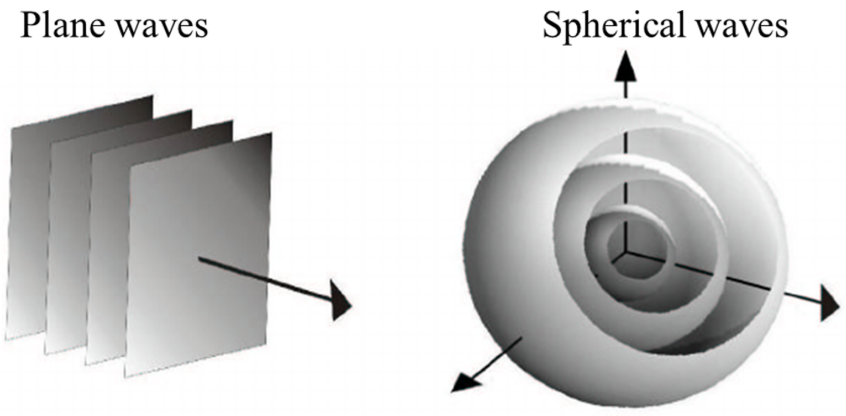

Figure 1.1: Plane and spherical wave-fronts

As it was said, arbitrarily shaped waves with asymmetrical wave-fronts can be decomposed using spherical waves. This is what states the Huygen's Principle [Wilhjelm et al., 2013]. Every point on a wave-front can be regarded a secondary source of spherical waves, and the position of the wave-front after a given time is the envelope of these secondary wave-fronts [Norton, 2000] (see Fig. 1.2).

Two other important parameters to characterize an acoustic wave are its *frequency* and *wavelength*. The frequency f characterizes the number of complete oscillations per second and it is given in Hertz (Hz). Its inverse is named period T (in s), which is the time the wave requires to complete the cycle of an acoustic variable. The wavelength λ in a medium (in mm), is the distance to complete a cycle or also the distance between two points of equal phase (see Fig. 1.3).

Another important parameter to describe the acoustic waves is its intensity I, which describes the amount of energy that travels across an unit of area perpendicular to the wave propagation's direction per second.

If an acoustic field varies in time, it can be described by means of the *instantaneous acoustic intensity* $I(x,t)$ as:

$$I(x,t) = p(x,t)\mathbf{u}(x,t) \quad [W/m^2] \tag{1.2}$$

where p is the acoustic pressure and $\mathbf{u}$ the acoustic particle velocity.

Using the instantaneous acoustic intensity, the time-averaged acoustic intensity I_{av} can be defined as:

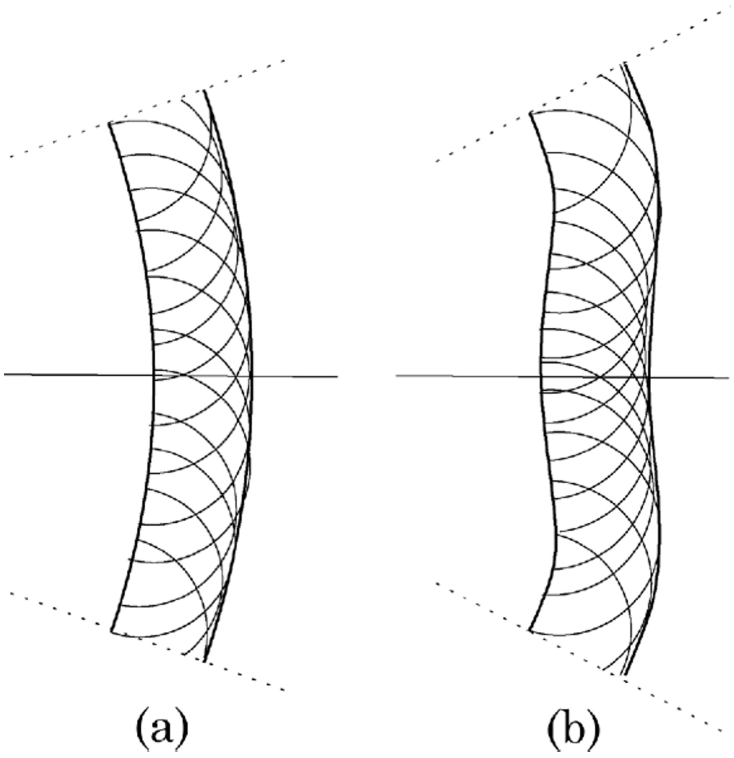

Figure 1.2: Illustration of the Huygen's Principle (a) spherical wave-front (b) irregularly shaped wave-front [Norton, 2000]

$$I_{av} = \frac{1}{T}\int_0^T I(x,t)dt = \frac{1}{T}\int_0^T p(x,t)\mathbf{u}(x,t) \tag{1.3}$$

It is sometimes also of interest to know the relative intensity I_{rel} of the acoustic wave in comparison with the intensity at other reference position I_0. This *relative intensity* in usually expressed in decibels (dB):

$$I_{rel}\ (dB) = 10\ log_{10}\frac{I}{I_0} \tag{1.4}$$

Using the acoustic intensity, it is also possible to define the *sound power* P, which is the rate at which acoustic energy is flowing across a surface S:

$$P = \iint sI\mathbf{n}dS \quad [W] \tag{1.5}$$

where $\mathbf{n}$ is the unit normal to the surface S. If S is a closed surface, then it is only non-zero when the surface surrounds a source.

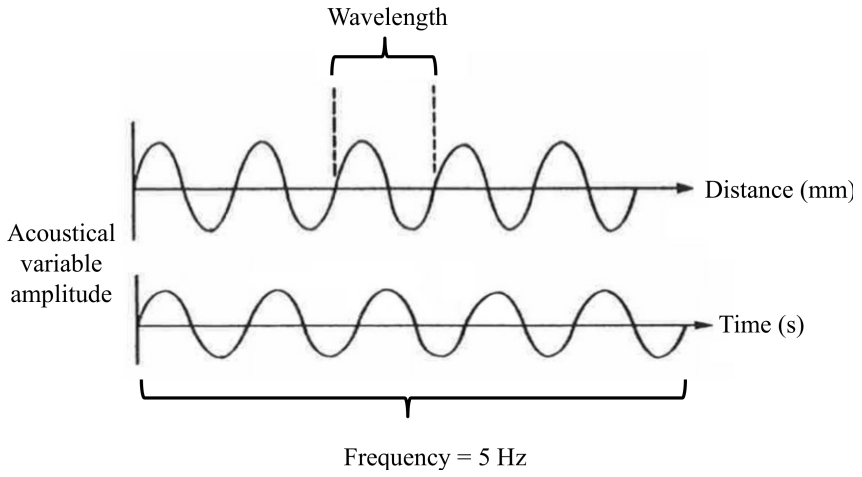

Figure 1.3: Concept of frequency and wavelength.

Another important fact related with the wave propagation is the *geometrical spreading*, which is a decrease in the pressure amplitude of the outgoing wave. If a spherical wave is emitted with a total energy E, then its intensity (energy per unit surface area) would be $E/4\pi r^2$, where r is the radius of the spherical wave. As the acoustic intensity is proportional to the acoustic pressure squared, the acoustic pressure amplitude of the spherical wave will fall off as $1/r$. In the case of a cylindrical wave, the intensity would be $E/2\pi rh$. Here h is the height of the cylinder and r is the radial polar coordinate. Therefore, the pressure amplitude in a cylindrical wave will fall off as $1/\sqrt{r}$.

1.1.2 Acoustic medium properties

The propagation of acoustic waves will be influenced by, and also can cause changes, in the acoustical properties of the medium it will travels through. In this section some of the main acoustic properties of the mediums are discussed.

1.1.2.1 Density

The density of a medium ρ is a factor that considerably affects the wave propagation. Density is defined as the mass of a substance divided by its volume (kg/m^3). Generally, larger molecules have more mass and if a medium is more dense because its constituent molecules are larger, the sound will travel slower on it. This happens because more energy is required to make large molecules oscillate.

Typical density values in soft tissues are around $1000kg/m^3$ due to its high content of water (water's density is also $1000kg/m^3$). Fat presents slightly lower values ($\sim 950kg/m^3$) and the skin higher values ($1150kg/m^3$) [Azhari, 2010].

1.1.2.2 Sound speed

A medium's sound speed c (in m/s), is the speed at which an acoustic wave propagates through that medium. It is related to the wavelength λ and frequency f with the following expression:

$$c = \lambda f \tag{1.6}$$

The sound speed is determined by the characteristics of the medium [Aki and Richards, 2002] (see table 1.1 where the sound speed values for several soft tissues are shown). Sound speed values in soft tissue presents a mean value of (1540 m/s [Curry et al., 1984]) and it can very from 1430-1750 m/s, with fat being in the lower end and skin being in the upper one. Others sound speed values of interest can be, for example, the sound speed in water, 1482 m/s and in air 343 m/s. Typical c values in bone are in the order of 2800-4080m/s, but in certain cases this value can be as high as 5500 m/s, which have been measured for tooth (enamel) [Azhari, 2010].

It is frequently said that acoustic wave with different frequencies travel at the same speed of sound in a given medium. Nevertheless, there is some variation of the speed with frequency. This phenomenon is called *dispersion*. However, in the frequency range used for diagnostic and imaging (1-20 MHz), this variation is less than 1%. Therefore this effect can be neglected in the majority of the situations [Tole and Ostensen, 2005]. On the other hand, sound speed dispersion differs with the tissue type. Consequently, this property presents high potential as a tool for tissue characterization, which still requires to be explored [Tole and Ostensen, 2005].

The sound speed can also be affected by the medium's temperature. Nevertheless, a temperature variation around the few degrees causes very small deviations in the sound speed. As body's temperature is under homeostatic control, its temperature is generally considered constant in clinical ultrasound [Tole and Ostensen, 2005, Duck, 2013].

On the other hand, some modern ultrasound devices, as the ones employed for ultrasound computed tomography, employ water coupling between the transducers and the tissue. In those situations, there could be some differences between the corporal and the water temperature that should be controlled.

1.1.2.3 Elastic properties

The elastic properties are different for different materials and are related to the tendency of a material to keep its shape and not to deform when a force is applied to it. Rigid materials are characterized by atoms and molecules with strong forces of attraction among them. These forces can be figured of as springs that control the speed with which those particles can return to their equilibrium positions. It the particles are able to return fast to their equilibrium positions, they will be free faster to move again. Consequently, they can vibrate at higher speeds.

Table 1.1: Sound speed (SS) and acoustic attenuation (AA) values for different tissues and materials. Data was taken from [Hasgall et al., 2015]. The AA values in the mentioned reference was in (Np/m). Therefore, AA values have been converted using 1 Np = $20 \log e$ dB

Tissue	Sound speed (m/s)	Acoustic attenuation(dB/MHz cm)
Air	343,00	0,0034
Blood	1578,20	0,2056
Bone (Cortical)	3514,90	4,7385
Brain	1546,30	0,5909
Breast Fat	1440,20	0,3785
Breast Gland	1505,00	0,7500
Cartilage	1639,60	0,0382
Cervix	1629,00	0,7049
Connective Tissue	1545,00	1,2600
Diaphragm	1588,40	0,6175
Ductus Deferens	1569,10	0,6098
Esophagus	1500,00	0,4988
Eye (Cornea)	1562,50	0,0320
Fat	1440,20	0,3785
Heart Muscle	1561,30	0,3402
Kidney	1554,30	0,2438
Large Intestine	1500,00	0,4988
Liver	1585,70	0,6006
Lung	949,30	20,0594
Muscle	1588,40	0,6175
Nerve	1629,50	1,1496
Ovary	1595,00	0,6803
Pancreas	1591,00	0,8295
Placenta	1500,00	0,7337
Prostate	1559,50	0,8095
SAT (Subcutaneous Fat)	1477,00	0,8095
Skin	1624,00	1,8378
Small Intestine	1500,00	0,4988
Stomach	1500,00	0,4988
Testis	1595,00	0,2105
Thyroid Gland	1500,00	1,3456
Tongue	1588,40	0,2520
Tooth	4565,90	5,5976
Trachea	1639,60	0,0382
Ureter-Urethra	1569,10	0,6098
Urine	1537,70	0,0061
Uterus	1629,00	0,7049
Vagina	1500,00	0,4988
Vertebrae	3514,90	4,7385
Water	1482,30	0,0022

This explains why acoustic waves are able to propagate faster through mediums with higher elastic properties [Larson, 2010]. Generally, the elastic properties of a medium can be characterized by the compressibility of the medium k (in m^2/N or $1/Pa$), which is a measure of the relative volume change of a fluid or solid as a response to a change of pressure. The relation between the sound speed, the density and the compressibility can be seen in Eq. 1.7. Additionally, c can be calculated through the medium's elastic bulk modulus K (in Pa), which is the reciprocal of k, and acts as a measure of the medium's tendency to be deformed elastically, when a force is applied to it.

$$c = \frac{1}{\sqrt{\rho k}} = \sqrt{\frac{K}{\rho}} \tag{1.7}$$

1.1.2.4 Acoustic impedance

Another important property of the media is its *acoustic impedance*. It is defined as the product of the sound speed and the density of the material (see Eq. 1.8). It expresses the resistance of the medium to the acoustic wave propagation through the interface of different media.

$$z = \rho c \tag{1.8}$$

Where ρ is the density and c is the sound speed of the medium. The changes of impedance among different media and its consequences in the sound propagation through them, conforms the base of several medical and industrial equipment as it is explained later.

1.1.2.5 Acoustic absorption mechanism in tissue

When an acoustic wave propagates through a medium, it experiences a loss of kinetic energy by a phenomenon called*absorption*. It is important to bear in mind the differences between the acoustic absorption (which consist on the transformation of acoustic energy into thermal energy) and the acoustic attenuation (which also includes the effects of scattering, as will be discussed in the next section).

Absorption is a process intrinsic to the medium of propagation and can be attributed to several mechanisms. These mechanisms occur on both a cellular and molecular levels. Molecular mechanisms include processes like *viscosity* and*thermal conduction* and other *relaxation processes* (which are usually negligible at the frequencies used for diagnostic and imaging) [Hill et al., 2004, Treeby et al., 2011].

Viscous losses occur because of the diffusion of momentum among molecules with different particle's speed. This process can occur during relative motion between adjacent portions of the medium, such as the neighboring compressions and rarefactions that facilitate the propagation of the acoustic wave. These viscous losses are related with the frictional forces among particles

due to interact. Therefore, during the acoustic wave propagation, a portion of the acoustic energy is converted to thermal, resulting in energy loss. Viscosity dependence on frequency is given by f^2, being more significant at higher frequencies:

$$\alpha_{vis} \simeq \frac{f^2}{2\rho c^3}\left(\frac{2\eta}{3} + \eta_B\right) \tag{1.9}$$

where η is the coefficient of shear viscosity (due to molecules colliding between regions of different particle velocity) and η_B is the coefficient of bulk viscosity (refers to losses during compression, when some of the energy is not stored as elastic potential energy but is converted into heat).

Thermal conduction losses result from the conduction of heat from the higher temperature areas of the medium (during compression) to the lower temperature ones (during rarefaction). The increased acoustic pressure in the compression areas increases as well the kinetic energy which will dissipate by means of inter-molecular collisions from the warmer regions to the cooler ones.

Relaxation losses are asociated with the characteristic time delay or relaxation time required for energy recovery when a conversion of the kinetic energy to other energy states ocurrs [Herzfeld and Rice, 1928]. During the compression, kinetic energy is stored in the medium in several forms, for example, as rotational and vibrational energies. The stored energy is returned to the wave during rarefaction as the medium presents some tendency to return to its equilibrium state. If the relaxation time of the medium is of the same order as the period of the propagating wave, the differences in phase between the transfer of energy to and from the alternate energy state will result in an energy dissipation Treeby et al. [2011]. The relation between the absorption per wavelength, α_{rel}, and the relaxation time T , is given by:

$$\alpha_{rel} \propto \frac{Tf}{1 + (Tf)^2} \tag{1.10}$$

Where f is the frequency in Hz of the wave.

The absorption mechanisms at cellular level include viscous relative motion and heat conduction due to the inhomogeneous regions properties, in addition to scattering effects. See Refs. Treeby et al. [2011], Hill et al. [2004] for a more complete dissertation about this subject.

The absorption of acoustic waves in a wide variety of lossy media can be characterized by an empirical power law function of frequency:

$$\alpha = \alpha_0 f^y \tag{1.11}$$

In Eq. 1.11 α is the absorption coefficient in units of Npm^{-1}, α_0 is the power law pre-factor in $Np(rad/s)^{-y}m^{-1}$ and y is the power law exponent.

Absorption following this model is observed in many different materials including marine sediments and biological tissue [Buckingham, 1997, Bamber, 1986]. This type of absorption model is accurate for situations in which the shear modulus is negligible, such as is often the case in soft biological tissue. The power law exponent, for soft biological tissues it is generally in the range of $0 < y < 2$ [Szabo and Wu, 2000, Chen and Holm, 2004, Treeby and Cox, 2010a]. However, classical lossy wave equations predict an absorption that can be either frequency-independent, or proportional to frequency squares [Markham et al., 1951, Treeby and Cox, 2010a].

Nevertheless, for acoustic waves in the low MHz range, it is also frequent to find works in which a linear dependence with the frequency is assumed [Carstensen, 1960, Li et al., 2008a, Pérez-Liva et al., 2016].

The reported values of absorption coefficient can be also find with units $dB/(MHz^y cm)$. See Table 1.1 as a reference for absorption coefficient values in several human tissues.

1.1.3 Acoustic waves interation with tissue

When an ultrasound wave travels through tissue, it experiences a combination of processes related with the characteristics of the given medium. As it is of our interests to study the propagation of ultrasound in tissue for medical applications, we analyze here the main processes that could occur: reflection, scattering, attenuation, refraction and diffraction.

1.1.3.1 Reflection

When a wave reaches the boundary between two media where there is a difference in acoustic impedance of the materials on each side of the interface, a portion of the wave experience reflection and other portion of the wave experience transmission across the interface (see Fig. 1.4). The amount of energy that is reflected strongly depends on the impedance differences on the two sides of the interface. If the difference in acoustic impedance is very large, all the ultrasound will be totally reflected. The reflected part of the wave is called an *echo* and the production and detection of echoes constitutes the basis of the conventional ultrasound imaging.

The angle of incidence of the wave at the interface θ_i is equal to the reflection angle θ_r as it can be seen in Fig. 1.6. The fraction of the incident wave intensity that is reflected and transmitted can be obtained from the reflection R an transmission T coefficients respectively. These coefficients are given by the following expressions:

$$R = \frac{Z_2 cos\theta_i - Z_1 cos\theta_t}{Z_2 cos\theta_i + Z_1 cos\theta_t} \tag{1.12}$$

$$T = \frac{2Z_2 cos\theta_i}{Z_2 cos\theta_i + Z_1 cos\theta_t} \tag{1.13}$$

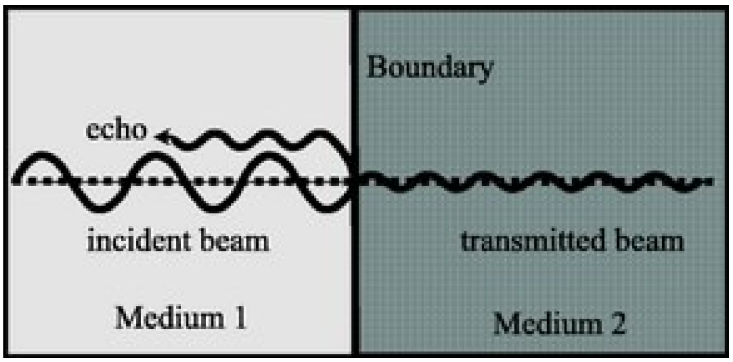

Figure 1.4: Schematic representation of the transmission and reflection at the interface between two media [Aldrich, 2007]

Where Z_2 and Z_1 are the impedance values of both media 1 and 2 respectively (see Fig. 1.4) Ref. [Brekhovskikh, 1948] can be consulted for the derivation of these expressions.

The simplest scenario to obtain the transmission and reflection coefficients occurs when the wave impinges normal to the surface. In that case, both coefficients can be calculated as follows:

$$R = \frac{Z_2 - Z_1}{Z_2 + Z_1} \tag{1.14}$$

$$T = \frac{2Z_2}{Z_2 + Z_1} \tag{1.15}$$

Typically, in soft tissues, the amplitude of an echo produced at a boundary is only a small percentage of the incident amplitudes, as listed in Table 1.2. Areas containing bone or air, will produce considerably large echoes and consequently, in those cases practically no wave is transmitted beyond the tissue interface.

Table 1.2: Percentage of ultrasound reflection at boundaries for normal incidence [Aldrich, 2007]

Boundary	Percent reflected
Fat/muscle	1.08
Fat/kidney	0.6
Soft tissue/water	0.2
Bone/fat	49
Soft tissue/air	99

1.1.3.2 Scattering

Scattering produces when an acoustic wave travels through an inhomogeneous medium. A medium is considered inhomogeneous when it contains objects or regions with different acoustic impedance (also known as scatterers). In those cases, part of the wave energy is diverted. This portion of the wave can either be delayed in time or altered from the original wave's direction.

The amount of scatter produced depends basically on two main factors:

- The ratio between the acoustic wavelength and the size of the scatterers of the medium.
- The impedance differences between the background medium and the scatterers.
- The density of scatterers in the medium.

Depending on the aforementioned ratio between the wavelength and the scatterer's size, three types of scattering can be defined:

- **Case 1** (Wavelength « scatterer's size): a phenomenon called *specular scattering or specular reflection* takes place when the surface of interaction is smooth. As a consequence, a considerable amount of acoustic energy will be reflected away or back (the later occurs in the case of normal incidence) to the transducer.
- **Case 2** (Wavelength > scatterer's size): a phenomenon called *diffuse scattering* originates. It occurs when the wave interacts with a rough interface and the details that causes roughness are smaller than the given wavelength. The wave's energy will be diverted in many different directions (which is the main difference with specular scattering) and only an small portion will be reflected back in the same propagating direction of the original wave (see Fig. 1.5). An important case of diffuse scattering is the *Rayleigh scattering*. This takes place when the structures that produce scattering are much smaller than the given wavelength, as it is the case of the biological tissue, which is composed by vessels and other very small structures [Shung and Thieme, 1992].
- **Case 3** (Wavelength $\sim$ scatterer's size): this type of scattering is called *diffractive scattering*. As consequence of this effect, the scattered signals are emitted in several directions. Interference patterns are produced as a result of the spatial variations in the reinforcement and cancellation of the wave.

1.1.3.3 Refraction

As it can be seen in Table 1.2, a portion of the wave's energy is not reflected when the ultrasound impinges an interface. This portion will be transmitted to the adjacent medium. Nevertheless, if both media present different sound speed, another important phenomenon of acoustic waves' interaction with tissue will take place; *refraction*. When an ultrasonic wave passes through an interface between two materials at an oblique angle, and the materials have different sound speed, both reflected and refracted waves are produced.

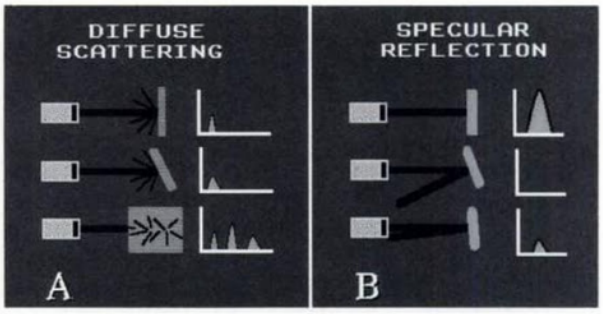

Figure 1.5: Differences between (A) diffuse and (B) specular scattering. Taken from [Shung and Thieme, 1992]

If a plane wave interacts with a planar interface, the reflected and transmitted waves will follow Snell's law. Snell's law describes the relationship between the angles of the refracted, reflected and transmitted waves with the speeds of the propagation media (see Fig. 1.6).

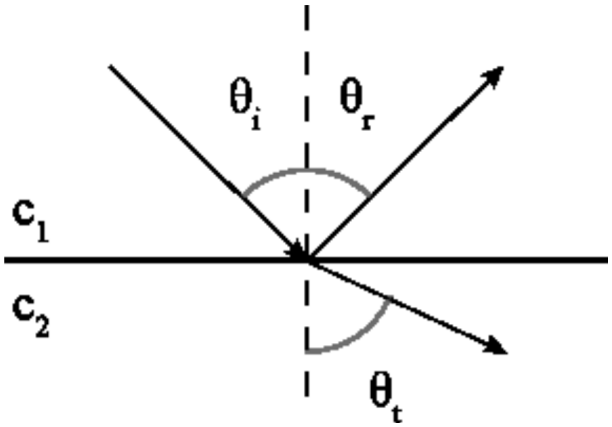

Figure 1.6: Schematic representation of the snell's law

The angle of the incident and reflected waves will be identical (as it was explained before). The angle of the transmitted wave will vary according to the expression:

$$\frac{\sin\theta_i}{\sin\theta_t} = \frac{c_1}{c_2} \tag{1.16}$$

1.1.3.4 Difraction

When the incident acoustic wave interacts with an infinite or practically infinite interface between two different media, as we mentioned, only reflection and refraction occur because. In those cases, the interface acts as an acoustic barrier. The region beyond the frontier is called *acoustic shadow zone*, as it becomes acoustically obscured due to the interface's presence.

However, when an incident wave's wavelength is finite in comparison with the sizes of the frontier, the wave will spread out and bend around the interface's edges. A similar phenomenon is observed when that frontier presents small openings.

This phenomenon causes the wave paths' bending. Consequently, regions that would have been shadowed otherwise will experience as well the presence of the wave. The amount of diffraction depends on the size of that interface or size of the opening, the distance to the source and the acoustic wavelength λ (or frequency f). Diffraction is enhanced at low frequencies, i.e., for wavelengths that are long when compared to the interface. On the other hand, if the wavelength is negligible compared to the size of the interface, diffraction is minimal. In addition, the closer the source is located to the barrier, the larger becomes the shadow zone on the other side of the interface.

1.1.3.5 Interference

When two acoustic waves interacts in the same place in space, a phenomenon called interference takes place. The main factor that influences this type of process is the phase of the waves. If both waves present the same phase (i.e. they are in-phase) at the location of interaction, then *constructive interference* takes place and a wave with an increased amplitude in comparison with the previous ones will result of the interaction (see Fig. 1.7). If the phase of the waves differs from each other (i.e. they are out-of-phase) in the point of interaction, an attenuated wave will result of the combination, as the waves will cancel each other (see Fig. 1.7)). This process is known as *destructive interference*.

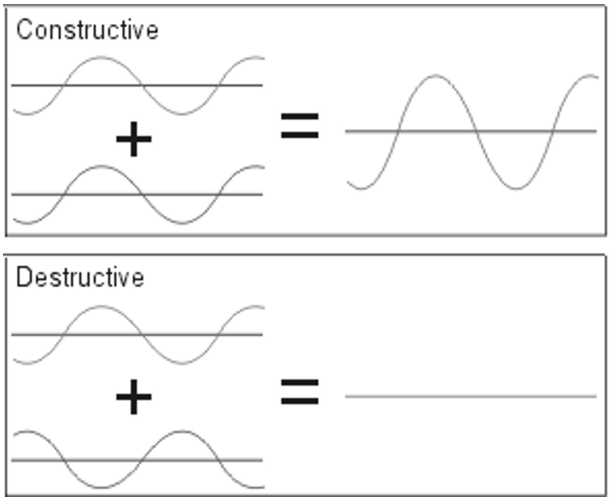

Figure 1.7: Constructive and destructive interference of two waves

1.1.3.6 Attenuation

When acoustic waves travel through a medium, its intensity decrease with distance. In non-realistic materials, the intensity of the wave is only affected by the wave's geometrical spreading ($1/r^3$ for spherical waves). Nevertheless, what will actually happen is that the wave's intensity will be affected, as mentioned before, by the other processes such as absorption and scattering. The combination os these effects is called *attenuation*.

Attenuation will limit the penetration of the beam. It has been shown experimentally, that attenuation is mainly produced by absorption. The amount of scattered energy of the wave is practically negligible in comparison with absorption [Hill et al., 2004, Treeby et al., 2011]. Furthermore, scattered energy will end absorbed in the medium. Therefore, the attenuation coefficient is generally assumed to be the same as the absorption coefficient α.

The amplitude change of a decaying plane wave can be expressed as:

$$A = A_0 e^{-\alpha(f)x} \tag{1.17}$$

In this expression, A_0 is the non-attenuated amplitude of the propagating wave at some location. The amplitude A is the reduced amplitude after the wave has traveled a distance x from that initial location. The quantity $\alpha(f)$ is the absorption coefficient of the wave traveling in the x-direction, that as it was mentioned before, presents a frequency dependence.

It is important to note that all the processes mentioned in the previous sections consider a linear propagation of the acoustic waves. The aforementioned linearity is a good approximation for several applications of biomedical ultrasound, especially when low acoustic pressures are employed (such as in imaging systems). Nevertheless, in other applications, where it is necessary the use of very high amplitudes, several non-linear processes appear in the acoustic wave propagation ([Kinsler et al., 1999, Kyriakou, 2015]). We have not considered these non-linear processes in this work.

1.2 Breast imaging systems with ultrasound

In this section, the basic characteristics of ultrasonography systems are summarized (Sec. 1.2.1). After that, the main features of the few USCT systems currently available are explained (Sec. 1.2.2).

1.2.1 Conventional echography

The use of acoustic waves as a method of inspection to detect irregularities in solids such as metals, started many years ago, around 1929, by the soviet scientist Sergei Y. Sokolov, considered the father of the non-destructive ultrasonic testing [Sokolov, 1929]. These studies

used the modification of the transmitted amplitude of a wave to detect defects of in a given object.

The pulse-echo technique, which is the base of the current conventional ultrasound systems, was developed by Firestone [1942], who was the first to use pulsed ultrasonic testing by means of a single element that emitted an ultrasonic pulse and received the echos due to impedance changes in the medium. This method made use of the delay time between the pulse emission and the reception of the echos, and presented several advantages over amplitude-base mentioned techniques, as it was more sensitive to small defects which may cause only small variations of the sound pressure. The delay time also allowed the measurement of the reflector distance by using the propagation speed of the wave in the medium, and the time in which echos were registered.

The first ultrasonic equipment capable of obtaining a 2-dimensional image or *B-scan* was created by Wild and Reid [1952]. The technique required manually moving the emitter-receiver transducer, while generating an X-Y scan on an oscilloscope. The amplitude of the echoes modulated the Z axis, making it correspond with the brightness (giving the name of B-scan). This technology was adapted in the 60's to obtain the fist real time 2-dimensional (2D) images of human organs [Krause et al., 1969]. This was obtained applying a single element probe and mechanical movement of this probe, so-called static scanning. Although the images had poor spatial resolution, they provided novel images of the human organs and fetus.

Advances in materials technology allowed the development of *arrays* of transducers, which are a set of small piezoelectric elements located together. Each element is individually controlled, both in emission and in reception in a coordinated way, enabling deflection and electron beam targeting [Macovski, 1975]. The use of arrays was a revolution in the generation of ultrasonic images, giving rise to current ultrasound technology in the clinical and industrial fields. Since then, ultrasonic imaging has undergone an enormous development and several improvements have made ultrasound one of the most important imaging modalities in medicine.

Modern scanners for clinical use look similar to the one depicted in Fig. 1.8. This equipment can be found in almost all the hospitals and clinics, due to its capability to provide images of great quality in a wide range of modalities and because its compact format.

The schematic representation of the functioning principle of a conventional ultrasonic scanner can be seen in Fig. 1.9. An ultrasonic probe, T, sends a an ultrasound pulse that impinges the area of interest to study. A coupling gel is used between tissue and the probe in order to get a good acoustic coupling. When the ultrasonic wave reaches a boundary or interface inside the tissue (represented by B in Fig. 1.8), as we explained in previous sections, a portion of the wave will be reflected at the interface by spectacular reflection or by any of the scattering phenomena introduced. The reflected echo that will travel back to the probe. Inside the probe, the echo will interact with the piezoelectric crystal and will generate an electric signal. Using this signal the location of the interface can be estimated. To do that, the time interval between the pulse transmission and its reception is measured. Using that time and assuming a mean sound speed value of 1540 m/s in all the beam trajectory, 180 degrees of back-scattering and

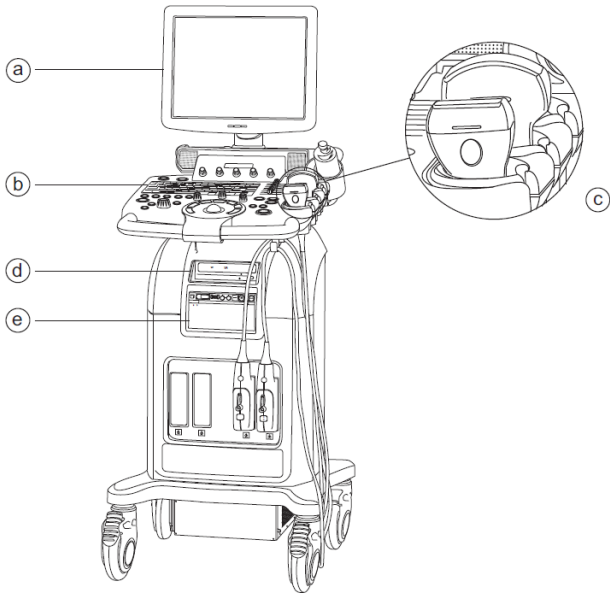

Figure 1.8: Modern ultrasound scanner with a monitor (a), manual controls (b), several probes (c), DVD-RW drive (d), and a printer (e) [Postema, 2011].

also straight line propagation, the amplitude of the recorded signal at the estimated time will be assigned to a determined position in the beam path.

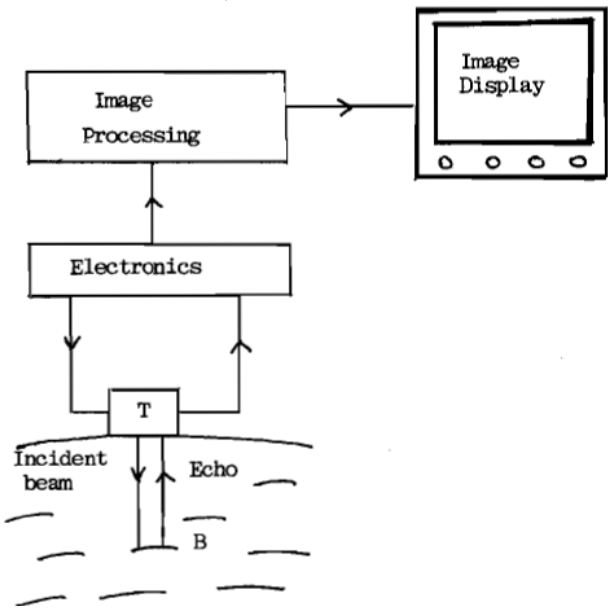

Figure 1.9: Basics of ultrasonic imaging [Tole and Ostensen, 2005].

It is important to say that the aforementioned description of the processes that take place is

just an approximation, because as it was explained, part of ultrasound beam will be transmitted in the frontier between different tissues and the other part will be scattered in several angles. Besides, due to the changes in sound speed of the different tissues, the ultrasound beam will experience refraction. Nevertheless, those simplifications constitute the foundation of echography and with them it is possible to obtain a close approximation to the reality inside the body.

The set of signals or echos recorded along one beam path are known as a *scan-line*. It provides one-dimentional information of the structures along found along the beam path. By deflecting in several directions the ultrasound beam across the subject (which is known as scanning), many other scan-lines are recorded to build a two-dimensional (2D) image of a plane in the subject, also known as *sector image*.

To perform the before mentioned deflection of the beam and also to locate its focus (also known as *beam-forming*), the array elements are delayed in time. There are several ways to operate with ultrasonic arrays to this end, and they differ in the way the emitted and received signals by each element of the array are combine to obtain an image. Among the most used are: *phased array* and *synthetic aperture* techniques. The former uses all the array elements, subsequently delayed in time, to focus the beam in a given direction, and delays are also applied during the reception process. The later (synthetic aperture), employs a reduced number of arrays elements to deflect the beam. For more information about this techniques, we recommend reading [Camacho Sosa Dias, 2011].

There exist several *modes* to display the echos's information recorded. Here some of the most used are mentioned [Cobbold, 2006]:

- The amplitude mode (A-mode): Is the 1D display of amplitude peaks of different heights that can be considered as an estimation of the echo size. It consists of a x and y axis, where x represents the depth and y represents the Amplitude (see Fig. 1.10). Because of the relationship between the distance of a reflector and the time of echo reception, the position of a peak along the time base is a measure of the distance of the associated reflecting boundary from the transducer.
- The brightness mode (B-mode): Is the most common form of ultrasound imaging. It is based on the 2D representation of brightness versus depth. The brightness depends on the amplitude of the echo. There is no y axis on this type of representation, instead, the z axis represents the echo amplitude, and a x axis represents depth.
- The motion mode (M-mode): Is the display of a one-dimensional image that is used for analyzing moving body parts commonly in cardiac imaging. This can be obtained by recording the amplitude and rate of motion, in real time, and periodically measuring the distance object-transducer. The transmitted pulse and received echos are displayed as dots of varying intensities, creating therefore lines across the screen.
- The transmission mode (C-mode): This type of image is created in a plane normal to a B-mode image. In this sense, it is more similar to a classic x-ray image. Instead of recording with the same emitting transducer the reflected echos, this mode employed

another transducer to record the pulse transmitted through the inspected material or tissue. A gate that selects data from a specific depth from an A-mode line is used; then the transducer is moved in the 2D plane to sample the entire region at this fixed depth. It conformed the foundations of USCT systems, which will be presented later.

- The Doppler mode: This mode makes use of the Doppler effect, ie. change in frequency caused by the reciprocal movement of the sound generator and the observer. Diagnostic ultrasound uses the change in frequency of ultrasound signal back-scattered from red blood cells. The frequency of the reflected ultrasound wave increases or decreases according to the direction of blood flow in relation to the transducer.

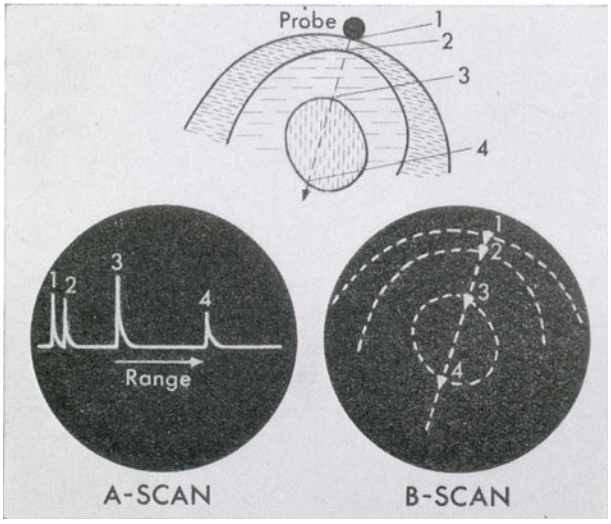

Figure 1.10: The upper picture represents the beam passing through the layers of the pregnant female abdomen: the skin (1), the uterus (2), and the two sides of the fetal head (3 and 4). In A-scan mode, the probe picks up the surfaces 1, 2, 3 and 4 as vertical blips. By contrast, the B-scan shows them as light dots (here shown as dashes), the positions of which correspond to the locations of each echoing interface in the body. Taken from [Donald, 1969].

Even when conventional ultrasound provide a way for real time data acquisition and display, there exist several trade-off that limit the image quality and result in a loss of diagnostic information. Due to the mentioned simplifications that are made for image formation (see previous section), important information that is actually behind the physics of the interaction of the ultrasound with tissue is lost in the process. For example, among these simplifications we may find the straight line propagation assumption, which is only a basic approximation (only valid in a homogeneous medium), as it will be shown in further sections. Moreover, the quality of the resulting image is strongly dependent of the expertise of the operator of the ultrasound system.

In order to fix the mentioned downsides, several equipment have been proposed. Among them are the Automatic Ultrasound Breast Ultrasound Systems (ABUS) [Gazhonova, 2017]. These equipment, as it name indicates, are automatic ultrasound breast systems and provide

several advantages against handheld, physician-performed examinations. In one hand, it reduces the duration of the study and allows scanning the whole breast in a few minutes. On the other hand, the quality of the exam does not depends on the expertise of the clinician performing the exam. However, these type of scanner can not cover all the insonification angles, as the tissue is not inspected in a tomographic manner. Consequently, the resolution is spatially dependent. One example of these type of systems can be seen in Fig. 1.11. The showed scanner is the The ACUSON S2000 ABVS. The transducer employed in this system receives the image of the entire breast volume in 1 min. Its main characteristics are: maximum depth of up to 6 cm, maximum frequency 14 MHz, average scanning frequency 10 MHz, width of 15.4 cm, 768 piezoelectric elements. Its field of view covers 16.8 cm and in a 3D volume it acquires 318 high-resolution slices for post-processing (resolution: axial 0.09 mm, lateral 0.16 mm, and sagittal 0.44 mm) [Gazhonova, 2017].

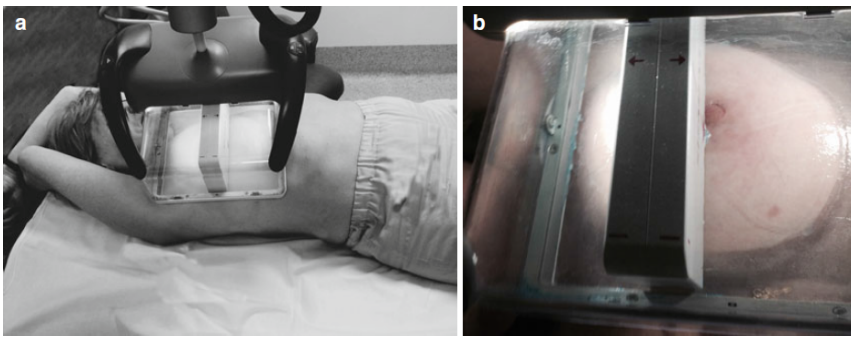

Figure 1.11: Example of an ABUS system for breast automatic exploration with ultrasound (ACUSON S2000 ABVS) [Gazhonova, 2017].

Another alternative to the above mentioned downsides of conventional echography is the Ultrasound Computed Tomography (USCT). These systems besides of using a automated acquisition, employ transducers surrounding the object which ensures full angular covering and therefore, uniform spatial resolution. As it is the center topic of this thesis, the main characteristics of these systems will be introduced in the next sections.

1.2.2 Ultrasound computed tomography systems

Greenleaf and collaborators in 1974 [Greenleaf et al., 1974] were the first ones to introduce the technique of USCT. In this technique, the tissue is imaged using a set of ultrasound transducers located surrounding a region of interest [**?**]. This technique has been mainly proposed to image the breast, basically because this region do not present neither bones nor air and all the inspected region is accessible from 360º. Nevertheless, some researchers have also used this technique for abdominal explorations [Nogami and Yamada, 2007].

Many geometrical configurations for the transducers locations have been investigated [Duric et al., 2015, Kretzek et al., 2015, Wiskin et al., 2007]. A typical configuration setup for

USCT consists on a water tank where the breast is introduced and surrounded with a ring of transducers (see Fig. 1.12 (a)). The reason to use the water bath is to create an acoustic coupling between the transducers and the breast tissues. As the sizes of the breast can vary substantially from one subject to another, the water bath give a convenient medium for coupling. The ring can be built from a single array of transducers (for the reflective modality) with a rotating movement (virtual ring) or with multiple, static or also movable array of transducers (see Fig. 1.12 (b) and (c) respectively). These arrangements allow acquiring tomograms (images slices) at different coronal planes to get the 3D full-volume image. This definition corresponds to the simplest USCT scanners that are only able to scan the object by slices. There are other possibilities consisting on 3D arrays of transducers

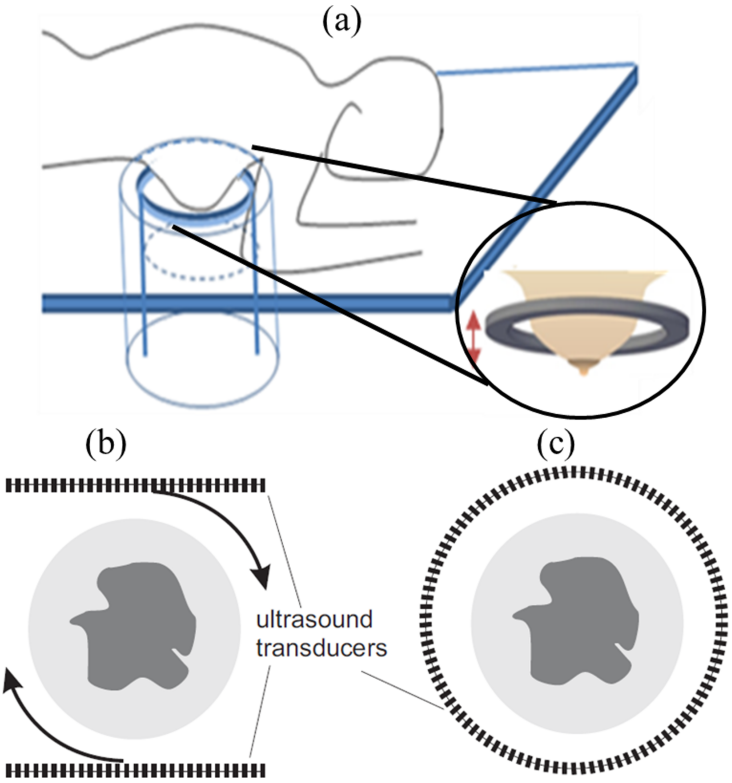

Figure 1.12: Schematic representation of an USCT system. (a) Water bath where the breast is introduced and surrounded with a ring of transducers. Acquisitions are taken at different coronal planes to get the 3D full-volume image. (b) Two linear opposite transducer arrays rotating mechanically around the object. (c) Ring shaped array enclosing the object. Modified from Medina et al. [2016], Stotzka et al. [2002]. Other configurations such as the one shown in Fig. 1.15 are also possible.

In all the cases, each of the transducers acts as the source of an ultrasound field in turn, while the rest of the transducers record the temporal ultrasound signals that carry information about the different structures encountered during propagation. The complete data set is used to recover the spatial distribution of acoustic properties within the tissue.

The aforementioned configurations ensure that both scattered and direct waves are detected within each 2D imaging plane. In the early years of USCT, the limitations in transducers and electronic technology and also the lack of computational power, promoted that the initial works were primarily focused on the development of the reconstruction algorithms and the theoretical basement of the technique. However, with more than four decades of research, there have been only a few systems actually developed and applied to patients. Examples of these systems are:

- **QT-Ultrasound**: Previously known as CVUS (Computerized volumetric ultrasound) [André et al., 2013, Johnson et al., 2007, Wiskin et al., 2007](see Fig. 1.13). This system is able to provide either reflection and transmission images of the breast. To obtain those images the system has a total of five transducers. In one hand, a pair of ultrasound detectors with 1536 elements distributed over eight vertical rows are used for the transmission modality ([Ashfaq, 2007]). On the other hand, three other arrays are employed for the reflection modality.

  For the transmission mode, the frequencies of the arrays are in the range of 0.3-2 MHz (central frequency of 1.1 MHz). For reflection mode, the transducers present a central frequency of 5 MHz with 80% bandwidth. The images are acquired first for the reflection mode and after than for the transmission mode. The total acquisition time is around 8 minutes. The system provides reflectivity images together with sound speed and acoustic attenuation maps.

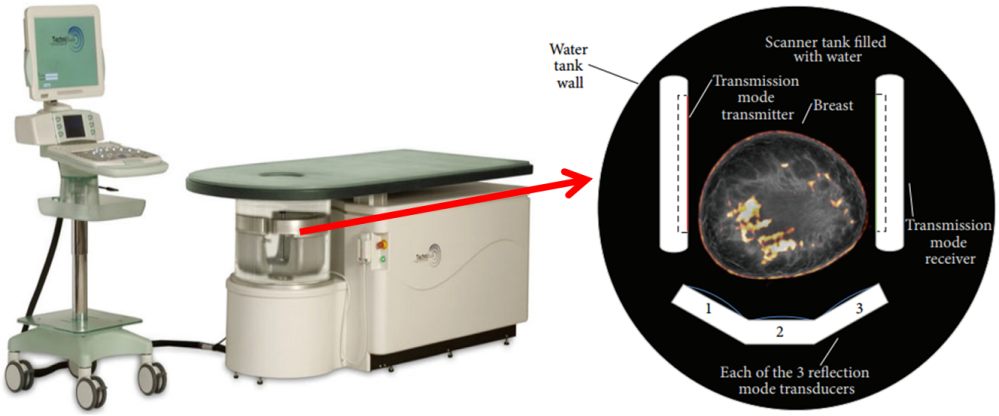

Figure 1.13: QT-Ultrasound scanner, system geometry [André et al., 2013, Johnson et al., 2007, Wiskin et al., 2007, Lenox et al., 2015]

- **SoftVue**: This scanner was created by the Karmanos Cancer Institute (KCI) and Delphinus Medical Technologies [Sandhu et al., 2016, Duric et al., 2008]. It is currently commercially available and used for clinical studies as well (see Fig. 1.14). This scanner consists of a ring of transducers that are able to provide simultaneously transmitted and the reflected images of the breast.

  It is comprised by 2048 transducer elements and uses 512 transmitter and 512 receiver

channels [Ashfaq, 2007]. Its central frequency is 3 MHz and the field of view is around 200 mm. The breast is scanned in the axial direction shifting the ring's axial plane. This can be done to obtain around 30-40 axial tomograms ($\delta z = 2.5$ mm). The total acquisition time for a whole breast takes $\sim$1 minute. The system provides reflectivity images together with sound speed and acoustic attenuation maps.

Figure 1.14: SoftVue scanner [Sandhu et al., 2016, Duric et al., 2008]

- **Karlsruhe Institute of Technology (KIT) scanner**: This system presents a very unique semi-ellipsoidal 3D setup comprised 2041 individual point sources transducers [Ruiter et al., 2017], using 628 as emiters and 1413 as receivers. The higher radius of the field of view is around 26 cm and the height of the cavity is 16 cm [Dapp et al., 2012, Kretzek et al., 2015, Ruiter et al., 2012]. Fig.1.15 shows this system.

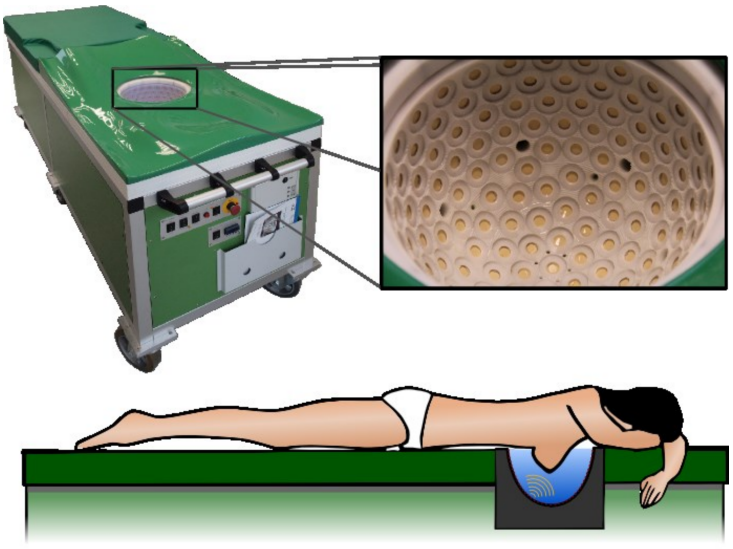

Figure 1.15: 3D USCT Karlsruhe scanner [Dapp et al., 2012, Kretzek et al., 2015, Ruiter et al., 2012]

The arrays present a central frequency of 2.5 MHz and bandwith of 1.5 MHz. Temperature is accurately controlled. The entire system can be rotated and translated, which creates further virtual locations of the transducers. The acquisition time for a whole breast is less than two minutes. The system provides reflectivity images together with sound speed and acoustic attenuation maps.

Characteristics of the USCT data

Fig. 1.16 schematically illustrates how the emitted and recorded signals look for an emitter-receiver pair of transducers in an USCT scanner. For each pair emitter-receiver, a signal similar to the one depicted in the figure is obtained. As result, a total of $N_{emitters} \times N_{receivers}$ signals are recorded for all the possible pairs employed, where $N_{emitters}$ is the number of sources that will emit in turn and $N_{receivers}$ is the number of receivers employed per emitter. Each individual signal contains information of the crossed medium due to its interaction with structures with different SS and AA. Every signal can be characterized by two main parameters, its time of flight (TOF) and its amplitude. This will, of course, reduce the information of the signal, which typically could contains hundreds or thousand non-zero values. The use of only two parameters of the wave, is an important simplification. There are approaches for image reconstruction for which this is enough information (geometrical acoustic methods). Nevertheless, other approaches consider all the wave signal (full-wave algorithms). Several methods to estimate the TOF and the amplitude of the signals will be analyzed in chapter 3.

Any temporal signal $f(t)$, as the one depicted in Fig. 1.16 (a), can be also described in terms of frequency components $F(f)$ via a Fourier transform (see Fig. 1.16 (b)). In the frequency domain there are several parameters commonly employed to characterize the signal. These are (see Fig. 1.17):

- Bandwidth: It is defined as the frequency range between which the input signal is attenuated to a 70.7% (or 3 dB) of its original amplitude (this is also known as the -3 dB point).
- Cut-off frequencies (f_1 and f_2): Those are the frequencies that define the points to measure the bandwidth of the signal.
- Central frequency (f_0): Is the geometrical mean frequency calculated with f_1 and f_2

$$f_0 = \sqrt{f_1 f_2} \tag{1.18}$$

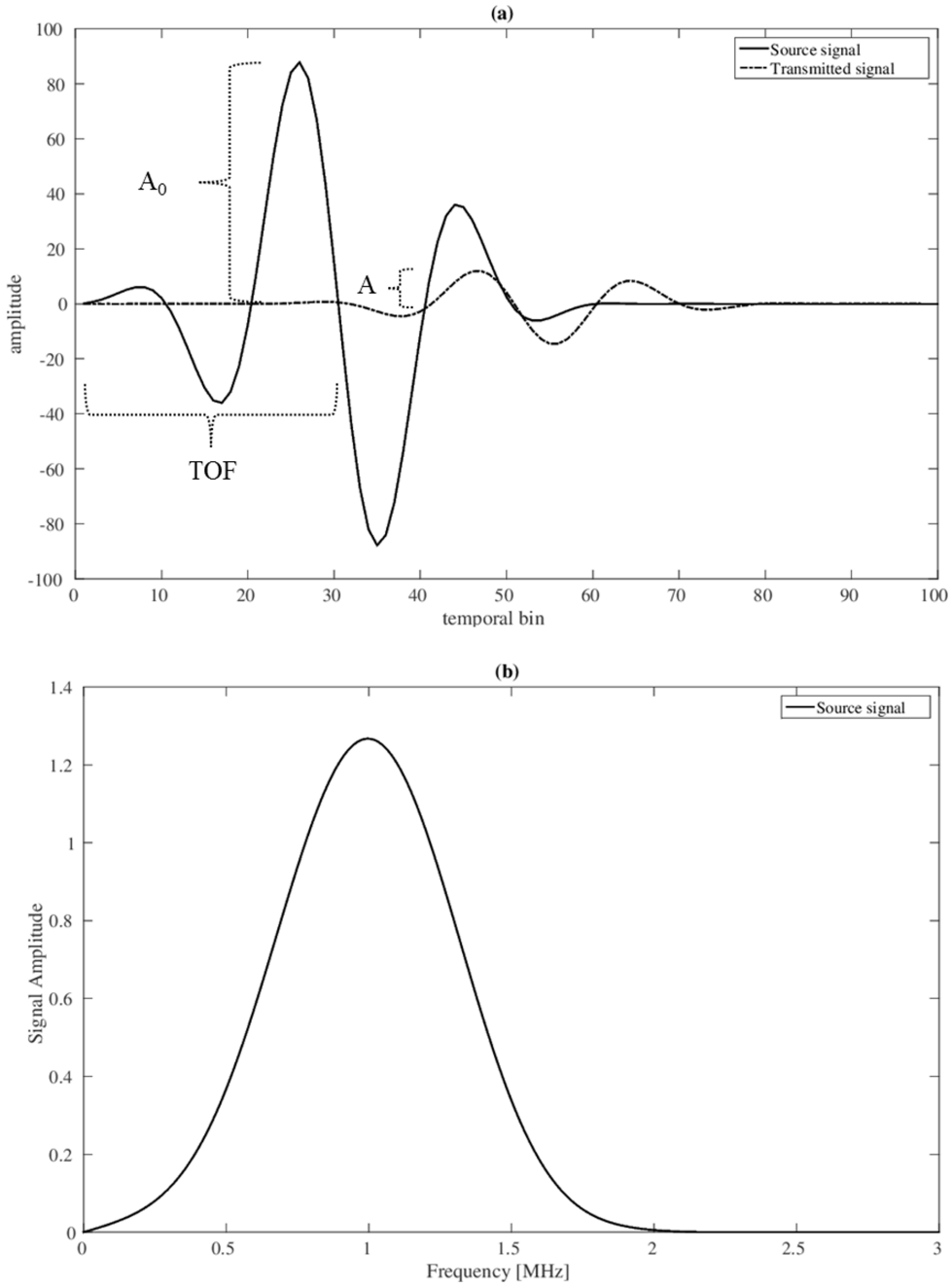

Figure 1.16: Schematic representation of the emitted and received signals for a pair of transducers. (a) Signal representation in the time-domain, each signals can be characterized by its TOF and amplitude. (b) Signal representation in the frequency domain of a signal with ~ 1 MHz of central frequency

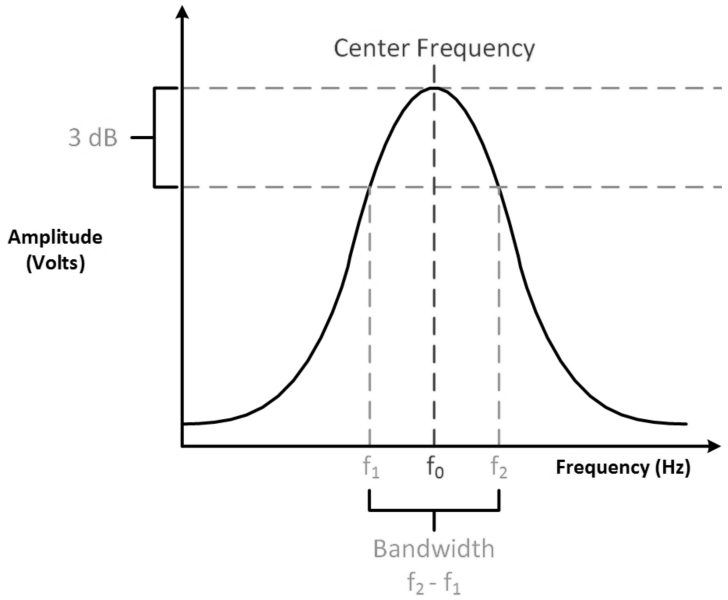

Figure 1.17: Relation among the central frequency, the bandwitdth, the cut-off frequency and the 3 dB point.

1.3 Reconstruction algorithms for USCT

In this section, the main algorithms of reconstruction employed in USCT are described. To perform the reconstruction of transmitted USCT data, several methods have been proposed [Simonetti et al., 2009, Devaney, 1981, 1982, Pérez-Liva et al., 2015, Wang et al., 2015, Roy et al., 2010, Wiskin et al., 2007, Li et al., 2009b]. In order to get an overall idea of the reconstruction in USCT, the following forward linear model can be used:

$$\mathbf{P} = \mathbf{A} \cdot \xi \tag{1.19}$$

Where **P** is the vector of the data (experimental measurements or observable parameters obtained from them), ξ is the vector of the unknown acoustic property model and **A** is the linear matrix that allows relate them.

The matrix **A** plays a relevant role in the inverse problem, as it will be responsible for the influence that the model will have over a given observed data value. This is due to the fact that the raw of **A** corresponding to a a given data value will be only different from zero in those points in the model space where will cause a influence in the data value. Consequently, **A** can be interpreted as a *sensitivity kernel*, that allows pointing those elements in the model space that are sensed by a point in **P**.

Within this linear model, the reconstruction process consist of solving the linear system for which many mathematical methods exist. Nevertheless, the large size of **A** (for example, when **P**

represents the whole acquired data) and the fact that **A** depends on ξ, makes the reconstruction problem challenging. In a more general framework, **A** represents an operator, and may include non-linear effects.

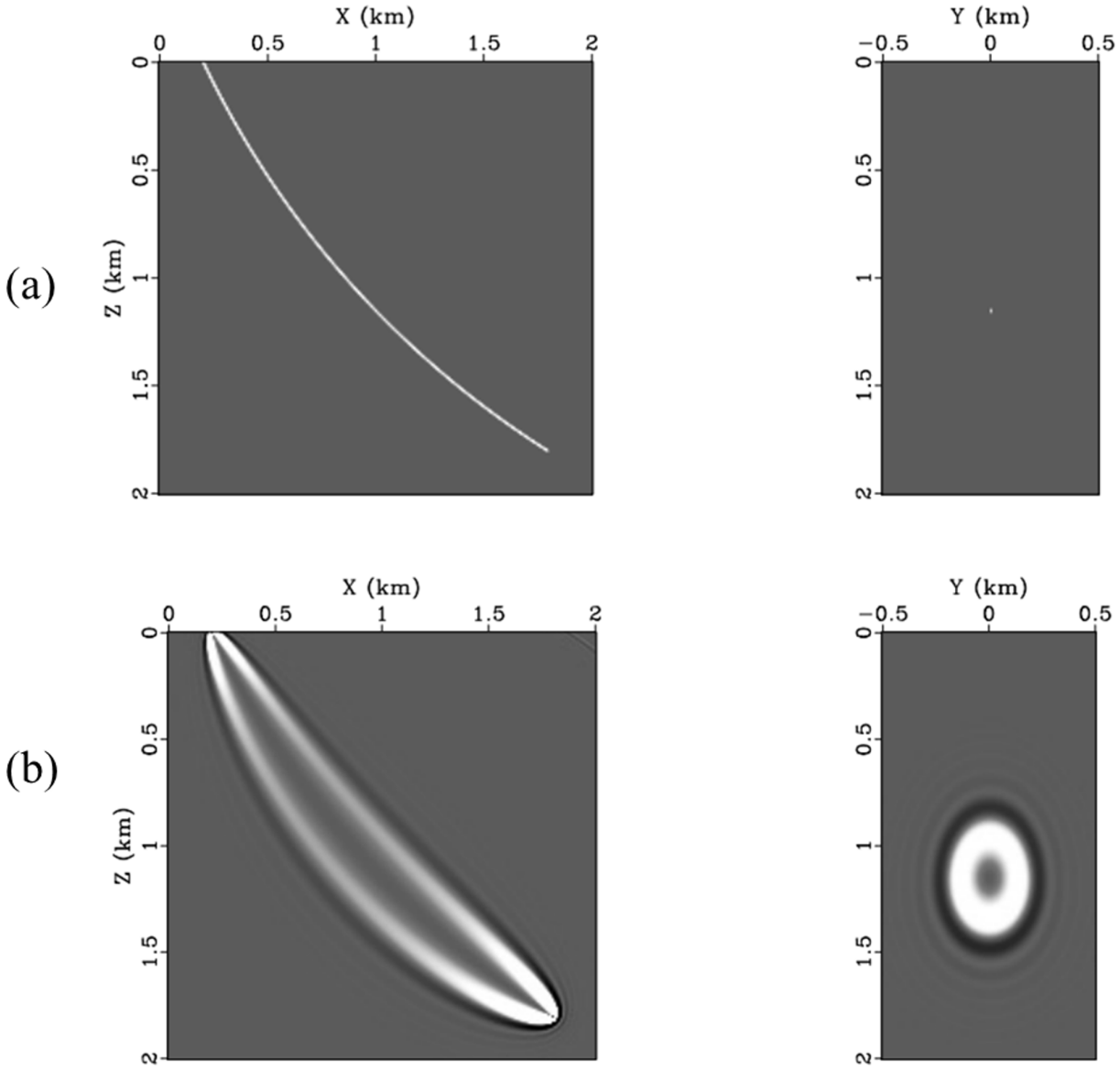

Figure 1.18: Sensitivity kernels for acoustic reconstruction. (a) Ray kenel correspondient with the high-frequency approximation of geometrical acoustics. (b) Banana-doughnut kernel obtained by solving the acoustic wave equation. Figures modified from the [Rickett, 2000]. Is should be mentioned that the image where obtained for seismic purposed what explains the large units that appear on it.

The reconstruction algorithms use different approximations to estimate values of the sensitivity kernel. There are two main models used for these kernels. They can be seen in

Fig. 1.18.

In one hand, Fig. 1.18 (a) shows the kernels that are employed in a set of approximate methods that correspond to what is called *Geometrical acoustics* (GAc) or *Ray theory*. It is explained in Sect. 1.3.1.

On the other hand, more realistic and accurate methods use the kernels employed in 1.18 (b). They are based on the solution of the acoustic wave equation. Methods that use this type of kernels are known as Full Wave Inversion (FWI) methods. This kernel is known as the *banana-doughnut kernel*, as in the plane of propagation it seems a banana, and in the transverse plane it looks like a doughnut. As the frequency of the wave increases, the bananas become thinner and the approximation of the ray kernel shown in 1.18 (a) (which correspond to a high-frequency approximation as it will be shown later) becomes more realistic [Rickett, 2000]. It is explained in Sec. 1.3.2.

1.3.1 Geometrical acoustics

Consider a medium with no absorption and no density variations. In this case, the changes produced in the medium by the propagation of acoustic waves, can be described by the following unbounded acoustic wave equation:

$$\frac{1}{c^2}\frac{\partial^2 p(r,t)}{\partial t^2} - \nabla^2 p(r,t) = 0 \tag{1.20}$$

Where p is the pressure field and c is the SS in the medium. Eq. 1.20 has a simple harmonic solution:

$$p(r,t) = A(r)e^{-if(\theta(r)+t)} \tag{1.21}$$

Where $A(r)$ and $\theta(r)$ are the wave amplitude and phase at position r respectively. When expression 1.21 is introduced into the wave equation 1.20, we obtain the following relation:

$$\mid \nabla^2\theta(r) \mid -\frac{1}{c^2} = \frac{\nabla^2 A}{Af^2} \tag{1.22}$$

Taking a high frequency approximation it can be assumed that the Laplacian of the amplitude of the wave is less relevant than the square of the frequency. According to that, the so-called *Eikonal* equation is obtained [Li et al., 2010]:

$$\mid \nabla^2\theta(r) \mid = \frac{1}{c^2} = S(\mathbf{r})^2 \tag{1.23}$$

Here, S is the slowness, which is the inverse of the SS. Eq. 1.23 allows defining the wave-front as the equality phased points of the domain. $\theta(r)$ will provide the TOF the wave requires to reach a point *r* in the domain of the propagation. According with the *Fermat's principle*, the sound travels along the path that takes the shortest time. Using Eq. 1.23, it can be described the time at which the wave-front will arrive at any given point of the domain.

Eq. 1.23 give rise to what is known as *Geometrical Acoustics (GAc)*. GAc describes the energy propagation of the wave along rays and as it was explained, it is a high-frequency approximation. Therefore, it does not account for finite-frequency processes such as diffraction or interference. On the other hand, it is capable to provide a very computationally efficient numerical description of the energy propagation of the wave. Codes based on approximate models like this one typically exhibit fast convergence but limited spatial resolution (see the comparison with full waves sensitivity kernels in Fig. 1.18), which is an important limitation considering the dimensions of the breast and the lesions of interest to detect.

1.3.1.1 Straight rays approximation

The earliest attempts for USCT reconstruction used transmission TOF and amplitude measurements along straight-rays combined with methods for CT reconstruction (analogous to x-ray CT and PET reconstructions). Greenleaf and colleagues [Greenleaf et al., 1974, 1975] were the first to present results with USCT in transmission mode, using straight rays. Glover and Sharp [Glover and Sharp, 1977] and Carson and colleagues [Carson et al., 1981] were the ones to present results in patients.

The straight rays approximation of geometrical acoustics, as it name indicates, consists on describing the energy propagation of the wave along rectilinear paths. If variations of $S(r)$ in Eq. 1.23 are assumed to be negligible, i.e., $S(r) = constant$, then $\mid \nabla\theta(r) \mid$ is a constant as well. Therefore, the minimum-TOF path between a transmitter and a receiver will be a straight line. Under this formulation, processes like refraction, diffraction and interference are not taking into account. Besides, this kind of methods do not account for any effects of multi-arrivals to a same receiver, which typically occurs and limits the accuracy of the reconstruction process. It is consequently, a very simplified model for sound propagation that will be on the other hand, extremely efficient from a computational point of view.

The images obtained with this method will suffer from a lack of resolution and therefore a lack of information of the reality of the explored tissues. Fig. 1.18 is a demonstration of the loss of resolution the rays-based algorithms are exposed to. Nevertheless, these methods could provide initial real time images to speed-up convergence of other more complicated methods of reconstruction, as will be explained later.

1.3.1.2 Bent-rays method

In order to recover the major characteristics of the explored tissues, it is important to choose an appropriate model for wave propagation not only looking for computational efficiency, but also, taking into account which are the dominant physical processes that take place in the studied medium (in this case, breast tissues). Zhu and Steinberg [1994] showed for both in vivo and numerical phantoms that it is refraction the main process that takes place, and also scattering in a secondary way what dominates the distortion of the ultrasound wave-front in breast tissue. This result supports the use of a second method of geometrical acoustics widely employed for USCT reconstructions, which is the bent-rays approximation. This approach, as it was shown in Ref. [Andersen, 1990], is capable to reproduce refraction of up to 20%, which is above the higher percentage of change in sound speed inside the breast. Typical speed changes in breast, around adjoin tissues, may vary up to 8%.[Li et al., 2010].

The expected limit for the maximum resolution achievable with these approximate ray-based methods, is bounded by $\lambda/2$ (being λ the acoustic wavelength is the medium) [Li et al., 2010]. Considering that the mean speed in the breast is 1550 m/s, and using a typical frequency of 1 MHz, the maximum acoustic resolution would be around ∼0.8 mm. Nevertheless, this value is very difficult to achieve in practice due to it also depends on many other factors, such as the geometrical configuration of the scanner, the width in frequencies of the signal spectrum, among others. Other values around 1-3 λ are, actually, more realistic.

1.3.1.3 Ray-tracing for SS reconstructions

To reconstruct the SS using geometrical acoustics, either with straight or bent rays, the measured TOF of the signals are employed. The algorithms used to obtain the SS map are based on the following system of equations:

$$TOF_i^{sim} = \sum_{j=1}^{n} A_{ij} S_j, \qquad i = 1 : M \tag{1.24}$$

Where j represents the scanned pixel, i identifies the receiving transducer, S_j is the slowness at the pixel j and the coefficients A_{ij}, are the sensitivity kernel elements that relate the data with the pixels connected with the ray representing the wave propagation. These coefficients represent the discretized version of the ray inside the image grid. TOF_i^{sim} is the simulated TOF value estimated at detector i.

With the previous equation, an estimate of the TOF value with a given model of the slowness can be obtained. This value will differ in an amount δT with the measured data:

$$\delta T_i = TOF_i^{exp} - TOF_i^{sim} \tag{1.25}$$

Where TOF_i^{exp} is the measured TOF at the detector i. Using the differences δT, an inverse problem can be formulated to reconstruct the SS distribution, as it is shown in the next sections.

1.3.1.4 The amplitude decay method for AA reconstructions

The amplitude decay method is employed to reconstruct the acoustic attenuation distribution using geometrical acoustics [Carstensen, 1960, Li et al., 2008a]. As it was explained in section 1.1, when the acoustic wave propagates through the medium, it will experience a lost of the initial amplitude by geometrical spreading and by the absorption characteristics of the medium of propagation ($A = A_0 e^{-\alpha(f)x}$, Eq. 1.17). The last statement constitutes the base of the method.

Several factors are assumed:

- A linear dependence on the frequency in the attenuation coefficient is employed

$$\alpha(f) = \alpha_0 f \tag{1.26}$$

- The attenuation in water is neglected.
- The energy is assumed to be concentrated at the central frequency of the signal ($f = f_c$ see Fig. 1.17).

Using the former assumptions and the measurements in water, a way to avoid calculating the geometrical spreading of the wave is obtained. A simple expression to formulate the inversion problem for the attenuation reconstruction can be obtained:

$$\sum_{j=1}^{n} A_{ij}\alpha_{0\ j} = \frac{1}{f_c}\, ln\left(\frac{A_{water}}{A_{phantom}}\right) \tag{1.27}$$

Where, as before, j represents the scanned pixel, i identifies the receiving transducer, $\alpha_{0\ j}$ is the absorption coefficient at the pixel j and the coefficients A_{ij} will relate the data with the pixels connected with the ray that represents the wave propagation. A_{water} is the amplitude of the signal at the i receiver when there is only water in the field of view (FOV) and $A_{phantom}$ is amplitude at the same position as before but with the phantom located in the FOV.

1.3.1.5 Analytic straight-rays approach to solve the inverse problem in USCT

Once the simulated and experimental data are compared, using the expressions (1.25) or (1.27), it is necessary to account with a method to use the observed differences to recover the characteristics of the medium. An analytical solution to the reconstruction problem was originally proposed in 1917, by Radon [Radon, 1917]. He proved that any two-dimensional

object can be reconstructed uniquely from an infinite set of its projections. A projection, using the Radon formulation, is the line-integral, along a given direction in the object. For example, a projection would give us the TOF between two ideal point detectors:

$$T = \int_L \frac{1}{c(x)} dx \tag{1.28}$$

If the object can be described, in an ideally infinitely thin slice, by a scalar function $\xi(x, y)$ (which could be a two-dimensional representation of any acoustical property of the tissues), a projection, considering the reference coordinate system of the object (see Fig. 1.19) and a parallel projection geometry, would be expressed by [Kak and Slaney, 1988]:

$$T(s, \phi) = \int_{-\infty}^{\infty} \int_{-\infty}^{\infty} \xi(x, y)(x \cos\phi + y \sin\phi - s) dx dy \tag{1.29}$$

Here, s is the radial coordinate of the line subtended by the detectors and the reference system of the object. ϕ is its the angular inclination, as it can be seen in Fig. 1.19.

The projections from all the possible angles $\phi \, \epsilon[0, \pi]$ and all possible radial coordinates s can be arranged in what is call as *sinogram*. A sinogram is a three-dimensional matrix in which all the projection values are stored in a system of coordinates ϕ vs. s (see Fig. 1.19). It constitutes the Radon transform of the object. The value of every matrix pixel is exactly the value of the projection defined by (s, ϕ). The name of sinogram comes from the shape that the projections of point will take in this matrix, which will look like a sin curve [Fahey, 2002].

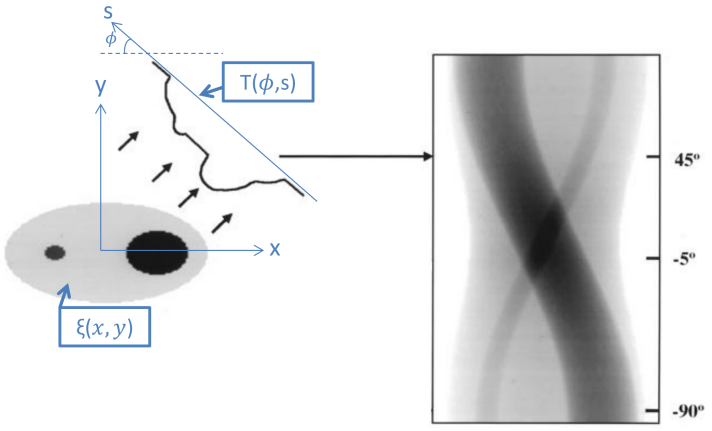

Figure 1.19: Sinograms and projections. A representation of the projections taken for parallel lines at a particular angle (45°) is also diplayed. The sinogram (right panel), contains all the projections of the object. Modified from Fahey [2002].

Using the sinogram of the object and the inverse Radon transform, the initial object can be reconstructed. This process can be figured as stepping back the value of each projection along

the infinitely thin line represented by its coordinates (s, ϕ). Subsequently, every stepped back line in the reference coordinate system of the object should be added. This process is also known as ***back-projection***.

The use of the inverse Radon transform, as it was formulated [Radon, 1917], presents several downsides to perform the reconstruction, because in one hand, only a finite number of projections can be actually measured. On the other hand, the measurements are only an approximation to the real line integrals across the object, as they are influenced by the finite sizes of the detectors, electronic noise and by several other processes that can perturb the straight propagation of the wave. Besides, the analytical expression of the inverse Radon transform does not present an efficient scheme to be computationally implemented [Jago, 1993]. All the mentioned facts produce considerable levels of blurring in the reconstructed objects using this method.

A more suitable method to reconstruct an object from its projections can be derived from the Fourier slice theorem, which states that [Hsieh, 2003]:

"*The Fourier transform of a parallel projection of an object $\xi(x, y)$ obtained at an angle ϕ equals a line in the two-dimensional Fourier transform of $\xi(x, y)$ taken at the same angle*"

Using this theorem, the reconstruction of the object can be efficiently done using its projections by means of the inverse Fourier transform. However, this method also presents some problems with its practical implementation, as the polar coordinate Fourier transform is not as efficient as the fast algorithms that have been developed for Cartesian coordinate transforms [Jago, 1993]. Therefore, intermediate interpolation processes are required, which, in one hand, can introduce errors in the reconstruction and on the other hand, increase as well the reconstruction time.

The previously introduced Fourier theorem can help us explaining the high levels of blurring that appear in the reconstructed images when only inverse Radon is used. Each projection in the two-dimensional image that constitutes the Fourier transform of the object represents a radius in this image. This means that the central component (equivalent to zero frequency) in the Fourier domain is reinforced, by every projection of the object. The same happens, with decreasing density, from lower to higher frequencies in the domain. Consequently, lower frequencies present larger weights than the higher ones when this method is used, which is the main cause of the blurring after the process of back-projection.

To avoid this effect, transform methods are generally used. Transform methods aim to approximate a discrete version of the inverse Radon transform. Among these methods is the commonly employed *filtered back-projection (FBP) method*. In this method, a frequency-dependent filter is added to compensate the variable sampling density with frequency. This is done by using a cone filter ν (also known as ramp filter). This type of filters accentuates higher frequencies and and reduces the lower ones [Alessio and Kinahan, 2006a].

The expression employed to calculate the spatial distribution of the acoustical property of interest from projection data using FBP is [Herman, 1980]:

$$\xi(x,y) = \int_0^{\pi} \mathcal{F}_1^{-1}\{|\nu_s|\mathcal{F}_1\{T(s,\phi)\}\}d\phi \tag{1.30}$$

Where $|\nu_s|$ is the one-dimensional ramp filter, which constitutes a section along the rotationally symmetric two-dimensional cone filter. $\mathcal{F}_1$ and $\mathcal{F}_1^{-1}$ are the direct and inverse one-dimensional Fourier transforms.

According to Eq. 1.30, the first step would be to Fourier transform the data and multiply by the ramp filter. After that, the inverse Fourier transform of the filtered projection is used to perform the back-projection and to obtain the image.

This method has the disadvantage that the CT images are usually band-limited and therefore, very high frequencies contains mostly noise. Consequently, the application of the cone filter accentuates the noise. To avoid that, the ramp filter is apodized using a smoothing window, for example the Hanning, Butterworths or sinc windows.

1.3.1.6 Iterative refraction corrected bent-rays-tracing

The simple straight-ray model have been demonstrated to be inappropriate for obtaining accurate USCT images. Despite of the low variations of sound speed in the breast, ultrasonic waves experience a non-negligible amount of refraction in breast. The inclusion of the refraction process to the rays reconstruction can be done with the solution of the Eikonal equation in 1.23. If instead of a constant $S(\mathbf{r})$ distribution we consider that it is spatially variant, the computation of the gradient $\theta(r)$, i.e. $\mid \nabla\theta(r) \mid$ will provide the bent-trajectory paths.

The methods used to perform bent-rays reconstructions in USCT present an iterative nature. To implement a method of this type there are two basic requirements. First, it is necessary to account with a method to obtain bent-rays trajectories with a given map of sound speed. Second, a method to obtain the image from the projections taken from the object (experimental measurements) is required.

Ben-rays tracing

Eq. 1.23 can be solve with several numerical methods. For example, in reference [Johnson et al., 1975] it was presented a method to perform ray-tracing by solving the second-order differential form of the Eikonal equation [Mamou and Oelze, 2013]:

$$\frac{\mathrm{d}}{\mathrm{d}s}\left(n\frac{\mathrm{d}\mathbf{r}}{\mathrm{d}s}\right) = \nabla n \quad with 0 \leq s \leq l \tag{1.31}$$

With the boundary conditions:

$$\mathbf{r}(0) = a, \quad \mathbf{r}(l) = b, \tag{1.32}$$

This equation describes the trajectory of a ray, $\mathbf{r}(s)$, parameterized by the arc-length s, i.e., $r(s) = [x(s), y(s), z(s)]$, and beginning at a and ending at b. $n(r)$ is the refractive index.

Eq. 1.31 allows computing numerically the bent-ray path passing through the points a and b. Because it is posed as a boundary-value problem, a *ray-linking* problem arises. Generally, the ray direction at a defining the specific path that intercepts the endpoint b is not known. One common approach to solve Eq. 1.31 is to employ the so-called **ray-shooting method**. Using this methods, the ray equation is numerically solved several times in order to make the ray intercept the endpoint. Such methods are slow and unstable, especially if the initial estimate of the ray direction is not correctly selected [Norton, 1987, Mamou and Oelze, 2013].

Another simple and robust solution proposed for the Eikonal equation is the **Fast Marching Method** [Sethian, 1996, Peyré, 2011, Li et al., 2010]. This kind of methods provides the shortest path and therefore, the TOF between the emitter and the receivers using a given SS map.

Fast Marching Method (FMM): FMM is a computationally efficient numerical method that is also very suitable for parallelization. As it was said before, it provides of a discrete solution of the Eikonal equation to describe the propagation of the wave-front using a given SS map. The method was proposed by Sethian in 1996 [Sethian, 1996] and it is based on a similar formulation proposed by Dijktra [Dijkstra, 1959] for computing the shortest path on a network.

The discretized Eikonal equation using the FMM can be written as follows (see Ref. [Gómez, 2013] to see how this expression is obtained and also for further information about the method):

$$max\left(\frac{\theta-\theta_1}{\Delta x},0\right)^2 + max\left(\frac{\theta-\theta_2}{\Delta y},0\right)^2 = \frac{1}{c_{i,j}^2} \tag{1.33}$$

Where Δx and Δy are the grid spacing in the i and j directions respectively and:

$$\begin{aligned} \theta &= \theta_{i,j} \qquad \text{arrival time of the wave-front to the voxel } (i,j) \\ \theta_1 &= min(\theta_{i-1,j}, \theta_{i+1,j}) \\ \theta_2 &= min(\theta_{i,j-1}, \theta_{i,j+1}) \end{aligned} \tag{1.34}$$

The function $\theta(\mathbf{r})$ produced by a traveling wave from a single source point, presents a unique global minimum (the origin or source point). It will not present any local minimum as the speed $c(r) \geq 0\ \forall \mathbf{r}$. The before mentioned condition ensures the monotonically expansion of the wave front (i.e. $\theta > \theta_1$ and $\theta > \theta_2$). Therefore, for points every time more distant from the source, the value of $\theta(r)$ can only grow.

Eq. 1.34 is iteratively solved using the following labels for the grid cells:

- **Origin cell:** Is the source cell from where the calculations are initiated.
- **Unknown cells:** Are those cells still not computed because the wave front has not reached those locations yet. Therefore its θ value is still unknown.
- **Narrow band cells:** These are the collection of cells where the wave-front will expand in the next iteration. Certain θ values have been calculated for them, but those values are temporary assigned because they could be modified during future iterations.
- **Frozen cells:** Cells already crossed by the wave. Its definitive θ value was already assigned.

The process starts assigning as frozen the origin cell ($i = i_0, j = j_0$ and $\theta(i_0, j_0) = 0$) and the rest as unknown. After that, in the first iteration, the narrow band cells are identified (see Fig. 1.20 iteration 1) and its respective θ_1 and θ_2 values are calculated. As in the next iteration the narrow band cells can change, they remain in that form for iteration two. During the following iterations Eq. 1.33 is solved for all the cells that comprise the narrow band. For those cells the lower arrival time is stored. Once Eq. 1.33 is solved for each member of the narrow band, those cells are classified as frozen. When all the cells have been classified as frozen and the narrow band is empty the process is ended. This is schematically represented in Fig. 1.20.

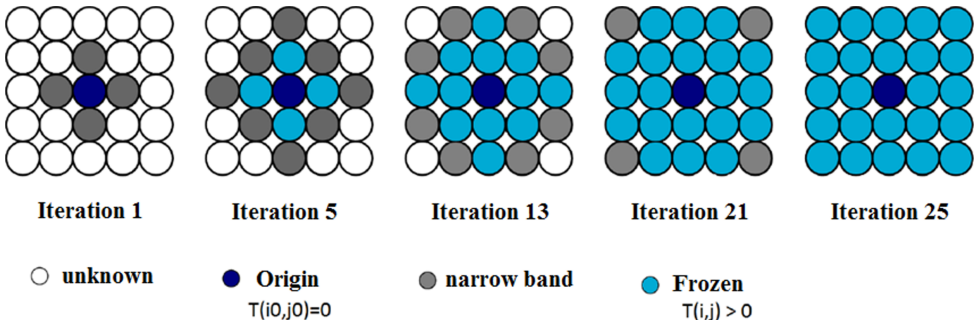

Figure 1.20: FMM iteration in a 5 $\times$ 5 grid with a single wave origin. Modified from [Gómez, 2013]

Iterative bent-rays-based reconstructions

Iterative methods for image reconstruction can provide better reconstructed image quality than analytic ones. These methods use several steps (iterations) in which the images are successively improved. This iterative process in one hand, improves the accuracy of the estimated image but, on the other hand increases substantially the computational burden of the computations. The way to improve the image is by applying corrections that are calculated with a selected optimization algorithm. There are several possible optimization schemes ([Byrne, 2006]), in this work it was used the Maximum Likelihood - Expectation Maximization.

Maximum Likelihood - Expectation Maximization (ML-EM): The Expectation Maximization (EM) algorithm [Dempster et al., 1977, Shepp and Vardi, 1982] is a general statistical

method that can be formulated to solve several different optimization problems. It offers a numerical method for determining a Maximum Likelihood Estimate (MLE). The expression for the ML-EM algorithm can be writen as follows [Alessio and Kinahan, 2006b]:

$$\xi_j^{(n+1)} = \frac{\hat{\xi}_j^{(n)}}{\sum_{i'} A_{i'j}} \sum_i A_{ij} \frac{p_i}{\sum_k A_{ik} \hat{\xi}_k^{(n)}} \tag{1.35}$$

where $\xi_j^{(n+1)}$ is the slowness or absorption coefficient value in the pixel j for the next iteration based on the value $\hat{\xi}_k^{(n)}$ at the current iteration.

The reconstruction process using ML-EM is performed according to the scheme shown in Fig. 1.21.

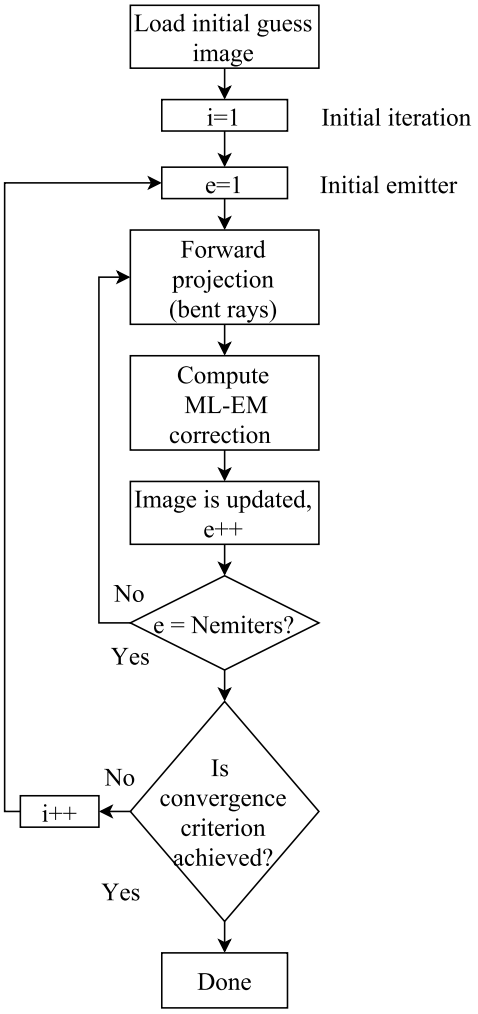

Figure 1.21: General flow diagram of the maximum likelihood-expectation maximization algorithm (ML-EM)

First, for the first emitter, the projections in all the receivers are estimated using a bent-rays method and an initial guess image (that could be for example, a homogeneous map). Next, the projections are compared to the measured data and corrections are calculated with the data simulated at each receiver using the expression of 1.35. After that, in order to update the SS or AA distribution, the corrections are back-projected into the image domain to obtain a correction factor for the initial image estimate. By means of the aforementioned step, an image of corrections is obtained. This image of corrections is updated with the corrections provided by all the emitters. The final image of correction is multiplied by the initial image and divided by a weighting term (based on the system model). In this way, the initial image is updated and used as initial guess in the next iteration. Finally, a convergence criterion is evaluated. If it is not fulfilled, the updated SS or AA distribution is used as the starting value for the next iteration. The whole process is repeated until the convergence criterion is satisfied.

As it is of our interest to reconstruct with this method both the SS and AA, the strategy with this type of methods to reconstruct both distributions consist on two consecutive steps. First, a formulation to obtained the bent-rays trajectories for the wave propagation is employed. With this formulation, the SS distribution is reconstructed. After that, the bent-trajectories that are obtained from the final SS map are employed to reconstruct the AA distribution without the need to recalculate the paths.

1.3.2 Full wave inversion

As it was mentioned in previous sections, one key requirement of any reconstruction algorithm is to account with a computational model to simulated the wave propagation process. When the geometrical acoustic approximation is employed, this computational model consists on straight or bent rays that only account for the transmission process of the wave in one case, and for transmission and refraction on the other. Alternatively to the geometrical acoustics, those algorithms that are based on computational models that directly solve the wave equation, also known as full wave inversion (FWI) methods, have shown the best results in terms of detectability, resolution and artefact control [Li et al., 2014, Wang et al., 2015, Roy et al., 2010, Anis et al., 2014, Wiskin et al., 2007]. Depending on the amount of processes incorporated into the wave equation, the simulated physics is more close to the reality of the propagation, but generally, at the same time the computation cost could be affected. FWI methods have been mostly adapted from the geophysical techniques of waveform tomography [Tarantola, 1987, Song et al., 1995, Pratt et al., 2007]. FWI not only facilitates the detection of very small masses, but also provides additional details of the shape and margins of the structures of the breast, which could also play a role in the discrimination between benign and malignant structures [Fornage et al., 1989]. Nevertheless, the use of the FWI has previously been limited due to its computational burden, as it involves solving a large-scale ill-posed non-linear optimization problem, with uncertainties not only in the measurements but also in the propagation models. Fortunately, the significant acceleration provided by parallel processing with graphics processing units (GPUs) has recently allowed a considerable reduction in execution times. Combined with the use of optimized numerical methods to solve the wave equation [Treeby and Cox, 2010b,a,

2014, Treeby et al., 2012b], this can significantly improve the efficiency of image reconstruction using FWI.

1.3.2.1 Notation and forward model

The linear propagation of acoustic waves in a lossy medium where the acoustic absorption follows a frequency power law like in Eq. 1.11, can be described by a series of coupled first-order partial differential equations based on the conservation of mass, momentum, and energy [Treeby et al., 2012b].

$$\begin{aligned} \frac{\mathrm{d}\mathbf{u}}{\mathrm{d}t} &= \frac{1}{\rho_0}\nabla p \\ \frac{\mathrm{d}\rho}{\mathrm{d}t} &= -\rho_0 \nabla \cdot \mathbf{u} - \mathbf{u} \cdot \nabla \rho_0 \\ p &= c^2(\rho + \mathbf{d} \cdot \nabla \rho_0 - L\rho) \end{aligned} \tag{1.36}$$

Here **d** represents the acoustic particle displacement, **u** is the acoustic particle velocity, p is the acoustic pressure, ρ is the acoustic density, ρ_0 is the ambient or background density, and c is the sound speed. The operator L in the pressure-density relation in Eq. 1.36 is a linear integro-differential operator given by

$$L = \tau_1 \frac{\partial}{\partial t}\left(-\nabla^2\right)^{\frac{y}{2}-1} + \tau_2 \left(\nabla^2\right)^{\frac{y+1}{2}-1} \tag{1.37}$$

The two terms in 1.37 account for acoustic absorption and dispersion, where τ_1 and τ_2 are given by

$$\tau_1 = -2\alpha_0 c^{y-1} \quad \tau_2 = 2\alpha_0 c^y tan\left(\frac{\pi y}{2}\right) \tag{1.38}$$

In the preceding equations, the ambient density, sound speed, and absorption proportionality coefficient may all vary as a function of spatial position r, and the pressure, particle displacement and particle velocity vary as a function of time and spatial position. When the system of coupled first-order partial differential equations given in Eq. 1.36 is combined, the fractional Laplacian wave equation is obtained [Chen and Holm, 2004, Treeby and Cox, 2010a]:

$$\Box_\alpha^2 p(\mathbf{r}, t) = S(\mathbf{r}, t) \tag{1.39}$$

where $S(\mathbf{r}, t)$ is the source of the ultrasound waves and $\Box_\alpha^2$ denotes the lossy D'Alembertian operator:

$$\Box_\alpha^2 = \frac{1}{c^2}\frac{\partial^2}{\partial t^2} - \nabla^2 - \tau_1(-\nabla^2)\frac{y}{2}\frac{\partial}{\partial t} - \tau_2(-\nabla^2)\frac{y+1}{2} \tag{1.40}$$

1.3.2.2 Inversion problem

As we said before, the task in USCT is to recover the spatial distribution of acoustic medium properties using a set of experimental measurements recorded by an array of ultrasound transducers, where each transducer acts as the source in turn. Using the reconstructed medium properties and accurate simulations of the wave propagation, it should be possible to reproduce the set of experimental measurements of the acoustic field. The reconstruction can be formulated as an inverse problem, namely as the minimization of a functional or cost function, for instance the least-squares misfit between synthetic (p) and observed data (p_{obs}). The use of the least-squares misfit function is a common method practically used in all the works that make use of FWI as reconstruction method not only for medical purposed but also in seismology (also called as seismic migration). This cost function has the following form:

$$\varepsilon = \frac{1}{2}\sum_{m=1}^{M}\int_0^T \Big[p(\mathbf{r}_m, t) - p^{obs}(\mathbf{r}_m, t)\Big]^2 dt \tag{1.41}$$

Given a ring array comprised of N detectors, here m represents each of the $M = N(N-1)$ pairs of emitter-receiver transducers of the tomographic ultrasound setup, r_m defines the positions of the receiving transducers, and T is the length of the time window employed to record the signals.

This functional depends on the acoustical variables of the medium that we want to recover. Therefore, the minimization of the cost function can be written as:

$$\xi^{opt} = arg\ min[\varepsilon(\xi)] \tag{1.42}$$

Where ξ represents the acoustical property distribution to be recovered, and $\varepsilon(\xi)$ is the error functional, i.e., the data fidelity term.

Minimization process: Minimization algorithms seek to find a local minimum of a function, i.e. to solve Eq. 1.42. This algorithms are generally iterative and initiate with an initial guess of the variable ξ. They generate a sequences of improved estimates of the variable $\xi^0, \xi^1, \ldots, \xi^{opt}$(which is called iterates or minimizing sequence) until they reach convergence (i.e. the local minimum is found). The element ξ^{opt} is a local minimizer of the objective function ε. When ε is convex, ξ^{opt} is also its global minimizer; otherwise, it is said that the algorithm is locally convergent. There are several methods which can be used to move from one iterate to the next, and many will determine the next iterate using the objective function ε or its derivative (generally the first and sometimes the second derivative is also used)[Nocedal and Wright, 2006].

All the methods require the calculation of a direction to move (ideally the direction to the global minimum) and a step size to define how fast in that direction to move. The algorithms available can be categorized as: **line-search methods** and **trust-region methods**. The main difference between them is the order in which the direction to travel and the step-length are chosen. Line-search methods first search for an appropriate direction $\mathbf{d}^k$ and then decide on a step-size λ^k calculating the next iteration estimate like:

$$\xi^{k+1} = \xi^k + \lambda^k \mathbf{d}^k \tag{1.43}$$

Trust-region methods first define a region around the current iterate in which to search for a suitable direction, i.e. they search for a ξ^k such that $\xi^k + \lambda^k \mathbf{d}^k$ lies inside the predefined trust-region.

The algorithm used to search for the direction $\mathbf{d}^k$ typically defines the method to be employed. If $\mathbf{d}^k$ is a descent direction, a small step in this direction will ensure the function ε will decrease. The step-size λ^k can be chosen with several methods. Nevertheless, a convenient choice is to travel along the direction in which ε decreases most rapidly, i.e. $-\nabla\varepsilon$, where $\nabla\varepsilon$ is the gradient or directional derivative of the function ε (see Fig. 1.22). In a rectangular coordinate system, the gradient is the vector field whose components are the partial derivatives of the ε

$$\nabla\varepsilon = \frac{\partial\varepsilon}{\partial x_1}\mathbf{e}_1 + \ldots + \frac{\partial\varepsilon}{\partial x_n}\mathbf{e}_n \tag{1.44}$$

where the e_n are the orthogonal unit vectors pointing in the coordinate directions.

The algorithms that use as direction to move $-\nabla\varepsilon$ are called *gradient-descent or steepest-descent algorithms*. This type of algorithms are specifically suitable for smooth functions although they are also applicable in a wide number of situations.

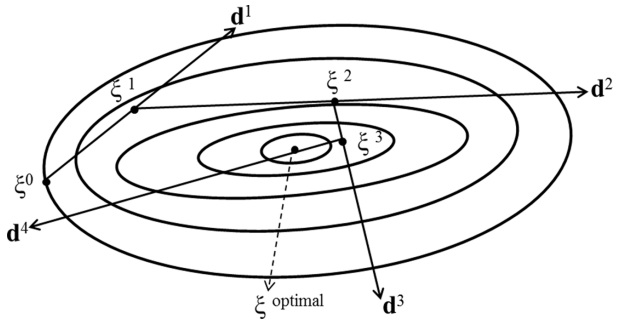

Figure 1.22: Sequences of steps of a line search steepest-descent algorithm

Backtracking line-search: There a several possible line-search methods. Nevertheless, one of the simplest is the so-called acktracking line-search. This is a line-search method that allows reducing ε in a "sufficient" way. It is one of the most popular algorithms employed for

optimization and it is sometimes also called the Armijo rule. The method assumes that the function $\varepsilon\ \mathcal{R}^n \rightarrow \mathcal{R}$ is differentiable and that a direction $\mathbf{d}$ of strict descent at the current point ξ^k is known (i.e. $\varepsilon'(\xi^k, \mathbf{d}^k) < 0$). If $\nabla\varepsilon(\xi^k \neq 0)$ this means that there exits an strict descent direction. The steps fallowed by the algorithm are as follows:

- Initialization: The variables $\gamma\epsilon(0,1)$ and $c\epsilon(0,1)$ are chosen.
- Computing the backtracking step-size:

$$\begin{aligned} \lambda^* = max\ \gamma^\nu \text{where } \nu\epsilon[0,1,2,\ldots] \\ f(\xi^k + \gamma^k \mathbf{d}^k) \leq \varepsilon(\xi^k) + c\gamma^\nu \varepsilon'(\xi^k, \mathbf{d}^k) \end{aligned} \tag{1.45}$$

- Chose the new ξ : $\xi^{k+1} = \xi^k + \lambda^* \mathbf{d}^k$

1.3.2.3 Gradient of the error functional

The previous section demonstrate how to perform the optimization process for a variable once the gradient of the error functional was obtained to ensure the descent direction. In this section it is going to be shown how to calculate the gradient of the error functional with respect to the acoustic property of interest. There are several methods to compute the gradient. In one hand we are going to refer to a computationally expensive but very accurate algorithm that is the finite-difference method (also called brute force algorithms). On the other hand we will present the Adjoint method, which is a robust method to calculate the gradient that offers several advantages in comparison with finite-difference methods.

Finite-difference method for gradient calculation: The most intuitive method to calculate the gradient of an error functional is by using a **finite difference method**. It consist on analyzing the sensitivity of the error functional 1.41 when each element in turn along all the grid elements of the image is perturbed in a amount $\Delta\xi$, where as before, ξ is the acoustic property under study. This is a computationally expensive procedure as it requires using computing the forward model as many time as the number of elements in the grid size, plus an additional calculation without any perturbation. The equation to compute the gradient for each element i of the grid is as follows:

$$\frac{\partial \varepsilon}{\partial \xi_i} = \frac{\varepsilon(\xi_i + \Delta\xi) - \varepsilon(\xi_i)}{\Delta\xi} \tag{1.46}$$

Where ξ_i is the value of acoustical property at location $\mathbf{r}_i$.

Adjoint method for gradient calculation: In inversion problems the actual medium is not known and what is desirable would be to have an algorithm that allow us to propagate the data-model misfit from our observation points directly back to the points in the medium where we need to make adjustments. This process is exactly the base of what an *adjoint model* does. The idea behind this methods is to back-propagate an *adjoint field*, which is comprised by the

differences between simulations and measurements at the receivers location, back to the points in the medium where the corrections are required. In this way, each point in the medium receive exactly the appropriate correction needed.

This method needs solving just two forward problems per iteration: the direct problem and its adjoint. The method is independent of the number of pixel of the image as well as the number of receivers employed. One simple introduction to this method was given by, Norton in 1999 [Norton, 1999]. He proposed a straightforward methodology to obtain the gradient of the functional error with respect to the sound speed using the scalar wave equation. The scalar wave equation is a frequency domain formulation of the wave propagation, and is given by:

$$\nabla^2 p(\mathbf{r}) + k^2 n(\mathbf{r}) p(\mathbf{r}) = -S(\mathbf{r}) \tag{1.47}$$

Where $k = \frac{f}{c}$ is the wave number, $S(\mathbf{r})$ denotes the source of monochromatic waves and $p(\mathbf{r})$ is the total pressure field composed by the direct plus the scattered waves. This equation describes the propagation of a monochromatic wave of frequency f.

The Norton's formulation is simple to follow an also to extend to more complex expressions of the wave equation in order to find the gradient of the functional error with respect to other acoustic parameters. We will explain the methodology followed by Norton in order to illustrate how the adjoint method he proposed works.

To find the $n(\mathbf{r})$ that optimize the cost function 1.42, is necessary to find the variation in ε, $\delta\varepsilon$, due to an infinitesimal variation in $n(\mathbf{r})$, δn.

$$\frac{\partial \varepsilon}{\partial n(\mathbf{r})} = \iiint_V \nabla \varepsilon d^3 r \tag{1.48}$$

This expression lead to the functional gradient or *Frechet derivative* (the Frechet derivative is the derivative of a functional) $\nabla\varepsilon$ of ε.

This variation in $n(\mathbf{r})$ will carry out a variation in the pressure field as well given by $\delta p\mathbf{r}$. If now we applied the infinitesimal variation to the scalar wave equation 1.47 it will be obtained:

$$\nabla^2 \delta p(\mathbf{r}) + k^2 n(\mathbf{r}) \delta p(\mathbf{r}) + k^2 \delta n(\mathbf{r}) p(\mathbf{r}) = 0 \tag{1.49}$$

and also taking infinitesimal variation in the error functional 1.42:

$$\frac{\partial \varepsilon}{\partial p(\mathbf{r})} = \mathrm{Re} \sum_{m=1}^{M} (p(\mathbf{r}_m) - p(\mathbf{r}_m)^{obs})^* \tag{1.50}$$

Now, the basic of the adjoint method will be introduced defining an *adjoint field* $p^*(\mathbf{r})$ that will be solution of the scalar wave equation 1.47 as follows:

$$\nabla^2 p^*(\mathbf{r}) + k^2 n(\mathbf{r}) p^*(\mathbf{r}) = -S^*(\mathbf{r}) \tag{1.51}$$

Being $S^*(\mathbf{r})$ the so-called *adjoint source* defined as:

$$S^*(\mathbf{r}) = \sum_{m=1}^{M} \Big[p(\mathbf{r}_m) - p^{obs}(\mathbf{r}_m) \Big]^* \delta(\mathbf{r} - \mathbf{r}_m) \tag{1.52}$$

Substituting Eq. 1.52 into Eq. 1.50 we can obtain:

$$\frac{\partial \varepsilon}{\partial p(\mathbf{r})} = -\operatorname{Re} \iiint_V S^*(\mathbf{r}) d^3\mathbf{r} \tag{1.53}$$

Using Eq. 1.51 into Eq. 1.53, integrating by parts and after some simple mathematical operations it will be obtained:

$$\frac{\partial \varepsilon}{\partial p(\mathbf{r})} = -\operatorname{Re} \iiint_V p^*(\mathbf{r}) [\nabla^2 + k^2 n(\mathbf{r})] d^3\mathbf{r} \tag{1.54}$$

Now let's substitute Eq. 1.49 into 1.55:

$$\frac{\partial \varepsilon}{\partial n(\mathbf{r})} = k^2 \operatorname{Re} \iiint_V p^*(\mathbf{r}) p(\mathbf{r}) d^3\mathbf{r} \tag{1.55}$$

Finally, if Eq. 1.55 is compared with Eq. 1.48 it is possible to obtain the desired expression for the gradient of the error functional with respect to the scattering potential $n(\mathbf{r})$:

$$\nabla \varepsilon = k^2 \operatorname{Re} p^*(\mathbf{r}) p(\mathbf{r}) \tag{1.56}$$

In the previous expression it is important to point out several aspects. First, the expression is independent the spatial sampling employed for the simulations. It does not depends neither on the number of transducer detectors comprising the USCT scanner. It only requires solving two forward problems per iteration: one for the forward propagation of the pressure field generated by the emitter to obtain p, and a second time for the backward propagation to obtain the adjoint field p^*. This operation has to be performed sequentially for each emitter in each iteration. This means that the total number of times the wave equation needs to be solved per iteration is twice the number of transducers (to obtain p and p^*). If this algorithm is employed together with a line-search method to update the scattering potential, the aforementioned number of evaluation of the forward problem would be incremented by the number of evaluations the line-search algorithm may need.

1.3.2.4 Regularization

One of the main challenges in FWI for USCT is that the inversion here is a typical ill-posed problem. This means that its solution is not unique and computationally unstable because the insufficient data available and because most of the data are affected by noise [Jackson, 1972].

Consequently, the employment of a method of regularization is indispensable in order to get a unique and stable solution and to eliminate artifacts due to noise.

However, to regularize the solution of an inverse USCT problem the most important step is the choice of the regularization method to be used. The regularization should be in agreement with the intrinsic characteristics of the problem to be study in order to obtain a correct and stable solution. There are two main types of regularization employed in FWI: *Tikhonov* and *Total Variation* (TV) regularization [Tikhonov, 1963, Rudin et al., 1992]. Tikhonov regularization enforces spatial smoothness uniformly on the output image. This regularization consist on a linear quadratic term that strongly penalize discontinuities smoothing each piece-wise discontinuous edge. Therefore, this regularization cause blurring and eliminates sharp edges structure. On the other hand, when the interest relies into recovering images that are piece-wise continuous, a regularization as the TV could result more suitable. It consist on a non-linear or non-quadratic term with highly edge-preserving properties. Consequently, the TV regularization avoids over-smoothing and to preserve the edge information of the structures present in the image. This type of regularization adapts perfectly to the characteristics of the breast tissues. As it was explained before the breast is comprised by several structures with quite different acoustic properties where it is possible to assume that each structure is composed by a set of pixels of the same value. Besides, the shape and margins of the structures of the breast, could also play a relevant role in the discrimination between benign and malignant structures [Fornage et al., 1989].

The TV regularization term, given by the functional R_{TV}, can be written as:

$$R_{TV} = \sum i, j \sqrt{\xi^2_{x,i,j} + \xi^2_{y,i,j} + \theta} \tag{1.57}$$

Where, $\xi_{x,i,j}$ and $\xi_{y,i,j}$ are the derivatives of the acoustical property ξ with respect to x and y respectively at the pixel (i, j). The parameter θ ensures R_{TV} be continuously differentiable.

1.4 Image quality in USCT

There are only a few of works were quantitative analysis of the reconstructed USCT images are presented. As USCT is still an under development technique, no quality protocols or figures of merit for the reconstructed images have been created yet or selected to be used in USCT. At present, several efforts are done by the USCT research community to address this issue. An example of this is the celebration of the first panel discussion for USCT at the SPIE congress 2017. As a result, a website for "USCT data exchange and collaboration" was created to discuss topics of interest in this field [Dat].

To analyze the image quality, some works have opted for a quantitative analysis of the reconstructed images based on the bias between the expected values and the reconstructed ones [Pérez-Liva et al., 2017, Li et al., 2008a, 2014]. This is done for simulated data or well-characterized in-vitro tissue mimicking phantoms. To do that, regions of interest (ROI) are

chosen inside several structures of the reconstructed images. A ROI consists on a set of pixel withing the studied structure. The mean values and standard deviation withing the selected ROI are generally analyzed. On the other hand some works have also explore the resolution of the images by using profiles across the reconstructed distributions. The resolution is then estimated as the distance required for the edge response to rise from 10% to 90% of its value [Li et al., 2014].

Chapter 2

Materials and tools

In this chapter the hardware and software tools employed in this thesis are described. First, in section 2.1 the main characteristics of the MUBI-USCT prototype used yo obtain experimental data and test some of the proposed methods are shown. After that, in section 2.2 the fundamental features of the ultrasound wave numerical simulator k-Wave is introduced. This code was employed in several aspects of this thesis, both to obtain synthetic data to test the proposed methods and for forward and backward propagation inside some of the reconstruction algorithms proposed.

2.1 The USCT-TOPUS prototype

The MUBI-USCT scanner is a low-cost USCT prototype (see Fig. 2.1(a)) [Medina-Valdés et al., 2015, Medina et al., 2016, Pérez-Liva et al., 2016, González-Salido et al., 2016] initially developed as part of the project ARTEMIS [S2009/DPI-1802, 2009-2013] and most recently improved as part of the project TOPUS [S2013/MIT-3024, 2013-2017]. It was developed as a proof-of-concept for the final USCT scanner that the TOPUS project aims to develop (consisting on a ring of fixed ultrasonic transducers).

MUBI is comprised by 2 coplanar medical, 128-element, linear array transducers, with a central frequency of 3.2 MHz and 50% of bandwidth (Prosonic, Korea). The array probes and the breast phantom are arranged inside a water tank to have good ultrasound coupling.

The arrays can be displaced independently using stepper motors with high mechanical resolution (0.1^{o}) to cover several locations around a breast phantom. The radius of rotation of the arrays is 100 mm but it also have two arrays holders that allow reducing this rotation radius up to $\sim$ 45 mm. The scanner counts with a modulus for beam forming (beam steering and dynamic depth focusing) that is employed for the reflectivity technique which consists on an ultrasonic equipment, SITAU 112 (Dasel, Spain). The measured data is transferred through a USB interface to a computer for data post-processing. Besides, trough the USB interface the

motors control is performed as well.

The MIBI-USCT system allows recording signals in reflection and transmission mode (in different steps). For the reflectivity modality and the Acoustic radiation Force Imaging (ARFI) only one of the transducers is employed, with the particularity of being able to perform beam forming in emission and reception of the signals. This allows this modality could be executed in real time by taking dozens of images per second (online).

To acquire transmission data, one of the arrays is employed as emitter and the other as receiver (as it is indicated in Fig. 2.1(a)). For each emitting position, the receiver's position is shift several times to cover a variable area that describes a fan-beam (see Fig. 2.1(b)). This process is sequentially executed changing the angular orientation of the fan-beam in order to scan the whole domain. The changes in the angular orientation of the fan-beam are done with fixed angular steps.

The pitch between transducer elements is of 1 mm. The total acquisition time with this initial prototype was 10 minutes per coronal plane, most of it employed in the arrays displacements.

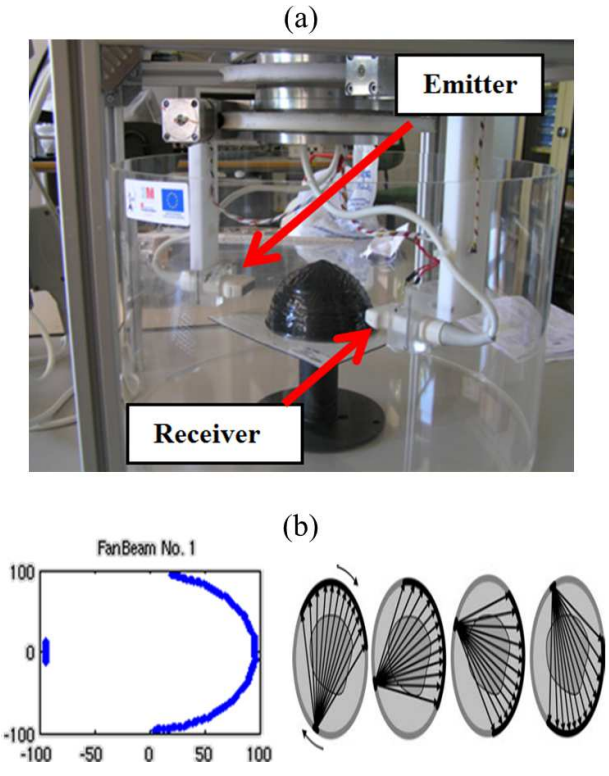

Figure 2.1: (a) Experimental arrangement of the TOPUS-USCT scanner. (b) USCT setup with rotating fan-beams. A variable number of fan-beams can be used in this setup to scan the whole field of view of the scanner.

2.2 The k-Wave code

As the goal of this work is to recover accurately both the SS and AA distributions in USCT, the acoustical wave equation employed should take into account the absorption process and the inhomogeneities of the medium. There are several available and well-validated codes that can deal with these requirements [Demi et al., 2011, Treeby and Cox, 2010b, Pinton et al., 2009]. Nevertheless, when choosing an algorithm for the propagation of acoustic waves in a domain with the typical sizes of an USCT scanner (in the order of tens of centimeters in each Cartesian direction), especial interest have to be put in the speed of execution and storage requirements of the simulations [Jaros et al., 2015].

The wavelength of the ultrasonic waves in water at the commonly employed frequencies in USCT (in the order of the few of MHz) is around 0.1-10 mm. These values analyzed together with the typical scanner sizes ($\sim$ 10 cm radius) demonstrate that to simulate the propagation of an ultrasound source in such domains, it is required the propagation over hundreds or thousands of wavelengths. If conventional finite-difference (FD) schemes are used for the propagation on a uniform Cartesian grid, at least 10 grid points per wavelength are needed to achieve numerical stability of the code. This means the resulting grid sizes can exceed 10^{12} grid points. Storing one matrix of this size in single-precision takes up to 400 GB or more of computer memory [Treeby and Cox, 2010b]. Besides, in many practical cases, the temporal evolution of the wave fields is also of interest, an again many small time intervals re needed to avoid numerical dispersion, which increase the storage demand. This can make the simulations intractable.

One interesting alternative code to ameliorate the aforementioned problems, is the code k-Wave [Treeby and Cox, 2010b, Treeby et al., 2012b]. k-Wave is an open-source code for the time domain simulation of propagating acoustic waves in 1D, 2D, or 3D. It can be found as a MATLAB toolbox (see Fig. 2.2) and it is also written in C++ and in a GPU paralellized version written in CUDA.

Figure 2.2: The k-Wave MATLAB toolbox

k-Wave is able to account for both linear and nonlinear wave propagation, an arbitrary distribution of heterogeneous material parameters, and power law acoustic absorption. To reduce the memory and the number of time steps required for accurate simulations,it uses the k-space pseudospectral method (or k-space method) [Treeby and Cox, 2010b, Treeby et al., 2012b] to solve the governing equations Eq. (1.36).

The k-space method combines the spectral calculation of the spatial derivatives present in the governing equations with a temporal propagator expressed in the frequency domain. This scheme present several advantages over the FD method. For the spatial derivative, FD method solves the wave equation at each point based only on the value of nearby points. This is the reason why it is considered as a local method. On the contrary, the k-space method uses the whole data to solve the wave propagation equations at each point by fitting to a Fourier series all the data. As the the amplitudes of the Fourier components can be computed using the Fast Fourier transform (FFT), this method is faster than FD and more accurate as it employs all the data. On the other hand, as the basis functions of the Fourier series are sinusoidal, only two grid points per wavelength are required, decreasing considerably the storage demand of the simulation. Once the data is fitted with Fourier series, the derivative can be easily computed as:

$$\mathcal{F}\left(\frac{\partial}{\partial x}f(c)\right) \;=\; -\frac{1}{2\pi}\int f(x)(-ik_x)e^{-ik_x x}dx = ik_x\mathcal{F}[f(x)] \tag{2.1}$$

Where k_x is the wave vector in the x direction.

For the temporal derivatives, k-Wave uses a modified finite-difference scheme based on a temporal propagator expressed in the spatial frequency domain or *k-space*. The name of k-space comes from the k-space operator κ that appears when the temporal increment ΔT of the FD method is replaced for $\Delta T\kappa$ where $\kappa = sinc(c_0 k\Delta T/2)$. Here c_0 is the reference sound speed and k is the wave vector. This replacement is done because in the standard FD method the FD approach for temporal derivatives need the size of the time step to be very small and carefully chosen in order to maintain numerical stability. The introduced approach of the k-space operator based on a periodic function, allows the use of larger time steps can be employed without introducing inaccuracy and instability.

The number of grid points per wavelength recommended to use for heterogeneous media with k-Wave is at least 4. For homogeneous media it is possible to work more close to the limit of two points (known as the Nyquist limit). To select the number of grid points and grid spacing in every Cartesian dimension in k-Wave is recommended to use the following formulas:

$$\begin{aligned} dx &= \frac{c_{0\_min}}{points\_per\_wavelength \cdot f_{max}} \\ Nx &= round\left(\frac{x\_size}{dx}\right) \end{aligned} \tag{2.2}$$

Where c_{0_min} is the minimum speed of sound in the media, $points\_per\_wavelength$ is the number of points per wavelength at the maximum frequency f_{max} and x_size is the size of the domain in the x dimension.

The temporal step in k-Wave is calculated as:

$$dt = \frac{CFL \cdot dx}{c_{0\_max}} \tag{2.3}$$

Where c_{0_max} is the maximum speed of sound in the media and CFL is the Courant-Friedrichs-Lewy (CFL) number, which is a parameter typically employed to establish the stability values of the numerical methods for wave propagation [Yang et al., 2006, Bakhvalov, 2001]. In k-Wave is recommended to use $CFL = 0.3$.

2.2.1 Performing k-Wave simulations

In this work both the MATLAB toolbox and the GPU parallelized version of k-Wave were employed. The former is suitable for low frequencies simulations where the number of grid points in all the Cartesian dimensions is not very large. This can be used as a prove-of-concept taking advantage of the excellent visualization and easy to adapt tools of MATLAB. The later is employed in large scale simulations where the speed of the computation is relevant. The MATLAB version provide a set of functions that allows defining in a simplified way several aspects of the simulation. All this functions can be called from a MATLAB script where the whole process of typical USCT simulation can be defined. The GPU version of the k-Wave requires all the input data for the simulation to be introduced by means a specific format file (.hdf5) that will be explained later. Nevertheless, this files can be easily created with the help of the k-Wave MATLAB toolbox in the same way a MATLAB simulation is created. First we will briefly explain how to create the input data required to run a k-Wave simulation in MATLAB and then how to create the input data for the GPU version of k-Wave. For the seek of simplicity, from now on, we will refer to the GPU version of k-Wave as k-Wave-CUDA, as it is written in CUDA language.

2.2.1.1 Using the MATLAB k-Wave toolbox

The k-Wave has an excellent and easy-to-follow documentation. For that reason only the main features of the code as well as the input and output structures will be mentioned in this section. For other details we recommend to consult the k-Wave manual [Treeby and Cox, 2010b].

Input files

The required entries to run a simulation in k-Wave are summarized in Fig. 2.3. It consisted on four basic structures (which should be defined as MATLAB structures):

- *kgrid:* Here the parameters to define the features of the computation grid where the wave propagation will be simulated are defined. It can be created by entering the desired values of Nx and dx to the k-Wave function *makeGrid*. This function will provide the vector of wave number k in all the Cartesian grid and serie of data that can be used together with the function *makeTime* to create the time array for the simulation.
- *Medium:* This is where the material properties of the medium are defined. The user can specify five different properties: the sound speed, the ambient mass density, the nonlinearity parameter, the power law absorption coefficient, and the power law absorption exponent.
- *Source:* The location and characteristics of the sources of the ultrasound field should be defined. There are three types of sources: an initial pressure distribution, a time varying pressure source and a time varying particle velocity source. In all these cases, a mask to identify the grid point that will act as source should be defined (source.p_mask). For USCT purposes, the time varying pressure source results very suitable and can be simply defined by using the function *tuneBurst*. This will return the time series that represent the source. The central frequency, number of lobes and the sampling frequency have to be specified:

$$
\begin{aligned}
&sampling\_freq = 1/dt; \qquad \text{\% [Hz]}\\
&tone\_burst\_freq = 1e6; \qquad \text{\% [Hz]}\\
&tone\_burst\_cycles = 3;\\
&source.p = toneBurst(sampling\_freq, tone\_burst\_freq, tone\_burst\_cycles);
\end{aligned}
$$

  This basically provide a Gaussian enveloped 3-cycle sinusoidal tone burst with a 1 MHz central frequency identical to the signal represented in Fig. 1.16(a).
- *Sensor:* Using this structure it is possible to define the features and positions of the grid points where the acoustic field will be recorded at each time step during the simulation. Similar to the source, this structure also requires to define a mask to identify the point of interest to be used as sensors. Among several other options described in the k-Wave manual, another important one is the decision of which data to record. For example, this allow us to record the acoustic pressure during all the time steps of the simulation.

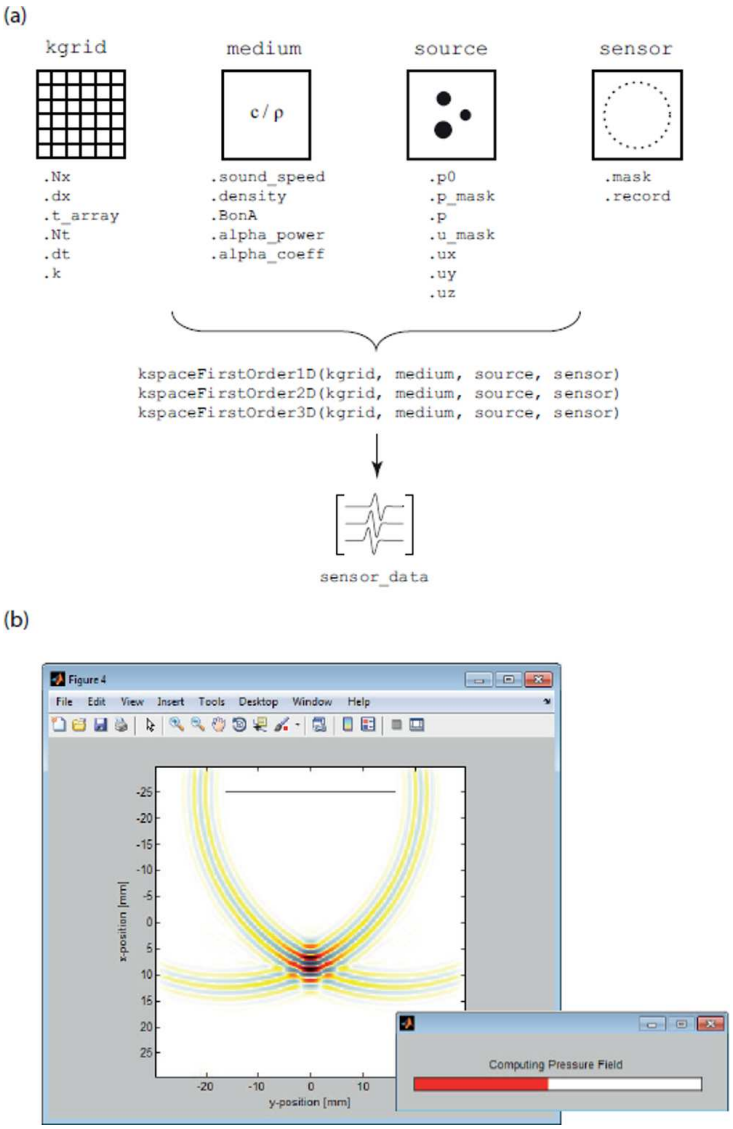

Figure 2.3: (a) Definition of the four inputs structures and the main input fields used for k-Wave. (b) Snapshot of a 2D simulation of a focused pulse using k-Wave. The source mask is shown as black line, and the progress of the simulation is illustrated by the status bar. Figure taken from [Treeby et al., 2012a]

Output files

When the four structures are defined, the user may start the simulation using one of the simulation functions available (1D, 2D and 3D). This function can be called as follows:

$sensor\_data = kspaceFirstOrder2D(kgrid, medium, source, sensor);$

$sensor\_data$ is an output structure where the time series recorded in every specified sensor

in all the time of the simulation is stored. This output is also given as an HDF5 file.

The Perfectly Matched Layer (PML)

The FFT transform that intervenes in pseudospectral and k-space numerical models requires assuming the periodicity of the wave field. Therefore, the waves leaving one side of the domain will reappear at the opposite side. To avoid that, k-Wave uses a Perfectly Matched Layer (PML). It consists in an array of grid points located at the edges of the domain in which the waves are gradually absorbed to avoid reflections at the edges of the domain. The two parameters that control this layer are the absorption parameter **PML_alpha** and the PML thickness **PML_size**. By default, k-Wave uses PML_alpha = 2 and PML_size = 20 for 1D and 2D simulations.

2.2.1.2 Using the k-Wave-CUDA

For simulations using large grid sizes, or large batches of moderate grid sizes (for example, when 3D domains are investigated), k-Wave also includes the function *kspaceFirstOrder3D-CUDA*, which is written using CUDA for NVIDIA GPUs.

In this code, all the critical calculations of gradients that employ FFT transforms are done in the GPU together with all the operations involved in the governing equations of propagation. This significantly improve the computation time [Jaros et al., 2016].

This code requires a single input file saved in the Hierarchical Data Format HDF5 format [Bhadauria et al., 2016]. This is a data model, library, and file format for storing and managing data. It allows managing efficiently high volume and complex data. The HDF5 technology suite includes tools and applications for managing, manipulating, viewing, and analysing data in the HDF5 format. The different structures mentioned before to feed the k-Wave simulation can be stored into an HDF5 file. This can be simply done by using the MATLAB k-Wave code. First, all the aspects of the simulation have to be previously defined. Then, is it just neccesary to run the function kspaceFirstOrder3D specifying to create the HDF5 file:

$$kspaceFirstOrder2D(kgrid, medium, source, sensor, `SaveToDisk', input\_data.h5);$$

Once the input data is dumped into the HDF5 file, the k-Wave-CUDA code can be called from a terminal window (Linux) or the command prompt (Windows).

As in the MATLAB toolbox, several output can be obtained from the program. The time series of the pressure field are of specific interest for for USCT. This output is also given in an HDF5 file.

Chapter 3

Ray tracing USCT tomography

3.1 Introduction

Geometrical acoustics (GAc) is currently the approach most employed to recover real and synthetic USCT data [Jago and Whittingham, 1991, Dapp et al., 2012, Qu et al., 2015, Hormati et al., 2010, Li et al., 2009a]. It is also the standard technique implemented in the USCT scanners that are currently under exploitation for clinical studies (see Sec. 1.2.2). The computational efficiency of GAc methods is very high and fast image reconstruction is crucial under clinical circumstances, in order to maximize the number of patients studied. Nevertheless, it is important to bear in mind that despite of their high performance, GAc algorithms provide reconstructed images with lower resolution in comparison with Full Wave Inversion (FWI) methods.

What makes GAc algorithms so computationally efficient, is the use of very simplified numerical wave propagation methods, as it was explained in Chapter 1.The majority of the algorithms employed for breast imaging use bent rays to correct for refraction. On the other hand, the use of straight rays based on inverse radon transform is also employed [Jago and Whittingham, 1991], especially when large regions are inspected, such as for abdominal USCT studies [Nogami and Yamada, 2007]. These straight rays algorithms exhibit very fast performance and present real time imaging capabilities. For example, in reference [Dapp et al., 2012] a comparison between straight and bent algorithms was established. They concluded that in two-dimensional reconstructions, bent rays can present a fast performance but, they are around 30-50 times slower than straight ray tracing. Moreover, for three-dimensional reconstructions, the increased computational cost makes that the improvements in image quality do not compensate the increased reconstruction time.

On the other hand, there are several approximations that allow obtaining bent trajectories:

- Some authors chose using ray-linking methods. For example, in reference [Qu et al., 2015], an algorithm based on Fermat's principle and the use of rays-linking with virtual

receivers is presented. This algorithm starts at the position of a given source and with a given initial angle, it continues to the next pixel position using the refracting index of the medium and the initial direction.

- Some studies [Hormati et al., 2010, Dapp et al., 2012] use a gradient descent algorithm to solve an optimization problem based on the L_2-norm. This functional is comprised by the times of flight differences between the measured and simulated signals. This method looks for the gradient of the L_2-norm cost function, using Fermat's Principle.
- Other set of very employed algorithms solve the Eikonal equation using methods like the Fast Marching Method (see Chapter 1) combined with algebraic reconstruction techniques [Li et al., 2010] or similar like Klimes' grid travel-time tracing technique and gradient methods to guide the bent rays as they propagate between emitters and receivers [Wang et al., 2006, Li et al., 2009a].

These numerical methods require as input very reduced information of the waveform, i.e. its time of flight (TOF) to obtain the sound speed (SS) maps, and its amplitude to recover the acoustic attenuation (AA) maps. The rest of information contained in the measured waveform is lost, which explains in a great extent the lack of resolution present in the images obtained with these methods.

An accurate estimation of the TOF and amplitude of the waveform has a tremendous impact on the reconstructed USCT images with any GAc algorithms. These estimations depend on two main factors. First, the mechanical precision of the experimental setup used for data acquisition. Once this aspect is addressed, the second most relevant factor that influences the reconstructed image quality is the efficiency of the methods used to characterize the first arrival signal. The estimated TOF and amplitude should be then efficiently combined with a robust GAc algorithm.

The main objective of this chapter is to investigate GAc algorithms to be used with the MUBI scanner. First, we studied accurate methods to estimate the TOF and amplitude of the measured signals in order to facilitate obtaining high quality SS and AA maps of the inspected tissues. We also investigated the quality and performance that different GAc algorithms can provide in order to establish a fast and accurate strategy based on GAc for the MUBI scanner. We focused in one hand, on the implementation of analytic reconstructions using straight rays due to its potential for fast 3D reconstruction and on-the-flight 2D reconstructions. On the other hand, we also studied bent ray tracing strategies for image reconstruction to compensate for the refraction experienced by the wave due to different breast tissues. All the studies in this chapter were done using synthetic data in order to extend the results obtained to experimental data in Chapter 6.

3.2 Methods

In this section the main component that compound a GAc algorithms are analyzed. First, in Secs. 3.2.1 and 3.2.2 several methods to estimate the TOF and amplitude will be discussed.

After that, Secs. 3.2.3 and 3.2.4 will be dedicated to the implementation of algorithms to obtain the straight and bent trajectories between emitters and receivers respectively. Finally, in Sec. 3.2.5 several reconstruction algorithms using GAc are analyzed.

3.2.1 TOF estimation algorithms

As we mentioned in the introduction of this chapter, the image quality obtained in the reconstruction of USCT data when using GAc algorithm is influenced by the accuracy in the determination of the positions of the detectors, and by the efficiency of the algorithms to estimate the TOF and amplitude. If we consider that the calibrations performed in the system are sufficiently precise (as it will be discussed in Chapter 6), the quality of the reconstructions is going to depend mainly on the methods used to characterize the first arrival signal together with the employed GAc algorithm. In this section we will focus in the estimation of the TOF of the first arrival signal.

To provide a simple, but illustrative, demonstration of the importance of the accuracy of the TOF estimation and its consequences in the quality of the reconstructions, we performed a numerical example similar to the one presented in ref. [Ashfaq, 2007]. In this example, we solely studied the effect of the TOF and ignored the attenuation and other common phenomena such as reflections and refraction (we will use straight rays approximation). Under these very ideal conditions, we considered a medium comprised by a SS background c_0= 1480 m/s with an rectangular heterogeneity of size L in which the SS will be given by the value c_1 (see Fig. 3.1). The variation perceived in the TOF due to the presence of the heterogeneity will be given by:

$$\delta_{TOF} = L(\frac{1}{c_1} - \frac{1}{c_0}) \tag{3.1}$$

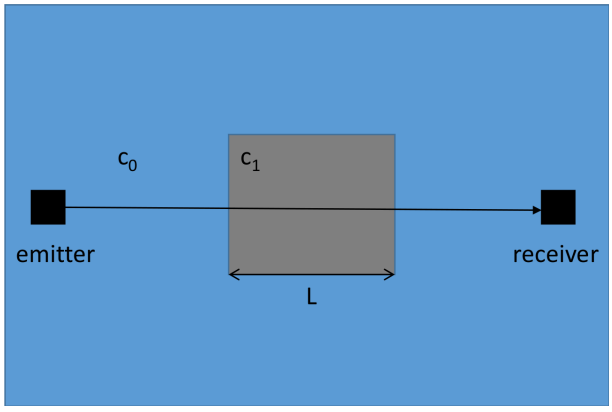

Figure 3.1: Computing the TOF along a heterogeous straight path

We can now calculate what would be the detected difference δ_{TOF} given by Eq. 3.1 for

several sizes of the heterogeneity (L) and different values of SS (c_1) in it. The objective of doing that is, given a certain sampling frequency of the signal, to calculate the number of sampling intervals that we would need to be able to detect a certain heterogeneity. Here is assumed that at least one time interval is required to differentiate two waveforms. We used a sampling frequency (Fs) of 20 MHz (remember that (Fs) is the inverse of the sampling period (Ts)), as the one used in our experimental prototype (see Chapter 6). The resulting change in the number of time intervals will be given by $\delta_{TOF}/cdotFs$. The modifications of this value when L is varied in a range between 0-10 mm and c_1 between c_0-$c_0 + 50m/s$ are presented in Fig. 3.2.

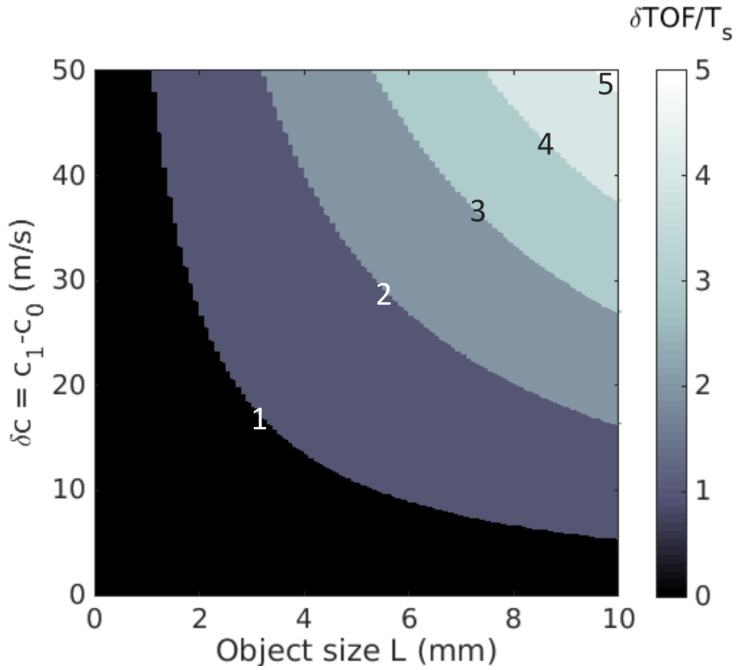

Figure 3.2: TOF variations due to the inclusion of an hetorogineity in the transmission path given in time intervals. The values of the lenght of the inclusion and it SS vary in the x and y axis respectively. The colorscale represents the calculated δ_{TOF} given by Eq. 3.1 multiplied by the sampling frequency

From Fig. 3.2, we can conclude that structures with sizes of 1 cm or lesser, are almost impossible to be detected with this sampling frequency, even if they present differences in SS of 5 m/s regarding the background. A structure of these characteristics will delay or move forward the signal in less than one time interval. Besides, a time shift in the signal of only two temporal bins, can allow us differentiating a structure that differs in ∼20 m/s from the background, with a size of 1 cm. This figure reveals the importance of accurately detecting the TOF of the signals.

3.2.1.1 Maximum-based TOF estimation

The easiest way to roughly estimate the TOF of the received signal, is to compare the time difference between the emitted and detected signals using their maximum value as reference (see Fig. 3.3). If we suppose the signal do not modify its shape during propagation, the maximum of the signal can be consider to appear always at the same lobe. The implementation of this method is very simple and only requires scanning the whole recorded signal to find the time interval of its absolute maximum value. Nevertheless, this method is very sensitive to the noise in the signals and also to the distortions that it can suffer due to interference with scattered signals at the interfaces between different structures.

Nevertheless, during the implementation of this method we found two additional issues that affected the performance of this method. First, the initial signal emitted is not always known in advance. If the information of the time interval at which the maximum value of the emitted signal appears is not used, the TOF could be strongly overestimated. Nevertheless, when the initial signal is known in advance (there are methods that allow its estimation, see Chapter 6), there are more stable methods to estimate the TOF, as we will shown in the next sections. The second problem that affects the TOF using this method, is when interference with other dispersed or diffracted signals occur. This fact makes that the maximum signal value does not correspond with the temporal location of the maximum of the directly transmitted signal. Therefore, this method is not actually suitable to accurately estimate the TOF.

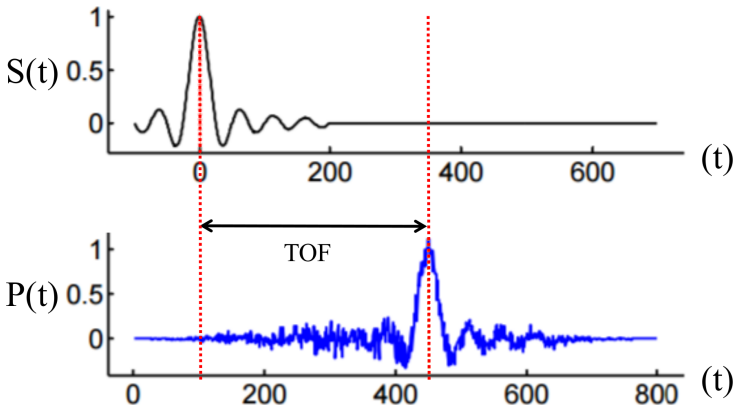

Figure 3.3: Time delay estimation using the maximum value of the signal. Very sensitive to noise and signal distortions

3.2.1.2 Threshold-based TOF estimation

This is also a very simple method to estimate the TOF (see Fig. 3.4). It consists on setting a threshold value to detect the first point that is above that threshold. The chosen value should be always above the noise level of the signal in order to avoid miss-estimated TOF values.

This makes the method unstable in the presence or high noise levels and especially at large

distances from the source where the signal is highly attenuated and can be comparable to the noise levels. To reduce this problem, an individual threshold based on each specific waveform can be chosen for every detector pair.

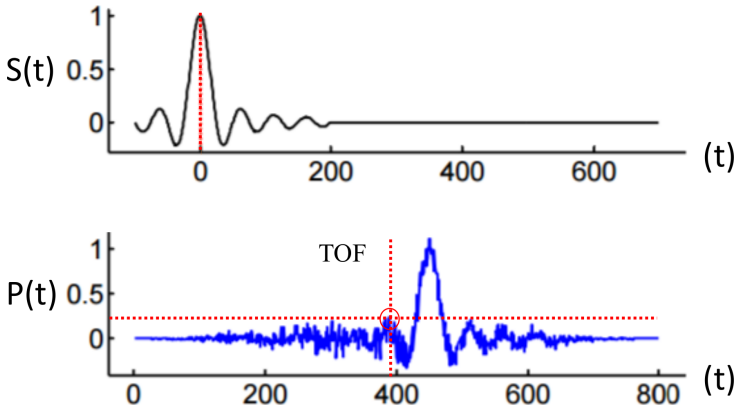

Figure 3.4: Time delay estimation using a given treshold.

The steps followed to implement this methods are as follows:

1. The maximum value of the source is estimated, as explained in the previous section.
2. A percentage of the maximum value is selected as threshold (in our case, 5 % of the maximum value).
3. In a selected time window of the measured signal, different from the location of the transmitted pulse, the standard deviation (σ) is calculated. The chosen threshold should be always higher than (3σ). Otherwise, it is incremented. In this done to avoid using threshold values lower than the noise level.
4. The first temporal interval at which the signal overcomes the threshold is assigned as TOF.

When using this method especial care should be taken when working with synthetic data in which high numerical dispersion may be present. It is recommendable to avoid this method in those cases. The parameters of the simulation can generally be adjusted to avoid this.

This method may fail in the presence of high levels of noise, because to overcome the noise, the threshold has to be incremented and therefore, the TOF is going to be overestimated.

3.2.1.3 Cross-correlation-based TOF estimation

Cross-correlation is a classical and robust method to obtain the delay between two signals [Knapp and Carter, 1976] (see Fig.3.5). It is based on the precept that the shape of the measured signal $p(t)$ is known *a priori*. In our case, for experimental data thisrequires a correct characterization of the source or emitted signal $S(t)$ and the assumption that the wave does not distort its shape during propagation. In the case of synthetic data, the initial signal is always

known, as it is a requirement for the simulations. The only modification that the wave will suffer under the before mentioned conditions are, a phase shift, and a decrease of its amplitude (due to geometrical spreading and attenuation).

This means that the received signal can expressed by $p(t) = AS(t - \Theta)$, where A modulates the change in amplitude and Θ is the time delay suffered by the wave due to it propagation. The value of Θ, also called *lag*, can be obtained by means of the cross correlation function:

$$(p \otimes S)(t) = \int_{-\infty}^{+\infty} p(t' + t)S(t')dt'$$

Substituting the value of $p(t)$:

$$\begin{aligned}(p \otimes S)(t) &= \int_{-\infty}^{+\infty} AS(t' + t - \Theta)S(t')dt' \\ (p \otimes S)(t) &= AS \otimes S(t - \Theta)\end{aligned} \tag{3.2}$$

The last expression in 3.2 corresponds to the auto correlation function of the source signal. The auto correlation of a signal with itself will always present a peak at a lag of zero, and its value will be equal to the signal power. Therefore, the expression presented in 3.2 presents a maximum at $t = \Theta$.

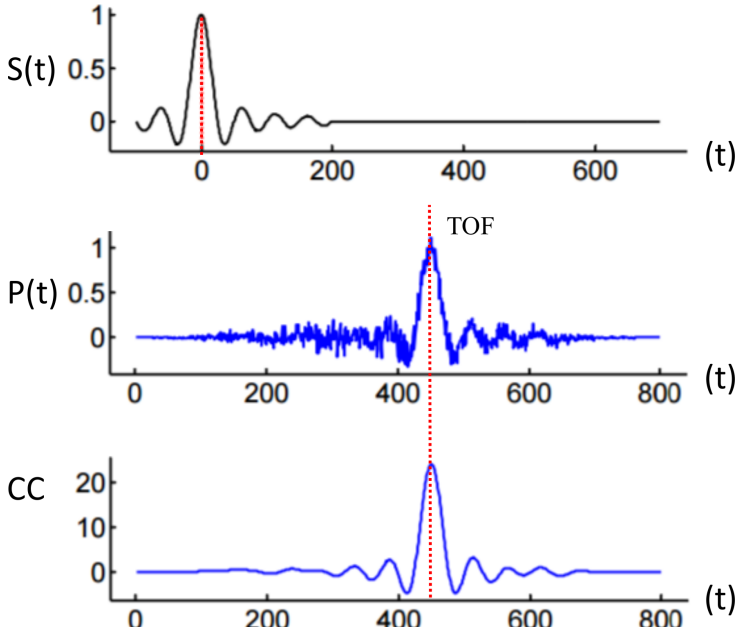

Figure 3.5: Time delay estimation using cross correlation. $S(t)$ is the source signal, $p(t)$ is the measured at the detectors position and CC is the cross correlation function between both functions.

The idea behind the implementation of the method is to calculate the integral of both functions product at each temporal position using several temporal displacements. When the measured signal and the displaced source signal match, the value of the integral is maximized (representing the overlap between them) (see Fig. 3.5).

The lag estimation via cross correlation is a robust method to obtain the TOF of the waveform, especially in the presence of noise. It is more accurate than using the maximum value of the signal and more stable than using the threshold. Nevertheless, it may fail when the waveform exhibits strong distortions or cancellations due to the interference of the direct and scattered signals near structures interfaces.

To implement this method, we used the *xcorr* function of MATLAB. This function returns the cross-correlation of two discrete-time sequences. To find the TOF using this function, the interval at which the lag is expected has to be estimated.

3.2.2 Amplitude estimation algorithms

The estimation of AA maps with GAc algorithms is a difficult task. The resolution these methods provide to obtain the AA maps, is very limited due to several factor. First, when using linear arrays to emit and detect the signals, the source can not being considered a point source, as some front-focusing and out-of-plane aperture is generally present Li et al. [2008a]. On the other hand, the amplitude estimation of the actual directly transmitted signal is very difficult, as phase aberration can be produced around structures with different impedance and sizes. In those regions, the direct waveform will be refracted and diffracted. As a result, the measured signals in the lines neighboring an interface with strong changes of impedance will present phase aberrations in a greater o lesser extent. This causes a very common artifact in AA reconstructions observed when GAc algorithms are used. As consequence of this effect, a halo, appears around the structures of the phantom [Li et al., 2008a].

3.2.2.1 Maximum -based amplitude estimations

This method is similar to the estimation of the TOF using the maximum amplitude of the signal. In this case, we simply use the value of the maximum of the signal as an estimator of its amplitude. Therefore, this is the simplest available method to obtain the amplitude, but, as it was mentioned before, this value can be affected by several processes. For example, if the wave presents phase aberrations due to destructive interference with other scattered signal, this value will no reflect the real amplitude of the directly propagated signal.

3.2.2.2 Amplitude of the envelope of the signal

The envelope of a signal is a robust method to estimate of its amplitude. This method is more stable against small phase aberrations the wave could suffer than the simple use of it absolute

maximum. Although, it can be still affected by this effect.

The Hilbert transform of a signal $\mathscr{H}$ allows obtaining its envelope [Li et al., 2008a, Taner et al., 1979]. It is defined as the convolution of a signals $p(t)$ with the signal $1/\pi t$ [Kschischang, 2006] and gives the response to $p(t)$ of a linear time-invariant filter (known as Hilbert transformer) that have impulse response $1/\pi t$

$$\mathscr{H}[p(t)] = p(t) \otimes \frac{1}{\pi t} = \frac{1}{\pi} \int_{-\infty}^{+\infty} \frac{p(t-t')}{t'} dt \tag{3.3}$$

A signal can be represented by a combination of this amplitude $A(t)$ and phase $\Theta(t)$ as follows:

$$p(t) = A(t) cos\Theta(t) \tag{3.4}$$

Its quadrature equivalent waveform is given by:

$$p(t) = A(t) sin\Theta(t) = -\mathscr{H}(p(t)) \tag{3.5}$$

The analytic waveform $y(t)$ can be expressed as:

$$y(t) = p(t) + ip^*(t) \tag{3.6}$$

And finally, the amplitude envelope can be obtained as:

$$A(t) = \sqrt{p(t)^2 + p^*(t)^2} \tag{3.7}$$

An example of the envelope of the signal obtained with this method using the Hibert transform function of MATLAB *hilbert* can be seen in Fig. 3.6

To implement the method of the envelope-based amplitude estimation we performed the following steps:

1. Calculate the Hilbert transform of the signal and obtain its real a imaginary projections using the Hilbert function of MATLAB as in Eq. 3.6.
2. Compute the amplitude envelope as in Eq. 3.7.
3. Calculate the maximum value of the amplitude envelope.

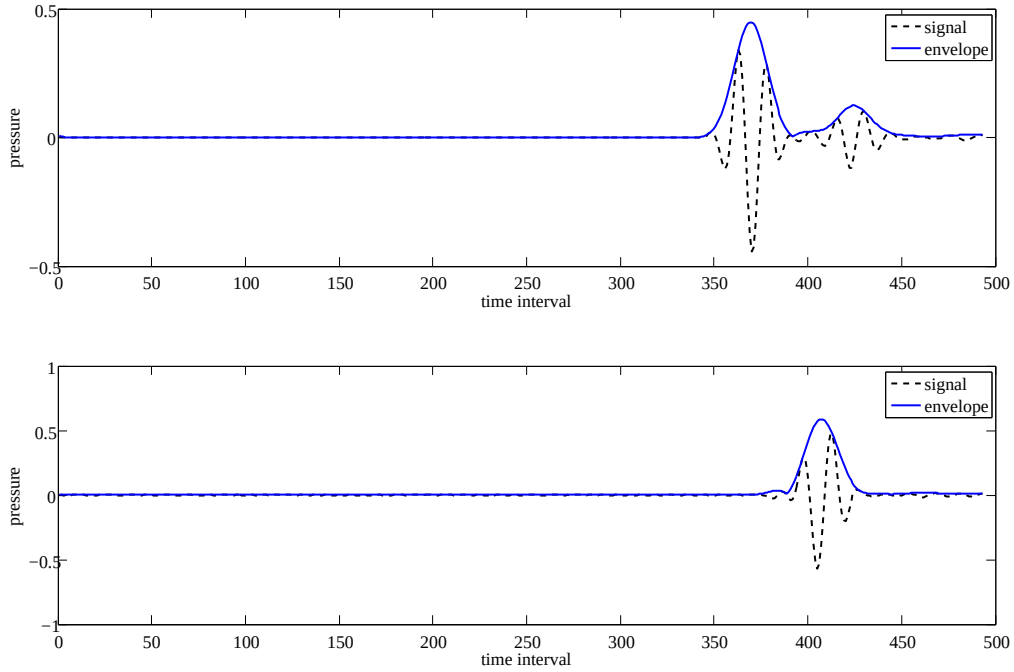

Figure 3.6: Example of envelope obtained with the Hilbert transform

3.2.3 Analytic GAc reconstructions

As we explained in Sec. 1.3.1.5 of Chapter 1, the reconstructions using straight rays are based on the use of the the filtered back-projection method (FBP) assuming a wave propagation along straight lines in all the possible orientations. Therefore, the backward propagation in this case can be simply done by the implementation of the inverse radon function. In this work, we employed the MATLAB function *iradon* for inverse radon transform of the data. Spline interpolation and Ram-Lak filter with a Hann window was employed to perform the FBP reconstruction in all the cases.

To use this function for the analytic reconstruction, the data should be organized in the form of a sinogram of the different projection of the object against the radial distance to the center of the Field of View (FOV). The sinogram for the case of the SS reconstructions will contain the TOF values of the different emitter-receiver pairs. In the case of the AA reconstruction, the sinogram contains the values calculated using the amplitude decay method, introduced in Chapter 1 Sec. 1.3.1.

Depending on the number of angular and radial bins chosen to create the sinogram, it may present several gaps where no information is available. If this lack of information is not compensated, it will be propagated directly to the reconstructed image creating artifacts.

Therefore, in this work we employed a gaps-filling method called "inpaint NaNs" [D'Errico, 2005]. It is based on sparse linear algebra and interpolates the gaps identified with NaN (not a number) in a 2D array using the rest of non-NaN elements. It is available as a MATLAB function called *Inpaint_nans* that offers several different approaches for the interpolation.

In the AA reconstruction, using this analytic method, the amplitude decay sinogram may be improved with a method called *Bow-tie* [Abella et al., 2009]. This method consist on a filtering scheme of the sinogram, using its frequency-domain representation. In this domain, the support region of an ideal sinogram frequency content presents a "bow-tie shape". The rest of the values correspond to noise and artifacts of the sinogram. Therefore, by applying this filter, we eliminate a significant amount of noise and artifact of the sinogram.

3.2.4 Iterative GAc algorithms

The reconstruction in USCT using bent rays is generally applied through iterative schemes (see Sec.1.3.1.6). These methods have two main components:

GAc methods for USCT based on bent ray tracing are generally iterative , Chapter 1).

- A forward model to simulate the energy propagation of the wave along bent rays, which is used for forward and backward projection. The use of this method allows obtaining an estimation of how close is the estimated acoustic image to the actual solution.
- An optimization algorithm to calculate and apply the needed corrections to the image. In this case, the bent trajectories are used to obtain the A_{ij} coefficients in the updating expression of the ML-EM algorithm (see Chapter 1). This is the approach used in our bent-rays algorithms to update the images.

In the next sections these three items are addressed.

3.2.4.1 Forward model for bent rays tracing

Fast marching method

FMM as we mentioned, is a classical method employed in bent rays tracing algorithms. Its fundamentals were explained in the introductory Chapter 1. There are several available implementations of the algorithm. In this work, we employed a GPU-version of J.V. Gomez et al., [Gómez et al., 2016].

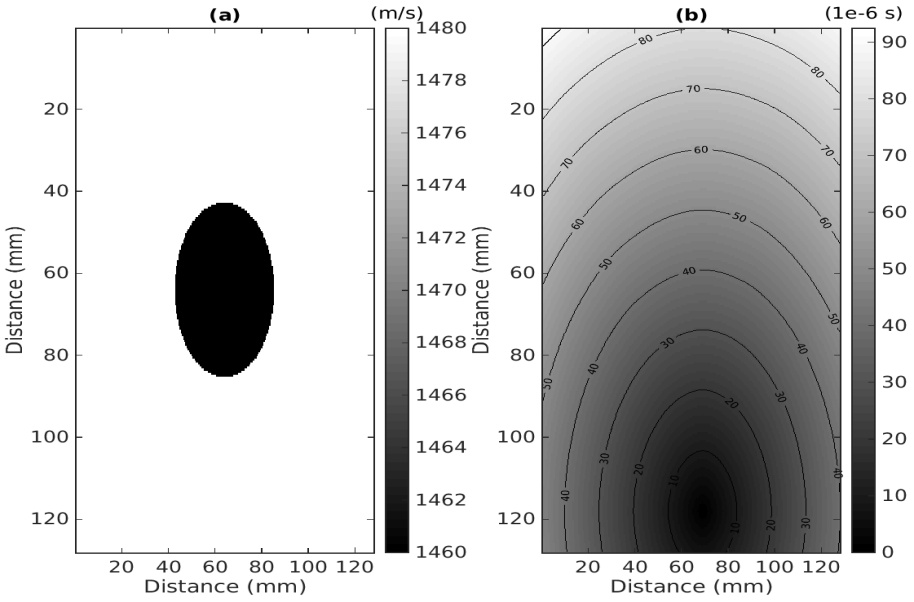

Figure 3.7: FMM simulation of the propagation of a single source using a water-fat numerical phantom. (a) numerical sound speed phantom. (b) delays map or $\theta(r)$ map for a single source simulation with the FMM.

Fig. 3.7 (b), shows an example of the propagation obtained with this code for for the object shown in Fig. 3.7 (a), that represents an interface water-fat. This figure (b) represents the delays, or $\theta(r)$ map, in the wavefront propagation from a source that was located at $x = 69\ mm$ and $y = 118\ mm$. These calculations are based on the given SS map. This implementation of the FMM is very fast and allows obtaining the mentioned map in $\sim 12\ msecs$.

The path between the source and any point in the domain, can be obtained using the delays map. The gradient of $\theta(r)$ map is employed as a guide to follow the decreasing direction of the delays. This is also known as finding *the geodesic path* in a surface [Peyré, 2011]. The process is started from the location of the receiver. Fig. 3.8 shows the comparison between the path obtained with this algorithm and a straight path, evidencing the large differences that could occur between the straight rays approximation and the bent rays.

In this case, the TOF is estimated as the value of the delays map at the receivers position.

Bezier polynomial method

The use of the FMM to compute the path between an emitter-receiver pair, given a SS map, requires several time-consuming steps, even when the method is parallelized. The total time is

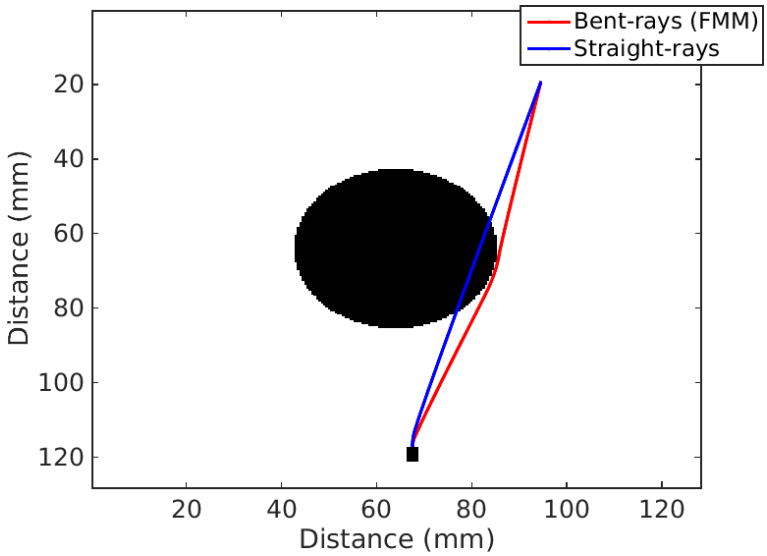

Figure 3.8: Comparison between a bent and straight trajectories in an interface water-fat

comprised of obtaining the delays map, calculating the gradient of the delay map, and obtaining the geodesic path.

In order to reduce the computation time of the bent-rays algorithm we propose an alternative simplified method to obtain bent rays trajectories using the SS map. There are multiple methods for linking two points using optimal curves. One possible approach is employing Bézier Polynomials. These type of smooth curves were introduced in 1962, by the french engineer Pierre Bézier, who later used them for profusion in the design of the various parts of the bodies of an automobile [Bézier, 1968]. After that, this family of curves has been applied in many different fields such as robot motion planning, mapping of textures in image process, the layout of fibers in composite material structures, tent manufacturing and cutting and painting path in industrial applications, among others [Noakes and Popiel, 2007, Forrest, 1972].

Using the Bézier's method, a given curve can be obtained with use of a polygon [Forrest, 1972]. If the curve is created as a polynomial of degree n the polygon will have $(n-1)$ vertices. We will defined these vertices with the vector **P**. The initial and final point of this vector, P_0 and P_n are going to represent the extremes of the curve. The Bezier curve defined this way will always pass through the extremes points but it not necessary has to pass through the rest of vertices of the polygon. The most common Bézier curves used are based on n =1-3. With n=1 the bezier curve consist of straight lines linking two given points. For n=2 the Bezier curve is a quadratic polynomial.

A quadratic Bézier curve, given by the function $\mathbf{B}(t)$ and determined by the vertices: $\mathbf{P}_0, \mathbf{P}_1$ and $\mathbf{P}_2$ is given by the following expression:

$$\mathbf{B}(t) = (1-t)^2\mathbf{P}_0 + 2t(1-t)\mathbf{P}_1 + t^2\mathbf{P}_2, t \in [0,1] \tag{3.8}$$

If $\mathbf{P}_1$ is shifted in both x and y directions, many curves can be obtained. This value will determine the characteristics of the Bézier curve. The parameter t provide points to sample the Bézier function and therefore, $\mathbf{B}(t)$ will contain the set of points that belongs to the Bézier curve.

If we have a family of paths using Bézier polynomials, we can obtain the optimal path calculating, with the SS map, the one with the lowest TOF.

The strategy we propose to use the Bézier curves (n=2) for bent-ray tracing is schematically represented in Fig. 3.9. The points P_0 and P_2 correspond to the coordinates or the emitter and the receiver respectively. The total set of points P_1 to obtain different curves can be obtained by providing a range of movement in the parallel and perpendicular directions to the straight line that link the detectors ($N_\perp$ and $N_\parallel$). Once the center point between them is found, if an step to promote the movement in each direction is given ($d_\perp$ and $d_\parallel$), is straightforward to move the point P_1 in the grid.

Evaluating the different points of the curves in the given SS map and using the following equation, a value for the TOF of the given path can be estimated:

$$TOF = \sum_{t=0}^{t=1} \left(\frac{1}{c_t}\right) dl_t \tag{3.9}$$

Where c_t is the SS at the pixel determined by t, and dl_t is the distance between two contiguous points of the curve.

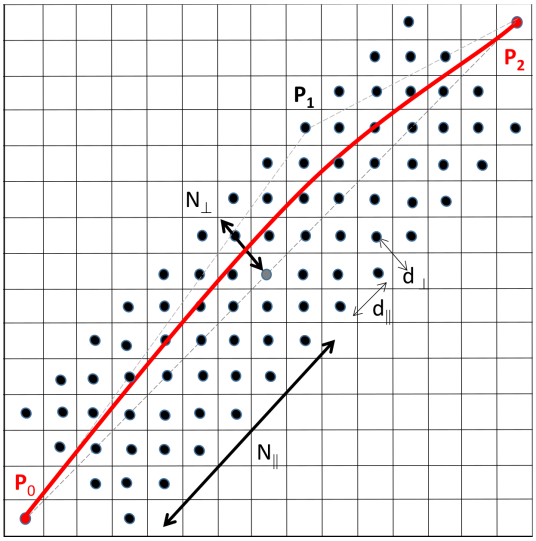

Figure 3.9: Bent-ray tracing with quadratic Bézier polynomial curves

We used CUDA to implement the method, as the different evaluations of the Bézier curves for different points P_1 can be done in parallel using GPU, which considerably speed up the

calculations.

In this method the curvature of the path can be controlled by changing the range in the parallel and perpendicular direction of P_1. In Fig. 3.10, we represented the differences between the paths obtained for a simple case of water-breast tissue (1480 m/s and 1550 m/s respectively). Due to the higher SS of the breast tissue, some of the rays around the interface will bend their trajectory. When using the FMM, some rays around the inclusion that only travel by water appear bent, which is not correct (see the ref arrows in the right panel of Fig. 3.10). Nevertheless, we can adjust the parameters of the Bézier to avoid this issue and still have the right behavior in the regions close to the inclusion.

We consider that the observed behavior of the FMM in those region, can due to the way in which the method is implemented. The use of squared voxels to propagate the wavefront, makes it strongly dependent of the angle between the emitter and receiver, in regard with the axis of the Cartesian system of reference. Other implementations like, for example, using blobs [Li et al., 2010], have demonstrated to provide better results.

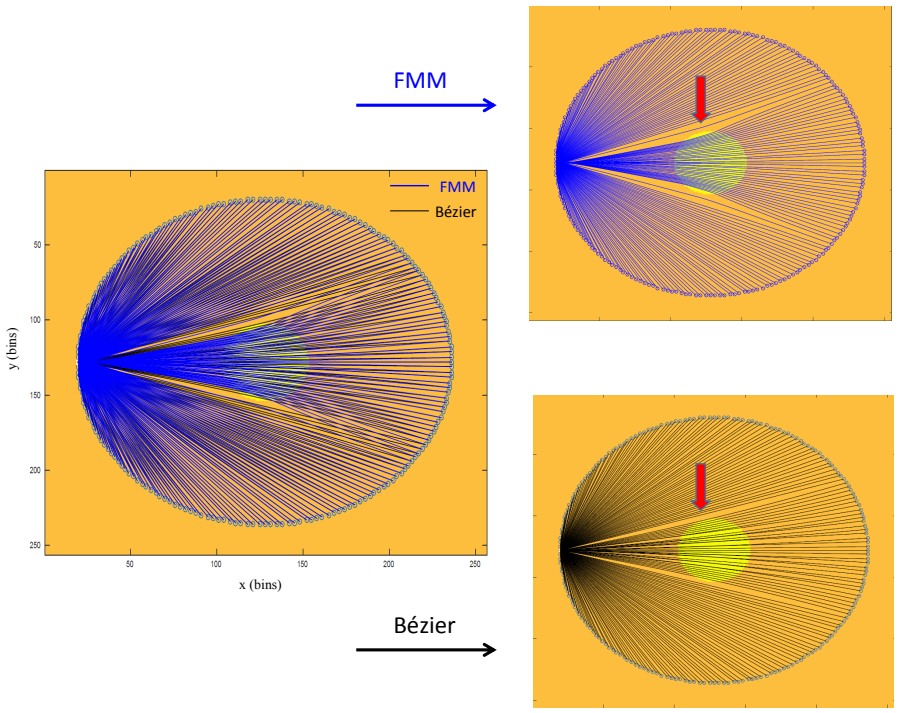

Figure 3.10: Comparison between the estimations with FMM and Bezier trajectories. Around the object FMM bent the trajectories even when rays travel along a homogeneous medium. Bezier ray tracing can be adjusted to overcome that.

3.2.5 Iterative bent ray-tracing algorithm

The scheme of the reconstruction method for the SS can be seen in the left panel of Fig. 3.11. It first starts with an homogeneous SS map. For each of the emitters, the geodesic trajectories using FMM or Bézier is obtained. In the first iteration these path will be straight. Using each path, the TOF with the given SS map is calculated and compared with the experimental TOF. Corrections using ML-EM are then calculated and stored to be added to the corrections provided by the rest of the emitters. After all the emitters have been used and a total matrix of corrections is obtained, these corrections are applied to the initial image. This process is repeated until convergence is reached. The stopping condition in this case was based on the behavior of the curve of the error behavior with the number of iterations. When the slope of the last points of this curve was sufficiently low the calculations were stopped. This error was estimated as:

$$Error(iter) = \sum_{emitter=1}^{emitter=Nem} \sum_{receiver=1}^{receiver=Nrec} (TOF_{sim} - TOF_{exp})^2 \tag{3.10}$$

Where $Error(iter)$ is the error of the iteration $iter$, Nem is the number of emitters, $Nrec$ is the number of receivers, TOF_{sim} is the TOF simulated with the current SS model and TOF_{exp} is the experimental TOF.

Once the SS image is converged, the paths for every emitter-receiver pair in the last iteration is saved. These paths are used to update the AA map. The scheme of the reconstruction is as shown if Fig. 3.11 right panel. First, the pre-calculated paths are read. The AA map is initialized with a homogenous value of water (0.0022 dB/(MHz cm)). For each emitter, using the path to all its receivers, the amplitude decay method is applied and the value of $A_0 dl$ is estimated. This value is compared with the logarithm of the amplitudes in water and with the object. After that, the corrections using ML-EM are computed. These corrections are accumulated for all the emitters. After that the image is updated. The process is repeated until convergence using the same criterion as for the SS is achieved.

3.3 Numerical experiments

To test the performance of the algorithms proposed in this chapter we used synthetic data simulated with k-Wave. For that purpose, we employed a numerical phantom with several inclusions and SS and AA values similar to the ones present in breast tissue (see Fig. 3.12).

The USCT geometry was a ring array of radius 54 mm with N=200 uniformly distributed transducers. The simulations were conducted on a $128 \times 128\ mm^2$ grid represented by 256×256 grid points with a 10 grid point perfectly matched layer positioned outside the domain. These values of the grid were chosen to support a central frequency of the wave of 1 MHz, which is lower than the central frequency of the arrays present in the MUBI scanner (which is 3.2 MHz with 50 % of bandwith).

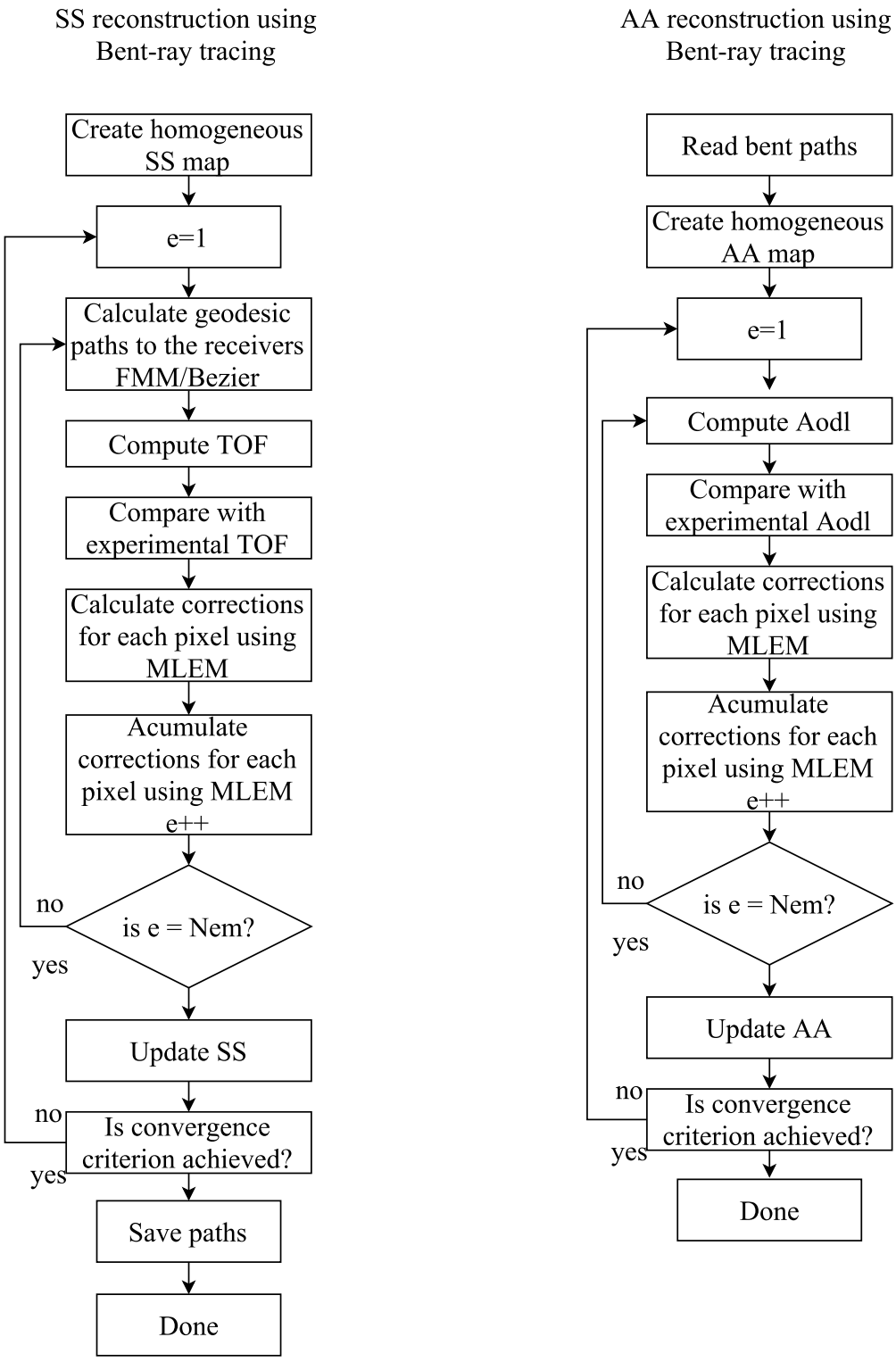

Figure 3.11: Flow diagram of the reconstructions using bent-rays tracing

The reason to use this value is to ensure the tractability of the simulations, as higher frequencies require larger spatial and temporal sampling which increase considerably the time of the calculations. The pressure field at the detector positions in the Cartesian domain was calculated from the pressure at the grid points at each time step via linear interpolation. The transmitted signal was a Gaussian enveloped 3-cycle sinusoidal tone burst and signals were sampled using 854 time points with a time step of 100 ns. The simulation time for each projection for a single emitter was 0.43 seconds using an Intel Core i7-3930K CPU 3.20 GHz with an NVIDIA GeForce GTX 780 GPU.

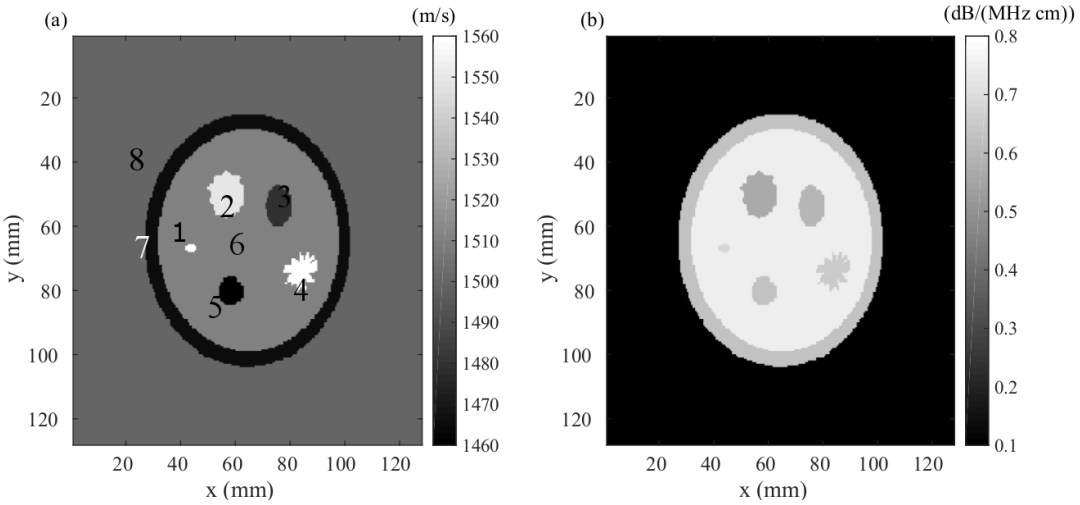

Figure 3.12: (a) Sound speed and (b) acoustic attenuation simulating breast tissue used used for numerical experiments

3.4 Results and discussion

TOF selection methods comparison

Fig. 3.13 shows results comparing the maximum-based, threshold-based, and cross-correlation-based methods to obtain the TOF of the first arrival signal.

In this figure, the left panel, shows in the background the time series of all the receivers associated with a given emitter collapsed in the pressure axis. In the right panel, a single time signal (pressure vs. time interval) corresponding to the frontal receiver of this emitter (receiver number 100) is shown. The maximum-based method tends to be the method that most overestimates TOF.

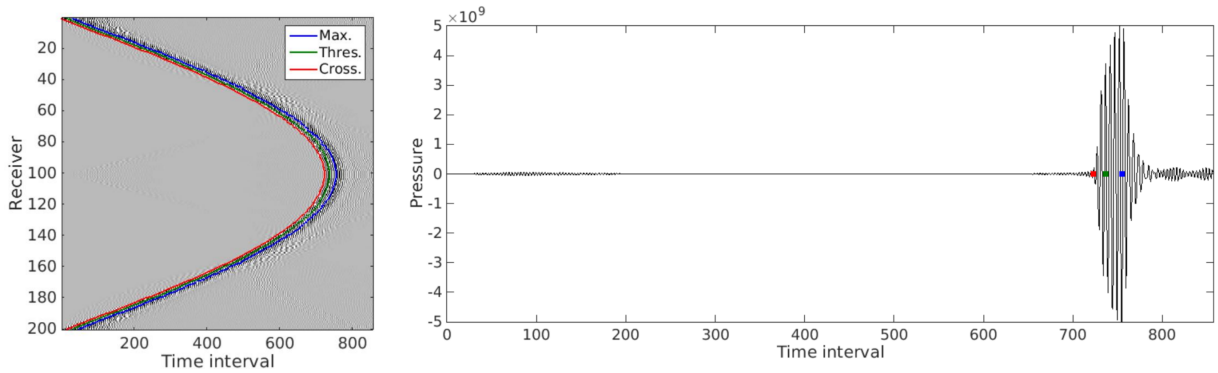

Figure 3.13: Comparison of methods to obtain the TOF from the received signals. The crosscorrelation method provides the most accurate results in comparison with the rest of the methods tested.

On the other hand, the threshold-based method overestimates the TOF values less than the maximum-based method. In this case, as some numerical dispersion may be present in the simulated signals, the threshold value was increased. This demonstrates the instability of the method against random perturbations in the signal.

The cross-correlation method is the one that provides the best solution as it can be observed in Fig. 3.13. No extra corrections need to be done for this method and it provides the most accurate TOF values. Therefore, it is the method employed for TOF estimations in our scanner.

Amplitude selection methods comparison

Fig. 3.14 shows the comparison between the two methods tested to estimate the amplitude of the first arrival signal. This figure represents the amplitude at the receivers from one emitter. The values obtained with both methods when the numerical phantom of Fig. 3.12 is used, were normalized to the values obtained in water. The logarithm of this term was applied in order to obtain the term $A_0 dl$ of the amplitude decay method. As it can be seen, both methods provide comparable results. It is difficult to know in advance which is the exact result, as the wavefront will experience several processes.

Nevertheless, we can compare with the value of $A_0 dl$ that is obtained when straight rays are projected with the given phantom. As it can be seen (see Fig. Fig. 3.14), these profiles are very different. The projection with rays varies softly in comparison with the amplitude estimations using the maximum value and the envelope method.

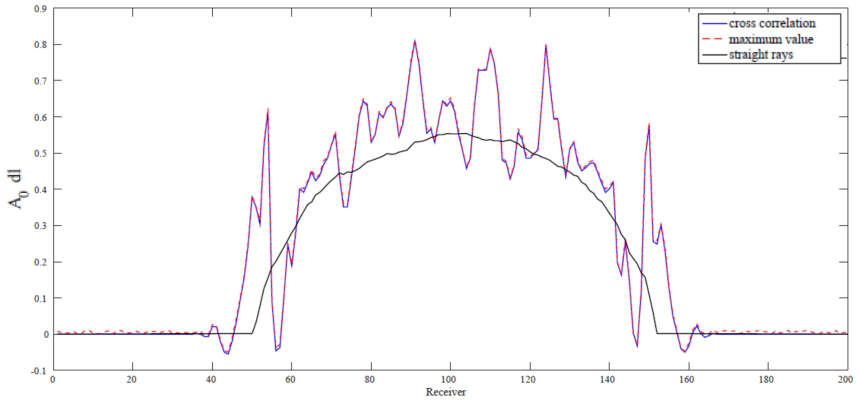

Figure 3.14: Comparison of methods to obtain the amplitude of the received signals. Values of amplitude were normalized to the amplitude in water, i.e when not object is located in the field of view. Both method shown comparable results

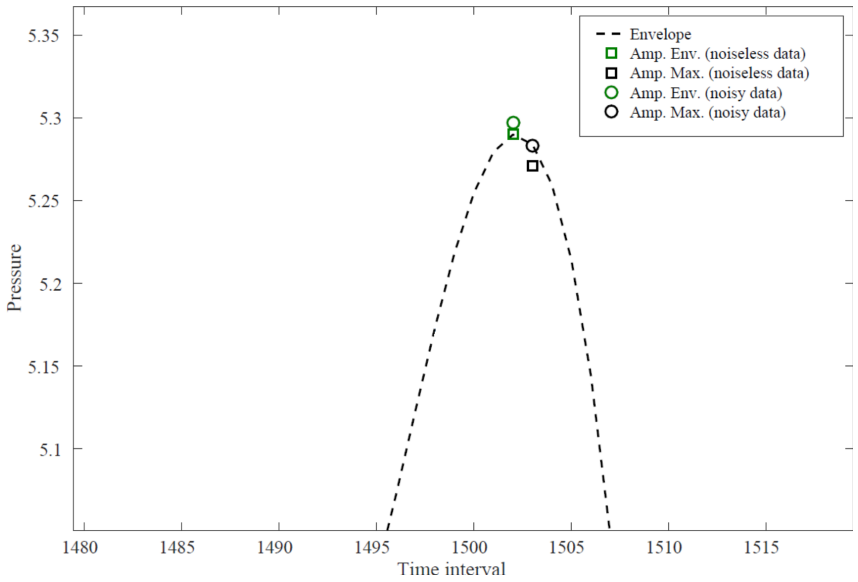

Figure 3.15: Estimation of amplitude using a noisy and a noiseless waveform. Squared represent the noisless data and circles data with noise. In green are represented the estimations of amplitude when the envelope method is employed. In black are the results when using the maximum amplitude method.

More conclusions can be taken from this image. First, in that figure we should not have any values greater than 1, as the phantom materials attenuate more than water. These values can be caused by phase aberrations around the edges of the phantom, and the same can be happening around the inclusions it contains. Therefore, it is expected that the AA reconstructions with rays present low resolution and several artifacts.

One possible solution to these effects when reconstructing the AA using rays could be to apply a smoothing filter to the data in order to make the comparisons between simulations and

referenced data more compatible. In this case, we used a median filter that uses 10 neighbor points to ameliorate the rippling present in the reference data.

As we said, the results obtained with the maximum of the envelope and the maximum of the signal are very similar. Nevertheless, this test was performed in the absence of noise. When noise is taken into account, for example, adding to the time series 40 dB of signal to noise ratio (SNR) of Gaussian noise, the estimated amplitudes vary. In Fig. 3.15 this experiment was done. The amplitude estimated with the envelope method displays a smaller amount that the amplitude estimated with the maximum value. Therefore, it is preferable to use the envelope method as it is less sensitive to noise than the maximum method.

FBP reconstructions SS reconstructions

The TOF sinogram obtained with the analytically FBP method can be seen in Fig. 3.16. The left panel of this figure shows the sinogram with gaps and the right one with the gaps filled. This process practically do not modify the reconstruction time ($\backsim$ 1 ms) and avoid using higher number of detectors to eliminate the gaps. Therefore, the gaps filling is a suitable way of accelerating the acquisition of the USCT data and decreasing the cost of the scanner. The time required to create the sinogram can be found in Table. 3.1.

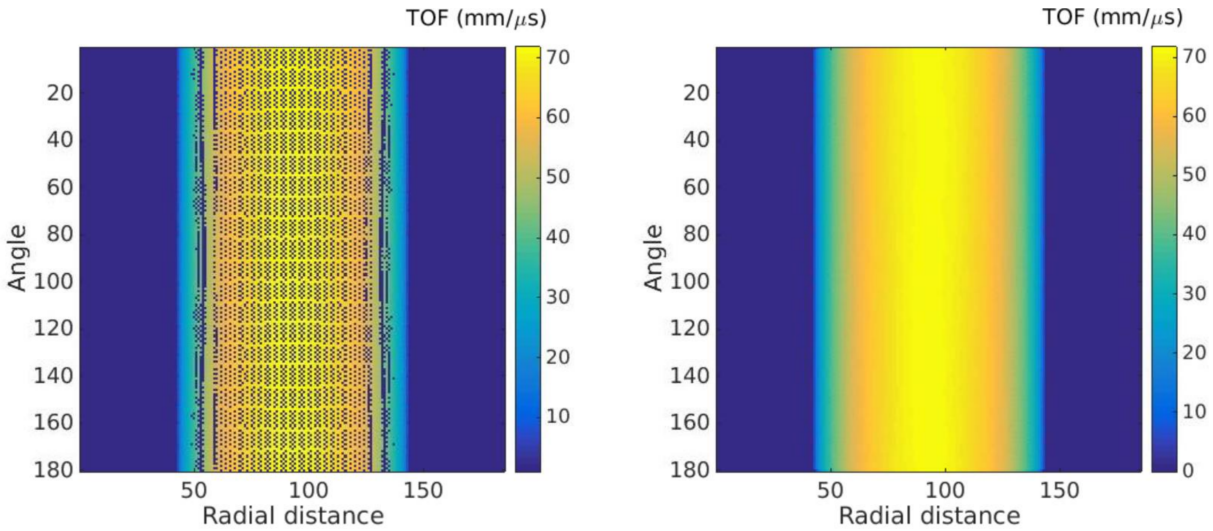

Figure 3.16: Left. Orginal TOF sinogram with gaps. Right. Gaps filled TOF sinogram

The reconstructed SS image using FBP can be seen in Fig. 3.17. The left panel shows the reconstructed phantom and the right panel displays the profiles of the reconstructed and reference phantom at $y = 53mm$. It can be seen that the FBP reconstruction of SS provides a low resolution version of the reference image. Practically all the edge information is lost, but we are able to see all the structures present in the phantom. This is achieved with high

computational efficiency, as this reconstruction only requires 1.02 seconds in total for creating the sinogram and performing the FBP reconstruction (see Table 3.1).

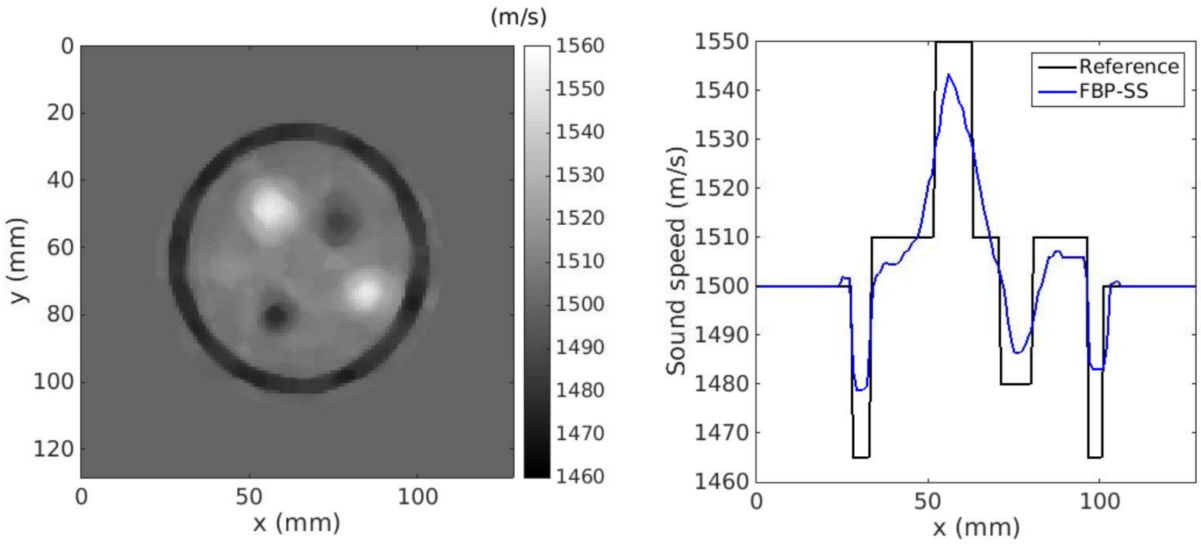

Figure 3.17: Left. FPB reconstructed SS map. Right. Profiles comparison between the reconstructed and the reference map along y = 64 mm

FBP reconstructions AA reconstructions

Fig. 3.18 displays the sinogram with gaps, gaps filled and with the application of the bow tie filter to correct for the artifacts present in the sinogram. The increased time in the reconstruction due to the use of the bow tie filter is practically negligible, as it lower that ($\backsim$ 0.1 ms).

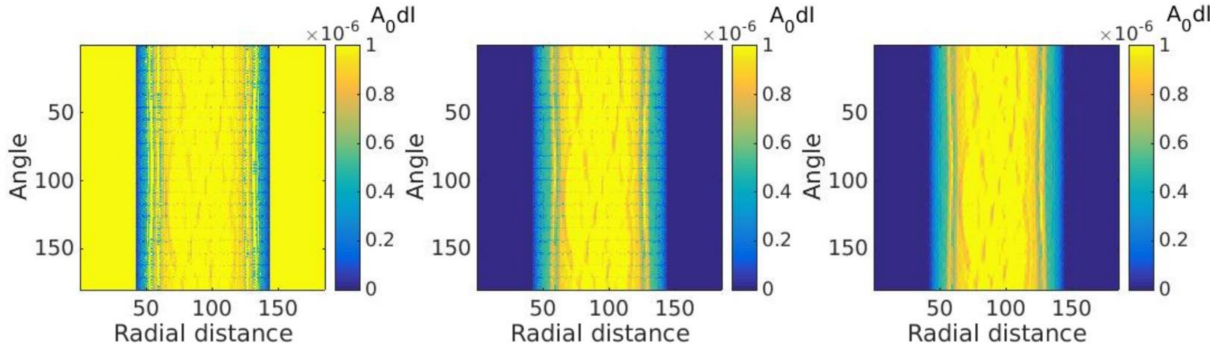

Figure 3.18: Left. Orginal Amplitude decay sinogram with gaps.Center. Gaps filled Amplitude decay sinogram Right. Sinogram with artifacts corrected using the bowtie filter

The reconstructed AA image and the profiles of the reconstructed and reference data are shown in Fig. 3.19. In this case, the use of the analytic GAc algorithms provide very low quality

images, as not only the edges are affected, but also the values of the reconstructed structures are miss-estimated. This is due to the phase aberrations present in the signals as this method is not able to account for interference.

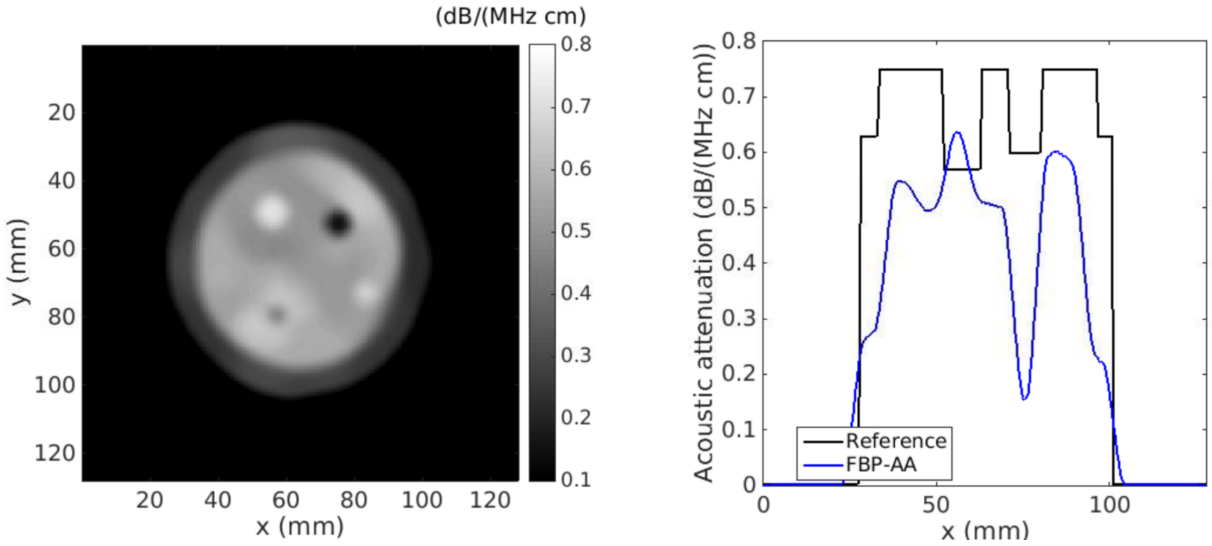

Figure 3.19: Left. FPB reconstructed AA map. Right. Profiles comparison between reconstructed and reference map along y = 64 mm

Bent-rays reconstructions of sound speed

Fig. 3.20 displays a comparison between the iterative bent-rays reconstructions using Bézier and FMM methods. As it can seen, Bézier-based reconstruction of SS provide better image quality than FMM as fewer artifacts and the better recovery of the different structures present in the phantom are obtained. As FMM miss-estimates the trajectory of the rays around the interface between different impedance regions, the sizes of the structures, especially at the interface water-tissue, are considerable distorted. This can be also seen at the bottom panel of this figure, observing the profiles comparison at the depth $y = 53mm$. Bézier profiles are closer to the reference value than the FMM-based reconstructed image. Moreover, the convergence is also obtained faster using Bézier, as the error decrease much faster with this method. The time required for both reconstructions per 10 iterations is given in Table 3.1. The Bézier's time for image reconstruction are considerably faster than the ones required by FMM.

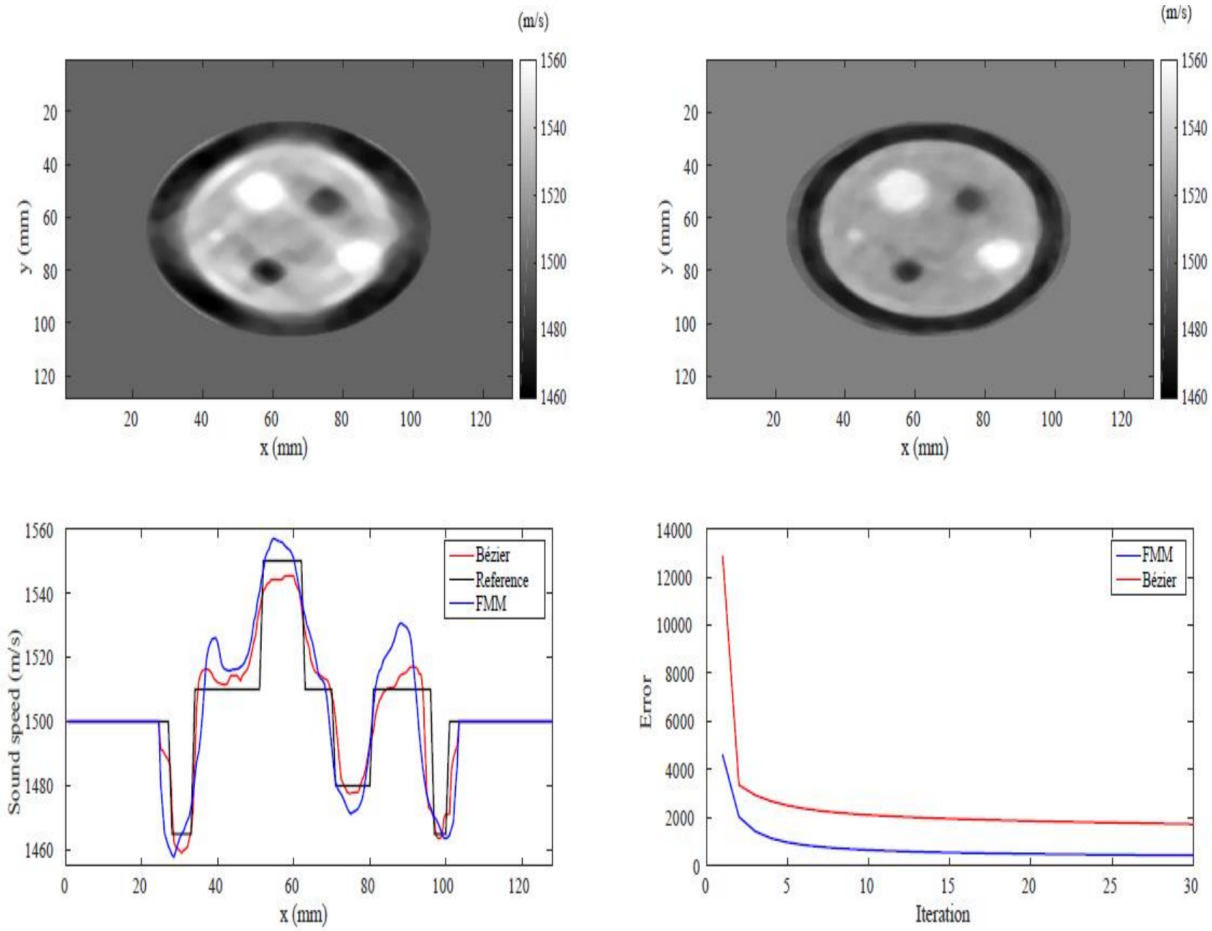

Figure 3.20: Left-top. FMM sound speed reconstruction.Right-top. Bézier sound speed reconstruction Left-bottom. Profiles comparison across the direction y = 53 mm for FMM, Bézier and reference images. Right-bottom. Error behavior with iterations

The capabilities of our proposed Bézier-based bent rays algorithm for GAc USCT SS image reconstruction are considerable better than our implementation of the commonly employed FMM method. In comparison with the analytic reconstructions using FBP, some improvements are obtained at the edges of the structures and also in their mean SS value. To demonstrate this, the mean values and standard deviations inside several Regions of Interest (ROIs) present in the figure are shown in Table 3.2. The bias obtained when using Bézier is smaller than for FMM and FBP. Nevertheless, as it was also pointed out in reference [Dapp et al., 2012] these differences are not significantly enough considerable to categorically ensure the superiority of bent rays algorithms over straight rays ones.

Bent rays reconstructions of AA

Fig. 3.20 displays the iterative bent-rays reconstructions using Bézier and FMM methods in the context of AA reconstructions. The images are obtained faster than the case of the SS reconstructions (see Table 3.1) because the paths were already computed from the SS reconstruction.

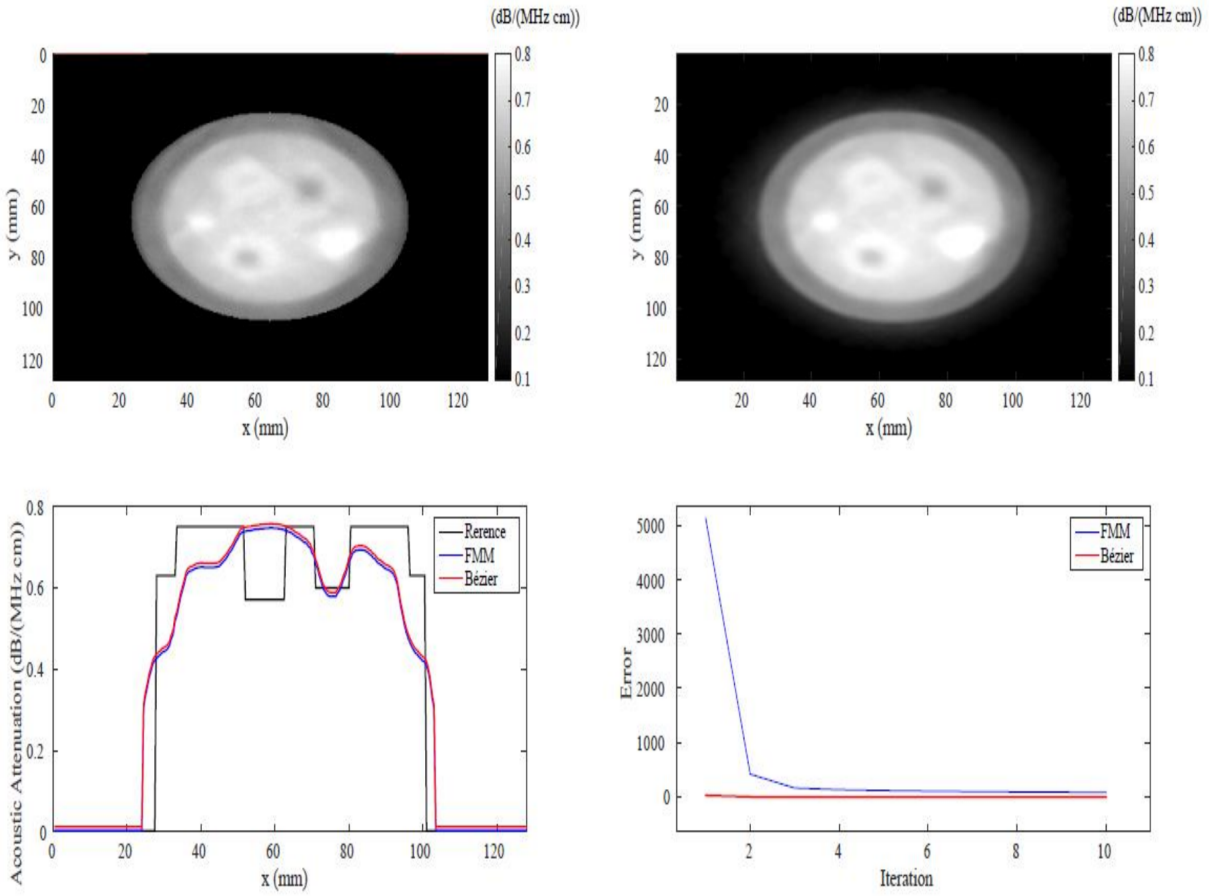

Figure 3.21: Left-top. FMM acoustic attenuation reconstruction.Right-top. Bézier acoustic attenuation reconstruction Left-bottom. Profiles comparison across the direction y = 53 mm for FMM, Bézier and reference images. Right-bottom. Error behavior with iterations

In this case both reconstruction are very similar and even when they present better results than the FBP reconstruction of AA, these images are very low quality. The halo effect explained in the introduction of this chapter is so considerable that the quantitative information of these images is practically lost. We can conclude form these results and the ones from the previous sections that the use of BR algorithms for reconstruction the AA attenuation provides only very low image quality and practically only qualitative images.

Table 3.1: Comparison of execution times (sec) among FBP, iterative FMM and iterative Bezier. For the iterative methods execution times are given per 10 iterations. For FBP, the top value indicates the time for creating the sinogram and the bottom, the time for reconstruction

FBP		**Iter. FMM**		**Iter. Bezier**	
SS	AA	SS	AA	SS	AA
0.9	0.82	114.76	84.3	48.01	28.34
0.12	0.13				

Table 3.2: Mean values, standard deviation, noise, expected values and bias at the ROIs shown in Fig. 4.6(a) for the speed of sound (SS) distribution.

ROI	**Exp. SS** (m/s)	**FBP-SS** (m/s)	**Std. dev**	**FMM-SS** (m/s)	**Std. dev**	**Bézier-SS** (m/s)	**Std. dev**
1	1565	1572	12	1546	4	1547	3
2	1550	1569	14	1555	6	1559	5
3	1480	1494	16	1495	9	1505	7
4	1557	1578	20	1561	9	1564	7
5	1466	1482	24	1485	12	1497	8
6	1510	1528	8	1522	4	1528	2
7	1465	1469	20	1467	9	1490	5
8	1500	1501	4	1500	3	1510	2

Table 3.3: Mean values, standard deviation, noise, expected values and bias at the ROIs shown in Fig. 4.6(a) for the speed of sound (SS) distribution.

ROI	**Exp. AA** (dB/(MHz cm))	**FBP-AA** (dB/(MHz cm))	**Std. dev**	**FMM-AA** (dB/(MHz cm))	**Std. dev**	**Bézier-AA** (dB/(MHz cm))	**Std. dev**
1	0680	2.524	0.542	0.822	0.008	0.797	0.007
2	0.570	0.933	0.430	0.762	0.009	0.740	0.011
3	0.600	0.187	0.563	0.644	0.038	0.621	0.034
4	0.650	1.143	0.408	0.842	0.016	0.806	0.017
5	0.630	0.032	1.040	0.712	0.033	0.687	0.037
6	0.750	0.612	0.217	0.754	0.008	0.733	0.011
7	0.630	0.958	0.142	0.475	0.008	0.467	0.014
8	0.002	0.513	0.056	0.222	0.041	0.183	0.046

3.5 Conclusions

In this chapter, several methods and algorithms for image reconstruction based on geometrical acoustics in USCT have been investigated. As these methods require the use of accurate TOF and amplitude estimations, different approaches to obtain these values were analyzed. Besides, several techniques of reconstructions based on analytic or iterative ray-tracing were also investigated in this chapter.

The comparison of the methods implemented to characterize the first arrival signals in terms of the TOF (interval of maximum value, threshold and cross correlation) indicates that the TOF estimations using the cross correlation method provide the most robust and accurate results.

For the case of the amplitude estimations, the use of the envelope and the maximum of the signal provided very similar results with noiseless synthetic data. Nevertheless, when noise was added to the synthetic waveforms, the envelope method was more robust. In any case, rays algorithms provided very different estimations than the reference image, extrated from the waveform, as these GAc algorithms can not take into account the processes that originate phase aberrations in the signals.

Regarding the reconstruction using analytic methods to recover the SS and AA map, we saw that both reconstruction could be obtained in $\sim$1 second. For the case of SS, the reconstructed images were a low resolution version of the reference map. The edge information in these images is practically lost. Nevertheless, they are able to provide a general information of the actual image. On the other hand, the FBP reconstructions of AA provide very low quality image and the AA information of the structures is very distorted.

The reconstructions using iterative bent-rays tracing for the SS present improved resolution. Nevertheless, this improvement is not strongly considerable and the reconstruction time is increased several orders of magnitude. The Bézier method provided faster reconstruction times and better image quality than FMM. For the AA reconstructions, the recovered AA images with both methods show halos around the structures that distort the values of the image. This demonstrate how unsuitable rays algorithms are to reconstruct the AA, indicating the need for implementing Full Wave inversion algorithms to this end.

Therefore, in order to employ fast ray algorithms in our scanner we suggest using FBP and, if some improvements in resolution are required, bent-rays with the use of the Bézier method can be used.

Chapter 4

FWI USCT tomography

4.1 Introduction

Current FWI methods used in USCT to reconstruct sound speed (SS) and acoustic attenuation (AA) maps are quite different. The reconstruction of SS using FWI has been studied in several works [Wang et al., 2015, Roy et al., 2010, Anis et al., 2014, Wiskin et al., 2007] and it is generally performed in the time domain neglecting the effect of AA. In contrast, the reconstruction of AA using FWI, despite being extensively studied in seismology [Tarantola, 1987, Song et al., 1995, Pratt et al., 2007] has been far less studied in the context of USCT.

In previous works [Li et al., 2014, Pratt et al., 2007, Sandhu et al., 2016], a frequency domain FWI formulation for USCT was introduced to obtain the quality factors of the tissues (which indicates the energy loss per cycle) to characterize AA. The method employs a combination of several carefully chosen fixed-frequencies (working from long to short wavelengths), which requires the solution of several minimization problems, increasing the computational cost of the inversion process. Moreover, due to the high non-linearity of the least squares cost function commonly employed in FWI, fixed-frequency algorithms are vulnerable to get stuck on erroneous solutions [Lin et al., 2000, Mast, 2000]. This is particularly remarkable at high frequencies, where this type of cost function generally presents a large number of local minima. Therefore it would be suitable the use of time domain methods where the entire bandwidth of the signals can be employed in the reconstruction process in a single step [Lin et al., 2000].

On the other hand, due to the fact that SS and AA can be obtained from the same transmitted data, it is desirable to have a common reconstruction framework capable of exploiting, in a computationally efficient manner, the image-quality advantages provided by FWI methods. In this chapter, we will present our FWI code *USCT-Rec*. USCT-Rec is a time domain USCT reconstructor code based on FWI that employs a modified version of the k-Wave-CUDA as forward and backward propagator to recover both SS and AA distributions.

4.2 Methods

Summarizing what was explained in chapter 1, an algorithm based on FWI has five main components:

- A computational model to solve the wave equation (i.e the propagation of the acoustic waves in the medium) with the desired level of physical accuracy. Even when this is commonly called a *forward problem*, this model is employed both for forward and backward wave propagation. In the later case, the acoustic waves are generated with adjoint sources.
- An optimization model to perform the inverse problem. This algorithm should allow for decreasing the mean-squares error functional that regulates the optimization problem.
- An strategy to calculate *the gradients of the error functional* with respect to the acoustical property of interest.
- A *regularization* method in order to get an unique and stable solution, and to remove noise artifacts.
- A *stopping criterion*, to finish the optimization process.

In the following sections these items will be addressed.

4.2.1 Forward problem

To simulate the propagation of acoustic waves in USCT-Rec, we employed a modified version of k-Wave-CUDA. This modification was done to improve the execution time of the propagation. k-Wave-CUDA saves the pressure field values in output HDF5 files sequentially every time step. This is done in order to keep tractable matrices storing the pressure field, ensuring neither GPU nor CPU could run out of memory.This slows down the calculations, as large amounts of time are consumed in the file-opening and writing processes.

For example, if one computes the size of a matrix that can store the whole pressure field (in all the Cartesian domain and in every time interval along the total time of the simulation) for a simulation of 2 MHz with k-Wave-CUDA, in a computational grid of 512×512 grids, and 1707 temporal bins in single precision, this requires around 1.8 GB.

Nowadays, practically all the modern GPU cards and computers handle considerable amounts of memory, like this one and even larger. Consequently, we modified the scheme of data handling in the k-Wave-CUDA to avoid saving data after every time interval, but recording it at the end of the simulation. The difference in time when the data is saved sequentially and when is only saved at the end of the propagation is around 48%. Especial care should be put in verifying that the limit of the available memory is not exceed.

4.2.2 Inversion problem

As it was explained, the idea behind FWI method is to minimize iteratively the least-squares error functional ε that represents the global deviations of experimental pressure field at the positions of receivers p^{obs} and the simulated signals p at the same locations. Nevertheless, as it is an ill-posed problem, and due to the lack of complete information, as well as the presence of noise in the signals, it is crucial employing a regularization method in the optimization process. Here, an edge-preserving regularization method based on TV is used (see Section 1.3.2.4). This regularization selects among the possible solution images that are locally piece-wise constant while avoiding over-smoothing. It also preserves edge information of the reconstructed images. The cost function when the TV regularization term is included can be written as:

$$\varepsilon = \frac{1}{2}\sum_{m=1}^{M}\int_0^T [p(\mathbf{r}_m, t) - p^{obs}(\mathbf{r}_m, t)]^2 dt + \mu R_{TV} \tag{4.1}$$

Here μ controls the relative importance of the TV regularization term given by the functional R_{TV}, whose expression was introduced in Chapter 1, Eq. (1.57).

To perform the minimization, the functional gradient of the cost function defined in Eq. (4.1) with respect to the acoustic property being recovered (i.e., the Frechet derivative) is employed. The functional gradient provides the direction in the vector space of the unknowns in which the distribution must be modified at each iterative step of the reconstruction algorithm in order to minimize the error. The parameters to recover are the spatially varying distributions of SS and AA, given by the functions $c(\mathbf{r})$ and $\alpha_0(\mathbf{r})$, respectively. Here $\mathbf{r}$ indicates position in the two or three dimensional domain Ω, where the optimization problem takes place.

In order to update both distributions, it is necessary to consider several factors:

- Despite being a problem intrinsically 3D, in this work the numerical experiments are performed in 2D to demonstrate the principle, with expedite computation times.
- The cost function given in Eq. 4.1 is affected by both SS an dAA distributions. However, it depends much more strongly on SS than on AA. Alternating minimization algorithms have been proposed in order to deal with this kind of problem [Niesen et al., 2009]. The idea behind them is to perform several sequential minimizations over a single material property, instead of solving the original problem over multiple properties simultaneously.
- In order to optimize both distributions independently, it is important to follow a certain order in the optimization process. This can be illustrated with a simple numerical example. Consider the recovery of the SS and AA maps in a homogeneous medium with $c = 1440m/s$ and $\alpha_0 = 0.5dB/(MHz^y cm)$ using a ring array with radius 54 mm and N = 200 evenly spaced transducers. With a single emitter, the global error resulting from a testing range of values of SS $(1400 - 1500m/s)$ and AA $(0 - 1dB/(MHz^y cm))$ can be calculated. In this case, due to the fact that no noise was taking into account in the signals, Eq. (4.1) can be used with $\mu = 0$. Due to the symmetry of the problem, it is not necessary to extend the calculations to all 200 emitters. The resulting error distribution is given in Fig. 4.1.

As it can be seen, the SS optimization has a relatively small dependence on the starting AA map. For the range of AA values tested, it is possible to reach the minimum of the global error with respect to the SS distribution, regardless of the starting AA value. On the other hand, the optimal reconstruction of AA strongly depends on the accuracy of the SS map. It is necessary to be close to the actual SS map prior to converge to the correct AA distribution. Consequently, in order to minimize both distributions, a reasonable approach is to first solve for SS distribution with an initial estimation of AA, and then employ this SS distribution to recover the actual AA distribution.

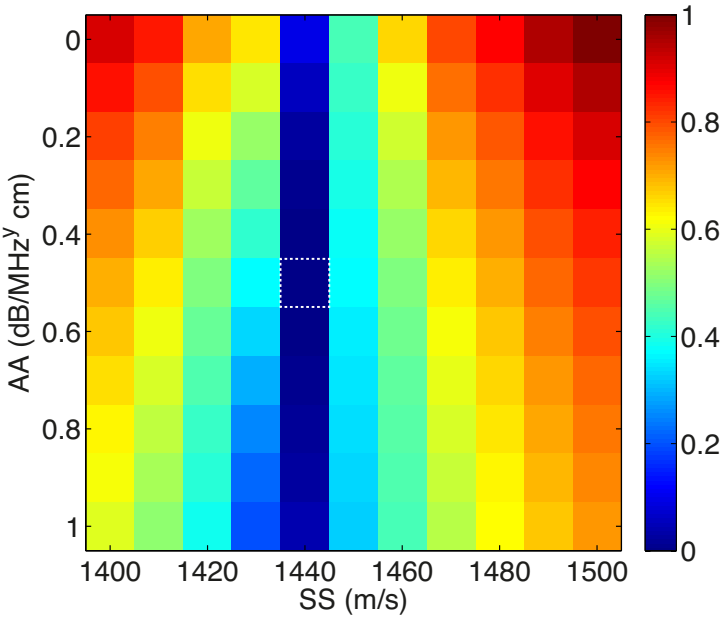

Figure 4.1: Example of the global error behavior (normalized to the maximum value) around the actual SS and AA values for a homogeneous distribution of acoustic material properties. The intersection of the true values (which corresponds to the global minimum) is shown with white dashed square.

Once the expressions for the functional gradient are known for both distributions of interest independently, i.e., $\delta\varepsilon/\delta c$ to update SS using a fixed AA map, and $\delta\varepsilon/\delta\alpha_0$ to update the AA map based on a fixed SS map, they can be used in a gradient-based minimization algorithm. Here, the method of steepest descent is used, where the update equations for SS and AA are given by:

$$c^{(n+1)}(\mathbf{r}) \;=\; c^{n}(\mathbf{r}) \;+\; \lambda_c^n \frac{\partial \varepsilon}{\partial c}^{n} \tag{4.2}$$

$$\alpha_0^{(n+1)}(\mathbf{r}) \;=\; \alpha_0^{n}(\mathbf{r}) \;+\; \lambda_{\alpha_0}^n \frac{\partial \varepsilon}{\partial \alpha_0}^{n} \tag{4.3}$$

Here λ^n is the step size for the n^{th} iteration, which is calculated in this work using the backtracking line-search method (see Chapter 1).

4.2.2.1 Functional gradients with respect to the sound speed

The derivative of the error functional ε with respect to the sound speed (i.e., the functional gradient) can be found from Eq. (4.1)

$$\frac{\partial \varepsilon}{\partial c} = \sum_{m=1}^{M} \int_0^T [p(\mathbf{r}_m, t) - p^{obs}(\mathbf{r}_m, t)] \frac{\partial p(\mathbf{r}_m, t)}{\partial c} dt \; + \; \mu \nabla R_{TV} \tag{4.4}$$

Here ∇R_{TV} is the gradient of the functional R_{TV} (see Eq. 1.57), which can be calculated numerically [Peyré, 2011] as will be explained later. An efficient way to calculate the functional gradient given in Eq. (4.4), can be found using the adjoint formulation [Norton, 1999] explained in Chapter 1. First, an equation for the derivative inside the integral (the Jacobian) can be found by considering that a perturbation to the sound speed Δc at a point $\mathbf{r}_p$ will cause a small change $\Delta p(\mathbf{r}, t)$ in the pressure field. Noting that $(x + \Delta x)^a \simeq x^a + a x^{(a-1)} \Delta x$, a perturbed version of Eq. (1.39) can be written as:

$$\begin{aligned} \Bigg\{ \left[\frac{1}{c^2} - \frac{2\Delta c \delta(\mathbf{r} - \mathbf{r}_p)}{c^3} \right] \frac{\partial^2}{\partial t^2} - \nabla^2 \\ + 2 \left[c^{y-1} + (y-1) c^{y-2} \Delta c \delta(\mathbf{r} - \mathbf{r}_p) \right] \alpha_0 (-\nabla^2)^{\frac{y}{2}} \frac{\partial}{\partial t} \\ - 2 \left[(c^y + y c^{y-1} \Delta c \delta(\mathbf{r} - \mathbf{r}_p) \right] \alpha_0 \, tan\left(\frac{\pi y}{2}\right) (-\nabla^2)^{\frac{y+1}{2}} \Bigg\} (p + \Delta p) = S \end{aligned} \tag{4.5}$$

Using Eq. 1.39 and discarding small terms, dividing by Δc, we obtained the following equation for the dependence of the pressure field on the sound speed:

$$\begin{aligned} \Box_\alpha^2 \frac{\partial p}{\partial c} = \Bigg\{ \left[\frac{2}{c^3} \delta(\mathbf{r} - \mathbf{r}_p) \right] \frac{\partial^2}{\partial t^2} - 2(y-1) c^{y-2} \delta(\mathbf{r} - \mathbf{r}_p) \alpha_0 (-\nabla^2) \frac{y}{2} \frac{\partial}{\partial t} \\ + 2 y c^{y-1} \delta(\mathbf{r} - \mathbf{r}_p) \alpha_0 tan\left(\frac{\pi y}{2}\right) (-\nabla^2)^{\frac{y+1}{2}} \Bigg\} p \end{aligned} \tag{4.6}$$

The corresponding adjoint wave equation can be defined as:

$$\Box_\alpha^2 p^*(\mathbf{r}, T - t) = \sum_{m=1}^{M} [p(\mathbf{r}_m, t) - p^{obs}(\mathbf{r}_m, t)] \delta(\mathbf{r} - \mathbf{r}_m) \tag{4.7}$$

Comparing Eq. 4.7 with Eq. 4.2, we may notice that, in practice, this can be implemented by defining the adjoint source term as the time-reversed difference between the simulated $p(\mathbf{r}_m, t)$ and the measured data $p^{obs}(\mathbf{r}_m, t)$, through a change of variables $t \rightarrow T - t$, solving for the adjoint field $p^*(\mathbf{r}, t)$ and then again reversing this in time to give $p^*(\mathbf{r}, T - t)$. Alternatively, the wave model could be run backwards in time. Next, multiplying Eq. (4.5) by $p^*(\mathbf{r}, T - t)$ and Eq. (4.6) by $\delta p/\delta c$, subtracting the resulting two expressions, and then integrating over time and space, yields:

$$\frac{\partial \varepsilon}{\partial c(\mathbf{r}_p)} = \int_0^T p^*(\mathbf{r}_p, T-t)(\gamma_1 + \gamma_2 + \gamma_3) p(\mathbf{r}_p, t) dt + \gamma_4$$

where:

$$\gamma_1 = \frac{2}{c^3}\frac{\partial^2}{\partial t^2} \quad \gamma_2 = -2\alpha_0(y-1)c^{y-2}(-\nabla^2)^{\frac{y}{2}}\frac{\partial}{\partial t}$$
$$\gamma_3 = 2\alpha_0 y c^{y-1} tan\left(\frac{\pi y}{2}\right)(-\nabla^2)^{\frac{y+1}{2}} \quad \gamma_4 = \mu \nabla R_{TV} \tag{4.8}$$

Where we have used Eq. 4.4 and the fact that $\iint \left[p^* \Box_\alpha^2 (\delta p/\delta c) - (\delta p/\delta c)\Box_\alpha^2 p^*\right] dt\, dV = 0$. As the point of the perturbation $\mathbf{r}_p$ was arbitrary, Eq. 4.8 holds for any $\mathbf{r}$.

When the relative contributions of the terms $\gamma_1 p$, $\gamma_2 p$ and $\gamma_3 p$ in Eq. (4.8) to the overall solution is analyzed numerically (using a typical SS and AA), it can be seen that the terms $\gamma_2 p$ and $\gamma_3 p$ are several orders of magnitude smaller than γ_1 (see 4.2). Consequently, these terms can be neglected from the expression of the functional gradient in order to simplify and speed up the calculations.

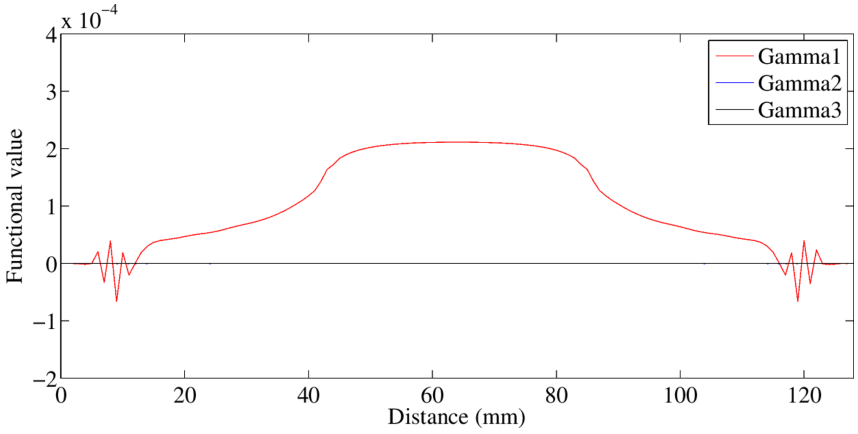

Figure 4.2: Relative contributions of the terms $\gamma 1, \gamma 2$ and $\gamma 3$ to the overall functional gradient. This numerical example consisted on a reference background sound speed (SS) of 1500 m/s and a circle centered with SS = 1510 m/s. The reference absorption coefficient (AA) was homogeneos AA =0.5. The initial values were arbitrary chosen as SS = 1500 m/s and AA = 0.5 dB/MH cm. A 64 mm radius ring with 200 detectors was used.

The resulting approximate expression for the gradient when the contribution of $\gamma_2 p$ and $\gamma_3 p$ is neglected is:

$$\frac{\partial \varepsilon}{\partial c} \simeq \int_0^T \frac{2}{c^3} \left(\frac{\partial^2 p}{\partial t^2} \right) p*(T-t)dt + \mu \nabla R_{TV} \tag{4.9}$$

This expression coincides with previous works reported for the lossless medium approximation [Wang et al., 2015, Zhou et al., 1995]. Given that the update of SS distribution is practically independent of AA distribution, the optimization of this variable can be done with an approximate value for the distribution of the α_0 coefficient, as mentioned in Sec. 4.2.2.

The functional gradient in Eq. (4.9) requires running the computational model to solve the fractional Laplacian wave equation twice per iteration: once for the forward propagation of the pressure field generated by the emitter to obtain p, and a second time for the backward propagation to obtain the adjoint field p^*. This operation has to be performed sequentially for each emitter in each iteration. This means that the total number of times that the wave equation needs to be solved, per iteration, is twice the number of emitters (to obtain p and p^*), plus the number of evaluations the line-search algorithm may need. Once the functional gradient is computed, it can be used together with Eq. (4.2) to update the SS map.

For processes of high computational burden like this one, the ordered-subsets method provides an efficient way of improving the tractability of calculations and to speed convergence without significantly compromising image quality [Hudson and Larkin, 1994]. This approach consists on splitting the data into subsets, each of which contains a fraction of the total number of emitting transducers with its respective projections to receivers. The strategy to combine the ordered-subsets method and the adjoint formulation is as follows. The total number of emitters M is splitted into a given number of subsets. Each subset will contain M' emitters. The functional gradients are computed for each emitter (using all its receivers) of the set. In this case we cannot employ the global error functional as defined in Eq. (4.1) for all possible emitter-receiver pairs, but an approximation to the error functional is used instead for each subset.

$$\varepsilon^s = \sum_{m'=1}^{M'} \int_0^T [p(\mathbf{r}_{m'}, t) - p^{obs}(\mathbf{r}_{m'}, t)]^2 dt + \mu R_{TV} \tag{4.10}$$

The functional gradient of the error defined in Eq. 4.10 is calculated using a similar expression to Eq. 4.9, but in this case, the fields p^* and p are computed only with those emitters and receivers pairs included in the given subset. The same process is repeated for all subsets to complete a full iteration. This way, the entire data set from all the emitter-detector pairs are employed in a full iteration, but the estimation of the image is improved several times per iteration, speeding-up convergence. It is important to mention that the use of subsets makes impossible to ensure the optimization of the general misfit function given in Eq. 4.1, as every subset provides a slightly different image based on the partial information the set of emitters of that subset supplies. This is mainly because in our derivations we assumed the use of spherical

point sources. For these sources it is well known that they can only provide information about a certain part of the domain observed [Tromp et al., 2005b]. Therefore, it is advisable to use reasonably small number of subsets (and therefore a large number of emitters per subset) to ensure that each partial error functional contains as much information as possible of the whole domain. Initial FWI codes [Roy et al., 2010, Tarantola, 1987] employed equal number of subsets as the total number of transducers. This means the information of only one emitter was employed to perform an image update which explains to large extent the instability that characterized those initial formulations.

The reconstruction process is performed according to the scheme shown in Fig. 4.3. First, the data is split randomly into the number of subsets desired. The pressure field p generated by each emitter of the subset with the starting values of SS and AA is then computed using k-Wave (which solves Eq. 1.39) and recorded in every pixel of the computational the grid. Next, the adjoint source is computed employing the time-reversed difference between the simulated and measured pressure field at each receiver's position. Using the adjoint source term, the adjoint field p^* is then computed and recorded in all the pixels of grid, again using k-Wave. After that, in order to update the SS distribution, the contribution to the functional gradient for this projection is calculated (denoted FG_e in Fig. 4.3). This process is repeated for all the emitters included in the subset to obtain an estimate of the functional gradient for the subset (denoted FG_s in Fig. 4.3). As the TV term that intervenes in the functional gradient (Eq. (4.9)) is common to all the emitters of the subset (it only depends on the SS map used for the calculations), this is calculated at the end of the subset. Next, a backtracking line-search algorithm is run and after the step size is obtained, the SS distribution is updated according to Eq. (4.2). To complete a full iteration, the same process is repeated for all subsets. Finally, a convergence criterion (discussed in Sec. 4.2.3) is evaluated. If it is not fulfilled, the updated SS distribution is used as the starting value for the next iteration. The whole process is repeated until the convergence criterion is satisfied.

4.2.2.2 Functional gradients with respect to the attenuation

Following the same methodology of Sec. 4.2.2.1, the functional gradient with respect to the absorption coefficient is given by:

$$\frac{\partial \varepsilon}{\partial \alpha_0} = \sum_{m=1}^{M} \int_0^T [p(\mathbf{r}_m, t) - p^{obs}(\mathbf{r}_m, t)] \frac{\partial p(\mathbf{r}_m, t)}{\partial \alpha_0} dt \; + \; \mu \nabla R_{TV} \tag{4.11}$$

A small change in the absorption coefficient $\Delta\alpha_0$ at point $\mathbf{r}_p$ will result in a small change in the pressure field δp. The perturbed wave equation can be written as:

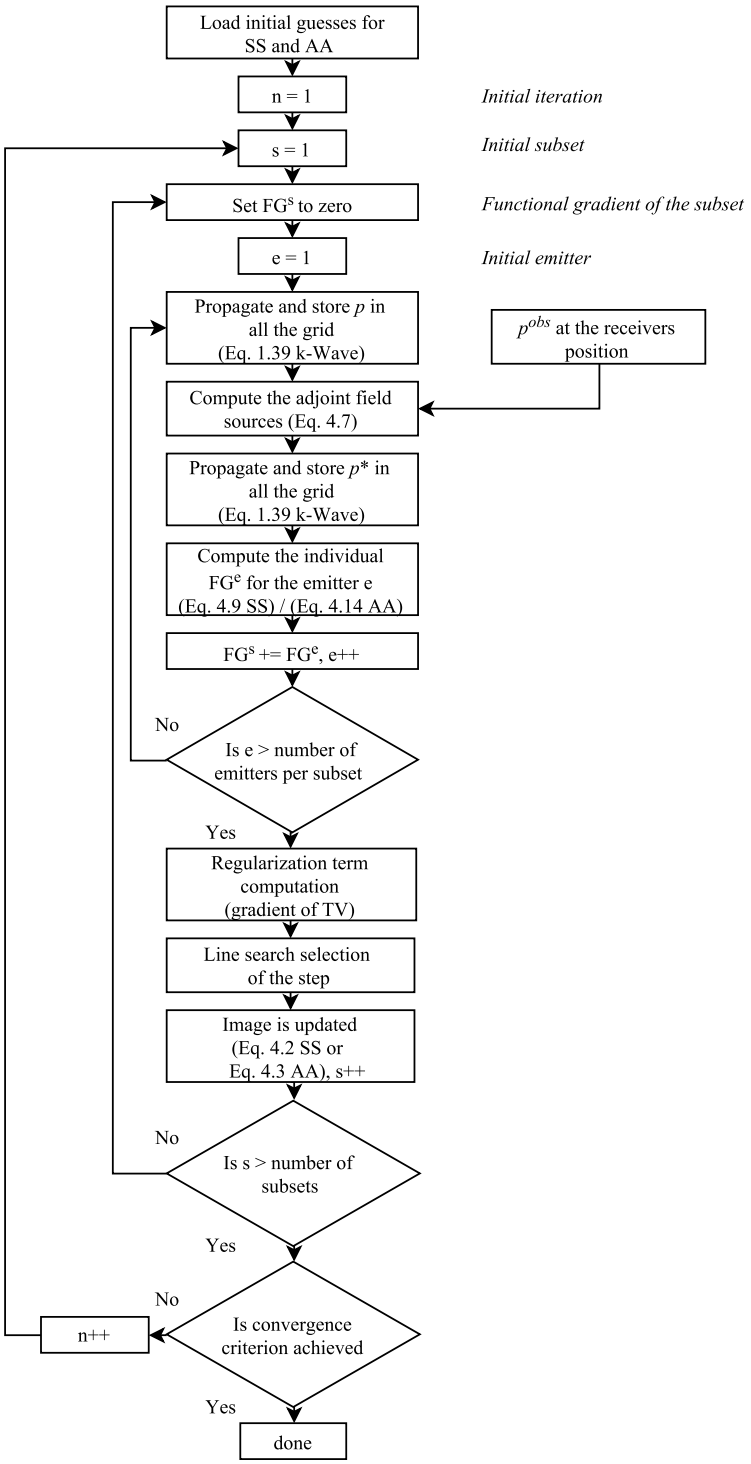

Figure 4.3: Flow chart of the reconstruction algorithm used to update the speed of sound (SS) and acoustic attenuation (AA) distributions

$$\left\{\frac{1}{c^2}\frac{\partial^2}{\partial t^2} - \nabla^2 + 2c^{y-1}(\alpha_0 + \Delta\alpha_0\delta(\mathbf{r}-\mathbf{r}_p))(-\nabla^2)^{\frac{y}{2}}\frac{\partial}{\partial t}\right.$$
$$\left. -2c^y(\alpha_0 + \Delta\alpha_0\delta(\mathbf{r}-\mathbf{r}_p))tan\left(\frac{\pi y}{2}\right)(-\nabla^2)^{\frac{y+1}{2}}\right\}(p(\mathbf{r},t) + \Delta p(\mathbf{r},t)) = S \tag{4.12}$$

Discarding small terms and using Eq. (1.50) yields

$$\Box_\alpha^2\frac{\partial p}{\partial \alpha_0} = -2c^{y-1}\delta(\mathbf{r}-\mathbf{r}_p)(-\nabla^2)^{\frac{y}{2}}\frac{\partial p}{\partial t}$$
$$+2c^y\delta(\mathbf{r}-\mathbf{r}_p)tan\left(\frac{\pi y}{2}\right)(-\nabla^2)^{\frac{y+1}{2}}p \tag{4.13}$$

As above, multiplying Eq. (4.13) by $p^*(T-t)$ and Eq. 4.7 by $\delta p/\delta\alpha_0)$, subtracting the resulting two expressions, and then integrating over time and space gives an expression for the functional gradient in terms of forward and adjoint fields:

$$\frac{\partial \varepsilon}{\partial \alpha_0} = \int_0^T p^*(\mathbf{r}, T-t)\left[-2c^{y-1}(-\nabla^2)^{\frac{y}{2}}\frac{\partial}{\partial t}\right.$$
$$\left. +2c^y tan\left(\frac{\pi y}{2}\right)(-\nabla^2)^{\frac{y+1}{2}}\right]p(\mathbf{r},t)dt + \mu\nabla R_{TV} \tag{4.14}$$

Here we have used Eq. 4.11 and the fact that $\iint\left[p^*\Box_\alpha^2(\delta p/\delta\alpha_0) - (\delta p/\delta\alpha_0)\Box_\alpha^2 p^*\right]dt\,dV = 0$. As the point of the perturbation $\mathbf{r}_p$ was arbitrary, Eq. (4.14) holds for any $\mathbf{r}$.

The fractional Laplacian term in Eq. 4.14 becomes simpler to compute using the Fourier pseudo-spectral method explained in Chapter 2 [Chen and Holm, 2004, Treeby and Cox, 2010a] This is a very common numerical method to compute these operands.

$$(-\nabla^2)^y p(r,t) = \mathcal{F}^{-1}k^{2y}\mathcal{F}[p(r,t)] \tag{4.15}$$

Where $\mathcal{F}$ and $\mathcal{F}^{-1}$ are the forward and inverse Fourier transforms, respectively, and k is the wave number matrix.

As Eq. 4.14 contains an explicit dependence on the SS distribution, small deviations in the SS distribution from the true values may propagate and create significant artifacts in the reconstructed α_0 distribution. Therefore, in the reconstruction of AA, it is important to use a SS distribution as close as possible to the actual one. The scheme proposed for the AA reconstruction is analogous to the one explained in the previous section for the SS update (see Fig. 4.3). The only difference with respect to the SS scheme is that the initial distribution of SS to update the AA distribution should be the converged map for the SS, while for the SS it was not very critical the AA map considered.

4.2.2.3 Comparison with finite-difference estimations

In order to verify that the expressions obtained in Secs. 4.2.2.1 and 4.2.2.2 for the functional gradients were correct, they were compared with functional gradients calculated using a computationally expensive finite difference approximation. The sound speed was perturbed by a small amount Δc at each point in turn along a given line through the image and the change in the error functional $\Delta\varepsilon$ was obtained. This way, a finite difference gradient can be computed as $\Delta\varepsilon/\Delta c$. This process was repeated in the same way for the absorption coefficient distribution to obtain the finite difference gradient $\Delta\varepsilon/\Delta\alpha_0$.

For both tests, the speed of sound and attenuation distributions shown in Figs. 4.4 (a) and (b) were used. A circular array of 200 transducers with a diameter of 128 mm and a central frequency of 1 MHz was employed for the simulations. Both distributions were perturbed along the line $y = 64mm$. Figs. 4.4 (c) and (d) show a comparison between the finite difference functional gradients and those obtained using the adjoint method (Eq. 4.9 and 4.14). Both methods give similar gradients, verifying that the adjoint method was formulated and implemented correctly.

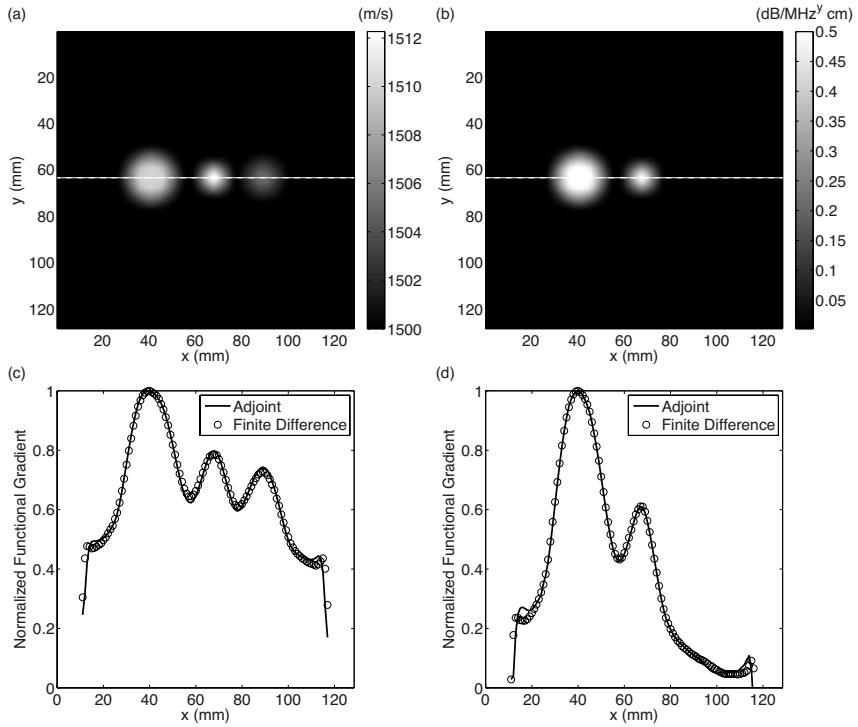

Figure 4.4: Comparison between the functional gradients obtained using finite differences and the adjoint method. (a) Speed of sound (SS) distribution employed for the simulations. (b) Acoustic absorption (AA) distribution. (c) Comparison of functional gradients for the SS. The gradient is taken through the SS map at the position shown with the white dashed line. (d) Comparison of functional gradients for the AA

The main differences between both distributions appear around the detectors. This is basically due to the estimation of the field around the detectors is not totally reliable, as a small number of finite elements are employed to compose the field in those areas.

It is worthy mentioning that the computation of the gradients obtained with the adjoint method is several orders of magnitude faster that the use of finite differences. In the former case, the gradients for every pixel are obtained in a single step while in the finite difference case, the error should be evaluated individually for every single pixel. Therefore the finite-difference method was only employed for verification purposes.

4.2.2.4 Numerical calculation of the term ∇R_{TV}

As it was mentioned, the term ∇R_{TV} can be computed numerically. In this work, the following expression was employed [Anagaw, 2009]:

$$\nabla R_{TV} = \frac{\xi_{xx,i,j}(\xi_{y,i,j}^2 + \theta^2) - 2\xi_{x,i,j}\xi_{y,i,j}\xi_{xy,i,j} + \xi_{yy,i,j}(\xi_{x,i,j}^2 + \theta^2)}{(\xi_{x,i,j}^2 + \xi_{y,i,j}^2 + \theta^2)^{\frac{3}{2}}} \tag{4.16}$$

Where:

$$\begin{aligned} \xi_{x,i,j} &= \frac{\xi_{i+1,j} - \xi_{i,j}}{\Delta x} \\ \xi_{y,i,j} &= \frac{\xi_{i,j-1} - \xi_{i,j}}{\Delta y} \\ \xi_{xx,i,j} &= \frac{\xi_{i+1,j} - 2\xi_{i,j} + \xi_{i-1,j}}{\Delta x^2} \\ \xi_{yy,i,j} &= \frac{\xi_{i,j-1} - 2\xi_{i,j} + \xi_{i,j-1}}{\Delta y^2} \\ \xi_{xy,i,j} &= \frac{\xi_{i+1,j+1} + \xi_{i-1,j-1} - \xi_{i+1,j-1} - \xi_{i-1,j+1}}{4\Delta x \Delta y} \end{aligned} \tag{4.17}$$

Here, as before $\xi_{x,i,j}$ and $\xi_{y,i,j}$ are the first order derivative at pixel (i, j) of the acoustical property of interest ($c(r)$ or α_0) in the x or y direction of the Cartesian grid. Analogously, $\xi_{xz,i,j}$, $\xi_{yy,i,j}$ and $\xi_{xy,i,j}$ are the second order derivative at pixel (i, j). The term θ is employed to ensure TV term is continuously differentiable in all the domain.

4.2.3 Implementation of the optimization algorithm

In order to integrate the modified version of the k-Wave-CUDA, the entire optimization algorithm, i.e. the body of the USCT-k-Wave, was implemented in C++. To calculate the

gradients of the error functional, the fractional Laplacian terms that appear in the functional gradient of the error functional with respect to the attenuation coefficient (Eq. 4.14) were also implemented in CUDA, using the Fourier pseudo-spectral method, as in Eq. 4.15.

After the gradient calculation, a backtracking line search algorithm is employed for the gradient minimization process until the convergence criterion is satisfied. The whole process was illustrated in the flow chart depicted in Fig. 4.3.

4.2.3.1 Stopping criteria

The convergence criterion employed, as explained in Chapter 1 was the slope of a line fitted to the norm of the global error, as a function of the image updates. The reconstructions were stopped when the slope for an entire iteration (in this case 50 image updates) was less than 0.1.

4.2.4 Description of numerical experiments

In order to test the performance of the algorithm proposed, simulated data from two numerical phantoms generated using typical values of SS and AA, in water and in several constituents of breast tissues [Hasgall et al., 2015, Szabo and Wu, 2000, Duck, 2013]. The USCT geometry was a ring array of radius 54 mm with N=200 uniformly distributed transducers. The simulations were conducted on a $128 \times 128mm^2$ grid represented by 256×256 grid points with a 20 grid points perfectly matched layer positioned outside the domain [Treeby and Cox, 2010b]. The simulations to obtain the reference data were performed sequentially from emitter 1 to 200 using all 200 receivers for each transmitter.

The pressure field at the positions of the detector in Cartesian space was calculated from the pressure at grid points at each time step via linear interpolation. The transmitted signal was a Gaussian enveloped 3-cycle sinusoidal tone burst with a 1 MHz central frequency. The signals were sampled for 854 time points with a time step of 100 ns. The simulation time for each projection for a single emitter was 0.43 seconds using a core of an Intel Core i7-3930K CPU 3.20 GHz with an NVIDIA GeForce GTX 780 GPU.

Each image update was performed using the functional gradient estimated from four emitters, i.e., the total data was divided into 50 subsets. Based on initial tests, this number of subsets provides a significant improvement in the total reconstruction time ($\sim 50\ x$ with respect to the use of 1 subset, i.e., using all the data in each image update), without introducing artifacts in the reconstruction. One full-iteration, using the signals from all 200 emitters, consists of fifty image updates.

4.2.4.1 Reconstruction of an ideal case

First, a very simple numerical phantom consisting of a homogenous map of water covering the whole field-of-view with two centered spots with either a change in sound speed or absorption was investigated (Fig. 4.5). In this example, the image was reconstructed from noiseless data, and no regularization was employed. This allows to evaluate the limits of the reconstruction method. The SS distribution was reconstructed as described in Sec. 4.2.2 using a FBP reconstruction for the initial SS distribution. The FBP-SS image is shown in Fig. 4.5 (b) and was obtained in 0.3 s. As the goal of this ideal case was to test the limits of the algorithms, the actual map of AA was employed when updating the SS distribution. Similarly, the AA distribution was reconstructed using the actual map of the SS (although in this case the SS is reconstructed perfectly), and a FBP reconstruction for the initial AA distribution. The FBP-AA image is shown in Fig. 4.5(e) and was also obtained in 0.3 s.

4.2.4.2 Reconstruction of a realistic simulated breast phantom

A numerical phantom with several structures simulating breast tissue was also investigated (see Figs. 4.6 and 4.7). After the forward simulation, random Gaussian noise was added to the recorded data to give a signal-to-noise ratio (SNR) of 50 dB. This is higher than the SNR achievable with our experimental TOPUS-USCT prototype. Due to the presence of noise in the data, the TV-based edge-preserving regularization was employed in the reconstructions. In this case, the parameters μ and θ (see Eqs. (9) and (10)) were set to μ = 9e-6 and $\theta = 0.2$ for the SS regularization, and μ = 1e-8 and $\theta = 0.2$ for the AA regularization. These values gave adequate artifact control without significantly compromising the image quality.

To quantify the quality of the reconstructions as it was explained in Chapter 1, the mean and standard deviation of the ROIs indicated in Fig. 4.6(a) were obtained and compared with the expected values (see Table 4.4). The noise level and bias of the reconstructed images were also calculated for each ROI. Furthermore, profiles across the reconstructed distributions were examined to estimate the resolution of the reconstructed images,computing response at edges to rise from 10% to 90%. This parameter was calculated at the phantom-water interface.

4.3 Results and discussion

The results of the reconstruction of the SS and AA maps for the ideal case discussed in section Sec. 4.2.4.1 are shown in Figs. 4.5(c) and (f). One-dimensional profiles across the reconstructions are shown in Figs. 4.5(g) and (h). In this ideal case, the method is able to achieve a perfect recovery of the margins and values of both the SS and AA distributions. This shows the capability of the algorithm to obtain the correct solution for both distributions in the absence of noise and when the alternate acoustic distribution is available (i.e., the AA to recover the SS and vice versa). It also demonstrates the advantages of the FWI formulation over ray-

tracing algorithms. The reconstruction of each acoustical property in this example was obtained in 27 minutes using 2 iterations.

The reconstructed SS and AA maps for the realistic case introduced in section Sec. 4.2.4.2 were obtained within two iterations (27 minutes). As it can be seen in Fig. 4.6(c), the SS distribution can be recovered with high accuracy. The bias between the reconstructed and expected values is below 0.5% in all ROIs (see Table 4.4). Moreover, the regularization employed in the reconstruction algorithm allows the influence of the noise to be ameliorated effectively. The noise levels are below 0.9% in all ROIs and the edges of the different structures are preserved. The resolution was estimated as 1 mm, which is close to the wavelength at the central frequency of the signals.

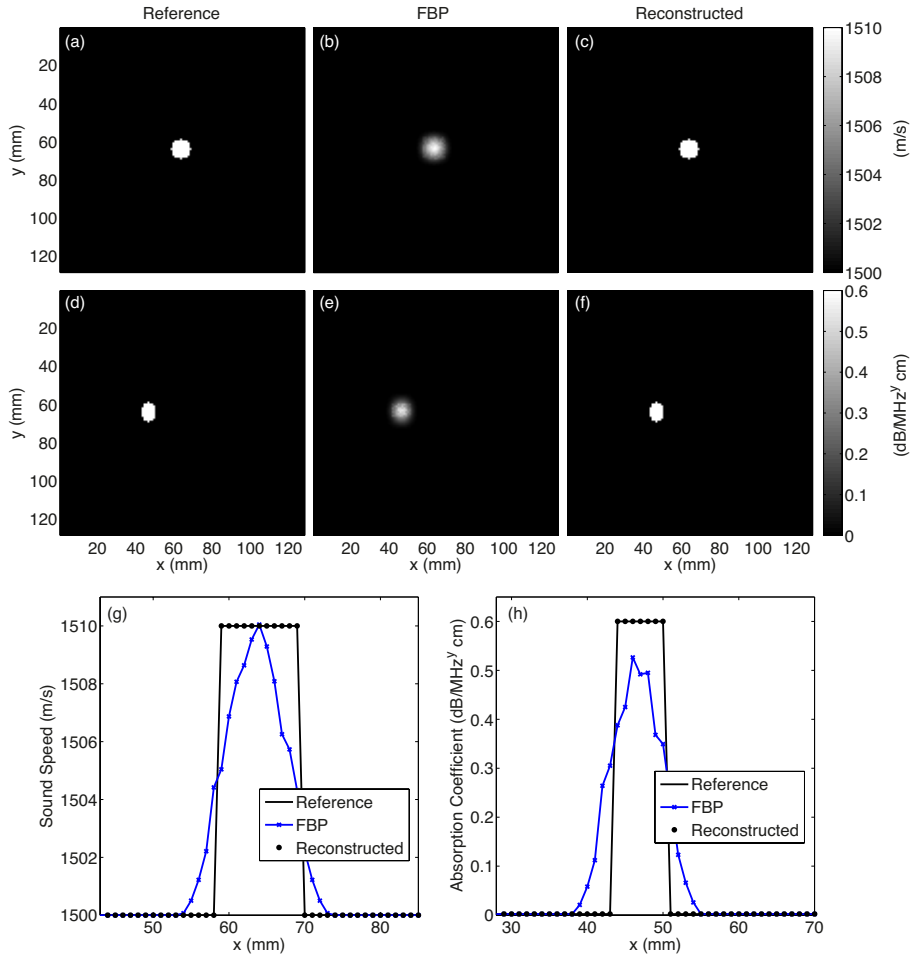

Figure 4.5: Reconstruction of a noiseless ideal case. (a) Reference speed of sound (SS) map. (b) Initial SS map reconstructed using filtered back projection (FBP). (c) Reconstructed SS map. (d) Reference acoustic attenuation (AA) map. (e) Initial AA map reconstructed using FBP. (f) Reconstructed AA map. (g) Profiles through the SS maps for the reference, FBP initial guess, and reconstructed image at the line y = 64 mm. (h) Profiles through the AA maps for the reference, FBP initial guess, and reconstructed image at the line y = 64 mm.

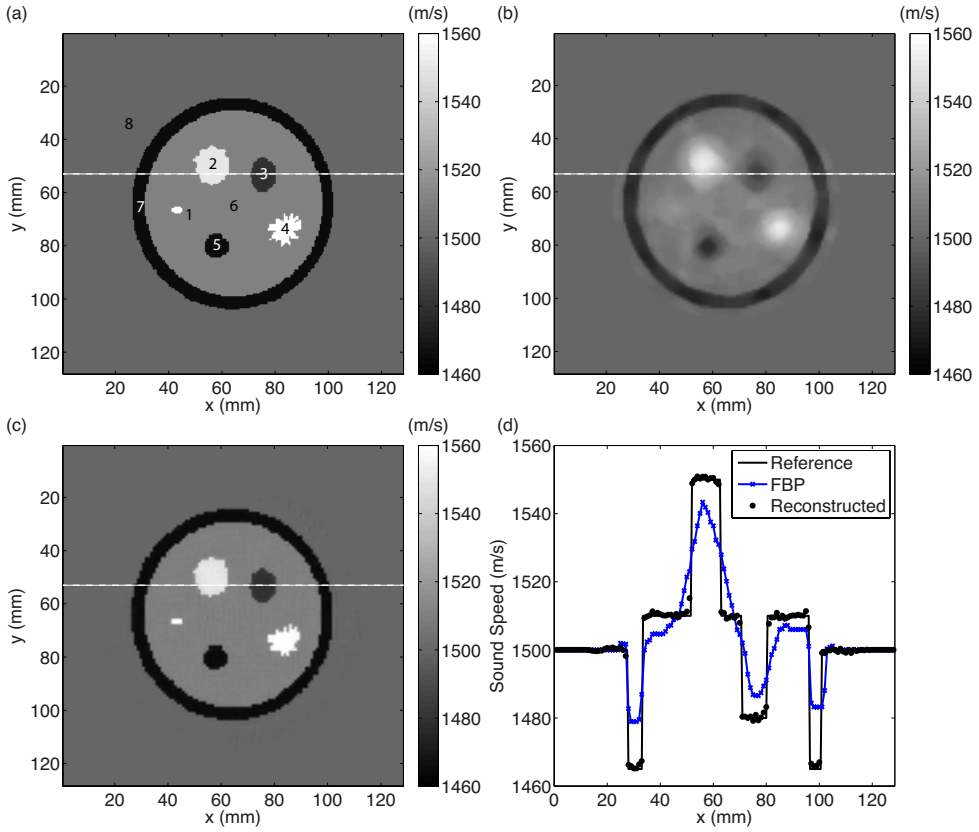

Figure 4.6: Reconstruction of the speed of sound (SS) for a breast phantom. (a) Reference SS map. The numbers correspond to regions of interest (ROIs) given in Table 1. (b) Initial SS map reconstructed using filtered backprojection (FBP). (c) Reconstructed SS map. (d) Profiles through the SS maps for the reference, FBP initial guess, and reconstructed image at the line y = 53 mm (shown with the white dashed line)

In comparison, the reconstructed AA distribution is more sensitive to noise and strongly dependent on any errors obtained in the reconstructed SS distribution Fig. 4.7. There are two contributing factors. First, errors in the sound speed map will affect the trajectory of the propagating waves, and consequently the attenuation experienced between the source and emitter pairs. Second, for the misfit function given in Eq. 1.41, the differences between the simulated and observed signals due to acoustic attenuation are much smaller than the differences due to time misalignments from changes in sound speed, i.e., the selected cost function is much more sensitive to variation in SS than AA [Tejero et al., 2015]. This may be an important limitation when the noise is comparable to the differences between simulated and observed signals due to attenuation, as in this case the adjoint source will be dominated by noise. This highlights that accuracy of the AA estimate is very sensitive to the SNR and the accuracy of the reconstructed SS map.

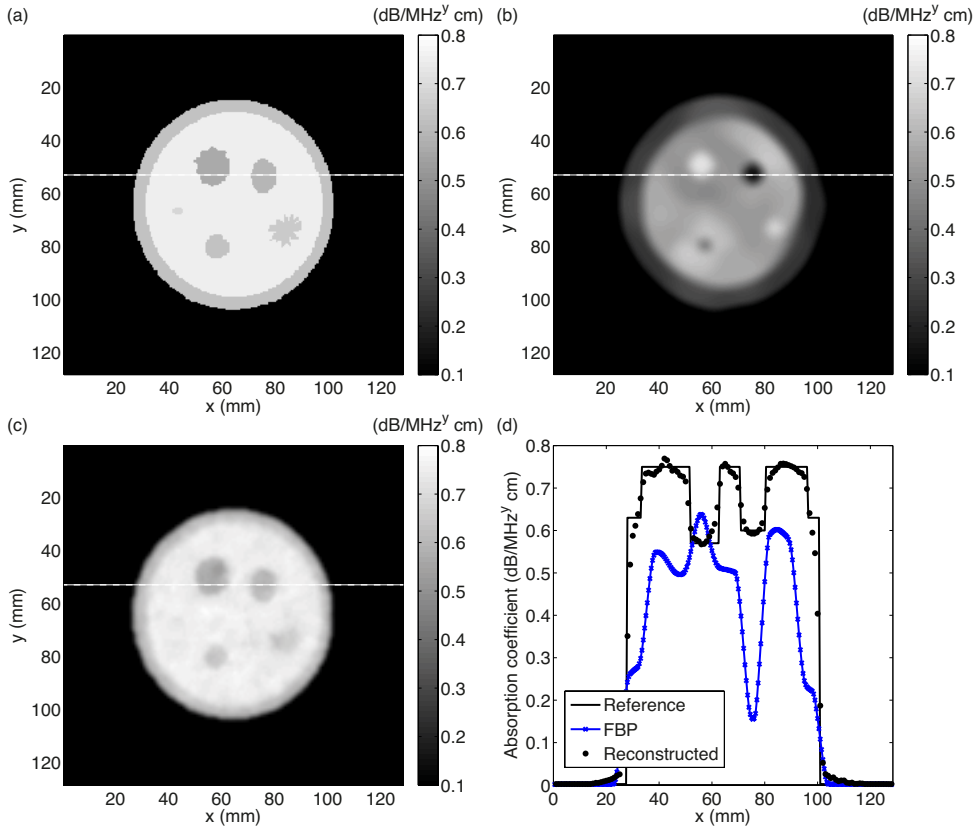

Figure 4.7: Reconstruction of the acoustic attenuation (AA) for a breast phantom. (a) Reference AA map. (b) Initial AA map reconstructed using filtered back projection (FBP). (c) Reconstructed AA map using the converged SS map. (d) Profiles through the AA maps for the reference, FBP initial guess, and reconstructed image at the line y = 53 mm (shown with the white dashed line)

In this example, the maximum noise level in the reconstructed AA map was 18% and the bias between simulated and expected values in the selected ROIs was typically below 10%. The exception is within water (ROI 8) where higher estimated values were obtained. This is due to the very small attenuation coefficient in water, and the large difference in AA values with respect to the other soft tissues. A possible extension would be to identify the water region from the SS map, and use this to constrain the reconstruction of AA. The estimated resolution in the reconstructed AA map was 6 mm.

For reference, these results can be compared to the performance of a frequency domain formulation of the adjoint field to obtain the functional gradients for SS and AA. For example in Li et al. [2014], both SS and AA distributions were investigated using a numerical phantom and noiseless data. For the SS, similar resolution can be obtained using both formulations (on the order of the acoustic wavelength). For AA case, the performance of both methods is also similar [Li et al., 2014, Sandhu et al., 2016, Pratt et al., 2007] and the reconstruction is, as reported here, dependent on the errors in the reconstructed SS distribution. Therefore, noisy

distributions are obtained as a result for AA with both methods. One distinct advantage of the time domain formulation is that it avoids having to select the right set of frequencies to be inverted and the appropriate number of iterations to perform at each frequency. This seems to be a key requirement of the frequency domain formulation to mitigate the ripples encountered in the reconstructed distributions [Li et al., 2014, Sandhu et al., 2016].

4.4 Conclusions

In this chapter, a time domain FWI algorithm for the reconstruction of both SS and AA distributions in ultrasound computed tomography is proposed. The algorithm is based on an adjoint formulation derived from the fractional Laplacian wave equation, and allows both distributions to be efficiently reconstructed within a common framework. The performance of the algorithm is shown with two numerical examples. In the ideal case of noiseless data, given the exact distribution of the alternate material parameter (i.e., AA to recover SS, and SS to recover AA), both AA and SS distributions can be reconstructed exactly. In the more general case using a realistic geometry, Gaussian noise added to the reference signals, and a FBP reconstruction for the initial estimations, the proposed algorithm is capable of recovering accurately the shape and values of the structures in the image.

Compared to ray-tracing algorithms, these results shown significant improvements in resolution and accuracy. Moreover, comparison of the resolution and noise with previous studies based on frequency domain algorithms supports the equivalence of both formulations. However, the time domain formulation presented here avoids the need to select the appropriate set of frequencies, a step required by the frequency domain formulations. The main limitation is the high dependence of the AA reconstruction on any errors present in the reconstructed SS and noise in the signals. It would be also useful to explore other possible ways to define the misfit function to mitigate this problem. While the convergence rates for the current study are reasonable, the use of other optimization schemes might also increase the rate of convergence. The application of this method for the reconstruction of real data, and the extension to 3D will be explored as part of future work.

Table 4.1: Mean values, standard deviation, noise, expected values and bias at the ROIs shown in Fig. 4.6(a) for the speed of sound (SS) and the acoustic attenuation (AA) distributions.

	ROI number	Mean value (m/s)	Standard deviation	Noise (%)	Expected value (m/s)	Bias (%)
	1	1481.47	4.43	0.30	1480	0.10
	2	1555.56	11.25	0.72	1560	0.28
	3	1467.30	7.72	0.53	1470	0.18
SS	4	1561.97	14.00	0.90	1570	0.51
	5	1548.41	6.07	0.39	1550	0.10
	6	1510.19	0.68	0.05	1510	0.01
	7	1467.01	6.82	0.46	1470	0.20
	8	1499.90	0.24	0.02	1500	0.01
		Mean value (dB/MHz cm)			**Expected value (dB/MHz cm)**	
	1	0.626	0.028	4.47	0.60	4.33
	2	0.674	0.022	3.26	0.65	3.69
	3	0.657	0.025	3.81	0.63	4.29
AA	4	0.724	0.003	0.41	0.68	6.47
	5	0.591	0.035	5.92	0.57	3.68
	6	0.756	0.011	1.46	0.75	0.80
	7	0.565	0.103	18.23	0.63	10.32
	8	0.005	0.001	20.00	0.0022	127.27

Chapter 5

Generalized cost function for FWI in USCT

5.1 Introduction and motivation of the chapter

In Chapter 4 it was shown that full-wave inversion (FWI) algorithms achieve USCT images with high spatial resolution by solving the full wave equation describing the propagation of ultrasound waves in tissue. We also showed that the reconstruction of sound speed (SS) maps with FWI methods based on the minimization of the least-squares functional provides high-resolution SS images. Nevertheless, with the least-squares misfit, reconstruction of acoustic attenuation (AA) maps is more challenging than the reconstruction of SS maps. This is because this misfit function is more sensitive to variations in the phase of the signals than to their amplitude. This makes reconstructions of AA significantly biased when SS maps employed in AA reconstructions are not perfectly estimated, as occurs in real cases.

In the previous chapter we showed that, regularization reduces the effect of propagation of errors from SS map into the AA map. But, this is usually not enough, and regions where the SS maps are biased (mainly at the edges of the structures) present artifacts in the AA map, even after regularization.

Ideally, what we would need to solve this problem is to find a way of decreasing the phase dependence on the cost function. One other possible solution is to force the temporal alignment between simulated and observed time signals and then compare them using the standard least-squares cost function. However, this method has two main problems: First, if the process to obtain the SS map was finished correctly, at the end of the reconstruction the waveforms will present temporal delays comparable or even shorter than the time bin of the time signals (see Fig. 5.1). Consequently, we will need to interpolate the signals to get shorter temporal bins in order to find the correct time delay that aligns the waveforms. After that, we would need to downsample the resulting signal to match the ones from the simulations. The mentioned process will increase considerably the computational cost of the reconstruction and also, it is

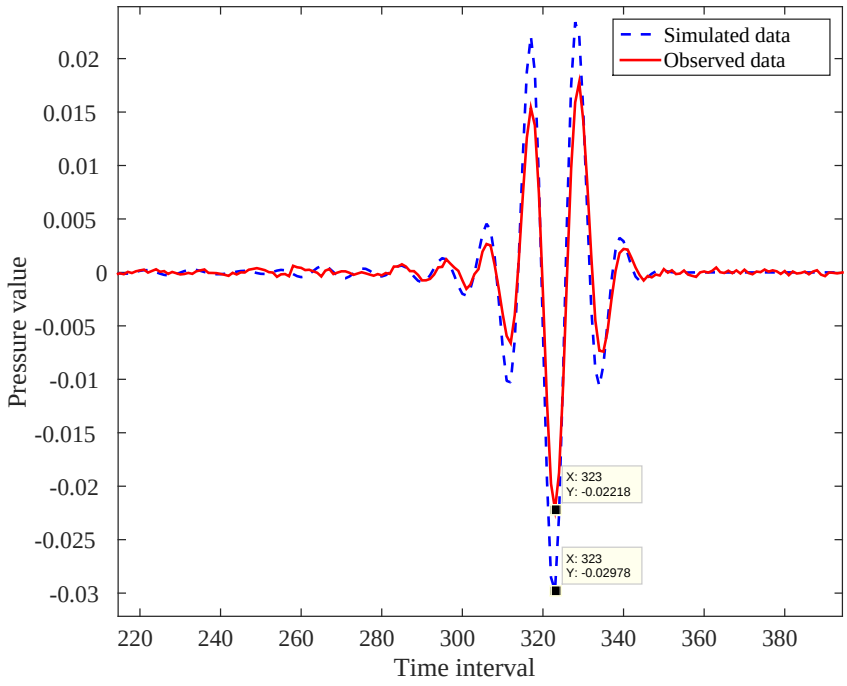

Figure 5.1: Comparison of simulated and observed waveforms after sound speed (SS) reconstruction. The resulting time-dalay between both waveforms is shorter than the temporal bin size employed in the simulation.

difficult to know in advance how much it is necessary to shorten the time bin in order to ensure that the alignment of the signals is correct.

Besides, depending on the attenuating properties of the tissues crossed by the wave and the direction of propagation, the frequency spectrum of the wave can be modified. This causes waveform distortions and therefore, affects the measured TOF of the signals [Ragozzino, 1981].

Another more robust solution would be to modify the L^2 based cost function employed in order to reduce its phase dependence. The election of the misfit functional is extremely important when using adjoint based optimizations. Many different misfit functions for FWI have been proposed in the literature [Bozdağ et al., 2011, Tejero et al., 2015, Tromp et al., 2005a] in order to highlight different aspects of the ultrasonic wavefield. We present here the misfit function based on the travel-time and amplitude differences. These functionals look for the right offset that maximizes the cross-correlation between simulated and observed data [Bozdağ et al., 2011]:

$$\epsilon_{\top} = \frac{1}{2}\sum_{m=1}^{M}[T_m(\xi) - T_m^{obs}]^2$$
$$\epsilon_A = \frac{1}{2}\sum_{m=1}^{M}\left[\frac{A_m(\xi)}{A_m^{obs}} - 1\right]^2 \tag{5.1}$$

Where $\epsilon_{\top}$ and ϵ_A are the travel-time and amplitude misfit functions respectively. $T_m(\xi)$ is the estimated time of flight (TOF) of the waveform at the location of the receiver m with the acoustic model ξ (i.e the SS or AA) and T_m^{obs} is the observed TOF. Analogously, $A_m(\xi)$ and A_m^{obs} are the amplitude of simulated and observed waveforms.

These travel-time and amplitude misfit functions have demonstrated to be robust as initial estimations for iterative reconstructions [Pratt and Shipp, 1999]. This makes them useful to reduce the number of local minima in the objective function in comparison with the standard L^2 misfit [Chauris et al., 2012].The number of local minima when using the standard misfit is particularly high if the initial model for the reconstructions is very far from the actual one or contains details of great complexity [Pratt and Shipp, 1999]. In those cases, it is very likely to get stuck in erroneous solutions. A good approximation to solve this problem could be to employ the travel time misfit to obtain a closer initial guess, and after that, to continue with the standard FWI [Pratt and Shipp, 1999, Yuan and Simons, 2014]. This strategy avoids the need of mixing FWI with high-frequency geometrical acoustics algorithms to recover the acoustic parameters of the medium. The entire reconstruction can be performed with a single FWI algorithm.

Furthermore, the aforementioned functionals help isolating the effect of a single acoustic property in the signals measured. Therefore, these functionals make the optimization problem more convex as these misfits are more linearly dependent on relative SS or AA perturbations.

However, an inversion based on these error functionals yields poor resolution images because they are insensitive to much of the information contained in the waveform. This occurs because the same correction is applied along the entire banana-shaped sensitivity kernel that relates the emitter-receiver pair. For each emitter-receiver pair, the functional error these misfits provides is a constant value. In contrast, the standard least-squares misfit yields an independent correction for each time interval across the whole waveform length. In conclusion, each one of the error functionals that we have mentioned (i.e. travel-time, amplitude, least-squares) presents certain strengths and weaknesses depending on the conditions under which they are applied.

The aim of this chapter was to investigate methods to improve the stability of the reconstruction of AA and SS using only FWI algorithms. Specifically, we were interested in the modification of the cost function needed to stabilize AA reconstructions in cases when SS maps differ from the actual model in certain regions of the image.

5.2 Methods

In this section, we refer to modifications that have to be implemented to the reconstruction method presented in Chapter 4 in order to make it more robust. First, in subsection 5.2.1, we will refer to the main features of the proposed generalized misfit. Second, we will explain how the inverse problem has to be modified, in subsection 5.2.2. After that, in subsection 5.2.4 we will investigate the relative weights that each term of the misfit proposed should present. Finally, in Sec. 5.2.5 a numerical experiment to test the capabilities of the method will be presented.

5.2.1 The generalized cost function

As we have seen, the standard least-squares misfit function provides high resolution images, as specific corrections for each temporal interval are applied, but it may fail if the error functional is affected by more than one material property, especially if the initial estimations of tissue properties are slightly far from the actual values. Therefore, we propose a generalized misfit function [Pérez-Liva et al., 2017] which combines the effect of the standard least-squares misfit, with the amplitude misfit functional and the travel time misfit.

With the combination of these functionals, our main objective is to make more convex the optimization problem for AA helping its convergence and making the reconstruction process more independent on possible errors in the estimated SS map. Additionally, we aim to a unique framework to perform FWI reconstructions without other type of acoustic approximations to wave propagation.

The cost function we propose to make the reconstruction of AA distributions more robust against deviations from the real SS model is given by:

$$\begin{aligned} \epsilon' &= \frac{1}{2}\sum_{m=1}^{M}\{\alpha\epsilon + \beta\epsilon_A + \gamma\epsilon_\perp\} + \mu R_{TV} \\ \epsilon &= \int_0^T [p(\mathbf{r}_m,t) - p^{obs}(\mathbf{r}_m,t)]^2 dt \\ \epsilon_A &= \left(\frac{A_m}{A_m^{obs}} - 1\right)^2 \\ \epsilon_\perp &= [T_m(\xi) - T_m^{obs}]^2 \end{aligned} \tag{5.2}$$

Here A_m and T_m are selected with the maximum-based methods presented in Chapter 3.

With this generalized misfit function we improved our FWI method of reconstruction in two directions:

- *SS reconstruction*: In this case, the reconstruction is initiated with only the travel-time misfits (i.e. α and β are set to zero, γ is set to 1) and only a few image updates are done, with a high level of subsets (in this case, we have seen that using a few image updates a good initial image can be obtained). In this case, the initial AA model employed can be just a homogeneous map of acoustic absorption of water. After that, we continue using the standard misfit function (i. e. $\beta = 1$ α and $\gamma = 0$) and the process is analogous to the one describe in Chapter 4.
- *AA reconstruction*: In this case, we combined amplitude and standard misfit functions, i.e. α =1, β different from zero, γ is set to 0.

To illustrate the performance of the misfit proposed in AA reconstructions, we present a numerical example similar to the one in Chapter 4, Sec. 4.2.2. We calculated the functional errors ϵ and$\epsilon^{'}$ (standard and proposed in this work Eq. (5.2)) for pulses delayed in time and modified in amplitude with respect to a reference signal, with fixed amplitude and time delays. This is equivalent to consider modifications in the TOF and amplitude of the signals due to modifications in the SS and AA maps of the medium. $\beta = 10$ and $\gamma = 0$ were employed in this test to evaluate the generalized misfit. The results are shown in Fig. 5.2.

As we demonstrated in Chapter 4 and illustrated in Fig. 5.2, when using the standard misfit function ϵ, it is crucial to use an initial estimate of SS very close to the real one before updating the AA distribution. With this misfit function it is not necessary that the initial guess for AA be very close to the actual one. In a similar way, the reconstruction of AA can not be performed with a rough initial SS model. On the other hand, the proposed error functional ϵ' does not require the exact value of SS in order to reach its actual minimum with respect to AA (Fig. 5.2. It makes the problem more convex in all the directions. Thanks to the fact that we are combining the properties of both functionals, some care should be taken when selecting the initial guess of SS for AA updating, as values very far from real ones can maximize the error instead of minimizing it (see Fig. 5.3).

5.2.2 Forward problem

As our method is based on the FWI reconstruction of USCT data, we used, as in Chapter 4, the solution of the Fractional Laplacian Wave Equation to simulate the propagation of acoustic waves in the medium. Analogously as before, the computational method to solve this problem was based on a modified version of the software k-Wave, written in Cuda and C++.

5.2.3 Inverse problem

In this section we used the same methodology of the adjoint method presented in Chapter 1, and explained in more detail with its combination with the Fractional Laplacian wave equation in Chapter 4. When the equations to calculate the gradients of the error functional are exchanged with the corresponding to the generalized misfit, the expression of the gradients

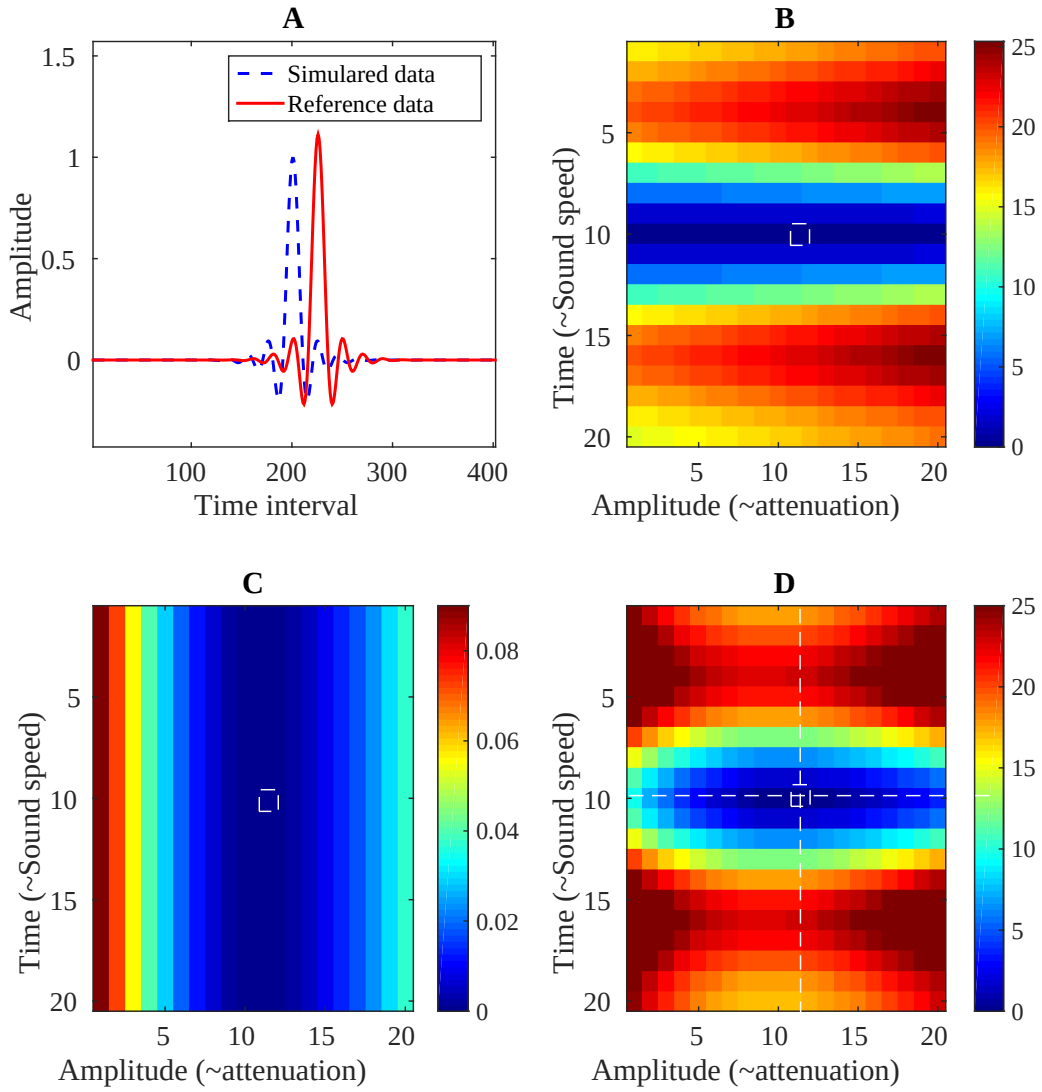

Figure 5.2: A. Example of simulated signals showing global error behavior with different misfit functions. Example of the global error behavior around actual Time of Flight and Amplitude values for a homogeneous distribution of acoustic material. B. Result obtained with the standard squared sum misfit function. C. Results obtained with the proposed misfit function. The intersection of the true values (which corresponds to the global minimum) is shown with a white dashed square.

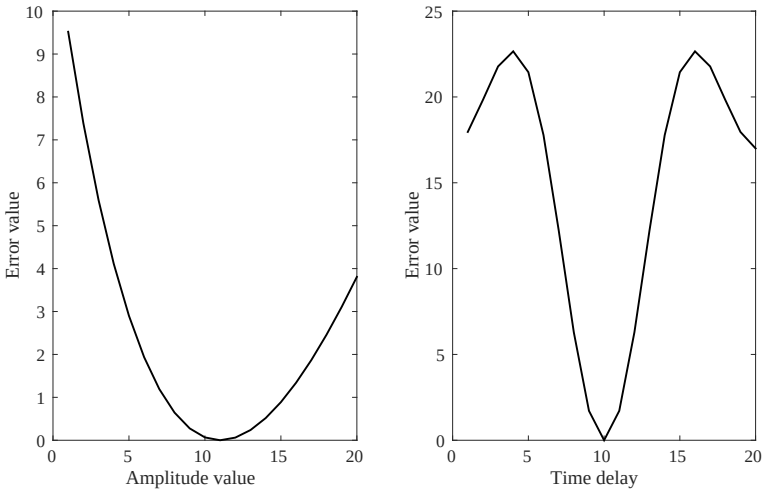

Figure 5.3: Profiles accross x (left) and y (right) axes of the error map given in Fig. 5.2 for the misfit functional proposed

to update SS and AA do not present any modification. We rewrite both gradients here for the sake of clarity.

$$\frac{\partial \varepsilon}{\partial c} \simeq \int_0^T \frac{2}{c^3}\left(\frac{\partial^2 p}{\partial t^2}\right) p*(T-t)dt + \mu \nabla R_{TV} \tag{5.3}$$

$$\frac{\partial \varepsilon}{\partial \alpha_0} = \int_0^T p^*(\mathbf{r}, T-t)\left[-2c^{y-1}(-\nabla^2)^{\frac{y}{2}}\frac{\partial}{\partial t}\right.$$
$$\left.+2c^y tan\left(\frac{\pi y}{2}\right)(-\nabla^2)^{\frac{y+1}{2}}\right] p(\mathbf{r}, t)dt + \mu \nabla R_{TV} \tag{5.4}$$

The new term included in the error functional modifies the expression of the adjoint source that generates the adjoint field (p^*). The new adjoint source is given by:

- *SS reconstruction*:

$$S^*_{\top}(\mathbf{r}, t) = \sum_{m=1}^{M} \alpha(\mathbf{r}_m, T-t) - p^{obs}(\mathbf{r}_m, T-t)]w(T-t)\delta(\mathbf{r}-\mathbf{r}_m)+$$
$$+\gamma \sum_{m=1}^{M}(T_m(\xi) - T_m^{obs})w(T-t)\frac{1}{N_m}\frac{\partial}{\partial t}p(\mathbf{r}_m, T-t)\delta(\mathbf{r}-\mathbf{r}_m) \tag{5.5}$$

Where w is a time window chosen to analyze only the desired part of the signals, and $p(\mathbf{r}_m, t)$ is the simulated pressure field at the receiver m in the total time interval t. The

term T is the length of the time interval in which the measurements are recorded. In this case, the terms are switched to obtain initial image or final reconstructed image, as we have explained above.

- *AA reconstruction*:

$$S^*(\mathbf{r},t) = \sum_{m=1}^{M}[p(\mathbf{r}_m, T-t) - p^{obs}(\mathbf{r}_m, T-t)]w(T-t)\delta(\mathbf{r}-\mathbf{r}_m)+ \\ +\beta\sum_{m=1}^{M}\left[\frac{A_m^{obs}}{A_m}-1\right]p(\mathbf{r}_m, T-t)w(T-t)\delta(\mathbf{r}-\mathbf{r}_m) \tag{5.6}$$

The scheme of this reconstruction is very similar to the one presented in Chapter 4, but with the upgraded expressions for the error functional and the adjoint source (see Fig. 5.4):

1. To reconstruct the SS, we first use homogeneous SS and AA maps as initial guesses. After that, with only the travel-time misfit term turned on ($\gamma = 1, \alpha, \beta = 0$) in the generalized cost function we initiated the optimization process. To be able to obtain the initial SS image in a short time, we used only a small set of the total number of sources available. In this case, we only employed 50 evenly spaced sources from the total. Using that set of sources, we performed a full iteration with only one image update (1 subset). Note that this is different to the criteria explained in Chapter 4 to defined subsets, because in that case we only divided the emitters in subsets but all the receivers were employed. Here we used 50 emitters that also acted as receivers. Another important difference here with the scheme employed in the previous chapter lies in the calculation of the adjoint source using Eq. 5.5. With the updated SS obtained from this procedure, we continue to reconstruct the SS using only the standard misfit turned on, as explained in Chapter 4.
2. Once the SS image is obtained, it is used as initial model to update the AA distribution with standard and amplitude misfit functions turned on here ($\alpha, \beta > 0$ and $\gamma = 0$). This scheme of reconstruction is very similar to the one used in Chapter 4 with the difference in the calculation of the adjoint source using Eq. 5.6. The remainder of the reconstruction scheme is analogous as for the SS update.

With respect to the number of subsets, as we were just interested in testing the features of the misfit function without the influence of any other variable, this number was set to 1 (i.e only one image update per iteration using all available emitters). The image is iterated until small slope of the error curve against the number of iterations is reached.

5.2.4 Description of numerical experiments

In order to test the performance of the misfit function proposed, we employed the same numerical phantom of Chapter 4, Sec. 4.3. This simulated numerical phantom had several structures mimicking breast tissue. After the forward simulation, random Gaussian noise was added to yield a signal-to-noise ratio (SNR) of 40 dB. The USCT geometry was a ring array

of radius 54 mm with N=200 evenly spaced transducers. At difference with the numerical experiment performed in Sec. 4.3, here the transmitted signal used was a Gaussian-enveloped 3-cycle sinusoidal tone burst with 0.5 MHz central frequency. The reason to employ a lower central frequency than the one employed in the previous chapter, was to increase the errors around the edges of the reconstructed SS distribution (as the resolution depends on the wavelength). Besides, we aimed for speeding reconstruction time of our numerical experiment. The simulations in this case were conducted on a 128 mm x 128 mm grid represented by 128 x 128 grid points with a 10-grid point perfectly-matched layer positioned outside the domain. Under the conditions mentioned the simulation time for each projection for a single emitter was 0.23 seconds using one core of an Intel Core i7-3930K CPU @ 3.20GHz with an NVIDIA GeForce GTX 780 Ti GPU.

To quantify the quality pf the reconstructions, the mean and standard deviation of the pixel values within several regions of interest (ROIs) inside the lesions and structures of the numerical phantom were obtained and compared to the expected values in those ROIs.

5.2.5 Weights in the generalized misfit for AA reconstruction

The relative weight of both terms used in the proposed misfit function to reconstruct AA is basically controlled by a parameter β, as we fixed α=1. With $\beta = 0$, we recover the AA with the standard method, which is able to obtain high-resolution AA maps if the SS map is perfectly known, but creates significant bias when there are deviations in the estimated SS map. With β » 1, the amplitude misfit function is used, obtaining unbiased, but low-resolution images.

In order to study how to identify the appropriate value for β, the ones providing a good trade-off of bias and resolution we used the numerical phantom described in the above section. The ROI 1 in Fig. 4.6 as we mentioned in the discussion of Chapter 4, is one of the regions most affected of the phantom due to wrong estimations of SS in this region (the size of this region is comparable to the wave length in the medium that determines the achievable resolution). The effect of the borders in this region makes the values of AA very difficult to estimate accurately. Therefore, we used the bias obtained in this region, when the reconstruction is performed with several values of β, as a metric of the quality of the images. The results of this test are presented in Fig. 5.5.

Even when this parameter can be further refined, the value $\beta = 10$ provides an adequate reduction of the bias in this region. Nevertheless, as α and β are relative values, and they will depend on the scale of the terms of the gradient, it is advisable to calculate these parameters for each specific propagator model employed.

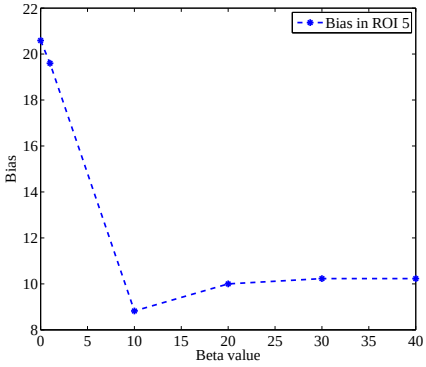

Figure 5.5: Bias behavior in ROI 1 (see Fig. 4.6) for different β values (see Eq. 5.2)

The effect of this parameter can be better understood with a comparison of the individual functional gradients given by the standard and amplitude misfits in 5.2 at the first iteration (see Fig. 5.6 (a and b)). The standard misfit provides a term for the gradient, that is around one order of magnitude lower than the one provided by the amplitude misfit. As we can see in the colorbar scale of these figures, with β=10 the relative importance of both terms is comparable. Another important information this figure provides, is the different levels of resolution that both terms contribute to the reconstruction process.

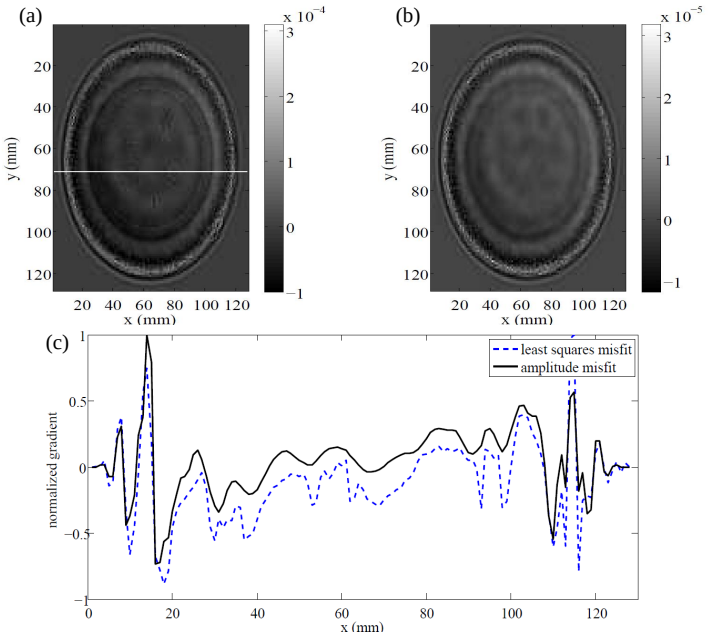

Figure 5.6: Gradient at first iteration obtained with (a) the standard misfit and (b) the amplitude misfit. (c) Normalized profiles compared along y = 64 mm in both maps. The amplitude misfit provides a low resolution version of the standard misfit.

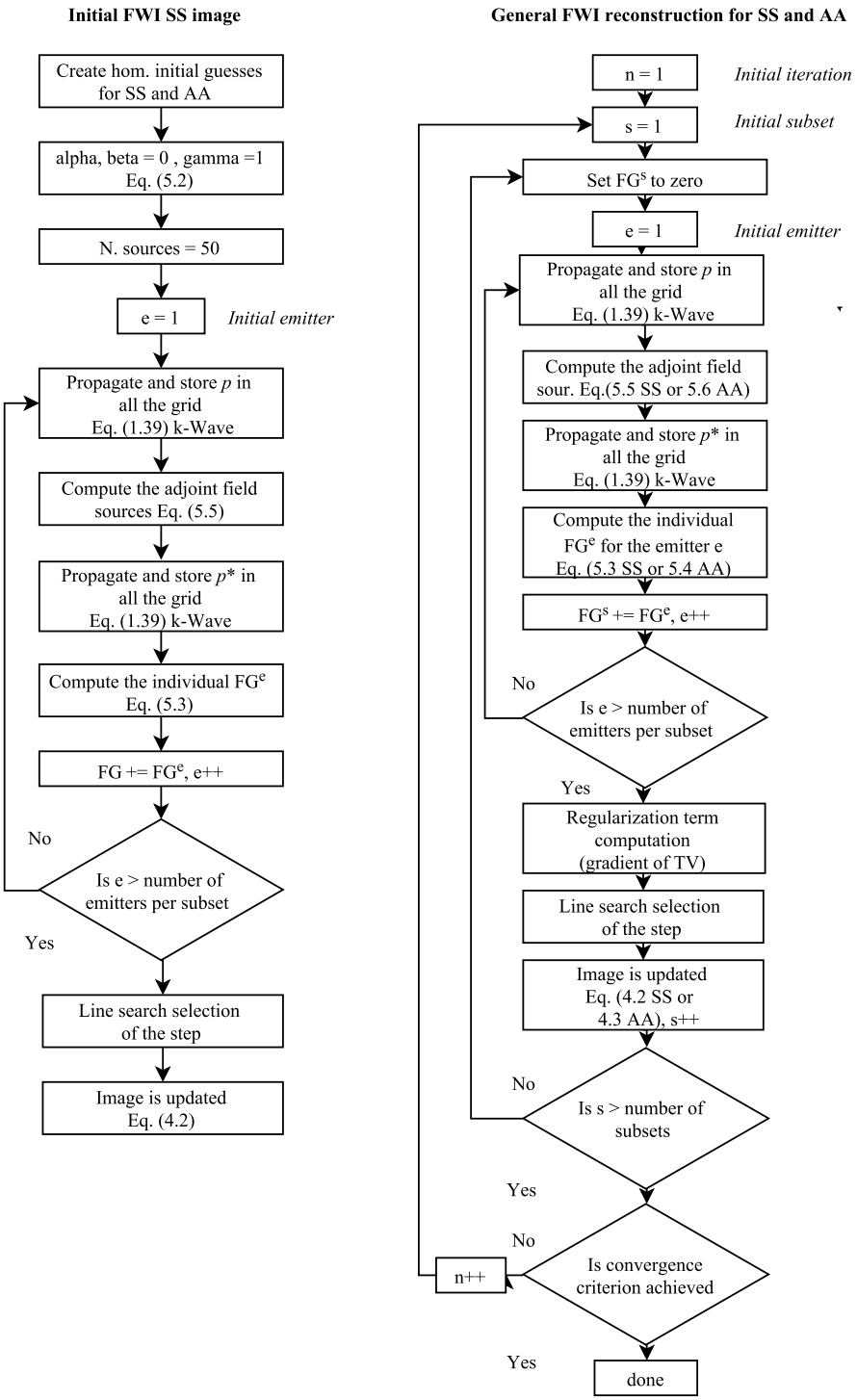

Figure 5.4: Flow chart of the reconstruction algorithm used to update the sound speed (SS) and acoustic attenuation (AA) distributions when the proposed misfit is employed. Left scheme to obtain the initial guess for SS reconstructions. Right General process

5.3 Results and discussion

The initial image reconstructed using the travel-time term included in the generalized misfit function was obtained in $\sim$ 1 minute with the reduced set of detectors explained in Sec. 5.2.3. This process just added a little extra time to the total reconstruction compared to the use of the FBP image as initial estimation (see Chapter 4). The image can be seen in Fig. 5.7. It provides in general an adequate amount of information of the actual map.

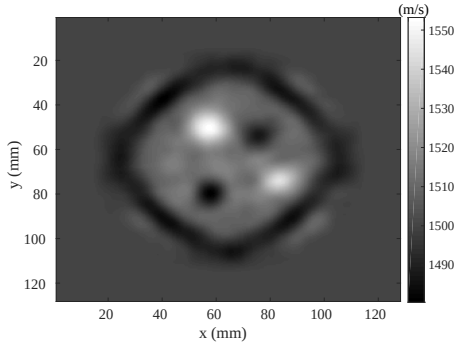

Figure 5.7: Initial image reconstructed with the travel-time term included in the generalized misfit function propoed in this chapter.

Figs. 5.8 A and B show the reconstructed SS distributions and the comparison of profiles between the reference and reconstructed images. This figure shows how small differences in the SS map create a significant bias in the AA map when using the standard least-squares misfit function (Fig. 5.9 B with respect to the reference AA map given 5.9 A). On the other hand, the method proposed reduces this bias (Fig. 5.9 C) considerably. The reduction of this bias can be seen in more detail in Table 5.1.

The most significant result that we can see in Table 5.1 is the homogenization of the bias, i.e. all the bias values obtained with the proposed misfit vary less than the ones obtained with the standard misfit. This means that our objective of making the reconstruction more independent on the SS map was achieved. Therefore, the proposed misfit is capable of making the reconstruction of the AA distribution more robust with respect to deviations in the SS map that normally appear in the reconstruction process. The improvement achieved depends on the characteristics of the evaluated region, because the bad behavior the least-squares misfit function is remedied in a large extent but not completely removed.

One downside of this method is that some loss of edges' information is produced, but in exchange, the real values of AA in the different structures of the phantom are improved.

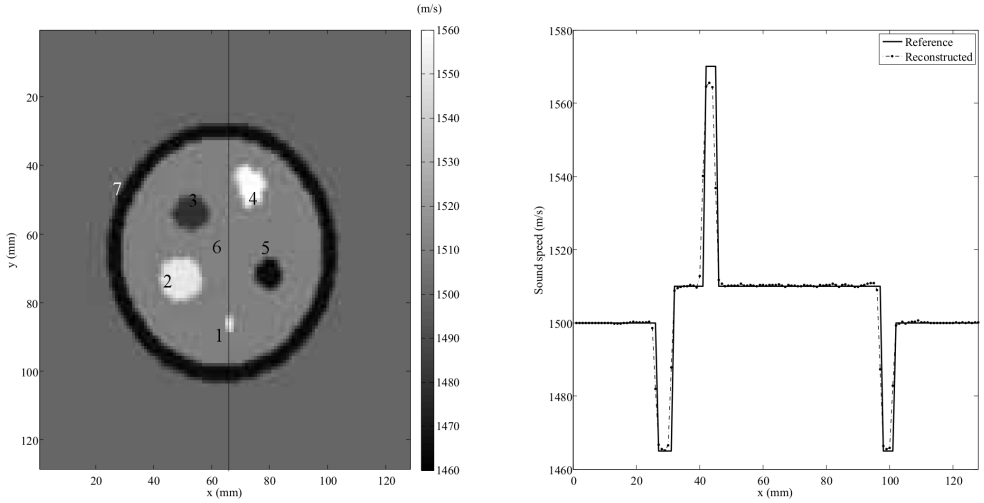

Figure 5.8: Left. Reconstructed sound speed (SS). Right Profiles comparison between the reconstructed and reference maps.

The use of the total variation regularization (TV) term, as we can see in the reconstructions improve the quality of the reconstructed images making it more piece-wise constant. However, as we pointed out at the beginning of this chapter, TV is not able of removing complete errors from the reconstructed SS map.

Table 5.1: Mean values and standard deviation for the reconstructed attenuation images using the standard least square and the proposed misfit functions

		Standard misfit function			**Proposed misfit function**		
ROI number	**Expected value** $(dB/(MHz^y cm))$	**Mean value** $(dB/(MHz^y cm))$	**Standard deviation**	**Bias** (%)	**Mean value** $(dB/(MHz^y cm))$	**Standard deviation**	**Bias** (%)
1	0.68	0.82	0.06	20.59	0.74	0.01	8.82
2	0.57	0.63	0.05	10.53	0.62	0.03	8.77
3	0.6	0.66	0.02	10.00	0.65	0.02	8.33
4	0.65	0.70	0.05	7.69	0.69	0.02	6.15
5	0.63	0.67	0.04	6.35	0.67	0.02	6.35
6	0.75	0.7400	0.0005	1.33	0.751	0.001	0.001
7	0.63	0.59	0.05	6.35	0.57	0.05	9.52

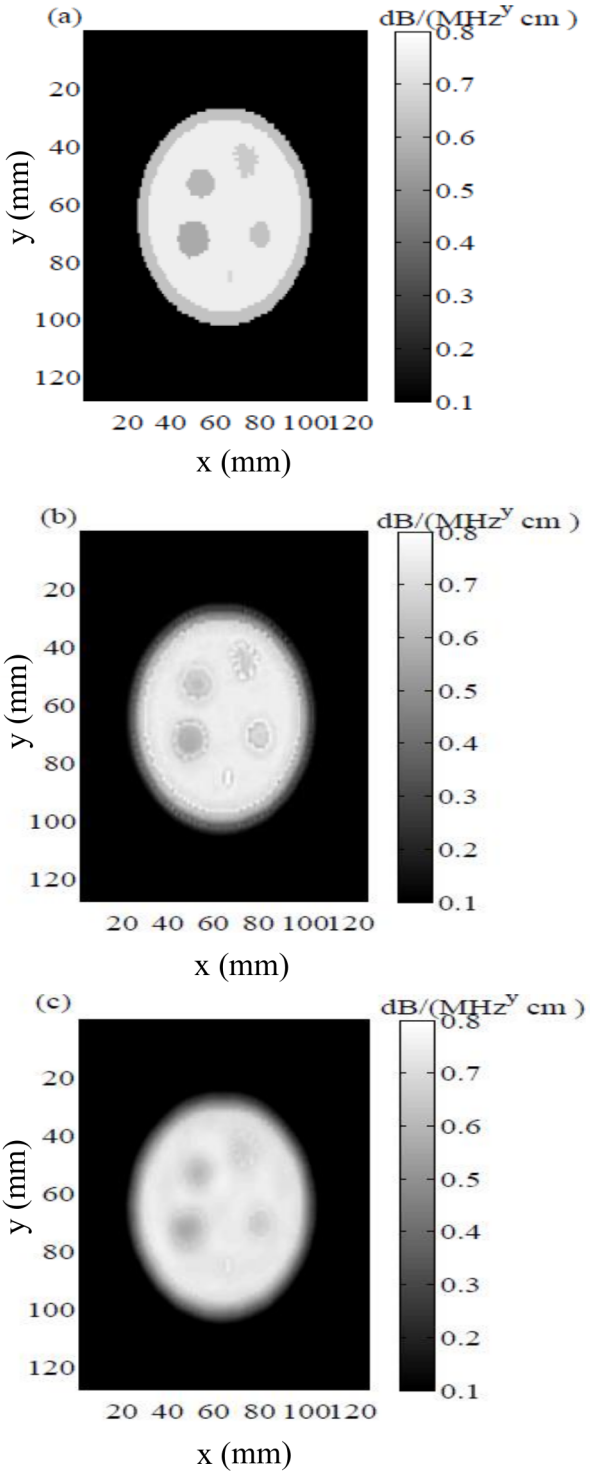

Figure 5.9: A. Reference acoustic attenuation map. B Reconstructed AA map with the standard least-squares cost function. C. Reconstructed AA map using the generalized cost function proposed

5.4 Conclusions

In this work we propose a new generalized misfit function to improve the reconstruction of AA and SS maps in USCT. The misfit function proposed includes additional terms besides the standard misfit function that makes it more sensitive to the amplitudes of the signals and, at the same time, provides the FWI method with the initial estimates of SS reconstruction.

The process to obtain the initial AA image with the travel-time misfit term included in our generalized misfit, added just an small extra to the total reconstruction time. In this sense we can conclude that the use of this term makes it possible to use a method based only on FWI to perform the whole reconstruction process.

On the other hand, the method proposed makes the problem more convex, and the convergence of the AA reconstruction more robust to possible deviations in the estimated SS map (which remains fixed during the reconstruction of the AA map). By incorporating also a TV regularization term, we can further reduce the noise and possible artifacts in the image while preserving the information of the edges. With the terms proposed we were able to reduce the bias in the AA reconstruction and, at the same time, we were able to obtain more homogeneous bias values in the different regions studied, showing that this generalized misfit is less sensitive to the SS distribution estimated.

As a general conclusion, we can say that the generalized misfit proposed improves the global performance of the FWI USCT reconstruction methods.

Chapter 6

Real data reconstruction in USCT

6.1 Introduction

In this chapter, our objective is to explore the reconstruction of real data in USCT. For this purpose, some methods for data processing and calibration were developed and modifications to our methods proposed in previous chapters had to be done in order to apply them to real data from the MUBI scanner. Conditions required to use geometrical acoustics (GAc) or full-wave inversion (FWI) methods with our current prototype were also analyzed.

The reconstruction of high-quality images from real USCT transmitted data is a very difficult task when using Full-Wave Inversion (FWI) methods. Several approximations have to be made:

- With the exception of the KIT scanner from Karlsruhe Institute of Technologies [Ruiter et al., 2012], practically all existing USCT scanners, including our MUBI scanner, employ arrays of transducers instead of spherical sources. Most reconstruction methods available assume transducers behave as point sources, even when they actually present focusing in the forward direction.
- The characterization of the source signal is a key requirement for FWI algorithms, as it has to be used as input to the numerical models of wave propagation. As USCT is an emerging imaging modality, there are not well-established methodologies yet to perform this estimation.
- It is difficult to estimate with accuracy the positions of the detectors employed to scan the object. This is particularly complicated when the detectors rotate. The rotation path, in these cases, will not describe a circle but a polygon. The positions of the detectors could be affected by small displacements of the array in the radial direction or because the front face of the transducers may not be pointing to the central axis of the scanner. These issues may lead to the rotation of emitting and receiving transducers with different mean radius.

- The numerical propagation models employed in the reconstructions are generally two-dimensional (2D), considering only one slice of the inspected object, to speed up the calculations. As the measurements are actually three-dimentional (3D), all the events that produce dispersion in other planes different from the one in which the simulation takes place will contribute to miss-estimations in the reconstructed image.
- The use of high frequencies is particularly important to improve the resolution of the reconstruction. In Chapter 4, resolution with FWI was seen to be of the order of the wavelength in the medium. On the other hand, the higher the frequency, the larger the discretization of time and space needed to reach numerical stability in the simulations.

All these reasons explain why only a few previous works presented results of real USCT data reconstructed using FWI [Li et al., 2014, Sandhu et al., 2016, Wiskin et al., 2007].

Most USCT works address reconstruction with geometrical acoustic methods, which achieve reconstruction times consistent with the requirements of clinical practice. Nevertheless, GAc methods are also affected by several of the aforementioned issues, especially the ones regarding the mechanical calibrations of the experimental setup and knowledge of the initial source signal.

The structure of this chapter is as follows. In the first section (Sec. 6.2), we introduce the details of the calibration performed in the data acquired. We also describe the different methodologies employed for data processing. After that, we refer to the characteristics of several *in-vitro* phantoms studied. To reconstruct these experimental acquisitions, the methods developed during the previous chapters of this thesis are applied: GAc methods based on straight rays with the inverse Radon transform, and bent rays with our proposed Bézier ray-tracing in one hand, and FWI methods using our derivations in time domain on the other hand. Results and discussion are given in section 6.3 and the conclusions in section 6.4.

6.2 Methods

6.2.1 Mechanical calibrations

The two mechanical calibrations needed in the MUBI system to evaluate the speed of sound (SS) of the water bath and to determined accurately the detectors position were proposed by the ITEFI group, at the Spanish Council of Research and are described in Ref. [Camacho et al., 2012]. For the sake of clearness, and because we performed these calibrations for each of our experimental acquisitions, we will briefly introduce the main features of this process.

6.2.1.1 Sound speed estimation of the water bath

The accurate estimation of the SS of the water inside the tank where the entire MUBI system is immersed, is a very important step previous to the acquisition of any measurement. This value

is needed to evaluate accurately the positions of the detectors, as will be explained later. In order to perform this estimation, a phantom consisting of two parallel 0.1 mm diameter copper wires separated by a distance accurately known is used (see Fig. 6.1). The wires are located in vertical position with the help of a fixing base in front of the arrays.

With one of the elements of the array in pulse-echo mode, that array is moved covering an angular sector to find the position in which the array element and the wires are aligned. This situation will occur when the time separation between echoes resulting from these wires is maximum. At that aligned position, the SS can be estimated as twice the spatial separation between wires divided by the time separation between echoes.

The temperature of the water bath is measured with a conventional mercury thermometer. The thermometer is introduced during several minutes inside the water tank to perform the measurement.

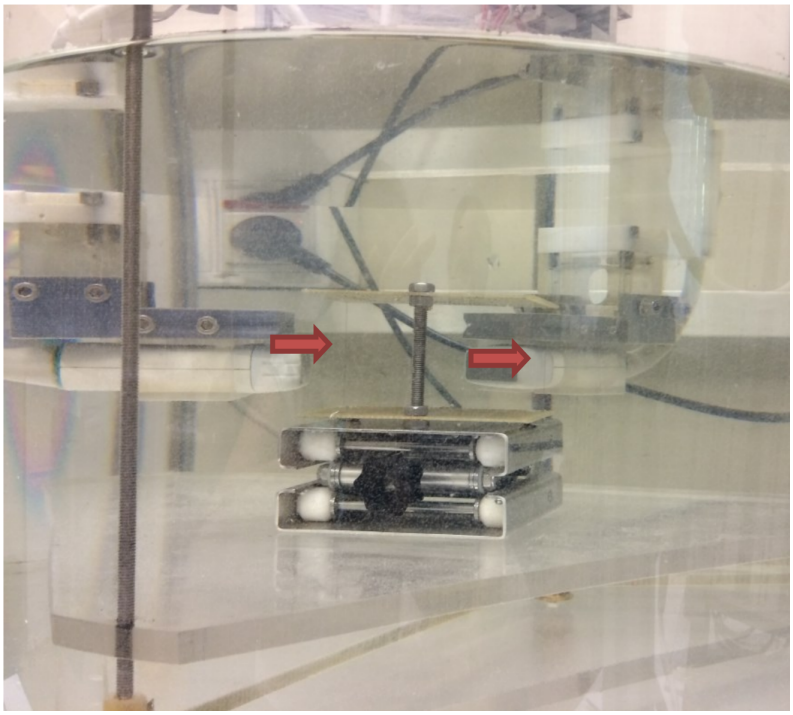

Figure 6.1: Wires phantom used to estimate the sound speed of the water bath in the MUBI scanner

6.2.1.2 Calibration of the angle and rotation radius of the arrays

This calibration aims to find the accurate location of the elements of the arrays. For this purpose, it is necessary to characterize two parameters, the radius of rotation R of the center of the array, and the inclination of its front face regarding the radius, given by the angle β (see Fig. 6.2). As the moving motors of the arrays are fixed to a circular structure, it can be assumed that the center of the arrays will describe a circular trajectory of radius R.

In this case, we used a single 0.1 mm copper wire normal to the array plane. This wire (see Fig. 6.3) is put in a random position (x_R, y_R), that will be related with a given element position (x_i, y_i) by means of the following equation:

$$\begin{aligned} r_i^2 &= (x_i - x_R)^2 + (y_i - y_R)^2 = (ct_i/2)^2 \\ x_i &= R\,cos\varphi + (i - (N-1)/2)d\,cos(\varphi - \beta - \pi/2) \\ y_i &= R\,sin\varphi + (i - (N-1)/2)d\,sin(\varphi - \beta - \pi/2) \end{aligned} \tag{6.1}$$

Where t_i is the measured round time-of-flight between the array element and the wire, c is the SS in water (previously measured), φ is the angle in the reference system of the center of the array, i is each of the N elements of the array and d is the pitch between elements. This is done for each single transducer in reflection mode.

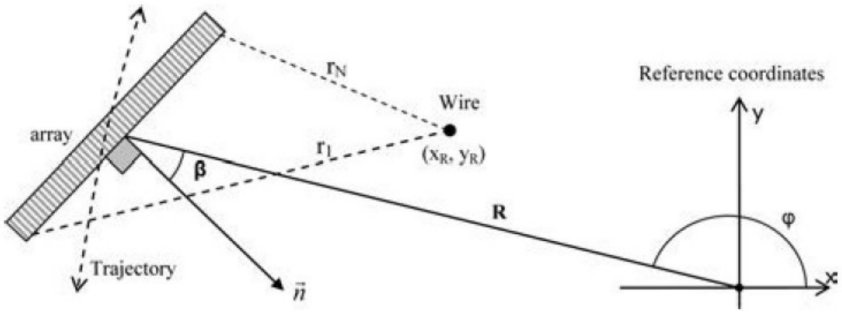

Figure 6.2: Schamatic representation of the parameters R and β used in the calibration of the detectors position, taken from Camacho et al. [2012]

Eq. 6.1 defines a system of $3N$ equations (depending on the number of elements in the array) with 4 unknowns (x_R, y_R, R, and β). As the different t_i values are quite correlated, it is important to change the positions of the wire and also the angular orientation φ of the array to break this correlation and to get a better estimation of R and β. In this work, we used the values obtained by [Camacho et al., 2012]: 8 angular positions with a step of 45 degrees and 4 positions of the wire.

As the initial shell of the transducer (lens) could vary from one array to another it is necessary to repeat this process in transmission mode, in order to take into account the different depths of this shell in each transducer. Central and right panels of Fig. 6.3 show the acquisition of the cooper wire phantom using the reflectivity modality (sector image and full angle spatial compound technique respectively). These images are used to show that the estimated positions are accurately calibrated. If this process would have failed, the wire in the compound image would not look circular but distorted.

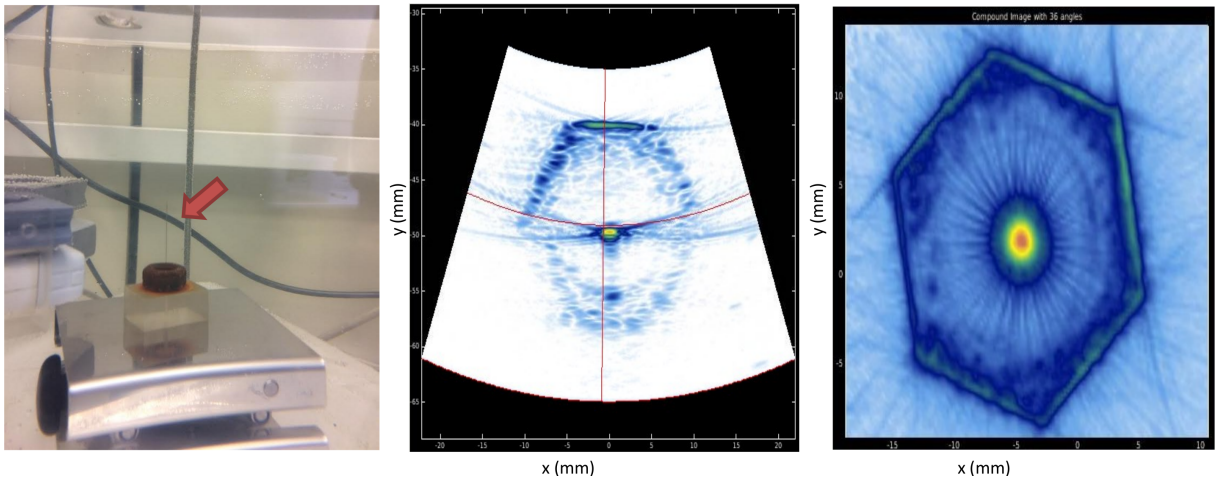

Figure 6.3: Wire phantom used to estimate the sound speed of the water bath in the MUBI scanner

Refinements to this calibration

The calibration previously explained considers that both arrays are in the same plane. Nevertheless, small leaning of the arrays with respect to the ideal plane containing them, can be also a source of errors in the given set of measurements. In fact, small deviations of the expected time of flight (TOF) of the signals in water (using the measured SS value), were generally observed in the measurements even after the corrections above mentioned. In order to compensate for this, we calculated a correction coefficient for each emitter-receiver pair. It is based on the differences observed between expected TOF (calculated from the distance between emitter and receiver and the SS measured value) and the one experimentally observed. Using these coefficients, each signal can be put forward or delayed by the necessary amount. Unfortunately, this method is not capable of compensating the amplitude shift produced during the variation of the path.

6.2.2 Characteristics of the experimental setup for data acquisition

We used our MUBI scanner to perform the acquisitions of real data. The acquisition scheme for USCT follows the fan-beam approach for CT systems (see Figs. 6.4 and 6.5). For each emitter array position, the receiving array is moved sequentially to cover a chosen angle (Fan-Beam angle) opposite to the emitter. For each position of the receiver, all (or a subset) of the emitter array elements are sequentially used as source, and the signals received by all (or a subset) of the receiving array elements are registered. Then, the emitter array is moved and the fan-beam acquisition is repeated. The central region where all the fan-beams overlap is determined by the angle of the fan-beam, being the zone where better reconstruction quality can be expected.

Depending on the size of the object to study, we can chose the angle of the fan-beam and the rotation radius of the arrays. The rotation radius can be modified by means of two array holders that allow displacing the arrays. We investigated the reconstruction of USCT data employing two cases for the rotation radius: the maximum value of the rotation radius achievable, 100 mm, and the minimum value that can be used, 50 mm (see Figs. 6.4 and 6.5). For the larger case, we choose 11 positions of the receiver array to cover with each fan-beam a wide angular sector that could be sufficient to include the objects to be study . For the small radius, we used 7 positions and in both cases, we used 16 of the 128 arrays elements (1 of every 8).

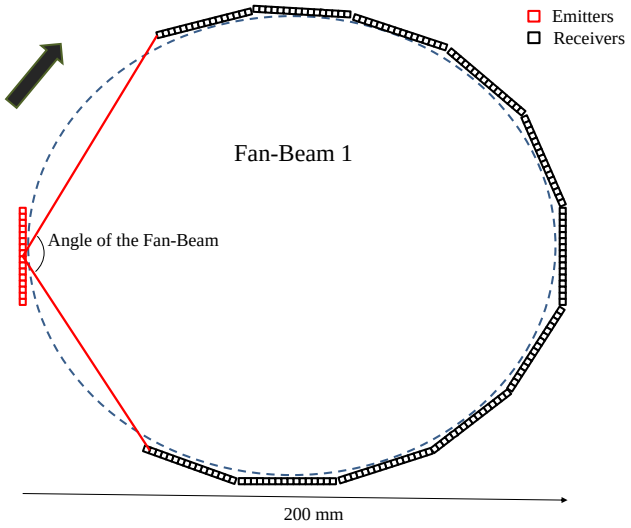

Figure 6.4: MUBI scanner configuration using the maximum transducer separation of 200 mm. Due to its large size, this configuration can be reconstructed only with geometrical acoustic methods

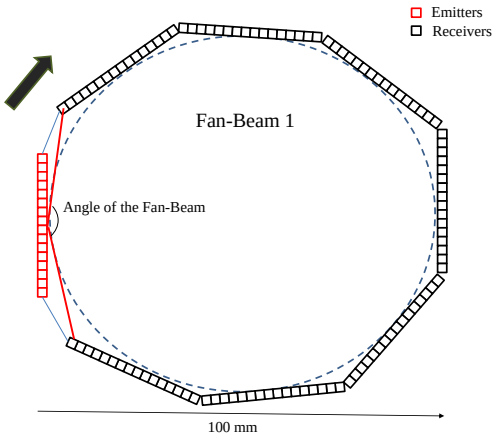

Figure 6.5: MUBI scanner configuration using arrays holders to reduce the radius of rotation to 100 mm. This configuration is suitable for FWI recontructions

Description of files and variables of the MUBI scanner

Each acquisition is stored in a .zip file, which contains a Fan-BeamXX.mat MATLAB file for each acquired fan-beam (23 in the large case and 10 in the short case). The signals acquired in each fan-beam are stored in the variable $Ascans\_rx$ which is indexed according to the following structure:

$$Ascans\_rx = [Receiver\ array\ position, Emitting\ element, ... \\ ...Receiving\ element, Samples\ recorded] \tag{6.2}$$

For example, the signal received by element 9 of the receiving array when located in the 5th position of the fan-beam and when emitting with element 1 of the emission array, is retrieved by

$$ascan = AScans\_rx(5, 1, 2, :); \tag{6.3}$$

Note that the $AScans\_rx$ variable only stores the signals registered with the active elements, in this case, 1 of every 8 real array elements. This causes the index pointing to the real array element nº 9 to be 2 (the second active element) when indexing the $AScans\_rx$ variable. The variables $activos\_tx$ and $activos\_rx$ into the "parametros.mat" file contains the emitter and receiving active elements for each array, respectively.

To reduce dataset size, the acquisition start is delayed with regards to the excitation moment to discard samples generated long before the pulse arrives to the receiving element. Delays are calculated for each pair based on the nominal speed of sound in water (included in file "meas_c.mat") and the known emitter-receiver separation, and a safety margin is included to be sure that the first arriving signal is always registered. The acquisition start time (measured in microseconds) is stored for each emitter-receiver pair in the variable tdlr_sitau (in parametros.mat), which is indexed by:

$$tdlr\_sitau = [Receiver\ array\ position, Emitting\ element, Receiving\ element] \tag{6.4}$$

Spatial coordinates of the elements are stored in the variables coordenadas in each fan- beam file. They are indexed in the following way:

$$coordenadas = [Receiver\ array\ position, Emitting\ element, Receiving\ element, ... \\ ...Emitter \mid Receiver(1 \mid 2), X \mid Y(1 \mid 2)] \tag{6.5}$$

6.2.3 Data processing

Before using any experimental data to recover the acoustic information of the medium, we analyzed our capabilities of using all the frequencies present in the measured signals with our reconstruction codes.

When using GAc algorithms, the higher the frequency, the better quality of the resulting image reconstructions. Therefore, to perform this type of reconstructions, we do not perform any processing beyond the extraction of time of flight (TOF) and amplitude from signals.

However, when usign FWI, with a central frequency of 3.2 MHz and a bandwidth of 50% we need to be able to propagate, avoiding numerical dispersion, signals with more than 4 MHz. With the propagator based on k-Wave (see Chapter 2), and a FOV of 100 mm^2, this requires a spatial sampling of around 1024×1024 cartesian grids. Time sampling required in this case would exceed 3000 temporal samples. A matrix of that size, to record the pressure field, is hardly tractable and difficult to store in computer memory. Besides, the time needed for such calculation could be extremely large.

Due to these limitations, we decided to filter the signals keeping only frequencies below 2 MHz (see Fig. 6.6). With this value, the Cartesian grid required was 512×512 bins and 1350 time intervals. In Fig. 6.6 is important to note the reduction of the spectrum's amplitude once the signals is filtered. This is because the frequency content of the signals below 2 MHz is low in comparison with the original one. The amplitude of the filtered spectrum is also affected by the characteristics and shape of the filter used. In this case, the filter applied also decreased the amplitude of the resulting signal.

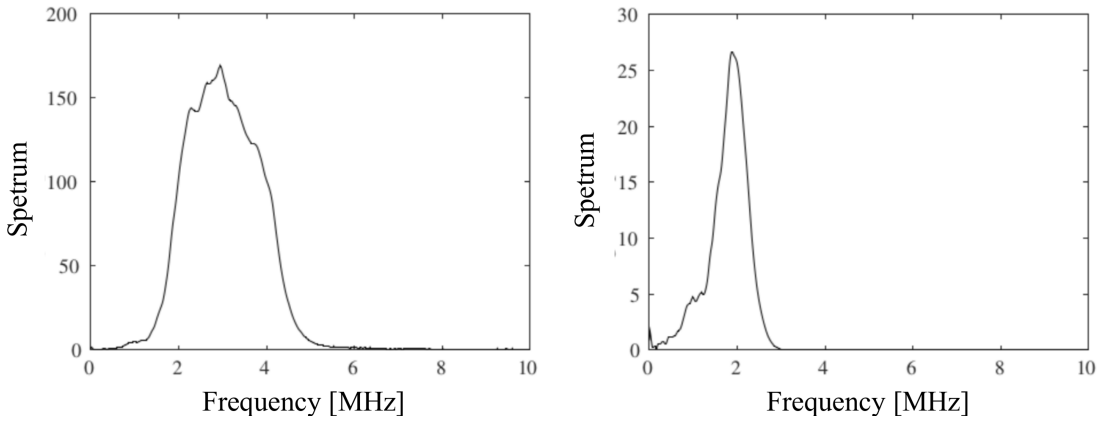

Figure 6.6: Left: Frequency spectrum of one of the experimental signals measured. Right: Low pass filtered signal up to 2 MHz. The signal chosen to this illustration was the one in front the first emitter.

The scale of the measured signals is another fact to be taken into account to perform FWI reconstruction with data acquired with the MUBI scanner. The scale of the measured signals is arbitrary and not given in units of pressure. It depends on the input voltage and other intrinsic characteristics of the transducers. In order to use these signals with k-Wave, which expects recorded signals with values equal or lower than 1 unit, we performed a normalization using the following steps:

1. Select a pair of opposing emitter-receiver.
2. Use the recorded signal for the chosen pair and calculate the absolute maximum value

(using the envelope method described in Chapter 3).

3. Use the inverse of the maximum obtained the as scale factor for all recorded signals.

Furthermore, the source signal should be normalized to one, and therefore, another scale factor should be applied. This value is given by the amplitude decay of a signal in water from the pair of opposed emitted-receiver arrays element chosen.

Another important step previous to the reconstruction, is the compensation of angular sensitivity of the transducer, as array elements do not detect with the same efficiency signals emitted in front of them and signals emitted from oblique directions. Signals coming from larger angles are detected with lower efficiency and therefore the amplitude measured do not represent the actual amplitude arriving to the point of measurement.

To compensate for this effect, we used a correction factor obtained comparing simulated and measured signals in water. The maximum value of the simulated (A_s) and measured (A_e) signals in water is calculated and used to obtain a factor ($corr\_sens$) that then will be used to correct measurements in other media.

$$corr\_sens = \frac{A_s}{A_e} \tag{6.6}$$

This factor is calculated for each emitter-received pair in a single fan-beam, as the rest of the fan-beams have the same relative positions between emitters and receivers. Fig. 6.7 depicts the value of this correction for each of the 16 emitters of the fan-beam and all receivers.

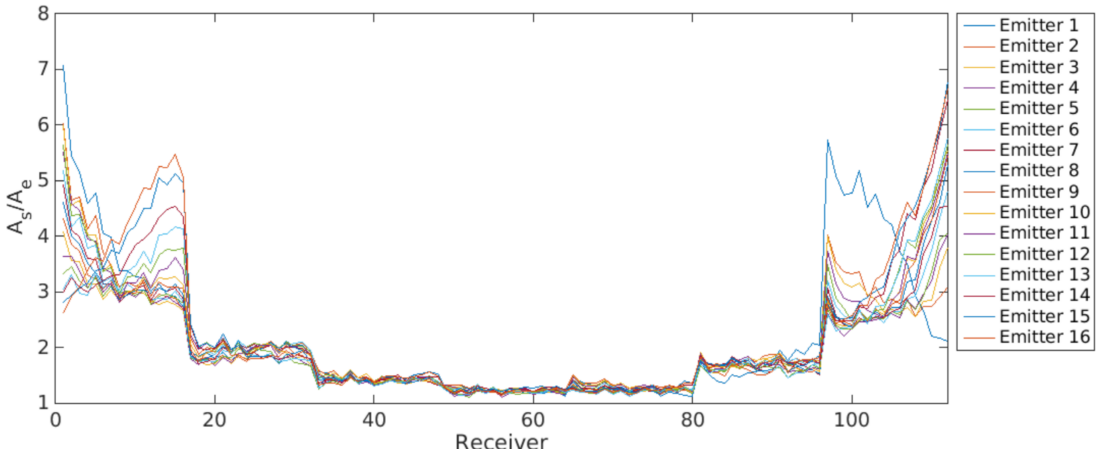

Figure 6.7: Sensitivity correction factors for each emitter recevier pairs in a fanbeam. As the angle between emitter and receiver increase, the correction is higher as the efficiency in the detection decrease.

Fig. 6.8 demonstrates the effect of these factors when they are applied to a set of measurements. All the signals received for a given emitter are represented in that figure. The correction strengthens the amplitude lost at large angles of emitter and receivers.

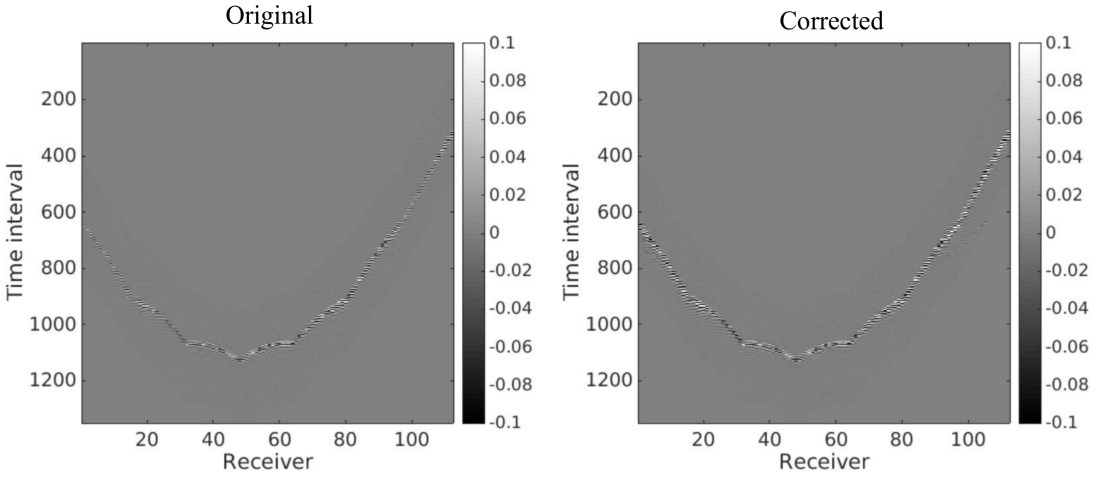

Figure 6.8: Data compensated by the loss of amplitude with lateral sensitivity of the transducer. The orginal signals (left panel) present distorted amplitude at wider angles. This effect is corrected with the application of the sensitivity correction factors (right panel).

6.2.4 Initial source estimation

The initial signal emitted by the source is generally unknown and difficult to measure with accuracy. Nevertheless, it has to be estimated to feed the FWI algorithm for image reconstruction. It is also needed to estimate the TOF of the signals based on cross-correlation and perform GAc reconstructions. One possible way to estimate the source signal is by using one of the recorded signals from opposing emitting-receiving array elements, measured in water. In this case we used the same pair selected to estimate the first scale factor. By using water, we ensured that no signals besides the directly transmitted were being used. On the other hand, using the signal from an opposed receiver we avoid losses in amplitude of the signal due to the angular sensitivity of the array.

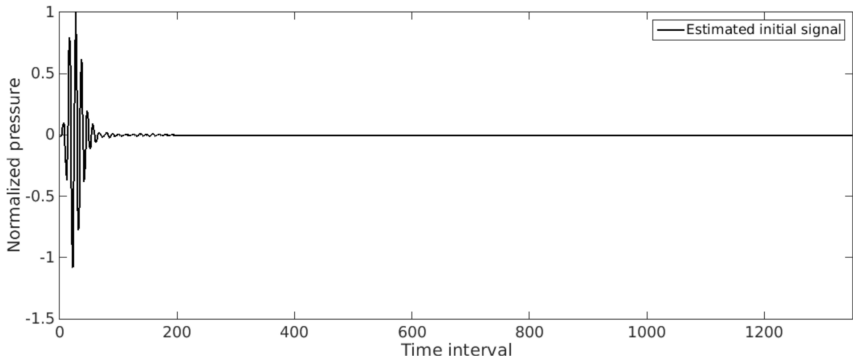

Figure 6.9: Estimated initial signal from the time reversed propagation of the measured signal in an opposed emitted receiver pair. After the propagation, the recorded signal at the emitter is fliped and normalized. The resulting signal is used as source.

Using the measured sound speed in water and k-Wave, we time reversed the measured signal at the chosen receiver and used it as a source located at the receiver location. Let us remember that the signal at the receiver was previously normalized to one because we chose that pair to calculate the first scale factor for the signals. Once the signal is propagated, we recorded the resulting signal at the emitter location and reversed it again in time to return to the actual order (see 6.9).

The source estimated this way will not be normalized to one, because its amplitude decayed due to geometrical spreading and small attenuation in water. We took its maximum value, using the envelope method, and divided all the recorded signals by this value. Consequently, the estimated source was normalized to one and the rest of the signals were compensated by the geometrical spreading when the source amplitude has maximum amplitude equal to one.

6.2.5 Description of phantoms and experiments

To test the performance of our codes we employed *in-vitro* data acquired with the MUBI scanner. For the larger acquisition setup, we designed an experiment with a tissue-mimicking phantom with three different regions where SS and AA vary. These values can be modified using different concentrations of water, gelatin, graphite, formaldehyde and Ethanol [Duck, 2013]. The amount of ethanol will change the SS of the medium and the graphite will modified the AA. We observed that graphite also produces small variations in the SS. The main characteristic of the tissue-mimicking phantom can be seen in Fig. 6.10 and Table 6.1. Two holes were performed inside the phantom. The first one is filled with water after the phantom was located inside the water cube (black area in Fig. 6.10 right panel). In the second one we varied the amount of alcohol and graphite to create a region with small differences in terms of SS with respect to the background (BG) (white area in Fig. 6.10 right panel), simulating a cyst. Both cylinders are integrated in a background described in Table 6.1. Thanks to the axial symmetry of the phantom only the acquisition of a central slice was required.

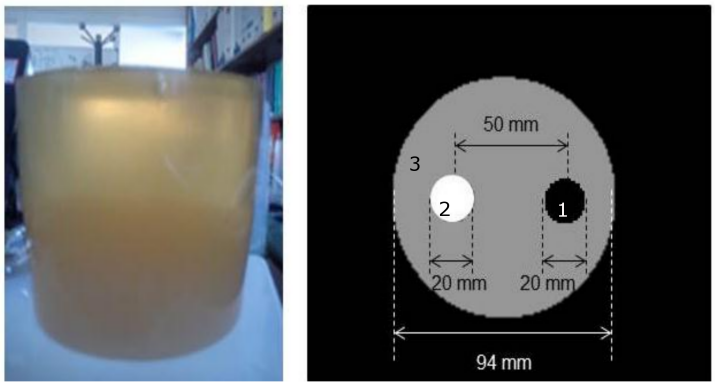

Figure 6.10: *In-vitro* tissue mimicking phantom created for USCT reconstructions. Left panel represents the lateral view of the phantom. Right panel depicsts a scheme of the top view of this phantom.

Table 6.1: Tissue mimicking phantom composition

Region	Water (ml)	Gelatin (ml)	Graphite (ml)	Formaldehyde (ml)	Ethanol (ml)
Background	800	63	78.4	2.4	64.16
Cyst	400	61	58.8	1.2	16
Water	-	-	-	-	-

To reconstruct this phantom we used analytic and Bézier-based reconstruction methods developed in Chapter 3. Due to the large dimensions of the FOV, FWI methods were not used (see Sec.6.2.3). To obtain TOF and amplitude values of the signals acquired, we used the cross-correlation and envelope-based methods respectively. To use the cross-correlation, an initial source signal without frequency filtering was estimated with the procedure explained in previous section.

With the reduced rotation radius configuration of the array, we scanned a boiled egg (see Fig. 6.11). This *in-vitro* type of phantom has been used in many other studies with ultrasound [Opielinski, 2007, Javanaud et al., 1984, Errabolu et al., 1987] where SS and AA values of the egg's white and yolk have been characterized. Table 6.2 provides these values as reference.

Table 6.2: Sound speed and acoustic attenuation for egg's white and yolk. [1]- measured at 22°C. [2]- Measured at 20-21°C and 2.10 MHz. [3]- Measured at 24°C.[4]- measured at 22.74°C and 2 MHz

Reference	Sound speed- egg white (m/s)	Sound speed- egg yolk (m/s)	Attenuation-egg white (db/(MHz cm))	Attenuation-egg yolk (db/(MHz cm))
Errabolu et al. [1987] [1]	1519	1503	-	-
Javanaud et al. [1984] [2]	1530	1507	-	-
Opielinski [2007] [3]	1530	1501	0.27	0.83
[Opieliński et al., 2014][4]	1495 - 1502	1510 - 1513	∼0.1-0.5	∼1-1.2

We inserted a needle in the phantom to simulate a micro-calcification (a concentration of calcium that generally appears inside the ducts [Boyd et al., 2010]). In a mammography, these structures appear as intense white dots and according with their aspect, distribution and size, they can be interpreted as an indicator of cancer. Generally, these micro-calcifications present dimensions around or lower than 0.5 mm. Therefore, they are difficult to detect with a mammography when dense breast are studied [Yunus et al., 2004]. We were interested in explore the capability of our system and methods to detect these structures. The diameter of the needle inserted in the phantom was around 0.2 mm.

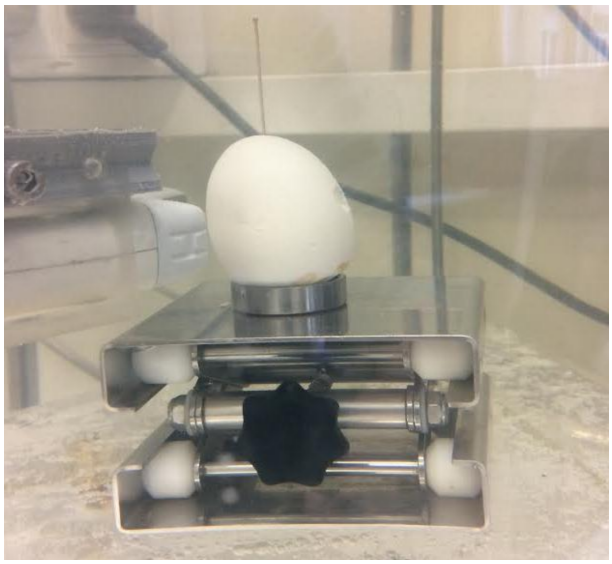

Figure 6.11: Acquisition of an egg with the reduced radius of the MUBI scanner

To reconstruct this egg phantom, we used the Bézier-based GAc method and the FWI algorithm developed in Chapters 3 and 4, respectively. For the reconstruction using Bézier, the signals without frequency filtering were used. As before, we extracted the TOF and amplitude with the cross-correlation using the estimated initial source signal and the maximum value of the envelope of the received signal. For the FWI reconstructions we used filtered signals (up to 2 MHz) following the procedure previously described. We performed the reconstructions using a single image update for iteration to ensure the most stable reconstruction possible.

For the reconstruction using BR we employed a grid size of 256×256 pixels. For the larger configuration, the grid size was selected as $FOV/grid\_size = 200/256 = 0.78$ mm. For the smaller configuration the grid size used was $FOV/grid\_size = 100/256 = 0.39$ mm. For the FWI reconstructions we employed a grid size of 512×512 pixels and the grid size was $FOV/grid\_size = 100/512 \simeq 0.2$ mm. For both the large and the small configurations, we analyzed the SS and the AA.

6.2.6 Comparison with the reflectivity modality

To provide a reference for our reconstructions, for all the transmission USCT acquisitions performed in the MUBI scanner, a high-resolution reflectivity acquisition of the same tomogram was also obtained. The reflectivity reconstructions are based on the technique Full Angle Spatial Compound (FASC) [Medina et al., 2015, Camacho et al., 2012].

FASC consist on compounding many sector images of the inspected object taken around 360º to create a tomogram. This composition allows to compensate the loss of resolution at large depths present in individual sector images. Additionally, this technique exhibits several

advantages: speckle noise is reduced improving the contrast-to-noise ratio (CNR), resolution is higher and more isotropic, and image artifacts are suppressed. The disadvantage of this modality is that it only provides qualitative images.

One problem of breast FASC imaging is refraction at the water-skin interface, due to sound speed differences between water and tissue. Refraction makes the ultrasound propagation to diverge from a straight ray path. If not corrected, the compounding process of sector images results in severe errors, image distortion and resolution and contrast losses. Following the Snell's law, the incident beam is refracted with an angle that is function of the incidence angle and the relationship of propagation speeds in the two media. To correct for that, an algorithm that performs interpolation of many scan lines in the compounding region, taking into account the refraction at the interface is used [Medina et al., 2015].

To calculate the refraction angle, the average value of sound speed in the object (once its edges are identified using the non-corrected FASC reconstructed image) is calculated. It is possible to estimate an appropriate value by modifying systematically the sound speed until the sharpness of the reconstructed image is maximised [Medina et al., 2015].

We compared the resulting images from our SS and AA reconstructions with a FASC-reflectivity map taken at the same slice of the transmission tomographic acquisition. We also compared the mean values in the reconstructed SS maps with the ones estimated with the above explained for SS estimation in the reflectivity modality. This provides a method to analyze the accuracy of our reconstructions. Additionally, we analyzed the noise in our reconstructions using the standard deviation divided by the mean values in regions of interest (ROIs) selected in different zones of the phantoms inspected.

6.3 Results and discussion

Fig. 6.12 shows SS and AA reconstructions of the phantom under study with analytic and Bézier iterative methods. The reconstruction time per slice was $\backsim 0.23$ seconds for both FBP-SS and FBP-AA (top and bottom left panels of Fig. 6.12 respectively) as the same angular and radial sampling is used for both reconstructions. The reconstructions using Bézier took $\backsim 1$ minute for the SS and $\backsim 43$ seconds for the AA, as for the AA reconstruction the bent-paths are taken from the last iteration of the SS.

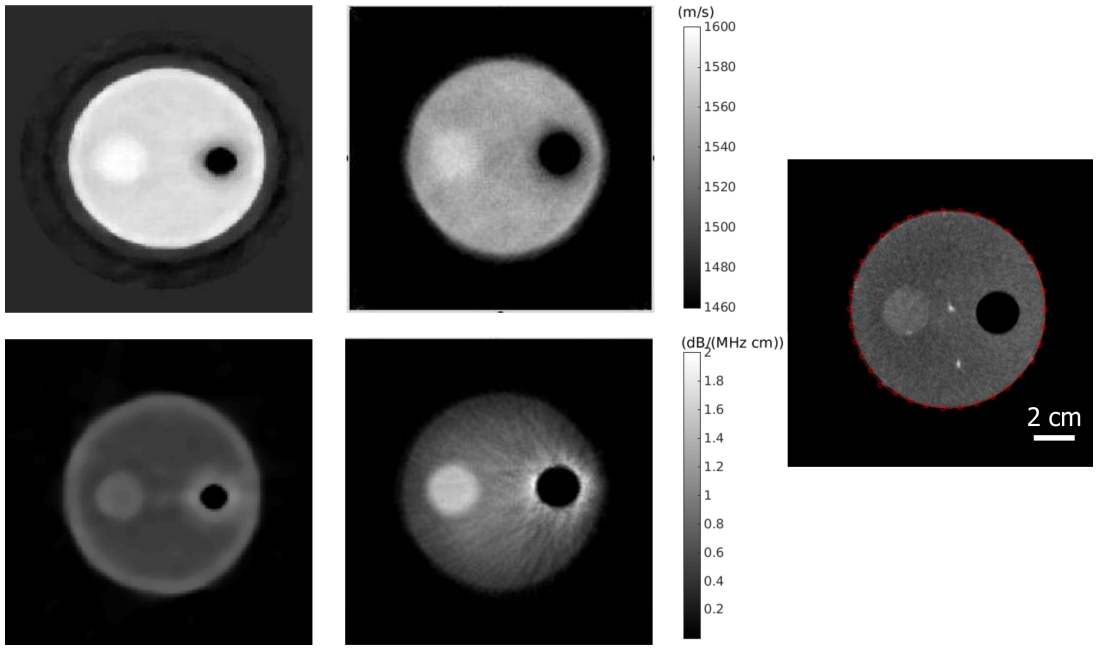

Figure 6.12: Sound speed (SS) and Acoustic attenuation (AA) reconstruction for the tissue-mimicking phantom. Left panel shows FBP reconstructions of the phantom, central panel Bézier-based bent rays reconstructions and right panel the reflectivity reconstruction as reference. At the top are SS reconstructions and at the bottom AA ones. FBP reconstructions miss-estimate the actual dimensions of the estructures in the phantom

The information obtained from both reconstruction algorithms is similar. Nevertheless, FBP reconstructions tend to miss-estimate the actual size of the structures inside the phantom, as it does not take into account refraction. Due to the considerable changes of SS in this phantom, refraction is an important phenomenon in order to obtain accurate reconstructions.

On the other hand, the use of high frequencies allow us to obtain good spatial resolution. This can be clearly seen when these images are compared to the ones obtained in our numerical experiments of Chapter 3 with 1 MHz central frequency. This evidences the need of using frequencies as high as possible for GAc recontructions.

The SS distribution with both methods shows an adequate definition of the different areas in the phantom. Nevertheless, the cyst (white area in Fig. 6.10) can be hardly differentiated from the background, which could be worse if its dimensions were smaller, as it was explained in chapter 3. On the other hand, the AA distribution has much higher contrast among different materials. The differences of areas of the phantom are remarkable and the cyst appears quite differentiated.

The halo effect around the water cylinder (black cylinder in 6.10) explained in chapter 3 is also presented here. As the frequency is higher than the one used in our numerical experiments in chapter 3, phase aberration artifacts are less likely to occur. Being the pulses narrower in duration it is more difficult that dispersed and direct signals coincide in the same time

Table 6.3: Reconstructed sound speed and acoustic attenuation values for the tissue mimicking phantom. ROI numbers were given as in Fig. 6.10

	ROI	**Sound speed (m/s)**	**Noise (%)**	**Acoustic attenuation (db/(MHz cm))**	**Noise (%)**
FBP	1	1480	0.07	1e-3	20
	2	1591	0.18	1.2	1.25
	3	1583	0.06	1.6	0.63
Average sound speed in the whole phantom 1580 m/s					
Bézier	1	1490	0.21	0.07	22
	2	1590	0.31	0.90	0.66
	3	1573	0.19	1.80	0.33
Average sound speed in the whole phantom 1570 m/s					

interval.

Table 6.3 shows quantitative results of the average values and noise inside the selected ROIs in the phantom. The real values of SS and AA of the phantom are unknown. There exits several methods to measure acoustic properties but unfortunately, with these type of phantoms it is difficult to ensure that measured values correspond with the slice analyzed as the variations of the acoustic properties with depth are significant. One important conclusion we got from the preparation of a phantom of this type, is that they are highly heterogeneous in depth, because its constituents tend to settle during the cooling process. It is recommendable for future works to employ pure materials such as oils, animal tissue, plastics, industrial chemical composes, etc.

The average SS value in the phantom obtained in this case from the reflectivity modality was 1567 m/s. The average value estimated with FBP is 1580 m/s and with the Bézier GAc method is 1570 m/s. Therefore, the Bézier-based reconstruction is closer to the real values of the phantom. FBP, as we seen in the chapter of ray-tracing USCT techniques, tends to miss-estimate reconstructed values more than bent-rays techniques. Noise values obtained with both methods of reconstruction are similar.

Figs. 6.13 and 6.14 illustrate the results of the reconstructions of SS and AA respectively, using the small configuration of the MUBI scanner. The FBP reconstruction were obtained in less than a second (both AA and SS), and the Bézier-based SS took $\sim$52 seconds using 15 iterations and the AA distribution was obtained in $\sim$30 seconds using 10 iterations. The reconstructions using FWI took 53 minutes using 10 iterations.

Both reconstruction methods provide results that are, in general, in agreement with the output of the reflectivity modality. The later exhibits several white points that we believe are air bubbles created during the boiling process. The needle is also appreciated just at the center of the egg's yolk. Nevertheless, this needle can not be seen in the SS reconstruction. As mentioned before, the sizes of the objects obtained with the FBP reconstructions are wrongly

estimated.

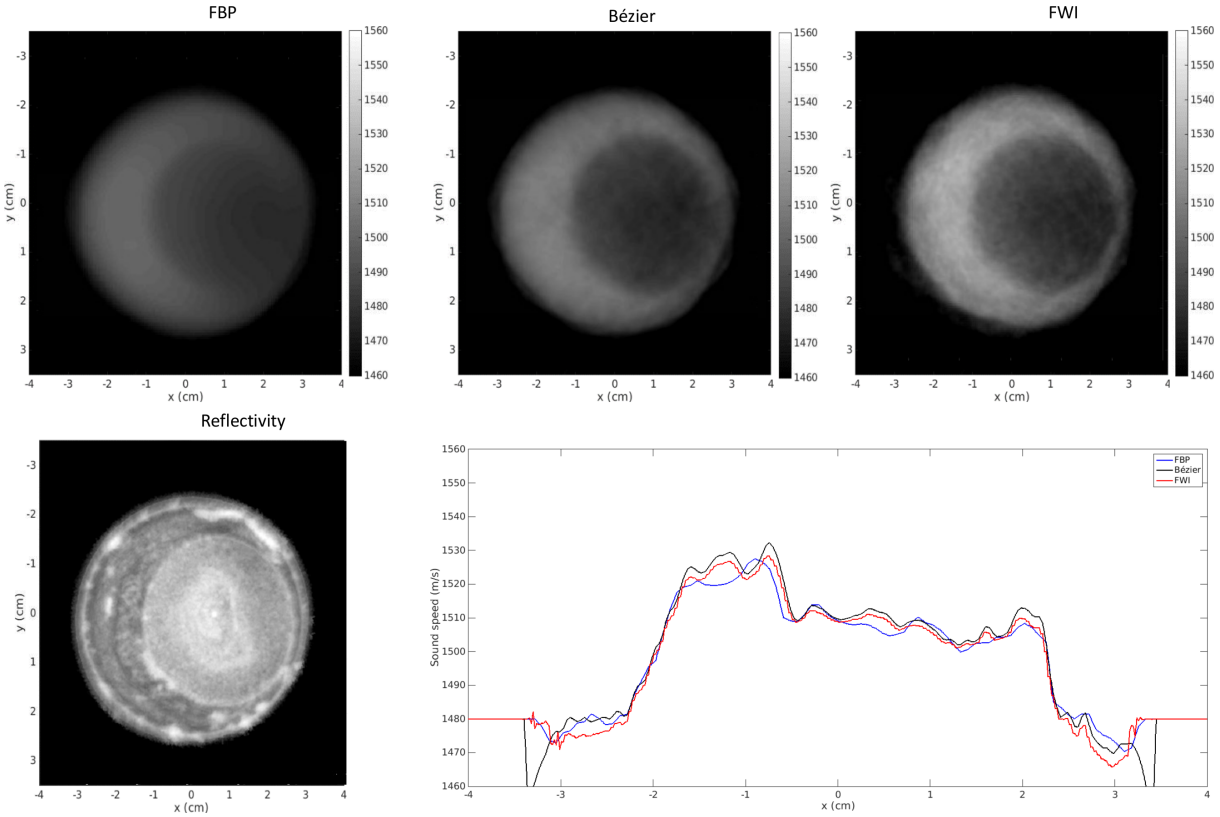

Figure 6.13: Top panels show the sound speed reconstruction using FWI and GAc Bézier algorithm from left to right. Profiles across the y=0 for both reconstruction are presented at the left bottom panel. The reflectivity image is also presented as reference at the right bottom panel.

Although, the SS values obtained for the different structures are very similar to the ones obtained with the other two reconstruction methods employed (see table 6.4). The mean value estimated with from the reflection modality is 1512 m/s meanwhile the mean value estimated with the FBP reconstruction is 1513 m/s. Therefore, we can conclude that, as it was mentioned before, the FBP method is capable of providing an adequate overall information of the inspected region, without providing fine details. Besides, as this technique allows very fast reconstruction times, it can be used in parallel to the acquisition process, to have an initial overview of the object.

In general, SS values obtained for the egg's white and yolk with all our methods are in agreement with the values published for other authors and presented in table 6.2. Bézier and FWI reconstructions offer very similar information in terms definition of the interfaces and the SS values. Bézier SS values are slightly higher that FWI reconstructions. The mean value of SS provided by the Bézier reconstruction is 1516 m/s and with FWI reconstruction is 1511 m/s. Here we can see that FWI mean value is closer to the mean value offer by the reflectivity

modality. Nevertheless, the mean values calculated in ROIs located at the white and yolk regions are very similar with both methods (see table 6.4). This fact shows that the Bézier method is good enough to perform USCT reconstructions of SS at the frequencies employed by the MUBI scanner.

Table 6.4: Reconstructed sound speed (SS) values for the egg phantom using the FBP and Bézier-based rays-methods and also FWI.

Method	**SS in a ROI at egg's yolk (m/s)**	**Standard Dev.**	**SS in a ROI at egg's white (m/s)**	**Standard Dev.**	Mean value in whole egg **(m/s)**
FBP	1510	1	1522	1.5	1513
Bézier	1511	2	1527	2.4	1516
FWI	1510	1.5	1523	3.1	1511

The attenuation reconstructions can be seen in Fig. 6.14. As it was explained in previous chapters, this reconstruction is more complicated to perform than the SS one. The resulting images present, in general, lower quality than the SS reconstructions. The ray-based reconstructions displays, in several regions, an enhancement of edges. Egg yolk boundary is fuzzy in both images (FBP and Bézier), and around this area, several fluctuations of the AA are observed. Moreover, a narrow area of strong increments of the AA around the interface water/egg can be also seen. In the Bézier AA map, also some zones of the egg's white appear faded. These artifacts are caused by the refraction and the diffraction of the wave on curved boundaries of heterogeneity areas.

The use of bent-rays overcomes to a great extent some artifacts present in the FBP reconstruction. Nevertheless, when these ray-reconstruction are compared with the FWI reconstruction, it can be seen that FWI provides better definitions of the different regions of the egg. Moreover, less artifacts are obtained, despite of the high noise presented in the image.

There are two important facts that affect the AA reconstruction with all the methods employed. First, as we described in Sec. 6.2.1.2, the data is compensated in terms of TOF due to small angles of the arrays with respect ro with the plane that contains them. Nevertheless, the amplitude shift produced by the path changes was not corrected, consequently biasing the actual amplitude values. We intended to address this downside in future works, by implementing out of plane corrections similar to the ones used to calculate the radius and angle of the array in Sec. 6.2.1.2. Second, it is important to bear in mind that the FWI reconstruction was performed using the standard least squares cost function. Due to that, those regions where the SS was worst estimated, the AA distribution was also affected. The application of the generalized misfit proposed in Chapter 5 could be a convenient way to improve the quality of this reconstruction, which will be explored in future works.

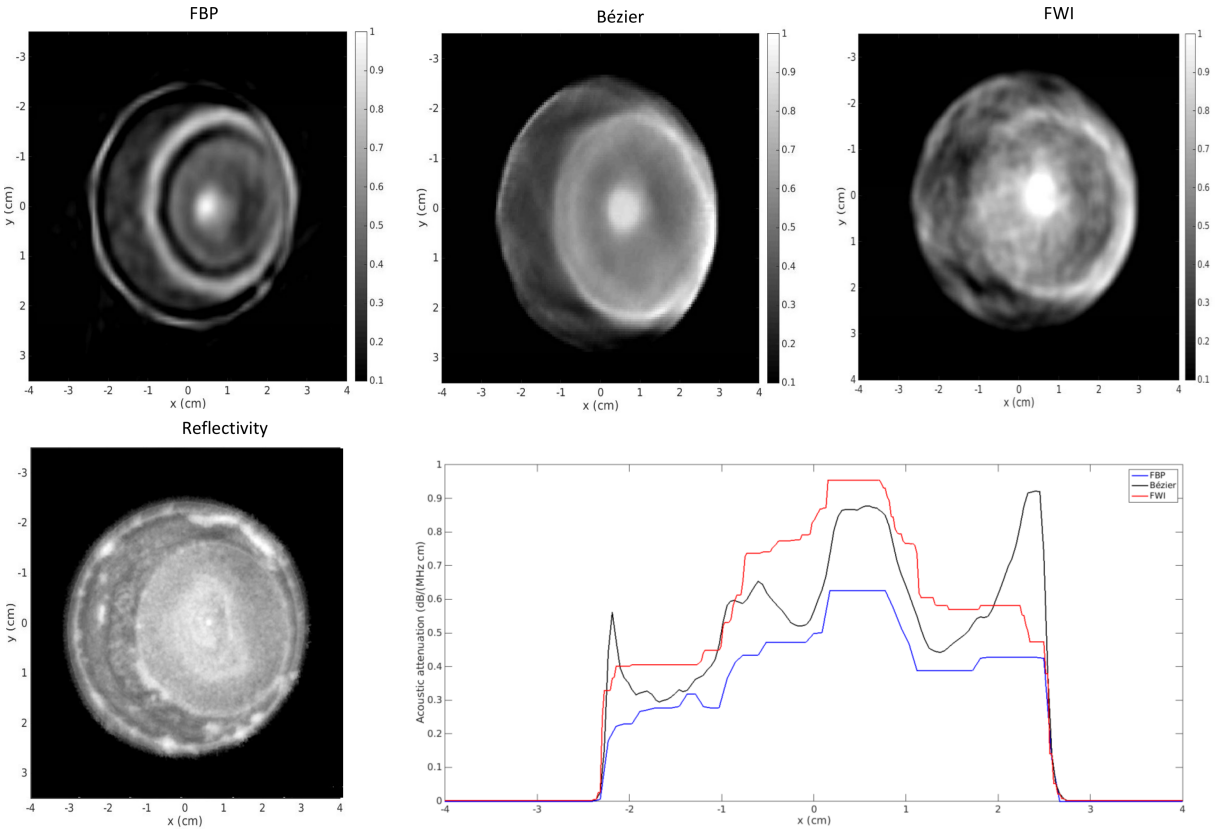

Figure 6.14: Top panels show the acoustic attenuation reconstruction using FWI and GAc Bézier algorithm from left to right. Profiles across the y=0 for both reconstruction are presented at the left bottom panel. The reflectivity image is also presented as reference at the right bottom panel.

On the other hand, in all the AA images is visible the needle at the yolk's center. The real sizes of needle are not recovered correctly, but this is expected due to the voxel size employed in the reconstructions. However, the capability of detecting it when AA maps are employed, has huge significance. Even when sizes are erroneous, this result means that we could be able to detect micro-calcifications in the inspected region, which could also be continued with reflectivity images.

The reconstructed AA values are similar to the values published by other authors and presented in table 6.2. As expected, the best agreement is obtained when using FWI. Contrary to what we conclude for the SS reconstruction, the recovery of the AA maps is strongly improved with FWI. We consider this is the most suitable method to obtain the AA map.

Table 6.5: Reconstructed acoustic attenuation (AA) values for the egg phantom using the FBP and Bézier-based rays-methods and also FWI.

Method	AA in a ROI at egg's yolk (m/s)	Standard Dev.	AA in a ROI at egg's white (m/s)	Standard Dev.
FBP	0.44	0.04	0.29	0.04
Bézier	0.55	0.02	0.33	0.02
FWI	0.75	0.07	0.37	0.1

6.4 Conclusions

In this chapter, the methods developed in the thesis were applied to the reconstruction of real data acquired in the USCT system MUBI. Two configurations for the experimental setup where employed to test our reconstructions, one with the largest possible radius of the arrays, 100 mm, and another with a smaller radius configuration of 50 mm. The largest configuration was used to scan an *in-vitro* tissue-mimicking phantom simulating breast tissue. The smaller one was tasted with a boiled egg in which it was inserted a needle to recreate a micro-calcification.

Due to the frequency content of the signals acquired, and the large setup configuration, the tissue-mimicking phantom was only reconstructed using our GAc algorithms: FBP and Bézier-based (which use straight and bent rays respectively). The high frequency employed showed very benefits for ray-algorithms and an improved resolution was observed in comparison with our numerical experiments performed in Chapter 3, for which lower frequency was employed. Both SS and AA were analyzed with this methods. The results were compared with the reflectivity map taken at the same slice and a general correct agreement was found between the structural information of our reconstructions and the mentioned map.

The results for SS in this case, confirmed that FBP mis-calculates, to a certain amount, the sizes of the structures present in the phantom. This is basically due to the fact that this method does not take into account refraction. Consequently, the Bézier-based method is able to get better results as it includes refraction effects.

We compared the average SS in the whole phantom with the estimation of this value used for the reflectivity modality to correct for refraction. Using this value, we saw that the FBP method also overestimates the reconstructed SS. The mean value obtained from the reflectivity modality was more similar to the mean SS calculated when using Bézier-based reconstructions.

The AA reconstruction presented lower quality than the SS reconstruction, and a halo effect around the different structures was also observed. These are artifacts caused by refraction (therefore we were able to decrease them in the Bézier-based reconstructions) and diffraction of the wave on curved boundaries of heterogeneity areas. Nevertheless, as the frequency used was higher than in the numerical experiments performed in chapter 3, this effect is reduced in comparison with those cases. This evidences the advantages of using higher frequencies, always

bearing in mind that attenuation is higher at larger frequencies, and therefore, the amount of signal detected will decrease.

For the egg acquisition, reconstructions using FBP, Bézier and FWI were performed. In order to improve the tractability of our reconstructions, the measured signals were low-pass filtered at 2 MHz. The most relevant result for the SS reconstruction, was the similarity between FWI and Bézier-based maps, showing the capabilities of this bent-rays method to obtain high quality SS maps. FBP on the other hand, provides similar qualitative information than FWI and Bézier methods. Moreover, the reconstructed SS values were in agreement with the SS of the egg's white and yolk reported by other authors.

The needle inserted in the egg, was not appreciated in the reconstructed SS. On the other hand, this needle was clearly seen in the AA map with the three methods employed, indicating the potential of these maps to detect micro-calcifications. AA maps present lower quality than SS reconstructions. Here the amplitude errors due to uncertainties in the positions ans sensitivity of the detectors, as well as the artifacts propagated from the errors in the estimation of the SS maps considerably affect the reconstruction quality. Despite this, the use of FWI improves considerable the quality of the AA reconstruction, evidencing the need to correct for the before mentioned issues.

The reconstruction times when using the FBP method, were less than 1 second (employed for data processing and FBP) and for the Bézier method, were around 1 minute. These times show the potential of our rays-algorithms to be compatible with the time requirements of clinical practice. On the other hand, were larger ($\sim$1 hour). Nevertheless, this time is reasonable and even low for these reconstructions [Wang et al., 2015], where generally several hours are required.

Compared to synthetic data, working with real data requires to consider many additional situations such as the need to accurately estimate the initial source representation or the positions of the detectors, among others. However, despite these issues we were capable of obtaining encouraging results.

Summary and conclusions

The main contributions and conclusions of the thesis are summarized in this chapter.

Development and implementation of geometrical acoustics algorithms for USCT

Chapter 3 of this thesis was dedicated to investigate several methods and algorithms for image reconstruction in USCT, using the approach of geometrical acoustics. We analyzed the reconstruction of two acoustic properties that present promising capabilities for the representation of soft tissues: the speed of sound and the acoustic attenuation. One of the basic requirements of these algorithms, is to account with accurate estimations of the time of flight and the amplitude of the measured signals that were transmitted across the investigated tissue. Different approaches to obtain these two parameters from the recorded signals were analyzed. These values were integrated into two types of geometrical acoustics approximations: one in which the energy propagation of the wave was assumed to happen along straight trajectories between the source and the receiver (considering heterogeneous acoustic mediums), and other in which the refraction experienced by the wavefront, due to impedance changes of the medium, was taken into account. To test all the methods and algorithms proposed in this chapter we used synthetic data obtained with the code *k-Wave* [Treeby and Cox, 2010b]

The conclusions of these studies were:

- The use of the cross correlation between the source and the measured signals provides a robust and accurate method to obtain the time of flight. The amplitude of the recorded waveform can be accurately estimated using the maximum value of its envelope, which only presents small variations in the presence of noise.
- Regarding the reconstructions using analytic methods to recover sound speed and acoustic attenuation maps, we saw that the method implemented allows for very fast estimations of both acoustic distributions ($\sim$1 second). These processing times make them suitable for real time reconstruction during the acquisition process. Nevertheless, the resolution of the resulting images was low, especially in the case of acoustic attenuation maps, where the actual attenuation information of the structures studied of the phantom was very distorted.

- Iterative bent-rays tracing methods improve the resolution of the sound speed reconstructions. However, the reconstruction time is increased in several orders of magnitude, while the resolution improvement is modest.
- We proposed a bent-rays method based on Bézier polynomials, simple and fast. It provides correct sound speed maps. However, the reconstruction of the acoustic attenuation maps with this methods does not improve significantly.
- Geometrical acoustic algorithms are not suitable to obtain high quality acoustic attenuation. They can not account for processes beyond transmission and refraction (when using bent-rays). The amplitude of the signals is affected by other processes that are also important during the wave propagation, such as diffraction or interference. Full-wave inversion (FWI) algorithms seem to be needed to obtain good quality acoustic attenuation maps.

Development and implementation of time domain FWI algorithms

Chapter 4 of this thesis was focused in a time domain FWI algorithm to obtain both speed of sound and acoustic attenuation distributions in USCT. The algorithm was based on an adjoint formulation derived from the fractional Laplacian wave equation, and allows for both distributions to be efficiently reconstructed within a common framework. The performance of the algorithm was demonstrated with synthetic data.

The main conclusions of this part of the thesis can be summarized as follows:

- The proposed algorithm is capable of accurately recovering the shape and magnitude of the structures in the image, both for sound speed and acoustic attenuation distributions. Particularly, attenuation maps are better reproduced in comparison with geometrical acoustics algorithms.
- The comparisons with previous studies based on frequency domain algorithms in terms of the resolution and noise obtained in the reconstructed images, supports the equivalence of both formulations. The time domain formulation we proposed avoids the need to select an appropriate set of frequencies, a step required by frequency domain formulations.
- The main limitation of the algorithm proposed is the dependence of the attenuation reconstruction on errors present in the sound speed maps. This was seen to be due to the cost function employed, which is more dependent on misalignments of the time of flight of the signals than on the differences of amplitudes.

Use of a generalized cost function for FWI reconstruction in USCT

In chapter 5 of this thesis, we proposed a new generalized misfit function to improve the reconstruction of sound speed and acoustic attenuation maps in USCT. Besides the standard least squares misfit function, the proposed misfit function includes two additional terms . These terms make the cost function more sensitive to amplitude differences of the signals and, at the same time, provide a FWI method to obtain the initial estimate of sound speed reconstruction.

This generalized cost function presents the following advantages:

- Obtaining the initial sound speed image with the travel time misfit term included in our generalized misfit, increased only slightly the total reconstruction time, and facilitates the use of only one method, based on FWI, to perform the reconstruction.
- The combination of the least-squares and amplitude misfit cost functions makes the reconstruction of the acoustic attenuation a more convex problem, with a convergence more robust against deviations in the sound speed map.
- By incorporating a total variation regularization term, we can further reduce the noise and artifacts in the image, while preserving the edges in the information.
- With the proposed misfit function, we were not only able to decrease the bias in the reconstruction of attenuation maps, but also we were able to obtain more homogeneous bias values in the different regions studied. This shows that this generalized misfit function is to a large extent, less sensitive to the sound speed distribution.

Reconstruction of real USCT data

Chapter 6 was dedicated to the application of the methods developed in previous chapters to the reconstruction of real data from the MUBI USCT scanner. Due to the many difficulties that appear when using real data in comparison with synthetic data, several methods to calibrate the system and methods for data processing, had to be derived. Two configurations for the experimental setup were employed to test our reconstructions, one with the larger possible radius of the arrays, 100 mm, and another with a smaller radius of 50 mm. The larger configuration was used to scan an *in-vitro* tissue mimicking phantom simulating breast tissue. The smaller one was tested with a boiled egg with a needle inserted to recreate a micro-calcification. Due to the frequency of the signals acquired and the large setup configuration, the tissue mimicking phantom was only reconstructed with our GAc algorithms. The smaller configuration, after low-pass filtering of the signals down to 2 MHz, allow us applying both rays and FWI algorithms to reconstruct the boiled egg.

The conclusions obtained are the following:

- The results for the reconstructions of the speed of sound using ray-algorithms confirmed that FBP miss-calculates, the sizes of the structures present in the phantom and also the values of sound speed. On the other hand, the Bézier-based method is able to get good results and improved image quality.
- The reconstruction of the acoustic attenuation with geometrical acoustics algorithms presented worse results than sound speed reconstructions. Nevertheless, as the frequency used was higher than the one used in the numerical experiments performed in chapter 3, this was not as important as for the numerical examples. This evidences the advantages of using higher frequencies.
- For the egg acquisition, we were able to confirm that FWI and Bézier-based methods provide very similar sound speed maps, showing the capability of this bent-rays method to obtain high quality sound speed reconstructions.
- The needle inserted in the egg was not seen in the sound speed maps with any of the methods implemented. On the other hand, the needle was very visible in attenuation map from the three methods employed, indicating the potential of attenuation maps to detect micro-calcifications.
- Acoustic attenuation maps were worse than speed maps for the three methods used. The quality of attenuation reconstructions was affected by two factors: first, errors in the amplitude due to uncertainties in the estimations of the location of the detectors, and second, artifacts propagated from the errors in the estimation of speed maps. Despite this, FWI methods improve considerable the quality of the attenuation reconstruction, evidencing the need to correct for the before mentioned issues to further improve attenuation images.
- The reconstruction times when using the FBP method, were below 1 second (for data processing and inverse Radon transform). For the Bézier method, they were around 1 minute. Our rays-algorithms bear the potential for being employed in clinical practice. On the other hand, FWI required larger reconstruction times ($\sim$1 hour). This is a considerable improvement for this type of reconstructions [Wang et al., 2015], where generally several hours are required.

General conclusion

As a summarizing conclusion, with this thesis we successfully included the transmission modality in the MUBI scanner. We provided several approaches for sound speed and attenuation reconstruction that are capable to provide fast and high quality images. To obtain real time reconstructions, we propose to use our analytic methods that are able to give general information of the inspected region. To improve this information, our Bézier-based bent-rays method can be used during post-processing of the data for sound speed reconstructions. If any suspicious region is observed (very high speed of sound), complimentary information can be

obtained from the FWI reconstruction of the acoustic attenuation. Further experimental tests are still required to validate our reconstruction algorithms. Nevertheless, either with the ray-based methods and the FWI, our algorithms have been tested with both synthetic and experimental data, showing very encouraging results in terms of quality and reconstruction times. We expect these results could be useful to expand and improve this promising technique.

Contributions of this thesis

The ideas and main contributions of this thesis appear in the following works:

JOURNAL ARTICLES (directly related with the thesis' subjects)

- **M. Perez-Liva**, J.L. Herraiz, J.M. Udías, E. Miller, B.T. Cox, B.E. Treeby. Full Wave Reconstruction in Time Domain of Attenuation and Speed of Sound in Ultrasound Computed Tomography. The Journal of the Acoustic Society of America,141(3), 2017.
- Cal-González, J., **Pérez-Liva, M.**, Herraiz, J. L., Vaquero, J. J., Desco, M., and Udías, J. M. (2015). Tissue-dependent and spatially-variant positron range correction in 3D PET. Medical Imaging, IEEE Transactions on, 34(11), 2394-2403.
- L.M. Fraile, J.L. Herraiz, J.M. Udías, J. Cal-González, P.M.G. Corzo, S. España, E. Herranz, **M. Pérez-Liva**, E. Picado, E. Vicente, A. Muñoz-Martín, J.J. Vaquero, Experimental validation of gallium production and isotope-dependent positron range correction in PET, Nuclear Instruments and Methods in Physics Research Section A: Accelerators, Spectrometers, Detectors and Associated Equipment, Volume 814, 1 April 2016, Pages 110-116, ISSN 0168-9002

CONFERENCE PAPERS (Peer reviewed and published in scientific journals)

- **Pérez-Liva M.**, Udías J.M., Herraiz J.L. (March 13, 2017). Improved misfit function for attenuation and speed reconstruction in ultrasound computed tomography. Proc. SPIE vol. 10139, Medical Imaging 2017: Ultrasonic Imaging and Tomography, pp. 101390O-101390O-7, doi:10.1117/12.2253849
- **Pérez-Liva, M.**, Herraiz, J. L., Udías, J. M., Cox, B. T., and Treeby, B. E. (2016, April). Full-wave attenuation reconstruction in the time domain for ultrasound computed tomography. In Biomedical Imaging (ISBI), 2016 IEEE 13th International Symposium on (pp. 710-713),doi: 10.1109/ISBI.2016.7493365
- **M. Pérez-Liva,** J. L. Herraiz, N. González-Salido, L. Medina-Valdés, J. Camacho, C. Fritch, J.M. Udías "Ultrasound Computed Tomography for Quantitative Breast Imaging", 2016 Global Medical Engineering Physics Exchanges/Pan American Health Care Exchanges (GMEPE/PAHCE), pp 1-6, 2016.
- N. González-Salido, L. Medina Valdés, J. Camacho, **M. Pérez Liva**, J. Herraiz JL, J. M.

Udías “Non-contact elastographic techniques”, 2016 Global Medical Engineering Physics Exchanges/Pan American Health Care Exchanges (GMEPE/PAHCE), pp 1-5, 2016.

- L. Medina Valdés N. González-Salido, J. Camacho, **M. Pérez Liva**, J. Herraiz JL, J. M. Udías “Refraction Correction in Full Angle Spatial Image Compounding”, 2016 Global Medical Engineering Physics Exchanges/Pan American Health Care Exchanges (GMEPE/PAHCE), pp 1-5, 2016.
- Medina-Valdés, L., **Pérez-Liva, M.**, Camacho, J., Udías, J. M., Herraiz, J. L., and González-Salido, N. (2015). Multi-modal Ultrasound Imaging for Breast Cancer Detection. Physics Procedia, 63, 134-140.

OTHER CONFERENCE PROCEEDINGS

- **M. Perez-Liva**, J.L. Herraiz, E. Miller, B.T. Cox, B.E. Treeby, J.M. Udías. "Sound speed reconstruction in full wave ultrasound computer tomography for breast cancer detection" Radiotherapy and Oncology, vol 119, pp. S454-S455, 2016.
- **Mailyn Pérez-Liva**, Joaquín L. Herraiz, Luis Medina-Valdés, Jorge Camacho, Carlos Fritsch, Bradley E. Treeby, and José M. Udías. Regularization of Image Reconstruction in Ultrasound Computed Tomography. Proc. IEEE NSS-MIC 2015 pp 1-3.
- Vaquero, J. J., Cal-Gonzalez, J., **Perez-Liva, M.**, Herraiz, J. L., Desco, M., and Udias, J. M. (2016). Improving the Image Quality of High Energy Positron Based Tracers Using a Novel Tissue-Dependent, Spatially-Variant Positron Range Correction. Journal of Nuclear Medicine, 57(2), 475-475.
- **M. Perez-Liva**, J.L. Herraiz, L. Medina-Valdés, J. Camacho, C. Fritsch, P. Ibáñez, J.M. Udías. Ultrasound Computed tomography for early breast cancer detection. Radiotherapy and Oncology, 2015, vol 115(S.1):65. 3rd ESTRO Forum. Barcelona, Spain, April 24-28, 2015.
- E. Herranz, J.L. Herraiz, P. Guerra, J.Cal-González, **M. Pérez-Liva**, R. Rodríguez, C. Illana,; M. Ledesma, J. Calama, J.M. Udías. Iterative Determination of Clinical Beam Phase Space from Dose Measurements. [54th Annual Meeting of the American Society for Radiation Oncology (ASTRO) Int. J. Radiat. Oncol. Biol. Phys., ISBN: 0360-3016. 84 - 3, Elsevier Science

OTHER JOURNAL ARTICLES ACHIEVED DURING THE THESIS

- Padilla-Cabal, F., **Pérez-Liva, M.**, Lara, E., Alfonso, R., and Lopez-Pino, N. (2015). Monte Carlo calculations of an Elekta Precise SL-25 photon beam model. Journal of Radiotherapy in Practice, 14(03), 311-322.
- E. Herranz, J.L. Herraiz, P. Ibáñez, **M. Pérez-Liva**, R. Puebla, J. Cal-González, P. Guerra, R. Rodríguez, C. Illana, J.M. Udías. Phase space determination of electron beam for intraoperative radiation therapy from measured dose data. Phys. Med. Biol. 2015; 60(1):375-401.

- Lică, R., Borge, M., Kurcewicz, J., Madurga, M., Rapisarda, E., Mărginean, N., ..., **Pérez-Liva M**. . . . and Mihai, C. (2016). Fast-Timing Study Of The L-Forbidden 12+→32+ M1 Transition In Sn 129 Physical Review C, 93(4), 044303.
- García Álvarez, J. A., López Pino, N., Díaz Rizo, O., Corrales, Y., Padilla Cabal, F., **Pérez Liva, M**. and Maidana, N. L. (2013). Measurement of the photoeffect cross section and the K-absorption edge energy of Dy, Ta, Pt and Au atoms using bremsstrahlung. Nucleus, 54.

WORKS PRESENTED IN CONFERENCES AT THE NATIONAL OR INTERNATIONAL LEVEL

- Modality: Oral presentation
  Title : Improved misfit function for attenuation and speed reconstruction in ultrasound computed tomography
  Authors: **Pérez-Liva M.**, Udías J.M, Herraiz J.L.
  Event : SPIE Medical Imaging 2016
  Date : February, 2017
  Place : Orlando, Florida, USA.

- Modality: Poster
  Title: Full-wave attenuation reconstruction in the time domain for ultrasound computed tomography.
  Authors: **Pérez-Liva M**., Herraiz J.L., Udías J.M., Cox B.T.,Treeby B.E.
  Event : IEEE Intl Symp Biomedical Imaging ISBI, 2016.
  Date : April 2016.
  Place : Prague, CZ.

- Modality : Poster
  Title : Sound speed reconstruction in full wave ultrasound computer tomography for breast cancer detection.
  Authors : **M. Perez-Liva**, J.L. Herraiz, E. Miller, B.T. Cox, B.E. Treeby, J.M. Udías
  Event : 13th ESTRO Congress.
  Date : May 2016.
  Place : Turin, Italy

- Modality : Oral presentation
  Title : Ultrasound Computed Tomography for Quantitative Breast Imaging
  Authors : **M. Pérez-Liva**, J. L. Herraiz, N. González-Salido, L. Medina-Valdés, J. Camacho, C. Fritch, J.M. Udías
  Event : IEEE Global Medical Engineering Physics Exchanges (GMEPE) and Pan American Health Care Exchanges (PAHCE),
  Date : 4-9 Apr. 2016.

Place : Madrid, Spain.

- Modality : Poster
  Title : Non-contact elastographic techniques
  Authors: N. González-Salido, L. Medina Valdés, J. Camacho, **M. Pérez Liva**, J. Herraiz JL, J. M. Udías
  Event : IEEE Global Medical Engineering Physics Exchanges (GMEPE) and Pan American Health Care Exchanges (PAHCE),
  Date : 4-9 Apr. 2016.
  Place : Madrid, Spain.

- Modality : Poster
  Title: Refraction Correction in Full Angle Spatial Image Compounding
  Authors: L. Medina Valdés N. González-Salido, J. Camacho, **M. Pérez Liva**, J. Herraiz JL, J. M. Udías
  Event : IEEE Global Medical Engineering Physics Exchanges (GMEPE) and Pan American Health Care Exchanges (PAHCE),
  Date : 4-9 Apr. 2016.
  Place : Madrid, Spain.

- Modality : Poster
  Title : Regularization of Image Reconstruction in Ultrasound Computed Tomography
  Authors: **Mailyn Pérez-Liva**, Joaquín L. Herraiz, Luis Medina-Valdés, Jorge Camacho, Carlos Fritsch, Bradley E. Treeby, and José M. Udías
  Event: IEEE NSS-MIC 2015.
  Date: 31 Oct -7 Nov, 2015
  Place: San Diego, USA.

- Modality: Poster and Poster discussion (5 minutes oral presentation)
  Title: Ultrasound Computed tomography for early breast cancer detection
  Authors: **Pérez-Liva M.**, J L Herraiz, L Medina-Valdés , J Camacho , C Fritsch , P Ibañez and J M Udías. Event: 3rd ESTRO FORUM 2015.
  Date: 24-28 abril de 2015
  Place: Barcelona, Spain

- Modality: Oral presentation
  Title: Application of the Fast Marching Method in Ultrasound Computed tomography for early breast cancer detection
  Authors: **Pérez-Liva M.**, J L Herraiz, L Medina-Valdés , J Camacho , C Fritsch and J M Udías.
  Event: IV Congreso Conjunto de la Sociedad Española de Física Médica y la Sociedad Es-

pañola de Protección Radiológica
Date: 23 al 26 de junio 2015
Place: Ciudad Politécnica de la Innovación de la Universidad Politécnica de Valencia, Spain

- Modality: Oral presentation
  Title: Full wave reconstruction method in time domain for ultrasound computer tomography
  Authors: **Perez-Liva M**, Herrainz JL, Miller E, Udias JM.
  Event: XXXV Reunión Bienal de la Real Sociedad Española de Física
  Date: 13-17 julio 2015
  Place: Gijón, Spain.

- Modality: Poster
  Title: Multi-modal Ultrasound Imaging for Breast Cancer Detection
  Authors: Medina-Valdés, L., **Pérez-Liva, M.**, Camacho, J., Udías, J. M., Herraiz, J. L., and González-Salido, N
  Event: 43rd Annual Symposium of the Ultrasonic Industry Association 2014.
  Date: 23-25 April,2014
  Place: Madrid, España.

- Modality: Poster
  Title: Spatially-variant positron range correction in 3D PET imaging
  Authors: J. Cal-González, J. L. Herraiz, **M. Pérez-Liva**, J. J. Vaquero, M. Desco and J. M. Udías
  Event: 2014 IEEE Nuclear Science Symposium and Medical Imaging Conference
  Date: 8-15 Nov, 2014
  Place: Seattle, WA, USA

- Modality: Poster
  Title: Iterative Reconstruction of Clinical Electron Beam Phase Space for Intra-Operative Radiation Therapy
  Authors: E. Herranz, P.Ibañez, J.L. Herraiz, **M. Pérez-Liva**, M. Vidal, P. Guerra, J.M. Udías.
  Event: ICTR-PHE 2014. February 2014
  Fecha : 10-14 Feb, 2014
  Place: Centre International de Conférences de Genève (CICG), Suisse.

- Modality: Poster
  Título: Phase space determination of electron beam for intraoperative radiation therapy from measured dose data
  Authors: Elena Herranz; Joaquín López; Paula Ibáñez; **Mailyn Pérez Liva**; Ricardo Puebla; Pedro Guerra;

Jose Manuel Udías. Event: XXXIV Reunión Bienal de la Sociedad Española de Física
Place: Valencia, Comunidad Valenciana, España
Date: 15-18 July, 2013

- Modality: Poster.
  Title: Verificación del algoritmo de determinación de espacios de fase para Radioterapia Intraoperatoria (RIO) a partir de medidas experimentales
  Authors: Paula Ibáñez; Elena Herranz; **Mailyn Pérez Liva**; Ricardo Puebla; Pedro Guerra; Carlos Illana;; Raul Rodríguez; Juan Calama; Miguel Ángel Infante; Elisa Lavado; José Manuel Udías.
  Event: XXXIV Reunión Bienal de la Sociedad Española de Física
  Place: Valencia, Comunidad Valenciana, España
  Date: 15-18 de julio 2013

Bibliography

Usct data exchange and collaboration. http://ipeusctdb1.ipe.kit.edu/~usct/challenge/. Accessed: 2017-03-20.

M. Abella, J. J. Vaquero, M. Soto-Montenegro, E. Lage, and M. Desco. Sinogram bow-tie filtering in fbp pet reconstruction. *Medical physics*, 36(5):1663–1671, 2009.

K. Aki and P. G. Richards. *Quantitative seismology*, volume 1. University Science Books, 2002.

J. E. Aldrich. Basic physics of ultrasound imaging. *Critical care medicine*, 35(5):S131–S137, 2007.

A. Alessio and P. Kinahan. Pet image reconstruction. *Nuclear medicine*, 2, 2006a.

A. Alessio and P. E. Kinahan. *Nuclear Medicine*, chapter "PET image reconstruction". Elsevier, 2006b. ISBN 978-0323028981.

R. Alteri, P. Bandi, L. Brinton, C. Casares, V. Cokkinides, T. Gansler, et al. Breast cancer facts & figures 2011-2012. *American Cancer Society*, pages 1–36, 2011.

A. Y. Anagaw. *Total variation and adjoint state methods for seismic wavefield imaging*. PhD thesis, University of Alberta, 2009.

A. H. Andersen. A ray tracing approach to restoration and resolution enhancement in experimental ultrasound tomography. *Ultrasonic imaging*, 12(4):268–291, 1990.

M. André, J. Wiskin, and D. Borup. Clinical results with ultrasound computed tomography of the breast. In *Quantitative Ultrasound in Soft Tissues*, pages 395–432. Springer, 2013.

F. Anis, Y. Lou, A. Conjusteau, R. Su, T. Oruganti, S. A. Ermilov, A. A. Oraevsky, and M. A. Anastasio. Investigation of the adjoint-state method for ultrasound computed tomography: a numerical and experimental study. In *SPIE BiOS*. International Society for Optics and Photonics, 2014.

M. Ashfaq. *Measuring and signal processing techniques for ultrasound computed tomography*. PhD thesis, Ruhr University, 2007.

H. Azhari. *Basics of biomedical ultrasound for engineers*. John Wiley & Sons, 2010.

N. Bakhvalov. Courant–friedrichs–lewy condition. *Encyclopedia of Mathematics*, 2001.

J. Bamber. Attenuation and absorption. In *Physical principles of medical ultrasonics*, pages 118–186. Ellis Horwood Limited Chichester, 1986.

B. Barnett, I. Kryczek, P. Cheng, W. Zou, and T. J. Curiel. Regulatory t cells in ovarian cancer: biology and therapeutic potential. *American journal of reproductive immunology*, 54(6):369–377, 2005.

J. Beutel, H. L. Kundel, and R. L. Van Metter. Handbook of medical imaging: Physics and psychophysics. 1, 2000.

P. E. Bézier. How renault uses numerical control for car body design and tooling. Technical report, SAE Technical Paper, 1968.

A. S. Bhadauria, C. A. de Saracibar, M. Chiumenti, and M. Cervera. Hdf5: A new approach to interoperability in finite element tools. In *2nd International Workshop on Software Solutions for Integrated Computational Materials Engineering*. ICME, 2016.

N. F. Boyd, L. J. Martin, M. Bronskill, M. J. Yaffe, N. Duric, and S. Minkin. Breast tissue composition and susceptibility to breast cancer. *Journal of the National Cancer Institute*, 2010.

E. Bozdağ, J. Trampert, and J. Tromp. Misfit functions for full waveform inversion based on instantaneous phase and envelope measurements. *Geophysical Journal International*, 185(2): 845–870, 2011.

L. Brekhovskikh. The propagation sound a liquid layer with constant propagation velocity gradient. In *Dokl. Akad. Nauk SSSR*, volume 62, page 469, 1948.

L. Brogoch, M. André, M. Ledgerwood, H. Ojeda-Fournier, L. Olson, M. Galperin, M. O'Boyle, C. Comstock, and M. Aiken. Reader variability and predictive value of breast imaging reporting and data system descriptors for lesions in breast sonography. *Journal of Ultrasound Medicine*, 29:S47, 2010.

M. J. Buckingham. Theory of acoustic attenuation, dispersion, and pulse propagation in unconsolidated granular materials including marine sediments. *The Journal of the Acoustical Society of America*, 102(5):2579–2596, 1997.

C. Byrne. The emml and smart algorithms. *UMass Library*, 2006.

J. Cal-González, M. Pérez-Liva, J. L. Herraiz, J. J. Vaquero, M. Desco, and J. M. Udías. Tissue-dependent and spatially-variant positron range correction in 3d pet. *IEEE transactions on medical imaging*, 34(11):2394–2403, 2015.

J. Camacho, L. Medina, J. F. Cruza, J. M. Moreno, and C. Fritsch. Multimodal ultrasonic imaging for breast cancer detection. *Archives of Acoustics*, 37(3):253–260, 2012.

J. Camacho Sosa Dias. *Imagen ultrasónica por coherencia de fase*. Universidad Complutense de Madrid, Servicio de Publicaciones, 2011.

P. L. Carson, C. R. Meyer, A. L. Scherzinger, and T. V. Oughton. Breast imaging in coronal planes with simultaneous pulse echo and transmission ultrasound. *Science*, 214(4525):1141–1143, 1981.

E. L. Carstensen. The mechanism of the absorption of ultrasound in biological materials. *IRE transactions on medical electronics*, (3):158–162, 1960.

H. Chauris, D. Donno, and H. Calandra. Velocity estimation with the normalized integration method. In *74th EAGE Conference and Exhibition incorporating EUROPEC*, 2012.

W. Chen and S. Holm. Fractional laplacian time-space models for linear and nonlinear lossy media exhibiting arbitrary frequency power-law dependency. *The Journal of the Acoustical Society of America*, 115(4):1424–1430, 2004.

R. S. Cobbold. *Foundations of biomedical ultrasound*. Oxford University Press, 2006.

T. S. Curry, J. E. Dowdey, and R. Murray. Introduction to the physics of diagnostic radiology. 1984.

R. Dapp, H. Gemmeke, and N. Ruiter. 3d refraction-corrected transmission reconstruction for 3d ultrasound computer tomography. In *SPIE Medical Imaging*. International Society for Optics and Photonics, 2012.

L. Demi, K. Van Dongen, and M. Verweij. A contrast source method for nonlinear acoustic wave fields in media with spatially inhomogeneous attenuation. *The Journal of the Acoustical Society of America*, 129(3):1221–1230, 2011.

A. Dempster, N. Laird, and D. Rubin. Maximum likelihood from incomplete data via the EM algorithm. *Journal of the Royal Statistical Society*, 39:1–38, 1977.

J. D'Errico. Inpaint nans, 2005. URL `https://es.mathworks.com/matlabcentral/fileexchange/4551-inpaint-nans`. Last Accessed: 2017-01-19.

A. Devaney. Inverse-scattering theory within the rytov approximation. *Optics letters*, 6(8):374–376, 1981.

A. Devaney. Inversion formula for inverse scattering within the born approximation. *Optics Letters*, 7(3):111–112, 1982.

E. W. Dijkstra. A note on two problems in connexion with graphs. *Numerische mathematik*, 1 (1):269–271, 1959.

I. Donald. *Practical obstetric problems*. Lloyd-Luke, 1969.

F. A. Duck. *Physical properties of tissues: a comprehensive reference book*. Academic press, 2013.

N. Duric, P. Littrup, A. Babkin, D. Chambers, S. Azevedo, A. Kalinin, R. Pevzner, M. Tokarev, E. Holsapple, O. Rama, and R. Duncan. Development of ultrasound tomography for breast imaging: Technical assessment. *Medical Physics*, 32(5):1375–1386, 2005.

N. Duric, C. Li, P. Littrup, C. Glide-Hurst, L. Huang, J. Lupinacci, S. Schmidt, O. Rama, L. Bey-Knight, and Y. Xu. Multi-modal breast imaging with ultrasound tomography. In *Medical Imaging*. International Society for Optics and Photonics, 2008.

N. Duric, P. Littrup, C. Li, O. Rama, L. Bey-Knight, S. Schmidt, and J. Lupinacci. Detection and characterization of breast masses with ultrasound tomography: clinical results. In *SPIE Medical Imaging*. International Society for Optics and Photonics, 2009.

N. Duric, P. Littrup, C. Li, O. Roy, S. Schmidt, J. Seamans, A. Wallen, and L. Bey-Knight. Whole breast tissue characterization with ultrasound tomography. In *SPIE Medical Imaging*. International Society for Optics and Photonics, 2015.

R. Errabolu, C. Sehgal, and J. F. Greenleaf. Dependence of ultrasonic nonlinear parameter b/a on fat. *Ultrasonic imaging*, 9(3):180–194, 1987.

F. H. Fahey. Data acquisition in pet imaging. *Journal of nuclear medicine technology*, 30(2): 39–49, 2002.

S. A. Feig. Screening mammography benefit controversies: sorting the evidence. *Radiologic Clinics of North America*, 52(3):455–480, 2014.

F. A. Firestone. Flaw detecting device and measuring instrument, Apr. 21 1942. US Patent 2,280,226.

B. D. Fornage, J. G. Lorigan, and E. Andry. Fibroadenoma of the breast: sonographic appearance. *Radiology*, 3:671–675, 1989.

A. R. Forrest. Interactive interpolation and approximation by bézier polynomials. *The Computer Journal*, 15(1):71–79, 1972.

V. Gazhonova. The history of abvs. In *3D Automated Breast Volume Sonography*, pages 1–3. Springer, 2017.

G. Glover and J. Sharp. Reconstruction of ultrasound propagation speed distributions in soft tissue: time-of-flight tomography. *IEEE Transactions on Sonics and Ultrasonics*, 24(4):229–234, 1977.

M. P. Goldie. Breast cancer: the latest science, 2011. URL `http://www.dentistryiq.com/articles/2011/10/breast-cancer-latest.html`. Last Accessed: 2017-02-14.

J. Gómez. Advanced applications of the fast marching square planning method. Master's thesis, Carlos III University, 2013.

J. Gómez, J. Pardeiro, and G. P. N-dimensional fast marching method v1.0, 2016. URL `https://github.com/jvgomez/fastmarching`. Last Accessed: 2017-03-19.

N. González-Salido, L. Medina, J. Camacho, M. Pérez-Liva, J. Herraiz, and J. Udías. Non contact elastographic techniques. In *2016 Global Medical Engineering Physics Exchanges/Pan American Health Care Exchanges (GMEPE/PAHCE)*, pages 1–5. IEEE, 2016.

J. F. Greenleaf, S. Johnson, S. Lee, G. Hermant, and E. Woo. Algebraic reconstruction of spatial distributions of acoustic absorption within tissue from their two-dimensional acoustic projections. In *Acoustical holography*, pages 591–603. Springer, 1974.

J. F. Greenleaf, S. A. Johnson, W. F. Samayoa, and F. A. Duck. Algebraic reconstruction of spatial distributions of acoustic velocities in tissue from their time-of-flight profiles. In *Acoustical holography*, pages 71–90. Springer, 1975.

P. Hasgall, F. Di Gennaro, C. Baumgartner, E. Neufeld, M. Gosselin, D. Payne, A. Klingenböck, and N. Kuster. "it'is database for thermal and electromagnetic parameters of biological tissues," version 3.0, september 01st, 2015, doi: 10.13099/vip21000-03-0., 2015. URL `www.itis.ethz.ch/database`. Last Accessed: 2016-11-29.

G. T. Herman. *Fundamentals of Computerized Tomography*, chapter "Image reconstruction from projections". Academic Press, 1980. ISBN 978-1-84628-723-7.

K. Herzfeld and F. Rice. Dispersion and absorption of high frequency sound waves. *Physical Review*, 31(4):691, 1928.

S. H. Heywang-Köbrunner, A. Hacker, and S. Sedlacek. Advantages and disadvantages of mammography screening. *Breast care*, 6(3):199–207, 2011.

C. R. Hill, J. C. Bamber, and G. ter Haar. *Physical principles of medical ultrasonics*, volume 2. Wiley Online Library, 2004.

A. Hormati, I. Jovanovic, O. Roy, and M. Vetterli. Robust ultrasound travel-time tomography using the bent ray model. In *Proceedings SPIE*, volume 7629, 2010.

J. Hsieh. *Computed tomography: principles, design, artifacts, and recent advances*, volume 114. SPIE press, 2003.

H. M. Hudson and R. S. Larkin. Accelerated image reconstruction using ordered subsets of projection data. *Medical Imaging, IEEE Transactions on*, 4:601–609, 1994.

D. D. Jackson. Interpretation of inaccurate, insufficient and inconsistent data. *Geophysical Journal International*, 2:97–109, 1972.

J. Jago and T. Whittingham. Experimental studies in transmission ultrasound computed tomography. *Physics in medicine and biology*, 36(11):1515, 1991.

J. R. Jago. Experimental and theoretical studies of ultrasound computed tomography. 1993.

J. Jaros, A. P. Rendell, and B. E. Treeby. Full-wave nonlinear ultrasound simulation on distributed clusters with applications in high-intensity focused ultrasound. *International Journal of High Performance Computing Applications*, pages 137–155, 2015.

J. Jaros, F. Vaverka, and B. E. Treeby. Spectral domain decomposition using local fourier basis: Application to ultrasound simulation on a cluster of gpus. *Supercomputing frontiers and innovations*, 3(3):40–55, 2016.

C. Javanaud, R. Rahalkar, and P. Richmond. Measurement of speed and attenuation of ultrasound in egg white and egg yolk. *The Journal of the Acoustical Society of America*, 76 (3):670–675, 1984.

S. Johnson, J. F. Greenleaf, W. Samayoa, F. Duck, and J. Sjostrand. Reconstruction of three-dimensional velocity fields and other parameters by acoustic ray tracing. In *1975 Ultrasonics Symposium*, pages 46–51. IEEE, 1975.

S. A. Johnson, T. Abbott, R. Bell, M. Berggren, D. Borup, D. Robinson, J. Wiskin, S. Olsen, and B. Hanover. Non-invasive breast tissue characterization using ultrasound speed and attenuation. In *Acoustical imaging" (, Netherlands*, pages 147–154. 2007.

I. Jovanović. *Inverse problems in acoustic tomography: theory and applications*. PhD thesis, 2008.

A. C. Kak and M. Slaney. *Principles of Computerized Tomographic Imaging*. Society for Industrial Mathematics, 1988. ISBN 978-0898714944.

L. E. Kinsler, A. R. Frey, A. B. Coppens, and J. V. Sanders. *Fundamentals of acoustics*. Wiley-VCH, 4th edition, 1999. ISBN 0-471-84789-5.

C. Knapp and G. Carter. The generalized correlation method for estimation of time delay. *IEEE Transactions on Acoustics, Speech, and Signal Processing*, 24(4):320–327, 1976.

W. E. Krause, O. H. Kresse, and R. E. Soldner. Ultrasound diagnostic apparatus, Oct. 7 1969. US Patent 3,470,868.

E. Kretzek, T. Hopp, and N. Ruiter. Gpu-based 3d saft reconstruction including attenuation correction. *SPIE Medical Imaging, International Society for Optics and Photonics, pp*, 9419, 2015.

F. R. Kschischang. The hilbert transform. *University of Toronto*, 2006.

A. Kyriakou. *Multi-Physics Computational Modeling of Focused Ultrasound Therapies*. PhD thesis, Eidgenössische Technische Hochschule ETH Zürich, 2015.

B. Larson. About NDT, 2010. URL `https://www.nde-ed.org/AboutNDT/aboutndt.htm`. Last Accessed: 2016-01-29.

M. W. Lenox, J. Wiskin, M. A. Lewis, S. Darrouzet, D. Borup, and S. Hsieh. Imaging performance of quantitative transmission ultrasound. *Journal of Biomedical Imaging*, 2015:13, 2015.

C. Li, N. Duric, and L. Huang. Comparison of ultrasound attenuation tomography methods for breast imaging. In *Medical Imaging*. International Society for Optics and Photonics, 2008a.

C. Li, N. Duric, and L. Huang. Breast imaging using transmission ultrasound: Reconstructing tissue parameters of sound speed and attenuation. 2:708–712, 2008b.

C. Li, N. Duric, and L. Huang. Breast ultrasound tomography with total-variation regularization. In *SPIE Medical Imaging*. International Society for Optics and Photonics, 2009a.

C. Li, N. Duric, P. Littrup, and L. Huang. In vivo breast sound-speed imaging with ultrasound tomography. *Ultrasound in medicine and biology*, 35(10):1615–1628, 2009b.

C. Li, G. S. Sandhu, O. Roy, N. Duric, V. Allada, and S. Schmidt. Toward a practical ultrasound waveform tomography algorithm for improving breast imaging. In *SPIE Medical Imaging*. International Society for Optics and Photonics, 2014.

S. Li, M. Jackowski, D. P. Dione, T. Varslot, L. H. Staib, and K. Mueller. Refraction corrected transmission ultrasound computed tomography for application in breast imaging. *Medical physics*, 37(5):2233–2246, 2010.

F. Lin, A. I. Nachman, and R. C. Waag. Quantitative imaging using a time-domain eigenfunction method. *The Journal of the Acoustical Society of America*, 108(3):899–912, 2000.

A. Macovski. Ultrasonic array for reflection imaging, Nov. 4 1975. US Patent 3,918,024.

J. Mamou and M. L. Oelze. *Quantitative ultrasound in soft tissues*. Springer, 2013.

J. J. Markham, R. T. Beyer, and R. Lindsay. Absorption of sound in fluids. *Reviews of Modern Physics*, 23(4):353, 1951.

T. D. Mast. Empirical relationships between acoustic parameters in human soft tissues. *Acoustics Research Letters Online*, 1(2):37–42, 2000.

A. McTiernan. Recent controversies in mammography screening for breast cancer. *Medscape women's health*, 7(2):3–3, 2001.

L. Medina, J. Camacho, and C. Fritsch. A characterization of ultrasonic full angle spatial compounding as a possible alternative for breast cancer screening. *Archives of Acoustics*, 40 (3):301–310, 2015.

L. Medina, N. González-Salido, J. Camacho, M. Pérez-Liva, J. Herraiz, and J. Udías. Refraction correction in full angle spatial image compounding. In *2016 Global Medical Engineering Physics Exchanges/Pan American Health Care Exchanges (GMEPE/PAHCE)*, pages 1–4. IEEE, 2016.

L. Medina-Valdés, M. Pérez-Liva, J. Camacho, J. Udías, J. Herraiz, and N. González-Salido. Multi-modal ultrasound imaging for breast cancer detection. *Physics Procedia*, 63:134–140, 2015.

U. Niesen, D. Shah, and G. W. Wornell. Adaptive alternating minimization algorithms. *IEEE Transactions on Information Theory*, 55(3):1423–1429, 2009.

L. Noakes and T. Popiel. Geometry for robot path planning. *Robotica*, 25(06):691–701, 2007.

J. Nocedal and S. Wright. *Numerical optimization*. Springer Science & Business Media, 2006.

K. Nogami and A. Yamada. Evaluation experiment of ultrasound computed tomography for the abdominal sound speed imaging. *Japanese Journal of Applied Physics*, 46(7S):4820, 2007.

A. Norton. *Dynamic fields and waves*, volume 6. CRC Press, 2000.

S. J. Norton. Computing ray trajectories between two points: a solution to the ray-linking problem. *JOSA A*, 4(10):1919–1922, 1987.

S. J. Norton. Iterative inverse scattering algorithms: Methods of computing frechet derivatives. *The Journal of the Acoustical Society of America*, 106(5):2653–2660, 1999.

K. J. Opielinski. Ultrasonic parameters of hen's egg. *Mol Quant Acoust*, 28:203–217, 2007.

K. J. Opieliński, P. Pruchnicki, T. Gudra, and J. Majewski. Conclusions from a test of multi-modal ultrasound tomography research system designed for breast imaging. In *Proceedings of 7th Forum Acusticum*, 2014.

M. A. Perazella. Current status of gadolinium toxicity in patients with kidney disease. *Clinical Journal of the American Society of Nephrology*, 4(2):461–469, 2009.

M. Pérez-Liva, J. Herraiz, L. Medina-Valdés, J. Camacho, C. Fritsch, P. Ibánez, and J. Udías. Pd-0137: Ultrasound computed tomography for early breast cancer detection. *Radiotherapy and Oncology, p*, 65, 2015.

M. Pérez-Liva, J. Herraiz, N. González-Salido, L. Medina-Valdés, J. Camacho, C. Fritch, and J. Udías. Ultrasound computed tomography for quantitative breast imaging. In *2016 Global Medical Engineering Physics Exchanges/Pan American Health Care Exchanges (GMEPE/PAHCE)*, pages 1–6. IEEE, 2016.

M. Pérez-Liva, J. Herraiz, J. Udías, E. Miller, B. Cox, and B. Treeby. Time domain reconstruction of sound speed and attenuation in ultrasound computed tomography using full wave inversion a. *The Journal of the Acoustical Society of America*, 141(3):1595–1604, 2017.

G. Peyré. The numerical tours of signal processing. *Computing in Science & Engineering*, 13(4): 94–97, 2011.

G. F. Pinton, J. Dahl, S. Rosenzweig, and G. E. Trahey. A heterogeneous nonlinear attenuating full-wave model of ultrasound. *IEEE transactions on ultrasonics, ferroelectrics, and frequency control*, 56(3):474–488, 2009.

M. Postema. *Fundamentals of medical ultrasonics*. CRC Press, 2011.

R. G. Pratt and R. M. Shipp. Seismic waveform inversion in the frequency domain, part 2: Fault delineation in sediments using crosshole data. *Geophysics*, 64(3):902–914, 1999.

R. G. Pratt, L. Huang, N. Duric, and P. Littrup. Sound-speed and attenuation imaging of breast tissue using waveform tomography of transmission ultrasound data. In *Medical imaging*. International Society for Optics and Photonics, 2007.

M. Pérez-Liva, J. M. Udías, and J. L. Herraiz. Improved misfit function for attenuation and speed reconstruction in ultrasound computed tomography, 2017. URL `http://dx.doi.org/10.1117/12.2253849`. Last Accessed: 2016-12-23.

X. Qu, T. Azuma, H. Nakamura, H. Imoto, S. Tamano, S. Takagi, S.-I. Umemura, I. Sakuma, and Y. Matsumoto. Bent ray ultrasound tomography reconstruction using virtual receivers for reducing time cost. In *SPIE Medical Imaging*. International Society for Optics and Photonics, 2015.

J. Radon. On determination of functions by their integral values along certain multiplicities. *Ber. der Sachische Akademie der Wissenschaften Leipzig*, 69:262–277, 1917.

M. Ragozzino. Analysis of the error in measurement of ultrasound speed in tissue due to waveform deformation by frequency-dependent attenuation. *Ultrasonics*, 19(3):135–138, 1981.

W. Rakowski, M. R. Andersen, A. M. Stoddard, N. Urban, B. K. Rimer, D. S. Lane, S. A. Fox, and M. E. Costanza. Confirmatory analysis of opinions regarding the pros and cons of mammography. *Health Psychology*, 16(5):433, 1997.

J. Rickett. *Traveltime sensitivity kernels: Banana-doughnuts or just plain bananas?* Citeseer, 2000.

O. Roy, I. Jovanović, A. Hormati, R. Parhizkar, and M. Vetterli. Sound speed estimation using wave-based ultrasound tomography: theory and gpu implementation. In *SPIE Medical Imaging*. International Society for Optics and Photonics, 2010.

L. I. Rudin, S. Osher, and E. Fatemi. Nonlinear total variation based noise removal algorithms. *Physica D: Nonlinear Phenomena*, 60(1):259–268, 1992.

N. V. Ruiter, M. Zapf, T. Hopp, R. Dapp, and H. Gemmeke. Phantom image results of an optimized full 3d usct. *SPIE Medical Imaging, International Society for Optics and Photonics, pp*, 8320:5–6, 2012.

N. V. Ruiter, M. Zapf, T. Hopp, H. Gemmeke, and K. W. van Dongen. Usct data challenge. In *SPIE Medical Imaging*, pages 101391N–101391N. International Society for Optics and Photonics, 2017.

S2009/DPI-1802. Advanced real-time multimodality medical imaging, artemis. *Comunidad de Madrid*, 2009-2013.

S2013/MIT-3024. Positron emission and ultrasound tomograpy, topus. *Comunidad de Madrid*, 2013-2017.

G. Y. S. Sandhu, C. Li, O. Roy, E. West, K. Montgomery, M. Boone, and N. Duric. Frequency-domain ultrasound waveform tomography breast attenuation imaging. In *SPIE Medical Imaging*. International Society for Optics and Photonics, 2016.

R. J. Santen and R. Mansel. Benign breast disorders. *New England Journal of Medicine*, 353(3): 275–285, 2005.

C. n. d. e. d. g. y. s. r. Secretaría de Salud. Manual de exploración clínica de las mamas. *Programa Cáncer de la Mujer, D.F. SS-CNEGySR, ISBN 979-970-721-456-9*, pages 1–42, 2007.

J. A. Sethian. A fast marching level set method for monotonically advancing fronts. *Proceedings of the National Academy of Sciences*, 93(4):1591–1595, 1996.

L. Shepp and Y. Vardi. Maximum Likelihood Reconstruction for Emission Tomography. *IEEE Trans. Med. Imaging*, MI-1:113–122, 1982.

K. K. Shung and G. A. Thieme. *Ultrasonic scattering in biological tissues*. CRC press, 1992.

F. Simonetti and L. Huang. Synthetic aperture diffraction tomography for three-dimensional imaging. In *Proceedings of the Royal Society of London A: Mathematical, Physical and Engineering Sciences*, volume 465, pages 2877–2895. The Royal Society, 2009.

F. Simonetti, L. Huang, N. Duric, and P. Littrup. Diffraction and coherence in breast ultrasound tomography: A study with a toroidal array. *Medical physics*, 36(7):2955–2965, 2009.

C. R. Smart, R. E. Hendrick, J. H. Rutledge, and R. A. Smith. Benefit of mammography screening in women ages 40 to 49 years. current evidence from randomized controlled trials. *Cancer*, 75(7):1619–1626, 1995.

S. Sokolov. On the problem of the propagation of ultrasonic oscillations in various bodies. *Elek Nachr Tech*, 6(454-460):92, 1929.

Z. Song, P. R. Williamson, and R. G. Pratt. Frequency-domain acoustic-wave modeling and inversion of crosshole data: Part ii-inversion method, synthetic experiments and real-data results. *Geophysics*, 3:796–809, 1995.

R. Stotzka, J. Wuerfel, T. O. Mueller, and H. Gemmeke. Medical imaging by ultrasound computer tomography. In *Medical Imaging 2002*, pages 110–119. International Society for Optics and Photonics, 2002.

T. L. Szabo. *Diagnostic ultrasound imaging: inside out*. Academic Press, 2004.

T. L. Szabo and J. Wu. A model for longitudinal and shear wave propagation in viscoelastic media. *The Journal of the Acoustical Society of America*, 107(5):2437–2446, 2000.

L. Tabar, G. Fagerberg, S. Duffy, N. Day, A. Gad, and O. Gröntoft. Update of the swedish two-county program of mammographic screening for breast cancer. *Radiologic Clinics of North America*, 30(1):187–210, 1992.

M. T. Taner, F. Koehler, and R. Sheriff. Complex seismic trace analysis. *Geophysics*, 44(6): 1041–1063, 1979.

A. Tarantola. *Inverse problem theory: Methods for data fitting and parameter estimation*. Elsevier, Amsterdam, 1987.

C. J. Tejero, D. Dagnino, V. Sallarès, and C. R. Ranero. Comparative study of objective functions to overcome noise and bandwidth limitations in full waveform inversion. *Geophysical Journal International*, 203(1):632–645, 2015.

A. N. Tikhonov. Regularization of incorrectly posed problems. SOVIET MATHEMATICS DOKLADY, 1963.

N. M. Tole and H. Ostensen. *Basic physics of ultrasonographic imaging*. World Health Organization, 2005.

B. Treeby, B. Cox, and J. Jaros. k-wave a matlab toolbox for the time domain simulation of acoustic wave fields user manual, 2012a.

B. E. Treeby and B. Cox. Modeling power law absorption and dispersion for acoustic propagation using the fractional laplacian. *The Journal of the Acoustical Society of America*, 127(5):2741–2748, 2010a.

B. E. Treeby and B. Cox. Modeling power law absorption and dispersion in viscoelastic solids using a split-field and the fractional laplaciana). *J. Acoust. Soc*, 4:1499–1510, 2014.

B. E. Treeby and B. T. Cox. k-wave: Matlab toolbox for the simulation and reconstruction of photoacoustic wave fields. *Journal of biomedical optics*, 15(2):021314–021314, 2010b.

B. E. Treeby, E. Z. Zhang, A. S. Thomas, and B. T. Cox. Measurement of the ultrasound attenuation and dispersion in whole human blood and its components from 0–70 mhz. *Ultrasound in Medicine and Biology*, 37(2):289–300, 2011.

B. E. Treeby, J. Jaros, A. P. Rendell, and B. Cox. Modeling nonlinear ultrasound propagation in heterogeneous media with power law absorption using a k-space pseudospectral method. *The Journal of the Acoustical Society of America*, 131(6):4324–4336, 2012b.

J. Tromp, C. Tape, and Q. Liu. Seismic tomography, adjoint methods, time reversal and banana-doughnut kernels. *Geophysical Journal International*, 160(1):195–216, 2005a.

J. Tromp, C. Tape, and Q. Liu. usct compress sensing buscarrrrr. *Geophysical Journal International*, 160(1):195–216, 2005b.

J. J. Vaquero, J. Cal-Gonzalez, M. Perez-Liba, J. L. Herraiz, M. Desco, and J. M. Udias. Improving the image quality of high energy positron based tracers using a novel tissue-dependent, spatially-variant positron range correction. *Journal of Nuclear Medicine*, 57(supplement 2): 475–475, 2016.

K. Wang, T. Matthews, F. Anis, C. Li, N. Duric, and M. Anastasio. Waveform inversion with source encoding for breast sound speed reconstruction in ultrasound computed tomography. *Ultrasonics, Ferroelectrics, and Frequency Control, IEEE Transactions on*, 3:475–493, 2015.

Y. Wang, T. Nemeth, and R. T. Langan. An expanding-wavefront method for solving the eikonal equations in general anisotropic media. *Geophysics*, 71(5):T129–T135, 2006.

J. J. Wild and J. M. Reid. Application of echo-ranging techniques to the determination of structure of biological tissues. *Science (New York, NY)*, 115(2983):226–230, 1952.

J. E. Wilhjelm, A. Illum, M. Kristensson, and O. T. Andersen. Medical diagnostic ultrasound-physical principles and imaging. *By Andersen Biomedical Engineering, DTU Elektro Technical University of Denmark, Ver*, 3(2), 2013.

J. Wiskin, D. Borup, S. Johnson, M. Berggren, T. Abbott, and R. Hanover. Full-wave, non-linear, inverse scattering. In *Acoustical Imaging"Full-wave, non-linear, inverse scattering,"*, pages 183–193. 2007.

World Cancer Report. International agency for research on Cancer . `http://www.iarc.fr/en/publications/pdfs-online/wcr/2008/wcr_2008.pdf`, 2008. Retrieved 2017-02-26.

World Health Organization. (WHO)Breast cancer: prevention and control. `http://www.who.int/cancer/detection/breastcancer/en/`, 2012. Retrieved 2017-02-26.

D. Yang, J. Peng, M. Lu, and T. Terlaky. Optimal nearly analytic discrete approximation to the scalar wave equation. *Bulletin of the Seismological Society of America*, 96(3):1114–1130, 2006.

Y. O. Yuan and F. J. Simons. Multiscale adjoint waveform-difference tomography using wavelets. *Geophysics*, 79(3):WA79–WA95, 2014.

M. Yunus, N. Masroor, and J. Yaqoob. Mammographic criteria for determining the diagnostic value of microcalcifications. *Journal-Pakistan Medical Association*, 54(1):24–28, 2004.

C. Zhou, W. Cai, Y. Luo, G. T. Schuster, and S. Hassanzadeh. Acoustic wave-equation traveltime and waveform inversion of crosshole seismic data. *Geophysics*, 60(3):765–773, 1995.

Q. Zhu and B. D. Steinberg. Wavefront amplitude distribution in the female breast. *The Journal of the Acoustical Society of America*, 96(1):1–9, 1994.